2D/3D Heterostructure Wide-Bandgap Perovskite Solar Cells for Efficient Tandem Photovoltaics

Zur Erlangung des akademischen Grades einer

DOKTORIN DER INGENIEURWISSENSCHAFTEN (Dr.-Ing.)

von der KIT-Fakultät für
Elektrotechnik und Informationstechnik des
Karlsruher Instituts für Technologie (KIT)

angenommene

Dissertation

von

Saba Gharibzadeh
geb. in Ardebil, Iran

Tag der mündlichen Prüfung: 01.08.2022

Hauptreferent: Tenure-Track-Prof. Dr. Ulrich W. Paetzold, Karlsruher Institut für Technologie

Korreferent: Prof. Dr. Michael Saliba, Universität Stuttgart

Kurzfassung

Um den zukünftigen weltweiten Strombedarf zu decken und gleichzeitig die CO_2-Emissionen durch fossile Energieträger zu senken, ist die Entwicklung von Photovoltaiktechnologien eine der wichtigsten Lösungen zur Stromerzeugung aus erneuerbaren Energiequellen. Gegenwärtig wird das enorme Wachstum der Photovoltaik hauptsächlich durch kristalline Silicium-Solarzellen (c-Si) vorangetrieben. Allerdings nähert sich ihr Wirkungsgrad (power conversion efficiency, PCE) bereits der theoretischen Grenze von 29%. Eine der vielversprechendsten Lösungen zur Überwindung dieses Limits ist die Kombination von Silicium als untere Zelle mit einer oberen Zelle mit breiter Bandlücke in einer Tandemkonfiguration (Mehrfachübergang). Organisch-anorganische Metallhalogenid-Perowskit-Solarzellen (perovskite solar cells, PSCs) gehören zu den aufstrebenden Photovoltaik-Technologien und weisen aufgrund ihrer hervorragenden optoelektronischen Eigenschaften, variablen Abscheidemethoden und ihres potenziell kostengünstigen Herstellungsprozesses ein großes Potenzial als obere Zelle mit einer breiten Bandlücke auf. Tandemsolarzellen auf Perowskit-Basis haben bereits einen hohen Wirkungsgrad von 29,8 % erreicht, der über dem theoretischen Grenzwert von Silicium-Einzelschichtzellen liegt. Um diesen Wirkungsgrad noch weiter zu steigern, muss, als entscheidende Herausforderung das große Leerlaufspannungsdefizit (definiert als E_g/q-V_{OC}, wobei E_g die Perowskit-Bandlücke ist) in PSCs mit breiter Bandlücke verringert werden. Dieses ist aufstarke nicht-strahlende Rekombination zurückzuführen, die hauptsächlich durch die defektunterstützte Rekombination im Inneren oder an der Oberfläche der Perowskit-Dünnschicht oder durch eine ungeeignete Bandanpassung an der Grenzfläche zwischen der Perowskit- und den Ladungstransportschichten verursacht wird.

Ziel dieser Arbeit ist die Reduktion dieses Photospannungsverlustes in PSC hoher Bandlückedurch die Entwicklung neuartiger Passivierungsstrategien unter Verwendung zweidimensionaler (2D) Ruddlesden-Popper Perowskit-Materialien, um die nicht-radiative Rekombination zu minimieren. In diesem Zusammenhang wird als Ausgangspunkt eine neuartige Strategie unter Verwendung einer 2D/3D-Heterostruktur als Oberflächenpassivierung und einer Elektronensperrschicht zwischen einem Perowskit mit großer Bandlücke (1,72 eV) und einem Lochtransportmaterial in PSCs mit n-i-p-Architektur eingesetzt. Die auf dieser Strategie basierenden Bauelemente weisen eine signifikante Verbesserung der V_{OC} von bis zu 80 mV auf, was 90 % der Shockley-Queisser-Grenze für die gegebene Bandlücke entspricht. Als Nächstes wird diese erfolgreiche Strategie in PSCs mit konstruierten Bandlücken angewandt, um die PCE von mechanisch gestapelten 4-Terminal (4T)-Tandemsolarzellen zu maximieren, indem die optimale Bandlücke des Perowskit-Absorbers bestimmt wird. Die Ergebnisse zeigen, dass die Oberflächenpassivierungsstrategie unabhängig von der Bandlücke des Perowskits zu einer Gesamtverbesserung von 45 mV für alle Bauelemente führt. Nachfolgend wird gezeigt, dass die Kombination der 2D/3D-Heterostruktur-PSCs verschiedener Bandlücken in 4T-

Perowskit/c-Si oder 4T-Perowskit/CIGS-Tandemsolarzellen eine vergleichbare PCE für den E_g-Bereich von 1,65-1,74 eV besitzt. Darüber hinaus zeigt dieses experimentelle Ergebnis zum ersten Mal, dass hohe Bandlücken (E_g > 1,74 eV) in PSCs nichtideal sind, um die höchste PCE in einer 4T-Tandemkonfiguration zu erreichen, was den Vorhersagen von Simulationen widerspricht. Schließlich wird angesichts der Bedeutung von PSCs mit p-i-n-Architektur für 2T-Tandemsolarzellen eine doppelte Passivierungsstrategie eingeführt, bei der ein langkettiges Alkylammoniumsalz sowohl als Additiv in der Perowskitschicht als auch zur Oberflächenbehandlung verwendet wird, um gleichzeitig die Korngrenzen und die Grenzfläche zwischen Perowskit und elektronentransportierender Schicht zu passivieren. Das dual passivierte Bauelement weist einen hohen PCE-Wert von 22,7 % auf, der einer der höchsten bisher für p-i-n-PSCs veröffentlichenWirkungsgrade ist. Darüber hinaus werden die p-i-n-PSCs mit breiter Bandlücke, die auf der entwickelten Doppelpassivierungsstrategie basieren, in 4T-Perowskit/CIGS- und 2T-Perowskit/Silizium-Tandemsolarzellen integriert, um die Effizienz von Perowskit-basierten Tandem-Bauelementen im Vergleich zu den Einzelzelleffizienzen weiter zu verbessern.

Abstract

To meet the global electricity demand in the future while lowering the energy-related CO_2 emissions, the development of renewable energy technologies based on photovoltaics is one of the key solutions. Currently, the enormous growth of photovoltaics is mainly driven by single-junction crystalline silicon (c-Si) solar cells. However, their power conversion efficiency (PCE) is already approaching the theoretical limit (29%). One of the most promising solutions to go beyond this limit is coupling silicon as the bottom cell with a wide-bandgap top cell in a multijunction (tandem) configuration. Organic-inorganic metal-halides perovskite solar cells (PSCs), as one of the emerging photovoltaic technologies, show great potential for such wide-bandgap due to their superb optoelectronic properties, variable deposition techniques and potentially low-cost fabrication process. The perovskite-based tandem solar cell has already demonstrated high efficiency of 29.8% which is above the theoretical limit of the single junction silicon cell. However, to improve this PCE one step further, one of the crucial challenges that are needed to address is reducing the large open-circuit voltage (V_{OC}) deficit (defined as $E_g/q - V_{OC}$, where E_g is the perovskite bandgap) in wide-bandgap PSC. This originates from the severe non-radiative recombination mainly due to the defect-assisted recombination within the bulk or at the surface of the perovskite or inappropriate band alignment at the interface between the perovskite and charge transport layers.

The aim of this thesis is to deal with this photovoltage loss in wide-bandgap PSC by developing novel passivation strategies using emerging 2D Ruddlesden–Popper perovskite materials in order to minimize non-radiative recombination. In this regard, as a starting point, a pioneering strategy utilizing a 2D/3D heterostructure is employed as surface passivation and electron-blocking layer between wide-bandgap perovskite (1.72 eV) and hole transport material in PSCs with standard **n-i-p** architecture. The devices based on this strategy demonstrate a significant enhancement in V_{OC} up to 80 mV, corresponding to 90% of the Shockley-Queisser limit for the given bandgap. Next, this successful strategy is employed in PSCs with engineered bandgaps in order to maximize the PCE of the mechanically stacked 4-terminal (4T) tandem devices by determining the optimum E_g of the perovskite absorber. The results show that regardless of the perovskite bandgap, the surface passivation strategy results in an overall improvement of 45 mV for all devices. In the following, coupling the 2D/3D heterostructure PSCs with engineered bandgap into 4T perovskite/c-Si or 4T perovskite/CIGS tandem solar cell exhibit a comparable PCE for the E_g ranging from 1.65-1.74 eV. In addition, this experimental finding for the first time reveals that wide-bandgap PSC with $E_g > 1.74$ is not the ideal bandgap to reach the highest PCE for the 4T tandem configuration, which contradicts predictions made by simulations based on the detailed-balance principle. Finally, in view of the importance of PSCs with **p-i-n** architecture for 2T tandem solar cells, a dual passivation strategy is introduced using a long-chain alkylammonium salt both as an additive into the perovskite bulk and for surface

treatment to simultaneously passivate the grain boundaries and the perovskite/electron transporting layer interface. The dual passivated device exhibits a high PCE of 22.7%, which is one of the highest reported for p-i-n PSCs so far. Further, the wide-bandgap p-i-n PSCs based on the developed dual passivation strategy are integrated into 4T perovskite/CIGS and 2T perovskite/c-Si tandem solar cells to further improve the efficiency of perovskite-based tandem devices with respect to the single-junction efficiencies.

Table of Contents

1. Introduction

The "Sixth Assessment Report" from the Intergovernmental Panel on Climate Change (IPCC) published on Aug. 2021 indicates that human activity has led to an increase in the average temperature of our planet by at least 1°C since the industrial revolution.[1] A substantial portion of this increase (40%) is attributed to the use of fossil fuels (oil, coal and natural gas) that release carbon dioxide (CO_2) and other greenhouse gases.[2–4] At the current rate, the temperature is expected to increase by 1.5°C by 2040.[5] This is a "**Code Red**" for humanity as we are already experiencing some of the uncontrolled consequences of climate change today: rising sea levels, enduring heat waves, periodic extreme colds and flash floods are becoming more prominent.[1] To avoid these profound effects of climate change, bold action must be taken to slow down the current rate of CO_2 emission in alignment with the goals of the 2015 International Paris Agreement, which aims to hold the average increase in global temperature below 1.5°C.[6] However, one also has to consider the growing global demand for energy. According to the 2021 outlook of the Energy Information Administration (EIA), energy demand is expected to rise nearly 50% by 2050 compared to the 2020 level due to population growth coupled with economic and technology development.[7] Therefore, a complete transformation of global energy infrastructure towards clean and renewable energy is imperative to secure a peaceful and sustainable future while meeting the demand for rising energy consumption.

Among all renewable energy technologies, photovoltaics (PV) plays an essential contribution in the ongoing energy transition, allowing for the direct conversion of sunlight into electrical energy.[8,9] Thanks to the abundant resource of the sun along with remarkable market potential and cost-effectiveness, the solar PV share of global power generation can rise to 25% by 2050 (reported by the International Renewable Energy Agency (IRENA) 2019).[8,10] In this context, the global installed PV capacity has increased up to 707 GW_p in 2020, which already represents a market growth of 30% as compared to the worldwide cumulative PV capacity in 2019.[11] Despite these advances, the pathway towards further investments, capacity expansion and installation of PV requires a steady reduction of prices to increase competitiveness compared to carbon-based energy resources such as coal or natural gas. This means a low levelized cost of electricity (LCOE), which refers to the cost of

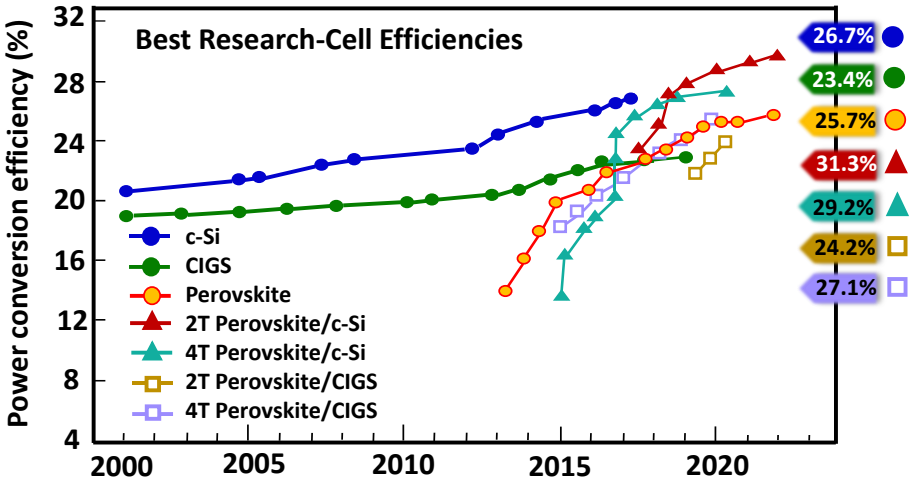

Figure 1-1: Power conversion efficiency evolution of single-junction perovskite, silicon (Si), Copper indium gallium selenide (CIGS) and perovskite-based tandem solar cells in a 2-terminal (2T) and 4-terminal (4T) configuration in combination with Si, and CIGS solar cells. Adapted from National Renewable Energy Laboratory (NREL) efficiency chart [13].

energy in €/kWh, is highly desirable. Prediction for forecasts in Germany shows that in 2040 the LCOE will be between 1.92 and 3.51 €Cent/kWh for ground-mounted PV systems, which will be remarkably lower than the average LCOE of any fossil fuel power plant in the same year.[11] To meet this prediction, increasing the power conversion efficiency (PCE) of solar PV is pivotal. In terms of the current market, silicon solar cells dominate more than 95% of the global market share.[12] However, the record PCE of crystalline-silicon (c-Si) solar cells has reached 26.7%,[13] which is already converging towards its theoretical efficiency limit (~29.4%).[14] Thus, further significant improvements are improbable for c-Si PV technology. A promising approach to overcome this limitation is to use a multi-junction solar cell configuration (so-called tandem solar cell) which utilizes materials of different bandgaps stacked atop of each other. The simplest multi-junction configuration combines two subcells, each of which absorbs a specific part of the solar spectrum more efficiently than an equivalent single-junction device, thereby increasing the theoretical PCE limit to around 45%.[15] Reaching such high efficiencies is indeed an attractive route to reduce the LCOE.

Currently, the most efficient tandem solar cell (with two subcells) is based on a III–V semiconductor (gallium arsenide) combined with c-Si, showing a champion PCE of 32.8% under 1-Sun illumination.[16] Although this high efficiency is an extraordinary achievement, complex manufacturing processes and high III–V material costs restrict such devices to space-based or concentrator PV applications.[17,18] A comparatively new PV material with a high-efficiency, potentially low-cost fabrication process and upscaling feasibility comes with the emergence of organic-inorganic halide perovskites absorbers.[19–21] In particular, the possibility of tuning the bandgap (E_g) of the perovskite absorber from 1.5 to 2.3 eV makes them a uniquely suitable candidate for inclusion in tandem solar cells.[22–25] In terms

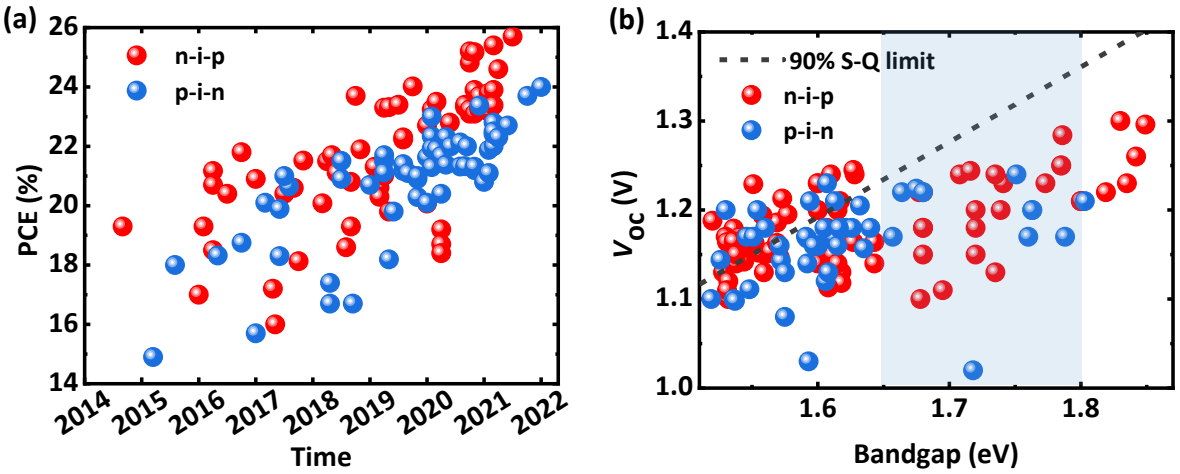

Figure 1-2: Champion (a) power conversion efficiencies (PCEs) of n-i-p vs. p-i-n perovskite solar cells and (b) open-circuit voltage (V_{OC}) as a function of perovskite bandgap obtained from the best mixed-halide perovskite solar cells having decent power conversion efficiency (PCE) >12% reported in the literature. The dashed line displays a V_{OC} representing 90% of Shockley-Queisser (S-Q) limit.

of single-junction architecture, perovskite solar cells (PSCs) have already demonstrated enormous progress in PCE, with an increase from only 3% in 2009[26] to a recent record PCE of 25.7%.[27] Recently, a similar stunning breakthrough is also observed for perovskite-based tandem solar cells in conjunction with c-Si, achieving a PCE of 29.8% (Figure 1-1).[13] This superior PCE compared to the respective single-junction devices indicates a great potential for perovskite-based tandem devices, facilitating their integration into the PV market in the near future. It is worth stating that several startup companies, such as Oxford PV, Swift Solar, and Tandem PV are already attempting to bring this technology into the global PV market.[28]

Perovskite-based tandem solar cells are typically fabricated in either a two- or four-terminal (2T or 4T) configuration, each of which has specific advantages and drawbacks (details of each configuration can be found in Chapter 2). The main advantage of the mechanically stacked 4T configuration is that both subcells are electrically isolated and can operate independently at their maximum power point. This allows a large degree of freedom in the fabrication process (e.g., temperature, solvent, substrate roughness, etc.) for each subcell, which is of particular importance for PSCs.[29–31] As a result, a top PSC can be employed in both two common planar architectures namely standard n-i-p or inverted p-i-n, which is defined based on the sequence of functional layers in the device (a detailed description of each architecture can be found in Chapter 2). However, one problem associated with the 4T configuration is the need for a second direct current/alternating current (DC/AC) inverter for the tandem system, which implies an additional cost to the PV module.[31,32] A possible alternative is a monolithically stacked 2T that exhibits the cost-effective tandem configuration, as similar to a single junction solar cell only two electrodes with one DC/AC inverter are needed.[24,31] Nevertheless, due to a series connection of both subcells, current-matching between the top and bottom cells is required to maximize the

PCE, which results in a limitation in the bandgap combinations.[30,33] Besides, as the top PSC is directly grown on top of the bottom c-Si or CIGS solar cells, the fabrication process of the top cell can easily damage the underlying bottom cell. For this reason, although so far single-junction PSCs with the n-i-p architecture have demonstrated the highest reported PCE (25.7%), applying them to the 2T perovskite/c-Si tandem solar cell is crucially inhibited due to their high-temperature fabrication process of electron transport layer and the lack of the sufficient optical transparency for hole-transporting layer.[34–37] Therefore, the monolithic tandem solar cell research is focused on PSC with p-i-n architecture. This highlights the importance of developing the high-efficiency p-i-n PSCs, as their PCE is still lagging behind in comparison with their n–i–p counterparts as shown in Figure 1-2a.

Notably, for both 2T and 4T perovskite-based tandem solar cells, a wide-bandgap perovskite absorber in the range of 1.65-1.85 eV (according to the detailed-balance calculation) is needed for optimal performance when used as the top cell absorber in conjunction with a low bandgap Si (1.1 eV) or CIGS (1.2 eV) bottom cell.[33,38] Such wide-bandgap absorbers play a critical role in harvesting the high-energy photons in a tandem configuration as well as yielding high open-circuit voltage (V_{OC}). The most straightforward way to widen the bandgap of the perovskite is by varying the halide ratio (for example by simple substitution of iodine (I) with bromine (Br)) in the composition of the perovskite material as we will discuss in detail in Chapter 2.[22,39] However, achieving a high V_{OC} (close to the theoretical limit) in such wide-bandgap PSCs is a great challenge, as increasing the bandgap is not directly accompanied by an increase in V_{OC}, resulting in high V_{OC} deficits (defined as E_g/q - V_{OC}).[40–43] The primary causes for this large V_{OC} loss arise from severe non-radiative recombination losses due to a high density of defects present: (i) in the bulk/grain boundaries of the wide-bandgap perovskite absorber layer and (ii) at the surface/interface between perovskite and selective charge transport layers (CTLs).[44–48] Furthermore, an inappropriate energy level alignment at the perovskite/CTL interface and phase segregation of the halide ions in the wide bandgap perovskite absorbers can also limit the V_{OC} as compared to low bandgap absorbers.[49–51] So far, there has been no report in the literature with a V_{OC} above 90% of the Shockley-Queisser (S-Q) limit for the wide-bandgap PSCs (1.65-1.85 eV), whereas this is not the case for low-bandgap PSCs in the range of 1.5 to 1.62 eV as displayed in Figure 1-2b.

In order to obtain the full potential for 2T or 4T perovskite-based tandem solar cells, the main aim of this thesis is to tackle the V_{OC} loss in various wide-bandgap PSCs in both n-i-p and p-i-n architectures. In this regard, recently, the technique of employing two-dimensional (2D) perovskites based on long-chain organic cations into the bulk or at the surface of the 3D perovskite absorber layer has been extensively reported due to effective reduction in non-radiative recombination and enhancement in device stability.[47,52–54] However, in terms of material and device engineering still numerous kinds of novel 2D perovskites can be investigated to boost the performance of PSC beyond the intrinsic limits.

Motivated by the excellent properties of 2D perovskites (as we will discuss in detail in Chapter 2), we explore novel 2D materials for our PSC together with the effective deposition strategy to reduce the V_{OC} loss by (i) passivating the defects at the surface/interface of the perovskite and the CTLs as well as at the grain boundaries of the 3D perovskite absorber and (ii) the formation of an electron or hole blocking layer.

The content of this thesis is outlined as follows:

Chapter 2: This chapter first provides a comprehensive introduction to the structural and physical properties of organic-inorganic perovskite semiconductors. Further, it outlines a fundamental review of the working principle of the PSCs as well as tandem solar cell configurations.

Chapter 3: This chapter focuses on materials, experimental and characterization techniques used within this thesis for the processing of opaque and semi-transparent PSC as well as their integration into 2T and 4T tandem configurations.

Chapter 4: This chapter deals with minimizing the large V_{OC} loss in mixed-halide wide-bandgap PSCs in the **n-i-p** architecture. A novel strategy utilizing a 2D/3D perovskite heterostructure is introduced both as an effective surface passivation and electron blocking layer at the interface between the perovskite and the hole transporting layer.

Chapter 5: This chapter presents the application of the high-efficiency wide-bandgap PSCs employing the 2D/3D perovskite heterostructure discussed in Chapter 4 in mechanically-stacked 4T tandem solar cells. First, we investigate the effect of the 2D/3D heterostructure on the performance of opaque and semitransparent double-cation PSCs with different bandgaps engineered from 1.60 to 1.85 eV. Further, the resultant semi-transparent PSCs based on 2D/3D perovskite heterostructure are applied as a top cell to 4T perovskite/c-Si and 4T perovskite/CIGS tandem solar cells to maximize the PCE of the 4T perovskite-based tandem devices based on the optimum bandgap of the top semi-transparent PSC.

Chapter 6: In view of the importance of p-i-n PSCs architecture for 2T tandem solar cells, this chapter deals with the reduction of the V_{OC} loss in PSCs in the **p-i-n** architecture. A dual passivation strategy is introduced using a long-chain alkylammonium salt both as an additive into the perovskite bulk and for surface treatment to simultaneously passivate the grain boundaries and the perovskite/electron transporting layer (ETL) interface. Further, the wide-bandgap p-i-n PSCs based on our developed dual passivation strategy are integrated into 4T perovskite/CIGS and 2T perovskite/silicon tandem solar cells to further improve the efficiency of perovskite-based tandem devices with respect to the single-junction efficiencies

Chapter 7: This chapter summarizes the key results presented in this thesis and, as an outlook, provides a roadmap for future research in this area.

2. Theoretical Background

This chapter introduces metal-halide perovskite semiconductors and briefly describes their outstanding optoelectronic properties. It is then followed by the basic working principles of perovskite solar cells (PSCs), device architecture as well as photovoltaic characteristics. In the last part, we explain the plausible ways to go beyond the efficiency limits of single-junction solar cells by introducing multijunction (tandem) configurations.

2.1. Organic-inorganic metal halide perovskite semiconductors

Perovskites are introduced for the first time with the discovery of $CaTiO_3$ by G. Rose and named after the Russian mineralogist Lev Perovski. In general, the component with the general formula ABX_3 represents the perovskite crystal structure, where A is a monovalent cation, B is a divalent metal cation and X is an anion. In this chapter, we provide an overview of the outstanding optoelectronic properties of the state-of-the-art perovskite with a complex composition "organic-inorganic metal halide perovskite".

2.1.1. Structural properties of ABX_3 perovskites

The cubic crystal structure of the perovskite material ABX_3 is illustrated in Figure 2-1, where the A site is surrounded by a corner-sharing octahedral BX_6 unit such that B is placed at the center of this octahedral $[BX_6]^{4-}$ cluster, forming a three-dimensional arrangement.[55] In

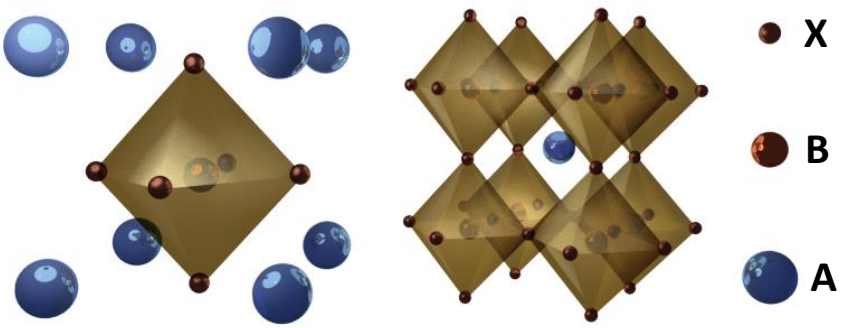

Figure 2-1: Schematic illustration of the perovskite crystal structure with the cubic phase. The left panel demonstrates the unit cell of the perovskite absorber.

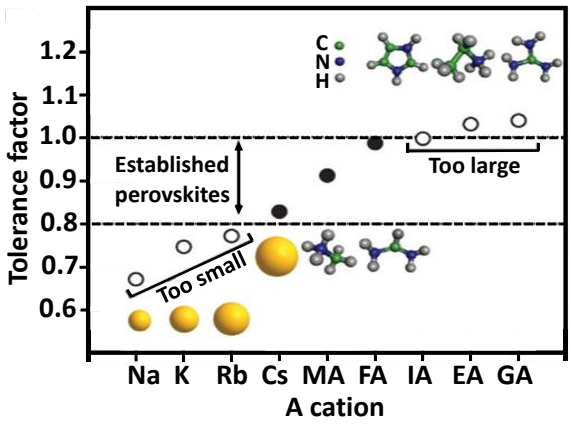

Figure 2-2: The tolerance factor of perovskite with the structure of ABX_3. Small A cations (sodium (Na), potassium (K) and rubidium (Rb)) present a tolerance factor lower than 0.8. This factor is between 0.8 and 1.0 for established A cations (Cs, MA, FA) and greater than 1 for too large cations (imidazolium (IA), ethylamine (EA), guanidinium (GA)), etc. Adapted from reference [57].

case of organic-inorganic perovskite crystal, the A site ions are commonly occupied by methylammonium (MA^+), formamidinium (FA^+), cesium (Cs^+), etc., the B site metal cations are lead (Pb^{2+}), tin (Sn^{2+}), etc., and the X site is chloride (Cl^-), bromide (Br^-) or iodide (I^-).[56] Depending on the A cation size and its interaction with the BX_6 octahedra, perovskites can also form other crystal structures such as orthorhombic or tetragonal.[57] The rule of thumb to determine if perovskites can form a stable crystal structure is based on Goldschmidt's Tolerance Factor (t),[58] which is defined using the following expression:

$$t = \frac{r_A + r_B}{\sqrt{2}(r_B + r_X)} \tag{2.1}$$

where, r_A, r_B and r_c are the ionic radii of the organic cation, metal cation and halide, respectively. A stable 3D cubic phase is expected to form when the value of t is within the range of $0.8 < t < 1$, whereas the lower range $t < 0.8$ results in a distorted structure due to the tilted BX_6 octahedra which decreases the symmetry of the structure.[55] As a result, only a narrow range of the organic cations such as Cs^+, MA^+, and FA^+ has a suitable size to fit into the structure and form a stable 3D lattice, as depicted in Figure 2-2.[59] Furthermore, when the size of the A cation is too large such that it cannot fit into the crystal lattice ($t > 1$), the perovskite lattice structure is transformed from the bulk 3D into lower-dimensional phases with different optoelectronic properties. This structure can either be a Ruddelsen-Popper[60,61] or Dion-Jacobson[62] phase of the perovskite absorber. Later in Section 2-1-3, we will explain in detail the formation of low-dimensional perovskites.

2.1.2. Optoelectronic properties of metal-halide perovskites

Benefiting from a high absorption coefficient ($\alpha > 10^{-4}$ cm^{-1}) with a direct optical bandgap, already a thin layer of the absorber (d ≈ 300-400 nm) is sufficient for the fabrication of high-efficiency PSCs. Thereby, challenges related to the effective collection of photogenerated

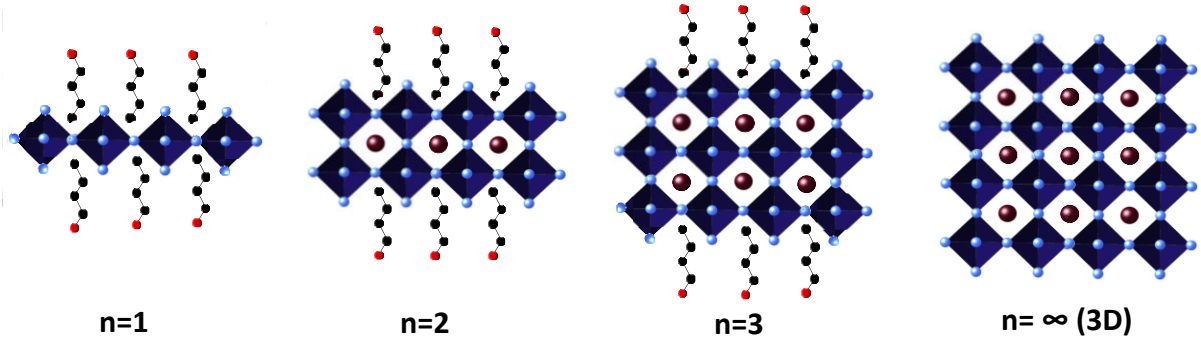

Figure 2-3: Schematic illustration of 2D perovskite demonstrating the dimensionality evolution from 2D (i.e., n=1) to 3D (n = ∞).

carriers are reduced.[63] The photogenerated excitons of the perovskite absorber also exhibit small binding energy (about 30 meV), meaning that only a low energy (room temperature) is needed to dissociate these excitons into free charge carriers, thus, a high number of free charge carriers can be created.[64] These free carriers demonstrate high mobility ($\mu \approx 10$ $cm^2 V^{-1} s^{-1}$) and a long charge diffusion length exceeding 1 µm, indicating that charge carriers can travel a long distance before recombining.[65,66] More importantly, tuning the bandgap of the perovskite absorber in a wide range between 1.2-3.1 eV is particularly interesting for multijunction solar cell applications.[67] This bandgap tunability is possible by simply varying the elemental composition, i.e. the stoichiometry, or dimensionality of the perovskite crystal. For instance, methylammonium-based perovskite ($MAPbI_3$) exhibits a bandgap of 1.6 eV. Substituting iodide (I) with smaller halides such as bromine (Br) or chlorine (Cl) can modify its bandgap to 2.3 eV and 3.1 eV, respectively.[68] In fact, the theoretical study based on density functional theory has shown that the valence band maximum in the metal-halide perovskite as a direct bandgaps semiconductor is formed by coupling an antibonding state of B cation s orbitals and X anion p orbital. On the other hand, a conduction band minimum is derived from the coupling of a less antibonding and more nonbonding B cation and X anion p orbitals.[69] As a result, any elemental substitution in the B or X sites of the perovskite structure can vary the overlap between the B-X site and modify the bandgap. In case the overlap or distance of the B-X site becomes larger, this can result in a perovskite with a low bandgap, while a reduction in the distance leads to the perovskite with a wide bandgap.[70] Therefore, these intrinsic properties make the perovskite absorber a superior candidate for various optoelectronic devices such as photovoltaics, light-emitting diodes (LEDs) and laser applications.[63,71,72]

2.1.3. Two-dimensional Ruddlesden-Popper perovskites

Inserting too large organic cations into the A site of the perovskite crystal leads to a deviation in the 3D lattice, forming a 2D (sheet), 1D (wire), or 0D (dots) structure.[73] Among all these structures, 2D layered as called Ruddlesden-Popper (2D-RP) or Dion-Jacobson perovskites are found to be superior materials for photodetectors, LEDs and solar cells applications, thanks to their tunable optoelectronic properties and exceptional

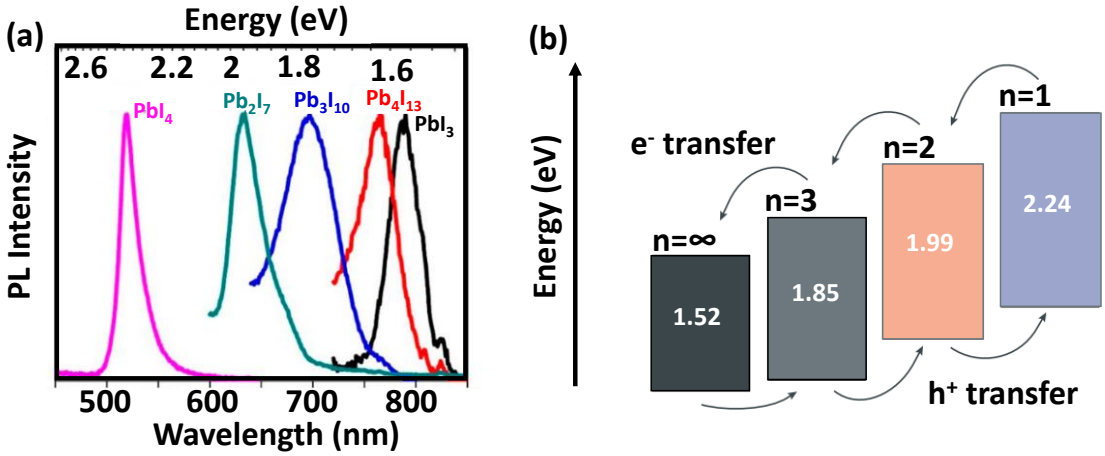

Figure 2-4: (a) photoluminescence emission of 2D-RP BA_2PbI_4 (n = 1), $BA_2MAPb_2I_7$ (n = 2), $BA_2MA_2Pb_3I_{10}$ (n = 3), $BA_2MA_3Pb_4I_{13}$ (n = 4), and $MAPbI_3$ (n = ∞) perovskite layer. (b) Schematic of band energy alignment of the corresponding $(BA)_2(MA)_{n-1}Pb_nI_{3n+1}$ perovskite with different n that presents the values of the bandgaps. Adapted from references [78,80].

environmental stability.[62,74,75] The 2D perovskites can be represented by the general formula $(R)_m(A)_{n-1}B_nX_{3n+1}$ (n=1,2,3,4,.., ∞), where R is long-chain aliphatic or aromatic alkylammonium cations acting as a spacer between the perovskite layers, m is either 1 for Dion-Jacobson phase (organic cations with two binding groups) or 2 for RP phase (organic cations with a single binding group), A is conventional cations (MA^+, FA^+, etc.), B is a metal cation (Pb^{2+}, Sn^{2+}, etc.) and X is halides.[76] Here, n represents the thickness of the 2D perovskite which is identified by the number of octahedra corner-sharing $[BX6]^{4-}$ layers sandwiched between two bulky organic spacer layers that are connected via a combination of Coulombic and hydrophobic forces.[77] Depending on the thickness of the 2D layer (n), the perovskite is categorized as 2D (n = 1), quasi-2D (n = 2-5) or 3D (n = ∞) phase, all exhibiting different optoelectronic properties as displayed in Figure 2-3. For example, for the 2D-RP $(BA)_2(MA)_{n-1}Pb_nI_{3n+1}$ perovskite thin film, by increasing the thickness (n) of the inorganic layer the bandgap varies from 2.24 eV for BA_2PbI_4 (n = 1) to 1.52 eV for pure $MAPbI_3$ with n = ∞ (Figure 2-4).[78–80] The example of the most common bulky organic cations are butyl ammonium (BA),[47] phenylethylammonium (PEA),[76] iso-butylammonium (iso-BA),[81] n-Octylammonium (OA), etc (Figure 2-5).[82]

Compared to 3D perovskites, 2D perovskite structures exhibit distinctive features such as higher ambient and operational device stabilities. This is mainly due to the hydrophobicity nature of bulky organic cations or the organic group's interaction (such as hydrogen, halogen bonds and van der Waals interactions) that protects the surface of the perovskite and the inner lattice from moisture and humidity degradation.[83,84] Moreover, the devices exhibit higher thermal stability due to the low volatility of the long-chain organic cations.[85] The first quasi-2D-based metal halide PSC was reported by incorporation of PEA into a $MAPbI_3$ perovskite absorber, having the structure of $(PEA)_2MA_2Pb_3I_{10}$.[84] Although the resultant devices demonstrated a very low PCE of 4.7%, the moisture stability of the devices

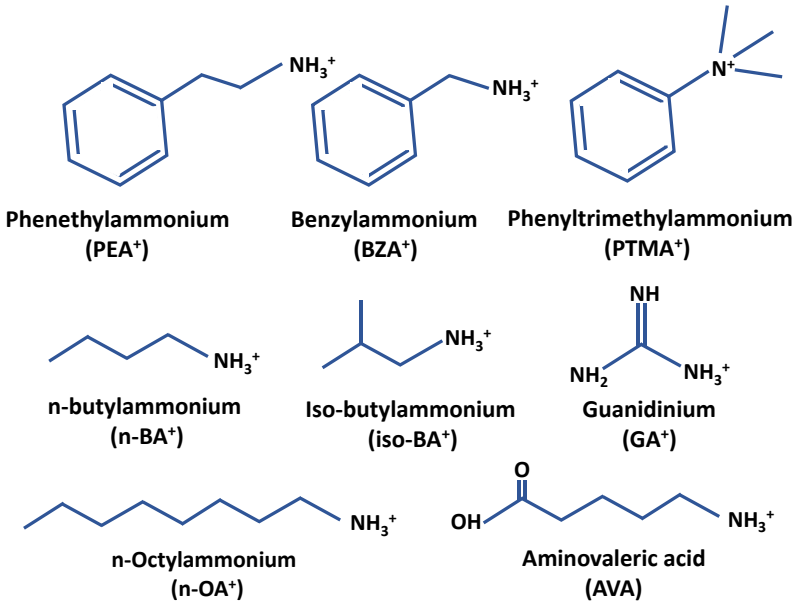

Figure 2-5: Molecule structure of large organic spacer cations commonly employed for the formation of 2D perovskites.

improved significantly after 46 days in an atmosphere with 52% relative humidity (RH) as compared to the reference. However, the performance of the 2D-based PSCs lags behind their 3D counterpart owing to the insulating nature of organic spacers which confines the charge carriers in two dimensions, leading to poor charge transport and consequently low FF and short-circuit current density (J_{SC}) in the devices. In principle, the 2D structure demonstrates a very high exciton binding energy associated with the large difference between the bandgap of the inorganic perovskite and the bulky organic layer as well as a large mismatch between the dielectric constant of the insulating organic spacer and the large mismatch between the dielectric constant of the insulating organic spacer and perovskite conductor layers.[77,86] This results in the quantum confinement of carriers within

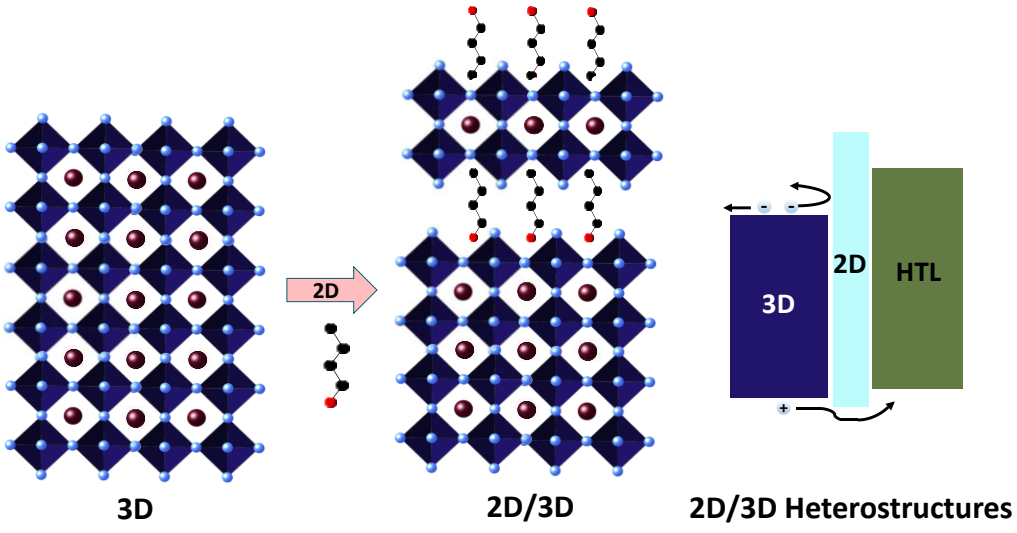

Figure 2-6: Schematic illustration of 2D/3D heterostructure formed between perovskite and hole transport layer (HTL) via the surface treatment of the 3D perovskite layer with large cations (2D materials).

the perovskite crystal, where the inorganic layer acts as a "well" while the organic spacer acts as a barrier.[87,88] As a result, this quantum confinement and the relatively low dielectric constant for the large organic cations affect the Coulomb interaction between the electron-hole pairs and strings the interaction between them. This prevents carrier migration to the contacts which deteriorates the performance of the 2D-based PSC.[88]

In addition, employing an ultrathin 2D-RP or quasi-2D perovskite layer increases the activation energy barrier for ion migration within the perovskite layer.[52,89,90] This does not only enhance the stability of PSCs but also hinder the accumulation of defects at the surface and grain boundaries (GBs) of the perovskite absorber, leading to an enhanced open-circuit voltage (V_{OC}) of the devices.[53,89–91] Besides, using long-chain bulky organic cations on the 3D perovskite surface can form a 2D/3D heterojunction that can act as a blocking layer (due to energy offset) to hinder the recombination of the charge carriers across the 2D/3D heterojunction (Figure 2-6).[47,92,93] Furthermore, as observed in many studies, employing an ultrathin 2D-RP layer into the bulk or at the surface of the perovskite layer results in prolonged lifetimes of charge carriers in comparison with the 3D perovskite layer due to the passivation of the 3D surface defects, thereby reducing the V_{OC} loss .[92,94–96] Therefore, with the knowledge of the superior electrical and optical properties of various 2D materials, along with their particular role in passivating the detrimental defects in PSC,[96–99]the main focus in this thesis is based on using these materials for reducing the V_{OC} deficit in wide-bandgap PSCs.

2.2. Perovskite solar cells

2.2.1. Working principle

The principle features of photovoltaic energy conversion in PSCs rely on five essential steps to generate power: (1) absorption of incident photons in the absorber material, (2) creation of excitons (bound electron-hole pairs), (3) dissociation of excitons into free charge carriers electron-hole), (4) separation and collection of charge carriers at selective contacts, (5) extraction of the electron and holes by electrodes, (Figure 2-7).[100] Therefore, a good solar

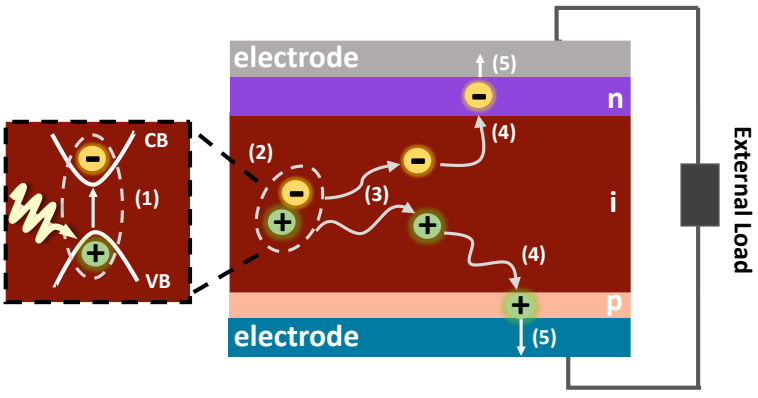

Figure 2-7: Schematic illustration of (a) fundamental processes in a perovskite solar cell.

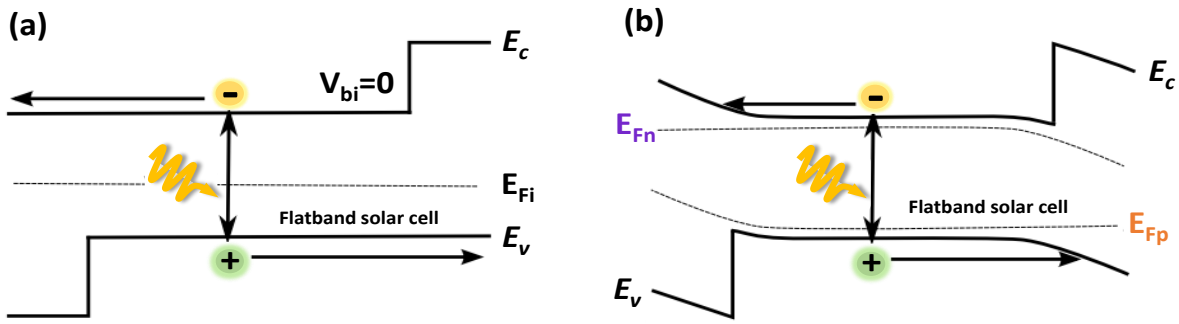

Figure 2-8: Schematic illustration of energy band diagram of a p-i-n heterostructure under illumination (a) at short-circuit and (b) under applied voltage. Adapted from reference [104].

requires a proper absorber layer with a high absorption coefficient, small exciton binding energy together with sufficient charge carrier mobility and long charge carrier diffusion length. As discussed in Section 2-2-1, all these intrinsic features can be found in the perovskite material's properties, making them an ideal absorber for solar cell application.

Typically, PSCs form a p-i-n (or n-i-p) heterojunction, where the perovskite absorber is considered as an intrinsic (i) semiconductor and sandwiched between the p-type (so-called hole transport layer (HTL)) and the n-type contacts (so-called electron transport layer (ETL)) that exhibit suitable bandgaps that provide selective carrier transport.[101–103] It should be noted that although PSCs have the p-i-n or n-i-p heterostructure layer stack, still there are ongoing investigations to understand its exact operation principle. Figure 2-8 demonstrates the band diagram of p-i-n solar cell under illumination at short-circuit and at operating conditions based on the flatband scenario which is used to understand the working principle in PSCs.[104–106] In this scenario, the separation and collection of charge carriers originate mainly from the chemical potential (i.e., diffusion of charges due to the nonuniform charge carriers distribution). Moreover, according to Würfel. *et al*, this is mainly the selectivity of the charge transport layers (CTL) which provide an efficient separation and collection of charge carriers and built-in voltage (drift) does not play a major role in the operation mechanism of PSC.[107] This means that differences in the conductivity of the large bandgap n-type and p-type contacts for charge carriers provide an easy pathway for the majority carriers to pass through their respective contact while blocking the minority carriers at that side and vice versa.[107] Bergmann *et al*, also demonstrated a field-free $MAPbI_3$ layer in a device configuration obtained by cross-sectional Kelvin probe force microscopy measurements, verifying that the diffusion is indeed the dominant mechanism for the separation of the charge carriers in the area of the perovskite film.[108] The schematics of the band diagram for the flat band solar cell (Figure 2-8a) demonstrate that under continuous illumination at short circuit condition, in which the contacts are connected through an external circuit without any applied voltage, the Fermi energy (E_F) equilibrates over the device and the collection of the generated electrons to the n-side and extraction of the generated holes to the p-side is facilitated by sufficient large band offset,

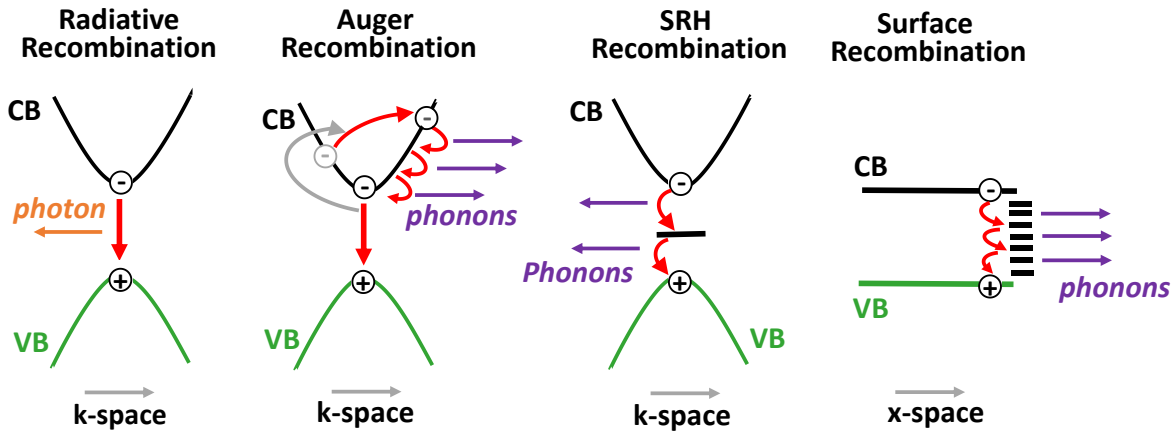

Figure 2-9: Schematic of common recombination mechanisms in semiconductors: direct, Auger, Shockley-Read-Hall (SRH), and surface recombination. Adapted from reference [111].

providing a net current flow (J_{SC}) in the solar cell. Under continuous illumination at an applied voltage (Figure 2-8b), the E_F splits into two separate quasi-Fermi levels, so-called quasi-Fermi levels for the electrons (E_{Fn}) and holes (E_{Fp}), aligning with the Fermi levels of the n-type and p-type contacts, respectively. In this case, the solar cell generates both voltage and current simultaneously and consequently the power is produced.

2.2.2. Recombination mechanism

Recombination is the process where the generated electrons and holes are annihilated, therefore leading to charge carrier losses. In general, free charge carriers can undergo a radiative process by emitting a photon (luminescence) or non-radiative Auger recombination, Shockley-Read-Hall Recombination (SRH) and surface recombination (Figure 2-9).[109–111] In PSCs, non-radiative SRH recombination and interface recombination are the dominant recombination mechanisms under solar irradiation conditions (1 Sun), and therefore the main driver for losses in V_{OC} and FF, while Auger recombination only becomes dominant at irradiation intensities above 100 Suns.[112] In the following, the different mechanisms are briefly described.[109,113]

Radiative recombination

Radiative recombination or direct band-to-band transitions is the inverse process of photon absorption where a light-generated electron from the conduction band directly recombines with a hole in the valence band and the excess energy is released in the form of a photon as schematically illustrated in Figure 2.9). This is also known as bimolecular recombination. As this process requires a free electron-hole pair, the radiative recombination rate depends on the product of the density of photogenerated charge carriers ($n_e n_p$). In case of hybrid perovskites which are direct semiconductors, the radiative recombination rate is around 10^{-10}-10^{-11} cm^3/s,[114] which is orders of magnitude higher than silicon (3×10^{-15} cm^3/s).[115]

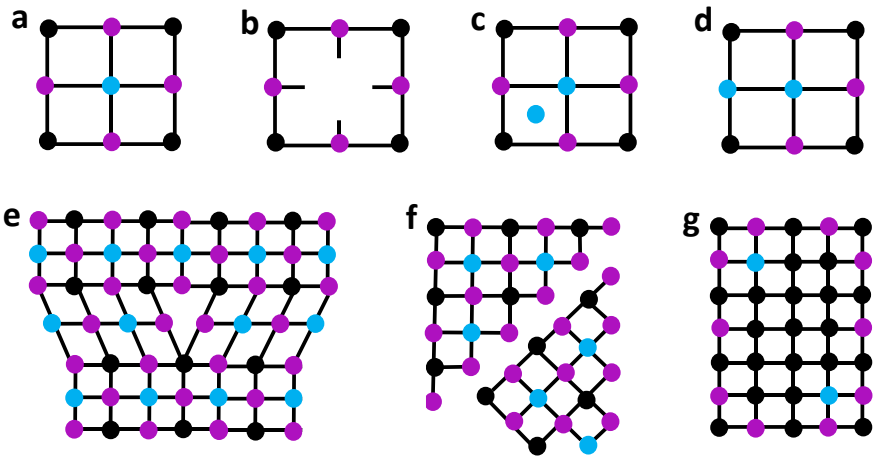

Figure 2-10: Schematic of different defects that exist in a perovskite crystal lattice: (a) ideal lattice; (b) vacancy at the A-site, (c) interstitial, (d) anti-site substitution, and higher dimensional defects such as e) edge dislocation, (f) grain boundary and (g) precipitate defects, respectively. Blue, black, and purple dots demonstrate the A, B, and X site ions from ABX_3 perovskite structure, respectively. The figure adapted from reference [119].

Auger recombination

Auger recombination is a trimolecular non-radiative recombination process involving three carriers, where the excess is induced by the recombination of an electron and a hole is given to another excited electron or hole instead of emitting a photon.[116] By subsequent thermalization process, this third carrier loses its excess energy and relaxes to the band edge. Therefore, the recombination rate in this process is proportional to the charge density to the power of three $n_e^2 n_p$ ($n_p^2 n_e$). Although Auger recombination plays a considerable role in silicon solar cells due to their high carrier concentration caused by doping and indirect bandgap,[115] it is negligible in PSC as the radiative recombination is considered to be a domination recombination mechanism due to its direct bandgap.[117]

Shockley-Read-Hall (SRH) recombination

SRH recombination (also known as trap-assisted recombination) occurs due to defects (trap)-induced energy states situated within the bandgap that can capture both electrons and holes and lead to non-radiative recombination. This process is accompanied by emitting phonons (lattice vibration) as shown in Figure 2-9 and dominates at low charge carrier densities. In crystalline semiconductors, defects can be classified as (i) crystallographic defects and (ii) impurities from foreign atoms in the lattice [118,119] These crystallographic or bulk defects can be originated from point defects which are positive or negative charged defects (vacancies, interstitials, anti-site substitutions) or higher-dimensional defects (dislocations, grain boundaries, precipitate) (Figure 2-10).[44,119,120] Therefore, controlling the defects of the perovskite thin-film via improving the quality of the perovskite, passivating defects located in the bulk and decreasing the number

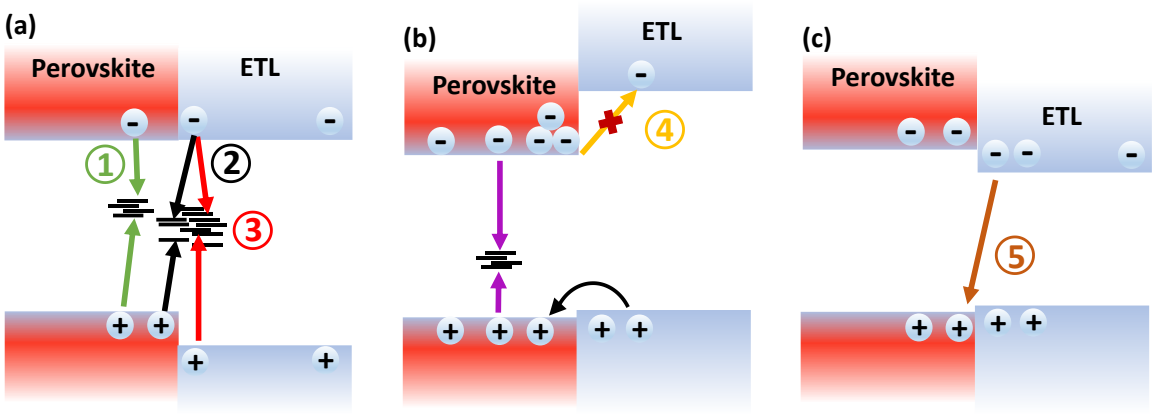

Figure 2-11: Schematic illustration of the band diagram for perovskite/electron transport layer (ETL) interface which present the different pathways of recombination at the surface/interface, including (a) high defect density at the surface/interface of the perovskite and ETL, (b) improper band alignment and (c) back-transfer-induced recombination.

of grain boundaries can significantly reduce SRH non-radiative recombination and consequently enhance the performance of PSCs.[44,110,121,122]

Surface/Interface recombination

Next to the carrier recombination in the bulk, the surface/across-interface recombination occurring at the surface of the absorber layer and at the interface between the absorber and charge-transporting layers (CTL) is the predominant responsible for the non-radiative recombination losses in PSCs, thus limiting the V_{OC}.[49,50,93,117,123] This recombination mainly originates from (i) high defect density at the surface of the perovskite layer due to the severe interruption of the crystal lattice at the surface, which is prone to produce a high number of dangling bonds (process (1), Figure 2-11a), (ii) deep trap states induced by the direct contact of perovskite layer with CTL (process (2) in Figure 2-11a), (iii) trap-assisted (SRH) recombination at the interface towards the CTL (process (3) in Figure 2-11a) and (iv) mismatched energy-level alignment at the interfaces (process (4), Figure 2-11b) and back-transfer induced recombination (process (5), Figure 2-11c).[109,117] All of these recombination factors reduce the steady-state charge carrier density under illumination, thus resulting in a reduction of the quasi-Fermi levels splitting (which is representative of the V_{OC} value) in the non-equilibrium state of the illuminated absorber. Therefore, key strategies such as surface passivation and interface engineering are particularly important in PSCs to surpass interfacial non-radiative recombination. In Chapter 4 and Chapter 6 we will discuss in more detail an efficient strategy in order to passivate the surface and the grain boundaries of the perovskite absorber layer.

2.2.3. Solar cell architecture

Depending on the device layer stack, opaque PSCs are typically fabricated in two common architectures: inverted planar p-i-n with a layer stack of transparent conductive oxide (TCO)

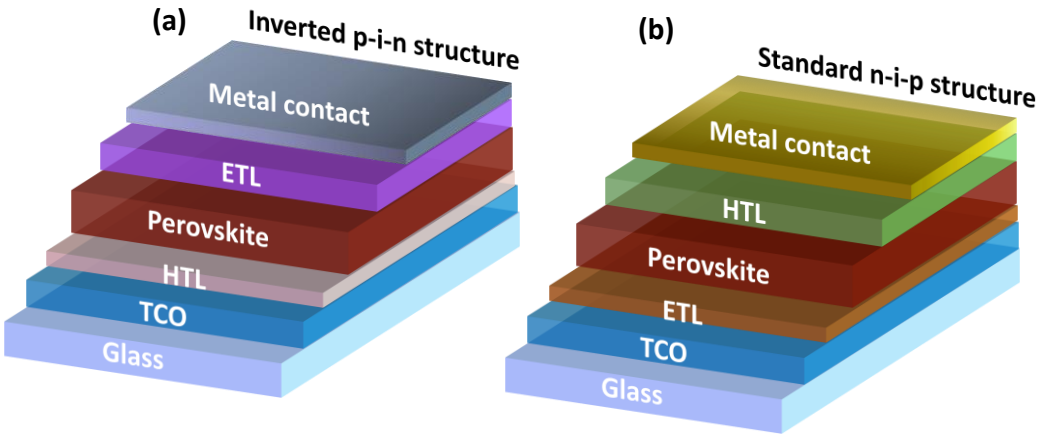

Figure 2-12: Schematic illustration of two common perovskite solar cell architectures with (a) inverted (p-i-n) and (b) standard (n-i-p) structures.

/HTL/perovskite/ETL/metal contact and standard n-i-p architecture with a layer stack of TCO/ETL/perovskite/HTL/metal contact (Figure 2-12).[124] In case of semi-transparent PSC for tandem application as we will discuss in detail in Chapter 3, a rear opaque metal contact is replaced with the TCO layer, and a thin buffer layer is generally employed between CTL and rear TCO contact to protect the layer from the sputtering damage during deposition of rear TCO contact. In general, as front contact a glass substrate coated with a TCO such as indium tin-doped indium oxide (ITO), zinc-doped indium oxide (IZO) or hydrogen-dope indium oxide (IO:H) is utilized, while a metal electrode (gold (Au), silver (Ag), or copper (Cu)) is used as a back contact in order to enhance the optical path length of incident light due to reflection. Opaque PSCs are illuminated from the glass substrate. In case of the p-i-n architecture, a p-type selective contact or HTL is deposited first on the TCO, followed by the deposition of a perovskite absorber and an n-type selective contact or electron transport layer (ETL), at the end (Figure 2-12a). The most commonly employed HTLs for the p-i-n architecture used in the literature are based on [2-(9H-Carbazol-9-yl)ethyl]phosphonic

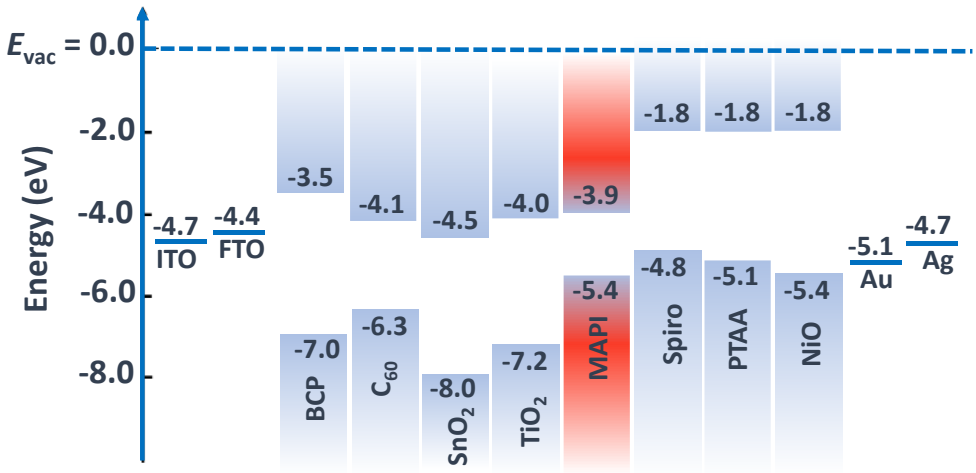

Figure 2-13: Schematic of energy levels diagram for common electron transport layers (ETL) (left), absorbers (middle) and hole transport layers (HTL) (right) used in perovskite solar cells according to references [126, 127, 129, 130].

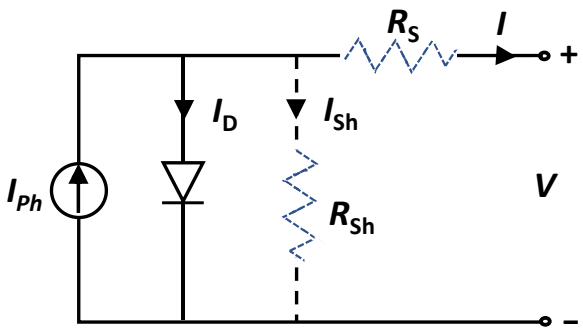

Figure 2-14: An equivalent circuit of a solar cell with a photocurrent source (I_{Ph}) connected in parallel to a diode (I_D) and shunt series resistance (I_{Sh}). Furthermore, a series resistance (R_S) is considered in a circuit.

Acid (2PACz), NiO_x and poly[bis(4-phenyl)(2,4,6-trimethylphenyl)amine] (PTTA).[124–127] For the ETL, [6,6]-Phenyl-C61-butyric acid methyl ester (PCBM) and Fullerene C_{60} are commonly used in this architecture.[124–127] In addition, a thin layer of Bathocuproine (BCP) is normally deposited at the ETL/metal interface as a hole-blocking layer in this structure. In case of n-i-p structure, the order of the CTL is changed (Figure 2-12b). Here, titanium dioxide (TiO_2) and tin(IV) oxide (SnO_2) are most commonly employed ETLs,[124,128,129] while for the HTL these are [2,2',7,7'-tetrakis(N,N-di-p-methoxyphenyl-amine)9,9'-spirobifluorene] (Spiro-MeOTAD) or Poly(triarylamine) (PTAA).[130,131] In total, depending on the energy band alignment of the CTL with the perovskite absorber, a large number of HTLs and ETLs have been developed and employed in PSCs as shown in Figure 2-13.

2.2.4. Photovoltaic characteristics

Current-density–voltage characteristics

The most direct method to analyze the performance of a solar cell are current density-voltage (*J-V*) measurements by measuring the current flowing through the cell by sweeping the bias voltage. The basic mechanism of the solar cell is represented by a simplified circuit that comprises a single diode, photocurrent source, a series (R_S) and a shunt resistance (R_{Sh}) to indicate any electrical resistance and leakage current path due to crystal defects, pinholes or impurity of the solar cell.[100] The diode equivalent circuit is depicted in Figure 2-14, where I_{ph}, I_D and I_{Sh} stand for a photogenerated current by solar irradiation, a dark current generated by an ideal p-n junction diode and a shunt current originates from device imperfections. The corresponding *J–V* characteristic is given by the Shockley Diode equation:

$$I = I_{\mathrm{Ph}} - I_D - I_{\mathrm{Sh}} \qquad 2.2$$

$$I = I_{\mathrm{Ph}} - I_0\left[e^{\frac{q\,V}{nk_{\mathrm{B}}\,T}} - 1\right] - \frac{I\,R_{\mathrm{s}} + V}{R_{\mathrm{sh}}}$$

Where I_0 is reverse saturation current, q is the electron charge, k_B is the Boltzmann constant, T is the absolute temperature and V is the voltage at the terminals of the cell.

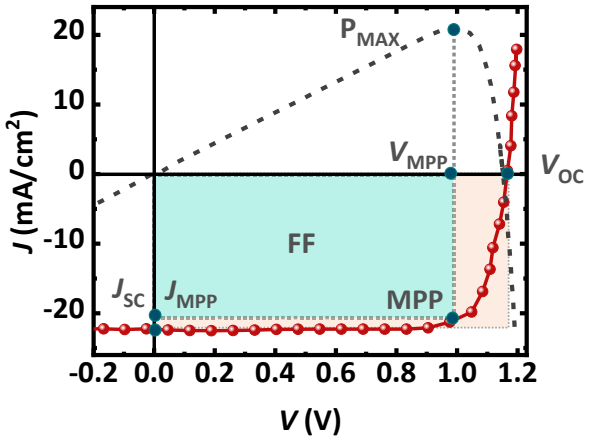

Figure 2-15: A typical current density-voltage (*J*–*V*) curve of a prototype solar cell measured under illumination and the corresponding electrical power output density. The green dots are an indication of the *J*–*V* characteristic: short-circuit current density (J_{SC}), the open-circuit voltage (V_{OC}) and the maximum power point output (P_{MPP}) where $J = J_{MPP}$ and $V = V_{MPP}$.

When the output terminal is shorted or $V = 0$, the current output of the solar cell with considering the ideal case ($R_S = 0$ and $R_{Sh} = \infty$) is called J_{SC} and defined as:

$$V = 0 \rightarrow I = I_{\mathrm{Ph}} - I_0\left[e^{\frac{q\times 0}{nk_{\mathrm{B}}T}} - 1\right] - 0 \quad \rightarrow \quad I_{SC} = I_{\mathrm{Ph}} \tag{2.3}$$

Furthermore, when no current flows through the ideal device ($I = 0$) or the output terminal is opened, V_{OC} is given by:

$$I = 0 \rightarrow 0 = I_{Ph} - I_0\left[\exp\left(\frac{q\,V_{OC}}{n\,k_{\mathrm{B}}\,T}\right) - 1\right] - 0 \tag{2.4}$$

$$V_{OC} = \frac{nk_{\mathrm{B}}\,T}{q}\,ln(\,1 + \frac{I_{ph}}{I_0})$$

Therefore, J_{SC} and V_{OC} are the maximum theoretical values that can be achieved for current density and voltage in a solar cell. Figure 2-15 shows the typical *J*–*V* characteristic of a solar cell derived from Equation 2-2. The power of the solar cell is defined by the product of the current density and voltage. The maximum power output (P_{MPP}) is obtained at the point where the product of current density and voltage is at the maximum operating point of the circuit:

$$P_{\mathrm{MPP}} = J_{\mathrm{MPP}}\,V_{\mathrm{MPP}} \tag{2.5}$$

The ratio between the maximum internally generated power to the product of $J_{SC} \times V_{OC}$ is defined as FF which determines the closeness of the *J*–*V* curve of the solar cell to the rectangle shape (large gray rectangular in Figure 2-15):

$$\mathrm{FF} = \frac{J_{\mathrm{MPP}}\,V_{\mathrm{MPP}}}{J_{\mathrm{SC}}\,V_{\mathrm{OC}}} < 1 \tag{2.6}$$

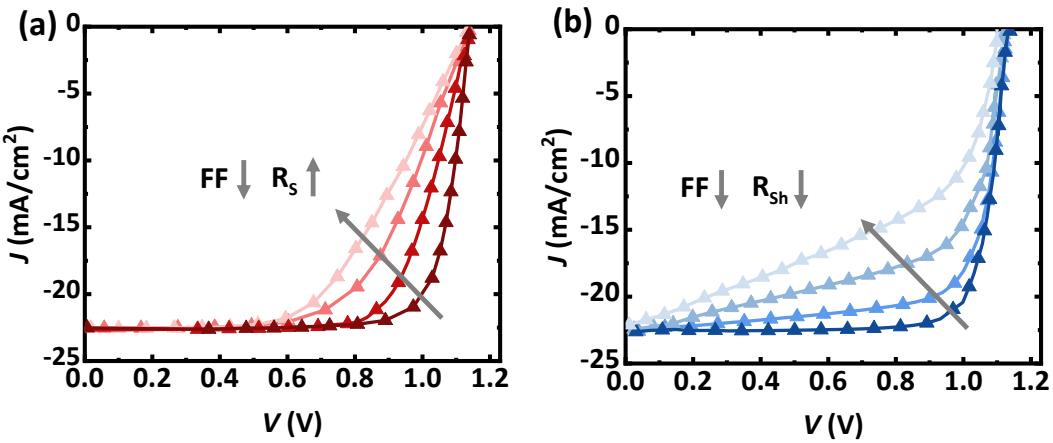

Figure 2-16: The effect of (a) series and (b) shunt resistance on the *J*–*V* curve of the solar cell.

As depicted in Figure 2-16, the presence of high R_S and low R_{Sh} flatten the slope of the *J*–*V* curve near the V_{OC} and J_{SC} respectively. This dominantly decreases the value of FF in the solar cells, as reflected in the *J*–*V* curve. Hence, FF can be used to describe a basic figure of merit for the solar cell. Finally, the power conversion efficiency (PCE) of a solar is calculated by the ratio of P_{MPP} to the power of incident light ($P_{incident}$):

$$\mathrm{PCE} = \frac{P_{\mathrm{MPP}}}{P_{\mathrm{incident}}} = \frac{\mathrm{FF}\, V_{\mathrm{OC}}\, J_{\mathrm{SC}}}{100\ \mathrm{mW/cm^2}} \qquad 2.7$$

the $P_{incident}$ is considered to be 1000W/m^2 as a standard AM1.5G solar spectrum used for the photovoltaic device, which is based on simulation of the sun's radiation at the earth's surface as we will discuss in Section 2-3.

External quantum efficiency

The external quantum efficiency (EQE) is a basic measurement for the solar cell that specifies the spectrally resolved response of the solar cell. It is defined as the number of charge carriers collected by the solar cell divided by the number of incident photons. In general, the EQE is a function of the photon wavelength that can be used to calculate the maximum photogenerated current achievable for a solar cell:

$$J_{\mathrm{SC}} = q \int_{300\ nm}^{850\ nm} \mathrm{EQE}(\lambda)\ \phi_{Ph}^{AM1.5}(\lambda)\ d\lambda \qquad 2.8$$

Here q is the elementary charge and $\phi_{Ph}^{\mathrm{AM1.5}}(\lambda)$ is the photon flux incident on the cell per unit area at the wavelength (λ). As the EQE measurement is independent of the spectral shape of the light source, the calculated J_{SC} by this method at zero voltage bias determines the accurate value compared to one obtained from the *J*–*V* curve. Monochromatic light is radiated on the sample and the spectral current generated by this excitation is measured. A typical EQE spectrum of the PSC with a p-i-n structure is depicted in Figure 2-17. In general, the shape of the EQE spectrum can provide information about the losses of

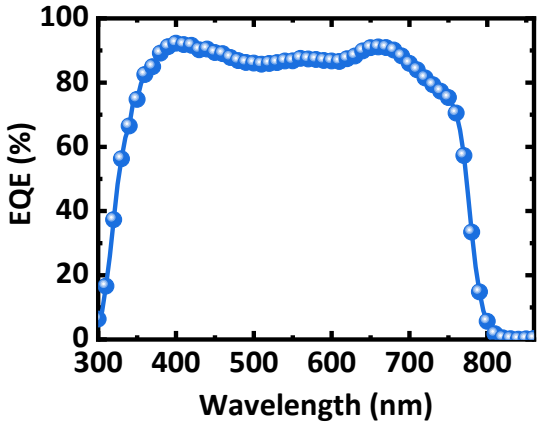

Figure 2-17: A typical external quantum efficiency (EQE) of a perovskite solar cell used in Chapter 6.

photocurrent density due to the combined effect of the total optical losses (e.g. reflection, parasitic absorption) and electrical losses (recombination).[132,133]

Hysteresis in the *J–V* characteristics of perovskite solar cells

A commonly observed phenomenon in PSCs is *J-V* hysteresis, which means a difference in the *J–V* curves of the device when measured at different scan directions (forward: $J_{SC} \rightarrow V_{OC}$ and backward scan: $V_{OC} \rightarrow J_{SC}$).[134] This results in different PCEs mainly due to a large deviation in FF as shown in Figure 2-18a, thus making it difficult to estimate the accurate PCE of the PSC. In this case, measuring a stabilized PCE via maximum power point (MPP) tracking under continuous illumination is established as a reliable performance measurement for PSCs (Figure 2-18b).[135] The amplitude of hysteresis can be determined using the hysteresis index (HI), which is defined as:

$$\mathrm{HI} = \frac{\mathrm{PCE_{Backward}} - \mathrm{PCE_{Forward}}}{\mathrm{PCE_{Backward}}} \qquad 2.9$$

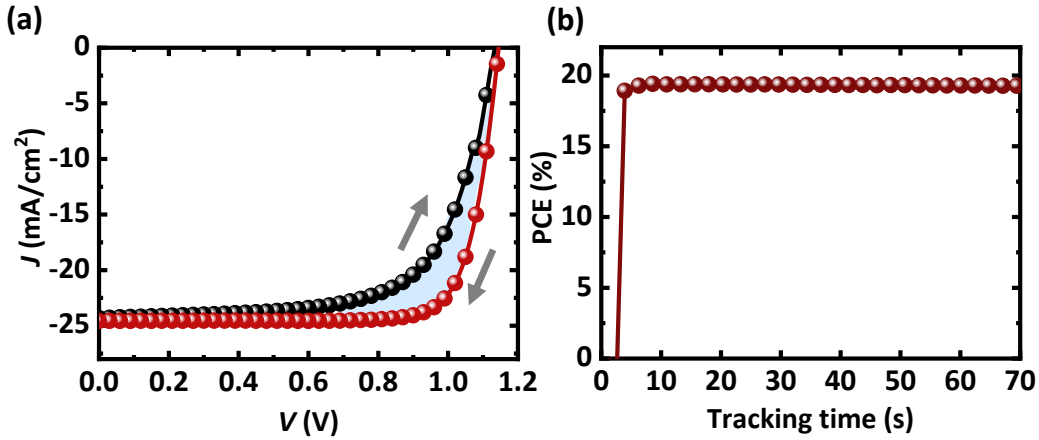

Figure 2-18: (a) a typical *J–V* characteristics of perovskite solar cell (PSC) measured from short-circuit to open-circuit (forward scan) and from open-circuit to short-circuit (backward scan), showing a pronounced hysteresis (blue area indicates the obvious difference in *J–V* curve from forward and backward scans). (b) A typical stabilized power conversion efficiency (PCE) of PSC determined by measuring the photocurrent at the maximum power point (MPP) under continuous AM 1.5G illumination.

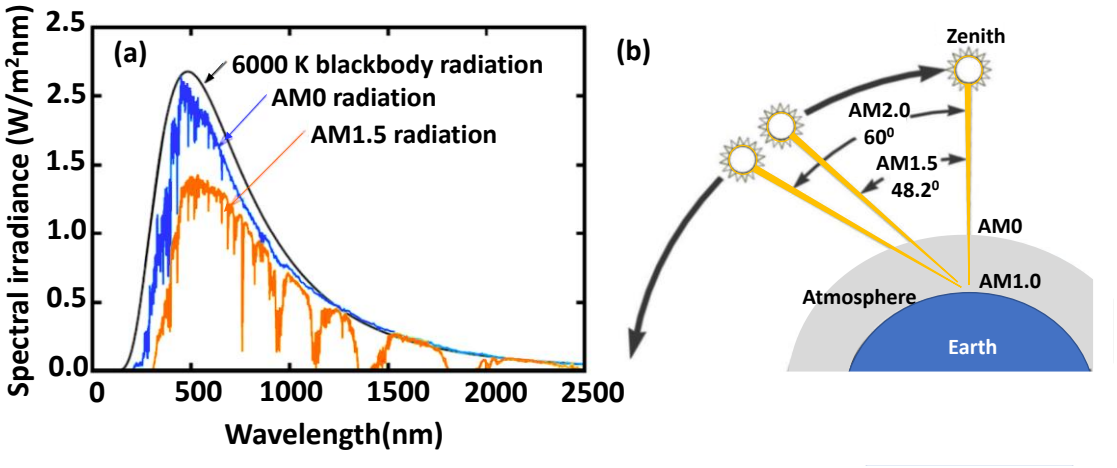

Figure 2-19: Spectral irradiance obtained from a black body at a temperature of 6000 K (black line), the sun outside the atmosphere (AM0 spectrum in blue line) and at the earth's surface with the angle of 48.2^0 (AM1.5G spectra in orange line. (b) A schematic of optical air mass definition when it is measured outside the earth's atmosphere and at the earth's surface with different angles. Adopted from reference [100].

Depending on the device architecture and *J–V* measurement parameters (e.g., different scanning rates), the degree of hysteresis effect can be different. Yet, the exact origin of the hysteresis has not been conclusively clarified. Various studies have identified the combination of ion migration in the organic-inorganic halide perovskite absorber and interfacial trap states as the main cause of hysteresis, which originates from the presence of defects in the crystal lattice of the perovskite layer (as discussed in Section 2-2-2).[108,136–138] These mobile ions (with low activation energy) can easily migrate towards the perovskite/ETL or perovskite/HTL interfaces and accumulate there, inducing trap states that increase non-radiative recombination. Moreover, transport processes of the charge carriers at non-selective transport layers also have a considerable impact on hysteresis due to the slow charge extraction via the interface and increased influence of interfacial trap states.[139] This highlights the importance of passivation strategies for reducing defects in the perovskite bulk and surface as well as selecting a proper ETL and HTL with suitable band alignment relative to the perovskite layer to hinder charge accumulation at the interface, thereby reducing the hysteresis effect.[140]

2.3. Theoretical efficiency limit of single-junction solar cells

Due to the surface temperature of the sun (5762 K), the solar spectrum can be described as the radiation of a black body at that temperature (Figure 2-19). The total solar irradiance at the surface of the earth is quantified by the length of the path through the atmosphere (defined as Air Mass (AM)), which depends on the orientation of the sunlight with respect to the normal to the earth's surface.[100] The AM0 spectrum represents the radiation intensity measured outside the Earth's atmosphere with the value of $\phi^{AM0} = 136.6$ mW/cm^2 (Figure 2-18b). However, a certain part of this spectrum is eliminated by passing through the atmosphere to the Earth's surface due to the absorption and scattering effect, lowering

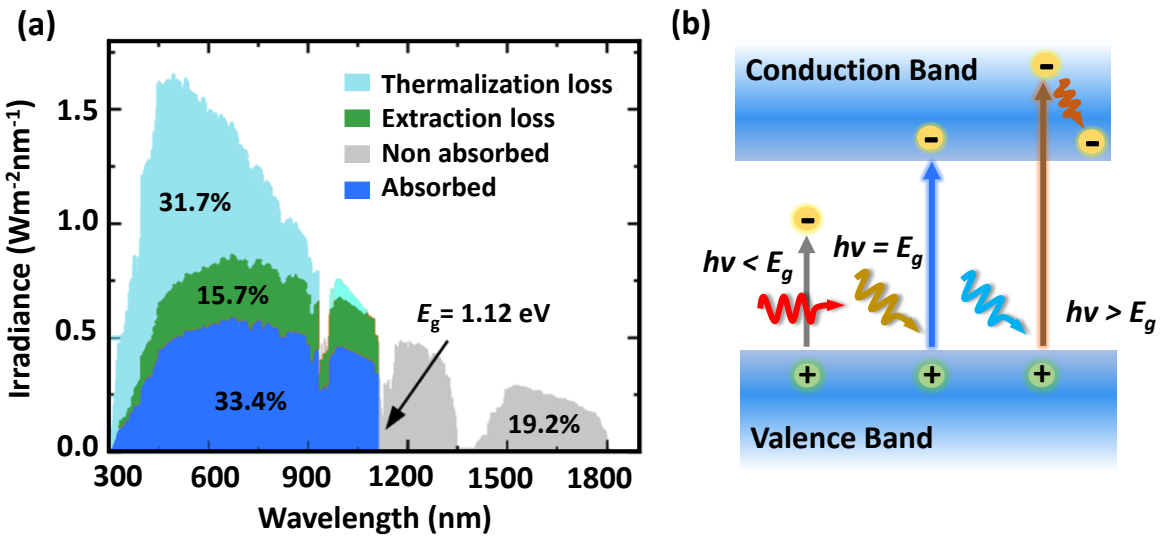

Figure 2-20: (a) Spectral irradiance of the AM1.5G. The blue area reflects the absorbed part of the solar spectrum for a single-junction silicon solar cell with a bandgap (E_g) of 1.12 eV. The light blue and gray areas represent the thermalization and non-absorbed losses due to the photons with energies above and below the bandgap, respectively, calculated from the Shockley-Queisser limit. Finally, the green area shows the extraction losses that can occur in the solar cell. (b) A schematic illustration of the corresponding fundamental loss mechanisms in a simple solar cell that limits the maximum possible efficiency of the solar cell. The data of the spectral irradiance of the AM1.5G spectrum were taken from reference [142].

the intensity to approximately 100.0 mW/cm^2. The standard spectrum used for photovoltaic device testing is the air mass 1.5G (AM1.5G) spectrum with an incident angle of 48.2°and a total irradiance of $\phi^{AM1.5}$ = 100.0 mW/cm^2 (Figure 2-19).[100]

Practically, a real solar cell cannot convert 100% of the sunlight into useful electrical energy (Figure 2-20a). In principle, upon the interaction of the incident photons with the absorber material, only photons with energy equal to bandgap ($E_{Ph} = E_g$) can be absorbed and contribute to photocurrent, while photons with lower energy ($E_{Ph} < E_g$) are transmitted (transmission losses). Photons with energy above the bandgap ($E_{Ph} > E_g$) are also absorbed and create electron-hole pairs, but the excess energy of the excited electron or generated hole is transferred to the lattice vibrations (phonons) to reach thermal equilibrium and cannot be extracted as electrical energy. These losses are called thermalization losses as illustrated in Figure 2-20b.[141] Additionally, not all generated charge carriers from the photons with energy $E_{Ph} = E_g$ can be collected and transferred from the absorber layer to the electrodes (extraction loss) due to the recombination losses as we discussed in Section 2-2-2, thereby, limiting the real device performance. Considering an AM 1.5G irradiance spectrum, the maximum PCE that can be achieved for a single-junction cell with a bandgap of 1.12 eV is ~ 33.4%.[142] This fundamental efficiency limit is determined by considering the detailed balance principle which was introduced by Shockley-Queisser (S-Q) in 1961.[143,144] The model considers the emission losses caused by black body radiation of the absorber and calculates the maximum PCE of the solar cell (without imperfection) by assuming:

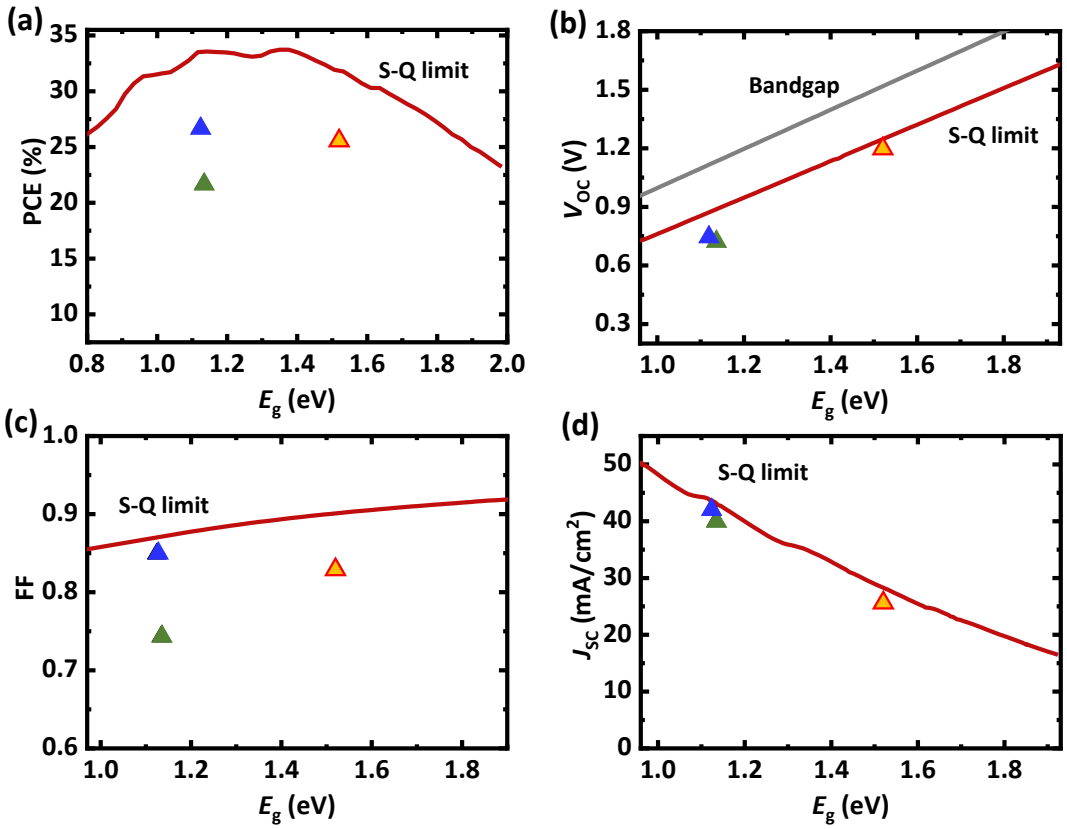

Figure 2-21: Maximum (a) power conversion efficiency (PCE), (b) open-circuit voltage (V_{OC}), (c) FF and short circuit current (J_{SC}) limits as a function of the bandgap obtained from Shockley-Queisser (S-Q) limit. The triangles represent the current records for c-Si (blue), CIGS (green) and metal halide perovskite solar cells (orange) with considering AM1.5G solar irradiance based on references [27, 145].

(i) 100% absorption for photons with $E_{Ph} > E_g$
(ii) 0% absorption for photons with $E_{Ph} < E_g$
(iii) a full generation of electron/hole pairs upon absorption
(iv) 100% collection (EQE = 100%) for all the photogenerated electrons and holes
(v) Only radiative recombination

the thermalization and transmission losses as well as considering the emission losses caused by black body radiation of the absorber (radiative recombination). Figure 2-21 displays the resulting photovoltaic parameters calculated from S-Q efficiency limits as a function of the bandgap obtained for different solar cell technology (Si, CIGS and perovskite) based on one-sun illumination with the standard AM1.5 light spectrum.[27,145]

2.3.1. Quantification of radiative and non-radiative open-circuit voltage losses

As discussed in Section 2-3, according to the S-Q limit, the calculation of the maximum conversion efficiency is based on the detailed-balanced principle and Planck's law,[146] which considers the radiative recombination of electrons and holes as the only allowed recombination for an ideal solar cell. This assumption implies that all incoming light is

absorbed by the solar cell and then emits radiation according to Planck's law. Accordingly, the saturation current density is defined as:

$$J_{0,\mathrm{SQ}} = q \int_0^\infty a(E)\, \phi_{bb}(E)\, dE = q \int_{E_\mathrm{g}}^\infty \phi_{bb}(E)\, dE \qquad 2.10$$

Where $a(E)$ is the absorptance which is equal to 1 for $E_{\mathrm{Ph}} \geq E_\mathrm{g}$ and 0 for $E_{\mathrm{Ph}} \leq E_\mathrm{g}$ in case of S-Q limit, and ϕ_{bb} is the black-body radiation of the solar cell at temperature T:

$$\phi_{bb} = \frac{2\pi E^2}{h^3 c_0^3} \frac{1}{\exp(E/k_B T) - 1} \approx \frac{2\pi E^2}{h^3 c_0^3} \exp\left(\frac{-E}{k_B T}\right) \qquad 2.11$$

Here h is Planck's constant, E is the photon energy, k_B is Boltzmann's constant and c represents the speed of light in a vacuum.[144,147,148] The approximate expression on the right is obtained by considering the Boltzmann approximation for $E \geq 3\, k_\mathrm{B}T$. The same assumption is applied to calculate the radiative dark current density at low mobilities which is also referred to as the recombination current density. However, in this case, instead of absorptance, the emitted and absorption of the light is presented by the external quantum efficiency:[144]

$$J_{0,\mathrm{rad}} = q \int_0^\infty Q_e(E) \phi_{bb}(E)\, dE \qquad 2.12$$

Assuming that all photogenerated charge carriers must radiatively recombine, the value of radiative current density (J_{rad}) is equal to J_{SC}. Therefore, radiative open-circuit voltage ($V_{\mathrm{OC\text{-}rad}}$) is defined as:

$$V_{\mathrm{OC-rad}} \approx \frac{k_B T}{q} \ln\left(\int_0^\infty Q_e(E) \phi_{\mathrm{sun}}\, dE \Big/ \int_0^\infty Q_e(E) \phi_{bb}\, dE \right) \approx \frac{k_B T}{q} \ln\left(\frac{J_{\mathrm{SC}}}{J_{0,\mathrm{rad}}}\right) \qquad 2.13$$

However, as discussed in Section 2-3, the real solar cell suffers from non-radiative recombination. According to the thermodynamic theory that all photons should be emitted again, the loss $\Delta V_{\mathrm{OC,non\text{-}rad}}$ due to non-radiative recombination in a real solar cell is correlated to the external photoluminescence quantum yield (PLQY) via:[149–152]

$$\Delta V_{\mathrm{OC,non-rad}} = V_{\mathrm{OC-rad}} - V_{\mathrm{OC}} = -\frac{k_B T}{q} \ln \mathrm{PLQY} \qquad 2.14$$

Where PLQY is defined as the ratio between the emitted photon flux (Φ_{em}) and the absorbed photons flux (Φ_{abs}): [151,152]

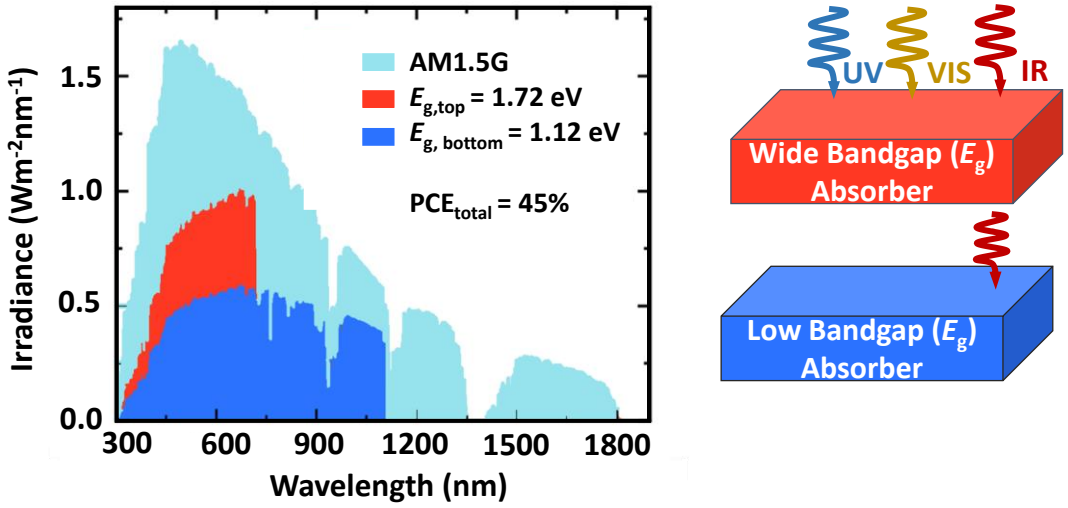

Figure 2-22: Spectral response of two absorber materials with different bandgap (E_g) in a tandem solar cell for the given solar spectral irradiance (AM1.5G). Based on the detailed balanced model, by combining the two subcells with E_g ~1.72 (top cell) and E_g ~1.12 (bottom cell), a maximum power conversion efficiency (PCE) of 45% can be achieved. The data of the spectral irradiance of the AM1.5G spectrum were taken from reference [142].

$$\mathrm{PLQY} = \frac{\Phi_{\mathrm{em}}}{\Phi_{\mathrm{abs}}} = \frac{J_{\mathrm{rad}}}{J_{\mathrm{G}}} = \frac{J_{\mathrm{rad}}}{J_{\mathrm{non-rad}} + J_{\mathrm{rad}}} \qquad 2.15$$

Here, J_G stands for the generation current which under open-circuit condition is equal to the recombination current $J_R = J_{rad} + J_{non\text{-}rad}$ since the net current flowing in the solar cell is zero. Equation (2.14) is experimentally useful as by measuring PLQY at 1 Sun irradiation and calculation of $V_{OC\text{-}rad}$, non-radiative losses in PSCs can be easily quantified. [50,153] Using V_{OC} = QFLS/q, where QFLS is the quasi-Fermi level splitting as defined in Section 2-2-1, equation 2-14 can be written in the form of:[152]

$$\mathrm{QFLS} = qV_{\mathrm{OC-rad}} + k_B T \ln \mathrm{PLQY} \qquad 2.16$$

2.4. Tandem solar cells

Operating principle of a tandem solar cell

As we discussed in Section 2-3, the PCE of a single-junction solar cell is mainly limited by two main factors: thermalization which accounts for the largest source of power loss (31.7%), and transmission losses. Tandem solar cells with stacking different absorber bandgaps have been pursued to considerably mitigate this thermalization loss by sequentially absorbing photons, thereby overcoming the PCE of the single-junction solar cell. In a double junction tandem, the top wide-bandgap absorber harvests high-energy photons but allows low-energy photons to pass through into the low-bandgap bottom cell, such that it utilizes a wide range of the solar spectrum. This is the principle concept of a multi-junction solar cell, as displayed in Figure 2-22. By considering the detailed balance

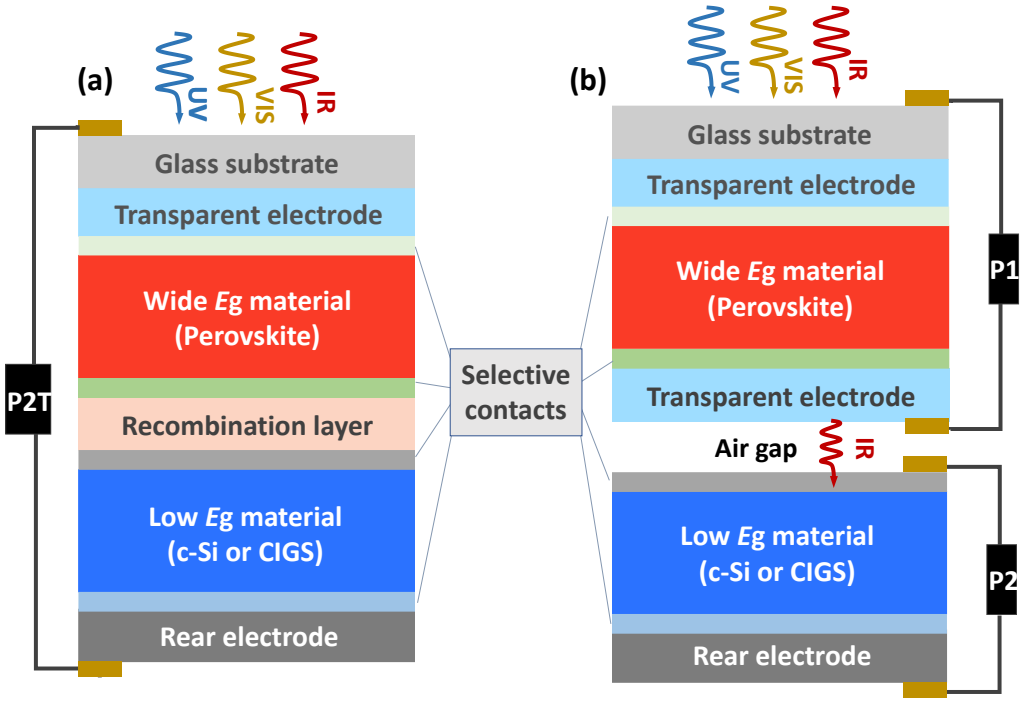

Figure 2-23: Schematic illustrations of a (a) 2-terminal (2T) and (b) 4-terminal (4T) tandem configurations. In case of 2T configuration both subcells are monolithically interconnected while in 4T tandem solar cell both subcells are optically interconnected and independently work at their maximum power point. Reproduced from references [23,25,29,33].

theory, the fundamental efficiency limit increases to 45% PCE for a tandem cell by combining two subcells with the ideal bandgaps (1.12 eV for the bottom cell and 1.72 eV for the top cell) compared to the single-junction solar cell.[151,154]

In general, tandem solar cells can be fabricated in different structures. The most common configurations are based on either monolithically interconnected two-terminal (2T) or mechanically stacked four-terminal (4T) configurations, each having its own advantages and disadvantages (Figure 2-23).[23,25,29,33,155] From a process development perspective, 4T tandem solar cells are the simple configuration where two subcells are electrically independent, as they are stacked separately on top of each other, thus the total power density is equal to $P_{4T}= (J_1 \times V_1) + (J_2 \times V_2)$. This allows higher degrees of freedom related to the fabrication process as well as the selection of the top solar cell absorber's bandgap (Figure 2-24a). Therefore, a high PCE can be achieved by utilizing a broad range of bandgaps.[38] In contrast, for the 2T configuration, the two subcells are connected in series, implying that the photocurrent generated in both the top and bottom subcells must be identical. Therefore, the power density of the 2T tandem solar cell is obtained by $P_{2T} = J \times V_{2T} = (V_1+V_2)\ J = V_1J + V_2J$. This results in a current matching requirement that restricts the bandgap combination of both subcells to a very narrow range (Figure 2-24b) and also raises the sensitivity of the configuration to spectral variations compared to the 4T device.[38,156,157] Apart from the current matching requirement, the processing of the 2T

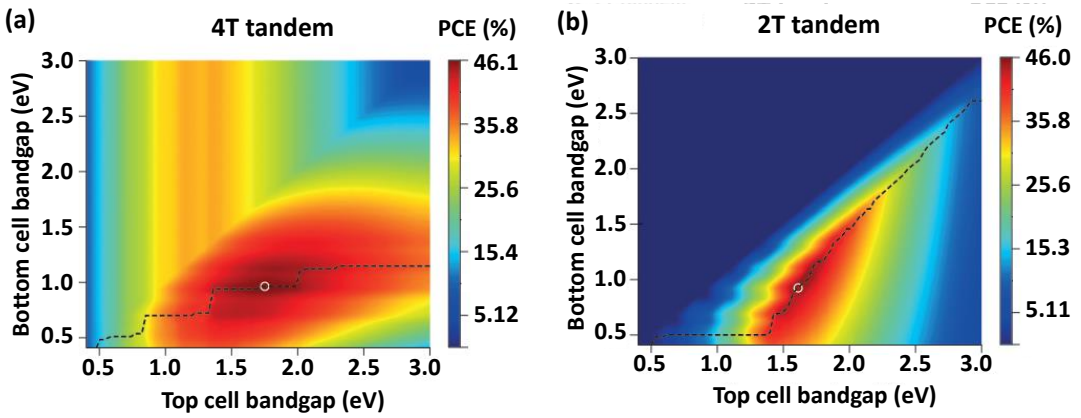

Figure 2-24: Maximum power conversion efficiency (PCE) map of (a) 2-terminal (2T) and (b) 4-terminal (4T) solar cells as a function of top and bottom subcell bandgap with considering 100% external quantum efficiency. The dashed line illustrates the peak efficiency that can be achieved by combining the optimum bandgaps of top and bottom subcells. Adapted from reference [33].

configuration is more challenging as the top solar cell is directly grown atop the bottom cell, meaning that the top cell fabrication can easily damage the underlying layers. On the other hand, thanks to the series connection, the monolithic tandem architecture requires only two external terminal connectors (contrary to the 4T configuration with 4 external terminals), which reduces the step and more importantly, only one of the contact electrodes must be a transparent layer to transfer the light into the device. This significantly reduces the parasitic absorption in this configuration, thereby implementing significantly lower optical losses to the overall device performance.[158,159] In contrast, as the top and bottom cells in the 4T tandem solar cell is optically interconnected, it utilizes three conductive transparent electrodes at: 1) the front side of the top cell to transmit the full spectrum, 2) the rear side of the top cell and 3) the front side of the bottom cell to transmit near-infrared region photons, as illustrated in Figure 2.23. As a result, these TCO electrodes along with additional charge transport layers and optical spacer imply more parasitic and reflection losses in this configuration that consequently lower the practical tandem performance. Recently, monolithic 3T architecture with one terminal at the front and two terminals at the rear contact has attracted scientific interest in photovoltaic research.[160–162] In contrast to the 2T with series connection, this configuration does not require a current matching between the subcells, exhibiting the next step in achieving higher energy yield which is the accurate figure of merit for determining the realistic outdoor performance of the solar cell.

3. Materials, Devices and Characterization Methods

In the following chapter, we present all the experimental methods and characterization used in this thesis for the deposition of all layers relevant to the fabrication of opaque and semi-transparent perovskite solar cells (PSC) and their integration into the two-terminal (2T) and four-terminal (4T) tandem configurations.

The first section provides the reader with detailed descriptions of the materials, device architecture (standard n-i-p and inverted p-i-n planar architecture) and the deposition process (spin-coating, thermal evaporation, sputtering and atomic layer deposition (ALD)) of PSC. The second section further explains the working mechanism of the measurement techniques used in this work including optical, electrical and material characteristics such as ultraviolet-visible spectroscopy, photoluminescence spectroscopy, X-ray diffraction, X-ray photoelectron spectroscopy, scanning electron microscopy, atomic force microscopy, along with current-density–voltage characteristics, maximum power point tracking measurement, external quantum efficiency, ideality factor of the devices and space charge limited current.

3.1. Perovskite solar cell fabrication

In this thesis, we fabricated PSC based on two different types of planar architectures: (i) standard n-i-p (ii) inverted p-i-n. The discussions below describe the materials and fabrication of each layer.

Material for preparation of the electron transport layer (ETL) solution

Nanoparticle-based SnO_2 (np-SnO_2; Alfa Aesar)
Fullerene-C_{60} (C_{60}; Sigma Aldrich)

Material for preparation of the perovskite solution:

Lead iodide (PbI_2; TCI)
Lead bromide ($PbBr_2$; TCI)
Lead chloride, ($PbCl_2$; Merck)
Formamidinium iodide (FAI; Dyesol and Dynamo)

Cesium iodide (CsI; Sigma Aldrich and Abcr)
Cesium Chloride (CsCl; Abcr)
Methylammonium Bromide (MABr; Dynamo)
Methylammonium Chloride (MACl; Dynamo)

Material for deposition of the 2D/3D perovskite heterostructure:

n-butyl ammonium bromide, (n-BABr; Greatcell solar)
2-phenylethylammonium chloride (PEACl; Sigma Aldrich)
2-phenylethylammonium bromide (PEABr; Sigma Aldrich)
2-phenylethylammonium Iodide (PEAI; Sigma Aldrich)
n-Butylammonium Chloride (n-BACl; TCI)
n-Octylammonium Chloride (n-OACl; Greatcell solar materials)

Material for preparation of the hole transport layer (HTL) solution:

2,2′,7,7′-tetrakis[N,N-di(4-methoxyphenyl)amino]-9,9′-spirobifluorene(Spiro-MeOTAD; Luminescence Technology)
4-tert-butylpyridine (4-tBP; Sigma Aldrich)
lithium bis(trifluoromethanesulfonyl)imide (Li-TFSI; Sigma Aldrich)
2-(9H-carbazol-9-yl)ethyl)phosphonic acid (2ACz; TCI)

Material for Buffer layer:

molybdenum oxide (MoOx; Sigma Aldrich)
Tin oxide (SnO_X)

Material for anti-reflection coating:

Magnesium fluoride (MgF_2; Sigma Aldrich)

Solvents:

Dimethylformamide (DMF; Sigma Aldrich, anhydrous)
Dimethyl sulfoxide (DMSO; Sigma Aldrich, anhydrous)
γ-butyrolactone (GBL; Merck)
Ethyl Acetate anhydrous (EA; Sigma Aldrich, anhydrous)
Ethanol (VWR Chemicals)
Isopropanol (IPA; Merck)
Chlorobenzene, (CB; Merck)

Preparation of transparent conductive oxide

In general, glass substrates coated with transparent conductive oxide (TCO) were cut in 0.16 cm × 0.16 cm and cleaned with acetone and isopropanol in an ultrasonic bath for 10 minutes each. The substrates were further treated with oxygen plasma for 3 min before the next step of deposition. Two different front contacts and two different back contacts TCO were used in this thesis. For front contacts, pre-patterned tin-doped indium oxide (ITO)

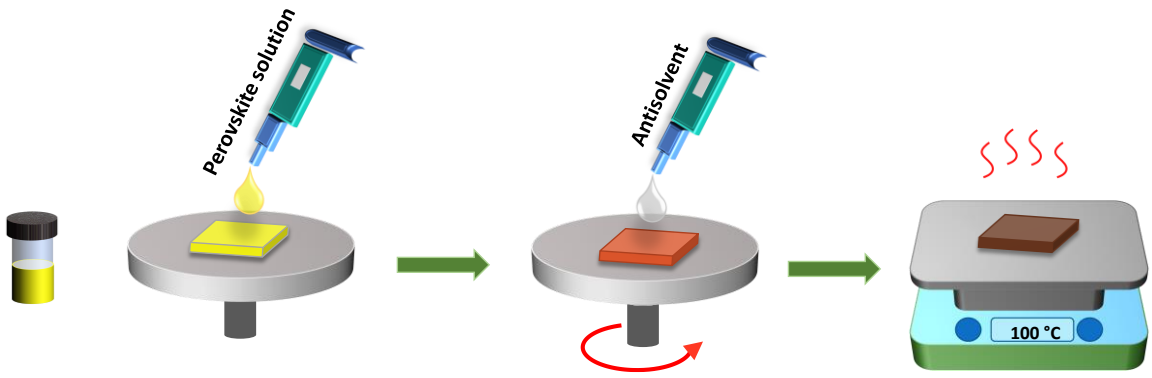

Figure 3-1: Schematic illustration of perovskite absorber layer deposition.

purchased commercially (Luminescence Technology, sheet resistance 15 Ω/sq, 140 nm thickness, CAS: 50926-11-9) or in-house hydrogen-doped indium oxide (IO:H) (sheet resistance 22 Ω/sq, 230 nm thickness) sputtered by the collaboration partner Zentrum für Sonnenenergie (ZSW)) were employed. For back TCO, in-house sputtered ITO (sheet resistance 60 Ω/sq, 160 nm thickness) or zinc-doped indium oxide (IZO) (sheet resistance 45 Ω/sq, 165 nm thickness) were used for fabricating semi-transparent PSC). The in-house TCOs were patterned by laser scribing using pulsed laser ablation.

3.1.1. Opaque n-i-p perovskite solar cell

The fabrication of opaque n-i-p PSCs, used in Chapter 4 and Chapter 5, comprises of the following device stack: Glass/ITO (front contact)/SnO_2 (ETL)/$Cs_{0.17}FA_{0.83}Pb(I_{1-y}Br_y)_3$; $0.24 \leq y \leq 0.56$ (double-cation perovskite)/Spiro-MeOTAD (HTL)/Au (Back contact).

Deposition of electron transport layer

The precursor solution was prepared by diluting a 15 wt% aqueous colloidal dispersion of SnO_2 nanoparticles in deionized water to a concentration of 2.04 wt%. A thin (≈ 30 nm) SnO_2 ETL was deposited on the ITO substrate by spin coating (4000 rpm for 30 s) in the ambient atmosphere, followed by an annealing step at 250 °C for 30 min and oxygen plasma treatment for 1 min.

Deposition of the perovskite absorber layer

The perovskite precursor solution was prepared by dissolving 0.83 mmol FAI, 0.17 mmol CsI, $((2 - 3 \times y))/2)$ mmol PbI_2 and $(3/2 \times y)$ mmol $PbBr_2$ in a 1 mL solvent mixture of DMF: DMSO 4:1 (v:v). In Chapter 4, this composition was prepared based on $y = 0.4$ ($Cs_{0.17}FA_{0.83}Pb(I_{0.6}Br_{0.4})_3$) with a bandgap ($E_g$) of 1.72 eV. Accordingly, in Chapter 5 the value of Br content changed between $0.24 \leq y \leq 0.56$ in order to obtain the perovskite absorber layers with various bandgaps between 1.65 to 1.85 eV. The double-cation perovskite absorber layer was deposited from the solution on top of the SnO_2 layer inside of the glovebox by a two-step spin coating process: i) 1000 rpm (acceleration 2000 rpm/s) for 10 s, ii) 5000 rpm (acceleration 2000 rpm/s) for 30 s. 100 µL CB was poured on the spinning

substrate 10 s before the end of the second step. The samples were annealed at 100 °C for 30 min in an inert atmosphere (Figure 3-1).

Deposition of interlayer 2D/3D perovskite heterostructure

The interlayers were processed by dynamically spin coating (5000 rpm for 30 s) 100 µL of n-BABr dissolved in isopropanol (concentration of 2, 5, and 7.5 mg/ml) on top of the perovskite absorber layer and subsequent annealing at 100 °C for 5 min in an inert atmosphere.

Deposition of hole transport layer

The HTL precursor solution was prepared with 80 mg spiro-MeOTAD dissolved in 1 mL CB with 17.5 µL Li-TFSI (520 mg/ml in acetonitrile) and 28.5 µL 4-tBP additives. The solution was deposited inside of the glovebox by spin coating method with a speed of 4000 rpm, 1000 ac for 30 s, followed by exposure to dry air in ≈25% relative humidity condition for ≈12 h.

Thermal evaporation of metal back electrode for completing opaque PSC

In this step, the edges of the perovskite substrates were swiped using GBL to allow the deposited back electrode to connect to the front electrode. Eventually, for completing the opaque PSC as shown in Figure 3-2, a 60 nm thick gold (Au) electrode was evaporated directly on the HTL by thermal evaporation through shadow masks to define the active area to 10.5 mm^2 (Figure 3-2).

3.1.2. Semi-transparent n-i-p perovskite solar cell

For preparing semi-transparent PSC with an active area of 10.5 mm^2, the following device stack is utilized in Chapter 5: Glass/ITO/SnO_2/$Cs_{0.17}FA_{0.83}Pb(I_{1-y}Br_y)_3$; $0.24 \leq y \leq 0.56$/Spiro-MeOTAD/MoO_X/Au/ITO/MgF_2 (Figure 3-2).

Thermal evaporation of buffer layer

After deposition of HTL (spiro-MeOTAD), a thin layer of MoO_X (10 nm) as a buffer layer was evaporated at a rate of 0.8 A s^{-1} using a Lesker Spectros system at 6×10^{-6} mbar pressure to protect spiro-MeOTAD during sputtering of rear contact on top of that.

Sputtering of rear transparent conductive oxide electrode for completing semi-transparent PSC

In the next step, the edges of the substrates were swiped using GBL to induce a connection between the rear and front electrodes. The semi-transparent PSC was completed by the deposition of a TCO electrode on the rear side. For this reason, a ≈150-160 nm ITO layer (used in Chapter 5) was deposited using a Kurt J. Lesker PVD-75 thin-film deposition system with sputtering parameters of Power 50 W, substrate temperature 25 °C, deposition time =2300 s, pressure = 0.8 mTorr and O_2 to argon ratio = 2.5%. To enhance the rear ITO

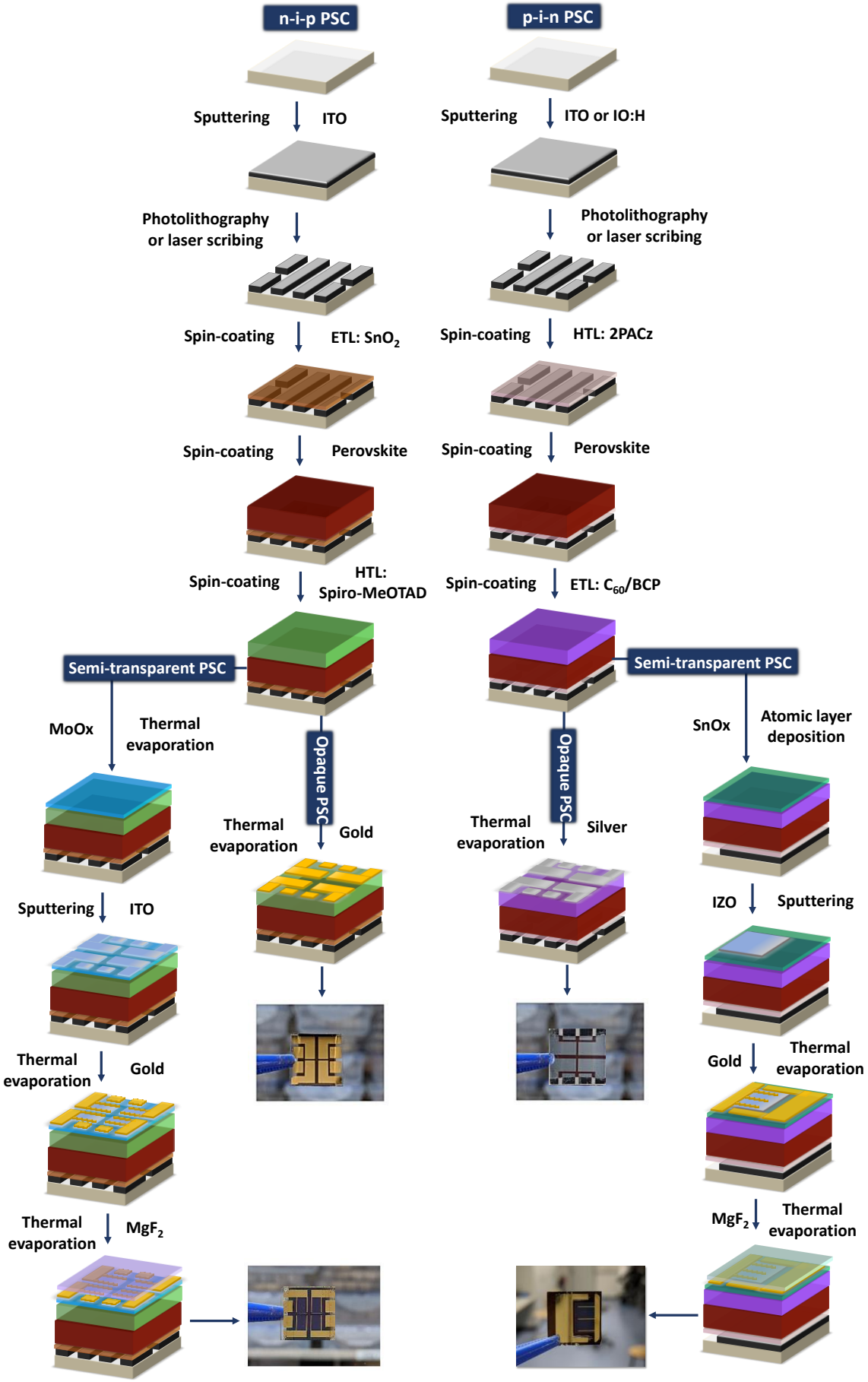

Figure 3-2: Schematic illustration of the opaque and semi-transparent perovskite solar cell (PSC) fabrication based on two n-i-p and p-i-n architectures.

conductivity, ≈ 75 nm Au fingers were deposited by thermal evaporation at a rate of 2 Å s^{-1} using a shadow mask.

Thermal evaporation of anti-reflection coating

Finally, to further improve the near-infrared (NIR) transmittance and light in-coupling as well, 150-155 nm MgF_2 as an anti-reflection coating was deposited by thermal evaporation on top of the rear ITO using Lesker Spectros PVD system at a rate of 3–4 Å s^{-1} at 6 × 10^{-6} mbar pressure.[163,164] It should be mentioned that deposition of the layers by the sputtering system does not produce sharp edges during the process, as it is not directional. Therefore, a shadow mask with the defined area was employed to make an accurate active area for the characterization of these semi-transparent PSCs.

3.1.3. Opaque p-i-n perovskite solar cell

The fabrication of opaque p-i-n PSCs, used in Chapter 6, comprises the following device stack: Glass/ITO (front contact)/2PACz (HTL)/$Cs_{0.18}FA_{0.82}I_3$/C_{60} (ETL)/BCP/Ag (Back contact) (Figure 3-2).

Deposition of hole transport layer

The 2PACz precursor solution was prepared by dissolving 2PACz in anhydrous Ethanol with a concentration of 1 mmol/ml. The prepared solution was put in an ultrasonic bath for 15 min before it was used. A thin layer of 2PACz HTL was deposited on the ITO substrate by spin-coating at 3000 rpm for 30 s and subsequently annealed at 100 °C for 10 min.

Deposition of the perovskite absorber layer

$Cs_{0.18}FA_{0.82}PbI_3$ (E_g ≈ 1.57 eV)

Reference perovskite film (Ref): The reference double-cation perovskite $Cs_{0.18}FA_{0.82}PbI_3$ precursor solution was prepared according to the literature by mixing PbI_2 (507 mg: 10% excess of PbI_2), CsCl (30 mg) and FAI (172 mg) in 1 mL solvent mixture of DMF:DMSO 4:1 volume ratio.[165] The reference perovskite film was deposited on the substrate using two steps spin coating method: i) 1000 rpm (acceleration 2000 rpm/s) for 10 s, ii) 5000 rpm (acceleration 2000 rpm/s) for 30 s. at 1000 rpm/s for 30 s. 150 µL antisolvent CB was quickly dropped on the spinning substrate 10 s before the end of the second step spin-coating. The samples were then annealed at 150 °C for 30 min inside the glovebox.

Surface passivated perovskite film (SP): In case of preparing the surface passivation layer, PEACl solution dissolved in isopropanol (optimized at a concentration of 1.5 mg/ml) is dynamically spin-coated on the surface of the reference perovskite layer with a speed of 5000 rpm (acceleration 2000 rpm/s) for 30 s, following with annealing at 100 °C for 5 min.

Grain boundary passivated perovskite film (GBP): For preparing the perovskite absorber layer with grain boundary passivation, 25 µL of $PbCl_2$:PEACl solution with a molar ratio of

1:1 dissolved in 1 mL DMSO (optimized at a concentration of 2 mol%) was added in the reference perovskite precursor solution. In the next step, the precursor solutions are spin-coated on top of ITO/2PACz and subsequently were annealed at 150 °C for 30 min. In the case of preparing the grain boundary passivated perovskite layer based on other chloride-based long-chain organic alkylammonium salts (n-BACl and n-OACl) the same procedure was applied.

Deposition of interlayer 2D/3D perovskite heterostructure

The grain boundary & surface passivated perovskites (GBP&SP) layer are prepared by the spin coating of PEACl interlayer on top of the grain boundary passivated perovskite film, followed by annealing at 100 °C for 5 min in a nitrogen atmosphere.

$Cs_{0.17}FA_{0.83}Pb(I_{0.92}Br_{0.08})_3$ ($E_g \approx 1.6$ eV)

Dual passivated perovskite layer: The precursor solution of the double-cation $Cs_{0.17}FA_{0.83}Pb(I_{0.92}Br_{0.08})_3$ perovskite absorber layer was prepared by dissolving 0.83 mmol FAI (143 mg), 0.17 mmol CsI (44 mg), 0.88 mmol PbI_2 (444 mg, 10% excess of PbI_2), and 0.12 mmol $PbBr_2$ (46 mg) in a 1 mL solvent mixture of DMF:DMSO 4:1 volume ratio. Afterward, as a bulk passivation additive, 35 µL of $PbCl_2$:MACl solution with a molar ratio of 1:1 dissolved in 1 ml DMSO was added to the reference perovskite precursor solution. The solution was deposited on top of the HTL by a two-step spin coating process: i) 1000 rpm (acceleration 2000 rpm/s) for 10 s, ii) 5000 rpm(acceleration 2000 rpm/s) for 40 s. 150 µL CB was poured on the spinning substrate 20 s before the end of the second step. The samples were annealed at 100 °C for 30 min in an inert atmosphere. In the next step, as a surface passivation interlayer, the PEACl solution dissolved in IPA (1.5 mg/ml concentration) was deposited on top of bulk passivated perovskite film with a speed of 5000 rpm (acceleration 2000 rpm/s) for 30 s, followed by annealing at 100 °C for 5 min in a nitrogen atmosphere.

$(Cs_{0.05}MA_{0.22}FA_{0.73}Pb(I_{0.77}Br_{0.23})_3$ ($E_g \approx 1.68$ eV)

Dual passivated perovskite layer: The precursor solution of the double-cation $Cs_{0.05}MA_{0.22}FA_{0.73}Pb(I_{0.77}Br_{0.23})_3$ perovskite absorber layer was prepared by dissolving 1.21M PbI_2 (558mg), 0.37M $PbBr_2$ (136.5mg), 1.11M FAI (191 mg), 0.34M MABr (38.2mg) and 0.075 CsI (19.5 mg) in a 1 mL solvent mixture of DMF:DMSO 4:1 volume ratio. In this case, as an additive for the bulk passivation strategy, 0.25 mg of PEAI was incorporated into the precursor solutions. The perovskite films were spin-coated on the substrates by a two-step program: 1000 rpm (acceleration 200 rpm/s)) for 10 s and 5000 rpm (acceleration 2000 rpm/s) for 30 s. 15s after the start of the second step, 150 µL of EA was poured on the spinning substrate. The samples were then annealed at 100 °C for 45 min in a nitrogen atmosphere. Here, we introduced 1 nm lithium fluoride (LiF) by thermal evaporation between the Perovskite and ETL which is used as a common effective interlayer for reducing interfacial recombination.[49,50,166]

Deposition of electron transport layer

23 nm C_{60} as an ETL and 3 nm BCP as a hole blocking layer were thermally evaporated, respectively, at an evaporation rate of 0.1-0.2 Å/s and a pressure of around 10^{-6} mbar using a Lesker PVD system

Evaporation of metal back electrode for completing opaque PSC

In this step, the edges of the perovskite substrates were swiped using GBL and the opaque devices are completed by evaporating Ag (≈ 125 nm) as a back contact through shadow masks using a Lesker PVD system to define the active area to 12.5 mm^2.

3.1.4. Semi-transparent p-i-n perovskite solar cell

For preparing semi-transparent PSC with an active area of 50 mm^2, the following device stack is utilized in Chapter 6: Glass/IO:H/2PACz/$Cs_{0.17}FA_{0.83}Pb(I_{0.92}Br_{0.08})_3$/$C_{60}$/$SnO_x$/IZO/ Au/$MgF_2$ (Figure 3-2). It should be noted that here instead of using ITO for the front contact, we employed IO:H to further reduce the optical losses, in particular in the NIR wavelengths.[167]

Atomic layer deposition of buffer layer

For fabrication of semi-transparent p-i-n PSC, instead of BCP after deposition of C_{60}, a thin layer of SnO_x (≈ 35 nm) was deposited by reactive ALD (Picosun R200) using TDMASn (pulse time 1.6 s, purge time 12 s) and water (pulse time 0.1 s, purge time 16 s) as SnOx precursors and high-purity Ar (99.999%) as carrier/purge gas. The line flows of TDMASn and water were set to 120 and 150 sccm, respectively. The TDMASn source container was preheated for 1 hour at 70 °C, to ensure thermal equilibrium. The deposition of the buffer SnO_x layer with high transparency, which also acts as a carrier-selective contact, is mainly due to the protection of the underlying organic C_{60} and perovskite layer from the sputtering damage during the deposition of rear TCO.[36,168]

Sputtering of rear transparent conductive oxide electrode for completing p-i-n semi-transparent PSC

In the next step, a 165 nm of IZO as a transparent rear electrode is sputtered through a shadow mask with an active area of 50 mm^2 and sputtering parameters of power 100 W, substrate temperature 25 °C, deposition time = 2555 s, pressure = 1.5 mTorr and O_2 to argon ratio = 1%. It should be noted that here we replaced the in-house sputtered ITO rear electrode used in Chapter 5 with the in-house sputtered IZO rear electrode to further reduce the absorption losses.[125,167,169] Finally, the semi-transparent p-i-n devices were completed by deposition of Au fingers by thermal evaporation at a rate of 2 Å s^{-1} using a shadow mask.

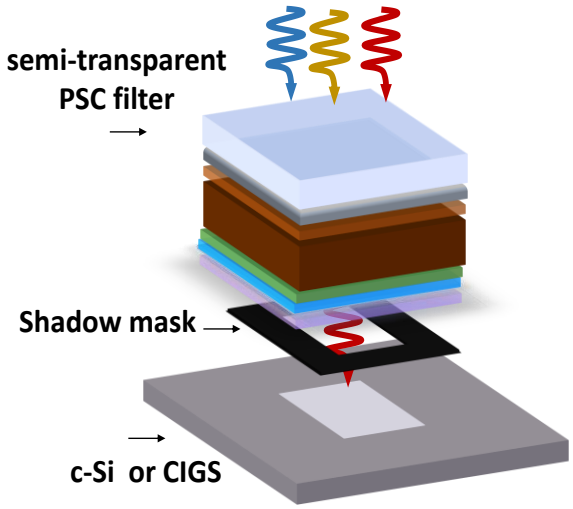

Figure 3-3: Schematic illustration of a 4-terminal (4T) perovskite/c-Si or perovskite/CIGS tandem solar cell.

Thermal evaporation of anti-reflection coating

For this case, a 165 nm MgF_2 was deposited on top of the rear IZO at a rate of 3–4 Å s^{-1} at 6×10^{-6} mbar pressure, while we attached polydimethylsiloxane (PDMS) anti-reflection foil textured with randomly-inverted pyramids on the backside of the IO:H front electrode to achieve better light trapping as well as more transmission from the top semi-transparent cell into the bottom cell for 4T tandem configuration.[170–173]

3.1.5. 4-terminal perovskite-based tandem solar cell

As we discussed in Chapter 2, in case of 4T tandem solar cells both top semi-transparent PSC and bottom c-Si or CIGS bottom cells are independently electrically connected while they are optically interlinked. As a result, we fabricated semi-transparent PSCs (as the fabrication process was described in Sections 3-1-2 and 3-1-4) and measured their PCE exactly in the same way as the single-junction opaque PSC. On the other hand, the PCE of the bottom cells was measured while a filter of top semi-transparent PSC with the opposite front TCO electrode is applied on top of the bottom cell as illustrated in Figure 3-4. It should be mentioned that a filter comprises of the same layer stack and optical properties as the semi-transparent PSC but with a larger area. A shadow mask with an aperture area of 165 mm^2 was used to define an aperture area in order to measure the bottom solar cells. The final PCE of the 4T devices is calculated by the sum of PCE obtained individually from the top semi-transparent PSC and bottom c-Si or CIGS solar cell when operating underneath the semi-transparent PSC filter. The bottom c-Si used for fabricating 4T tandem solar cells is an interdigitated back contact (IBC) c-Si solar cell provided by a collaboration partner from Institute for Solar Energy Research GmbH (ISFH)[174] and CIGS solar cell was provided by the collaborator Zentrum für Sonnenenergie und Wasserstoff-Forschung Baden-Württemberg (ZSW).[175]

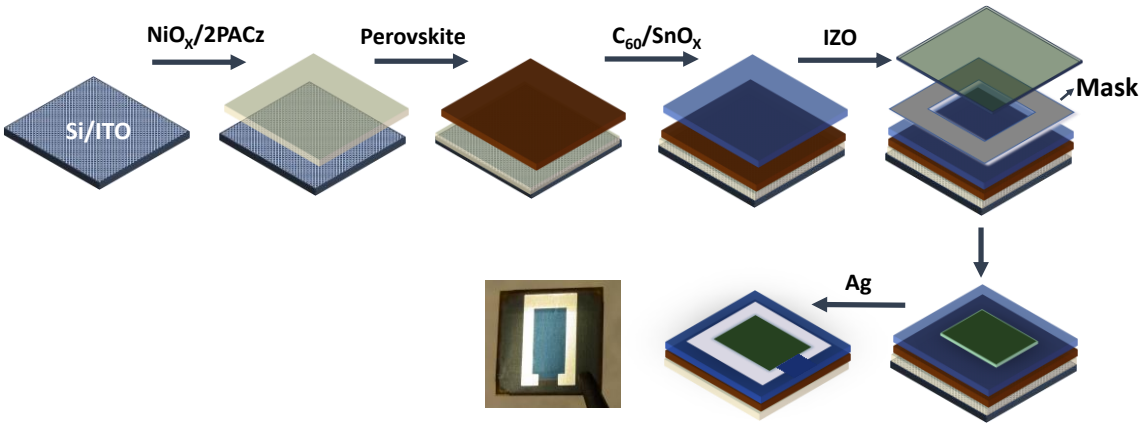

Figure 3-4: Schematic illustration of the fabrication process for 2-terminal (2T) perovskite/silicon tandem solar cell.

3.1.6. 2-terminal perovskite/c-Si tandem solar cell

2T perovskite/silicon tandem solar cells were fabricated in the p-i-n architecture. The silicon solar cells used in this thesis were provided by a collaboration partner (Meyer Burger company) with a size of 0.16 cm × 0.16 cm. It should be mentioned that the ITO recombination layer was already formed by the company on the front side of the substrate as illustrated in Figure 3-4. We started with cleaning the silicon wafers by using acetone and isopropanol via spin coating the substrates. After that, the back contact was formed by thermal evaporation of 300 nm silver with a rear of 0.5 Å s^{-1} at the backside of the silicon wafers using a shadow mask with an active area of 50 mm^2. For deposition of HTL, a very thin layer of NiO_X (15-20 nm) was sputtered in a pure argon atmosphere at a pressure of 1 mTorr and a power of 8 W in a PVD 75 Pro-Line sputter system (Kurt J. Lesker Company). The purpose of the NiO_X layer prior to deposition of the self-assembled monolayer (2PACz) was to enhance the surface coverage of the 2PACz on the substrate.[176] The samples were then transferred to the glovebox for deposition of 2PACz. At the next step, wide-bandgap double-cation $Cs_{0.05}MA_{0.22}FA_{0.73}Pb(I_{0.77}Br_{0.23})_3$ (E_g = 1.68 eV) and C_{60} layers were deposited in the same way as we proceeded the perovskite single-junction devices. Afterward, a thin layer of SnO_X (35 nm) was deposited by reactive ALD similar to the fabrication of semi-transparent p-i-n PSC. For deposition of the transparent front electrode, 160 nm of the IZO layer was sputtered under the same condition as the fabrication of p-i-n semi-transparent PSC. Finally, a c-shaped silver electrode was thermally evaporated using a mask with an active area of 50 mm^2. At the final step, 150 nm of MgF_2 was employed as an antireflective coating.

3.2. Characterization techniques

3.2.1. Current density-voltage characteristic

As discussed in Chapter 2, the standard test condition for measuring the current density-

voltage (*J*–*V*) characteristic of a solar cell is illuminated with a reference AM1.5G (100 mW/m^2) solar spectrum at the temperature of 25 °C. The typical *J*–*V* characteristic of a solar cell is shown in Figure 2-15. In this thesis, the measurement was carried out using a solar simulator (Newport, Oriel Sol3A) with a xenon lamp (Osram Licht AG). To adjust the light intensity to the global standard AM1.5G spectrum, it was calibrated using a certified silicon solar cell (Fraunhofer ISE) equipped with a KG5 bandpass filter for PSC and a KG_0 for monolithic perovskite/silicon solar cell. Meanwhile, during the measurement, the temperature of the devices was controlled by a house-made sample holder that is with a Peltier element for cooling and heating. To take into account the effect of the hysteresis on the performance of the perovskite solar cell (as discussed in Section 2-2-4 and Figure 2-17a), we measured the devices with a constant sweeping rate of 600 mV/s in both backward and forward directions. To derive a reliable PCE of the PSCs due to the hysteresis effect we measured the stabilized PCE under 5 min continuous illumination (Figure 2-17b) at a constant voltage close to the maximum power point (MPP) (Chapters 4 and 5) and at the MPP (Chapters 6 and 7).

3.2.2. External quantum efficiency

As we discussed in Section 2-2-4 in Chapter 2, the external quantum efficiency (EQE) is measured to determine the spectrally resolved response of the solar cell. In this thesis, the EQE measurement was performed by PVE300 photovoltaic QE system (Bentham EQE system) with a chopping frequency of ~570 Hz and an integration time of 500 ms to obtain the spectra a wavelength range from 300 to 850 nm. An illumination spot (1.5 mm) was utilized to acquire the average in the EQE spectra due to the variation introduced by inhomogeneous scattering and transmission from the perovskite layer. It should be noted that the reported J_{SC} for the 4T devices in Chapter 5 and 7 and the best-performing PSCs in Chapter 6 is corrected using the ratio of J_{SC} derived from the EQE and *J*–*V* measurements to obtain a further accurate determination of the J_{SC} and thus PCE for the fabricated devices.

3.2.3. Ultraviolet-visible spectroscopy

Ultraviolet-visible (UV-Vis) spectroscopy is an analytical technique to measure the transmittance (T) and reflectance (R) of thin films. In this measurement, a light beam is split into a monochromatic light (with the desired wavelength), focusing on the sample to measure either the reflection at the sample or the transmission through the sample. The central component in both cases is an integrating sphere, where its interior is an almost perfectly diffuse reflecting body (Figure 3-5). When transmittance is measured, the sample is attached to the input port of the integrating sphere and the exit side is closed by a white standard (Figure 3-5a). In case of reflectance, the sample is attached to the exit side of the integrating sphere and irradiated by an incident beam through the entrance port (Figure 3-5b). The transmitted or reflected light is collected using a detector placed inside an integrating sphere. Typical transmittance and reflectance spectra of the perovskite

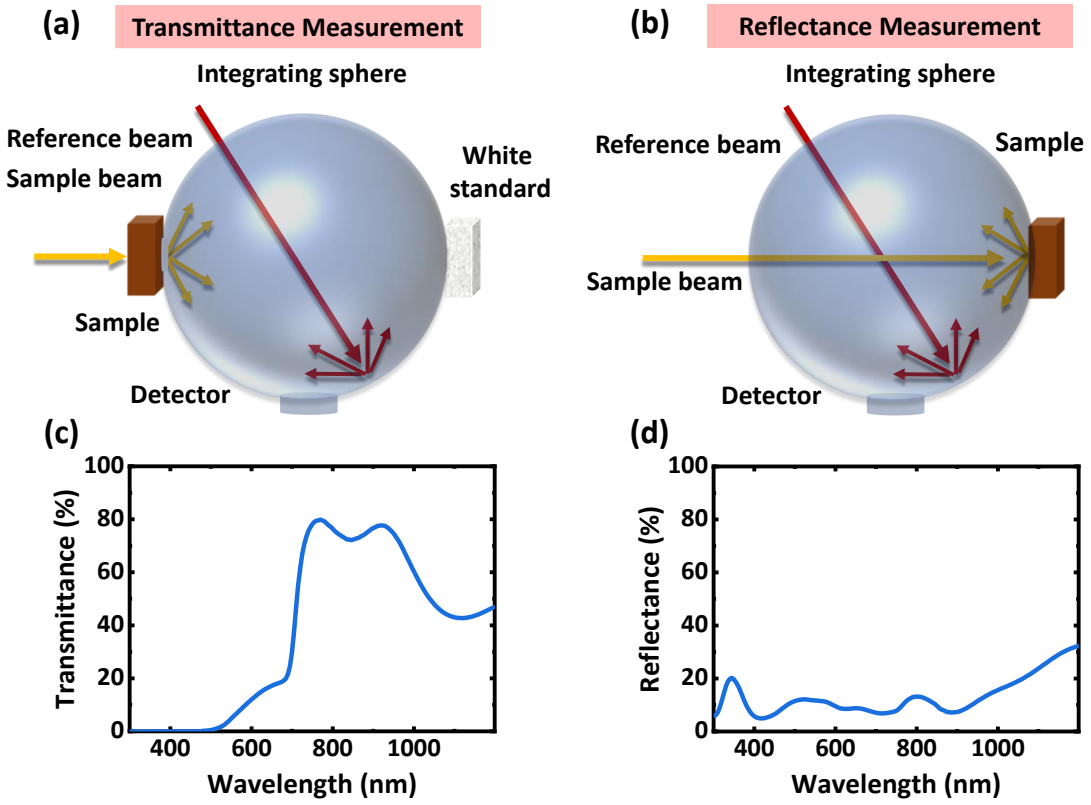

Figure 3-5: Illustration of (a) transmittance and (b) reflectance principle. The typical (c) transmittance and (d) reflectance measurement of semi-transparent perovskite solar cell used in Chapter 5.

absorber layer is demonstrated in Figures 3-5c and d. For calibration, at the beginning, a zero line and a 100% signal are measured without a sample. The absorptance (A) is determined by using the following equation:

$$A = 1\text{-}T\text{-}R \tag{3.1}$$

Moreover, this measurement can be used to calculate the absorption coefficient of a thin film with a thickness of *d*, which describes how far the light can penetrate into the material before it is absorbed. Therefore, according to Lambert-Beer's law:

$$\alpha = -\frac{1}{d}\ln\frac{I}{I_0} = -\frac{1}{d}\ln\frac{(1-R)^2}{T} \tag{3.2}$$

Where I_0 is the incident light intensity and I is the light intensity after passing through the perovskite layer. By knowing α and the energy of the photons ($h\nu$), the optical E_g of the perovskite can be determined from a Tauc plot method using the following equation:[177]

$$(\alpha h\nu)^{1/x} \propto B\,(h\nu - E_g) \tag{3.3}$$

where x is defined as the nature of the electron transition and is equal to 2 for the direct bandgap semiconductors.[178] By plotting $(\alpha h\nu)^2$ as a function of $h\nu$, the bandgap is

estimated by the intersection of the linearly fitted region and the x-axis where $(\alpha h\nu)^2$= 0.In this thesis, the transmittance and reflectance measurements of the perovskite absorber layer were performed using a PerkinElmer Lambda 1050 spectrophotometer using an integrating sphere. We set the illumination spot as large as possible to average the possible inhomogeneities of the films.

3.2.4. Photoluminescence

In a semiconductor, when the energy of the incident photons is equal or higher than the bandgap, a transition of an electron from the valence band to the conduction band occurs, resulting in a generation of electron-hole pairs (see Chapter 2, Section 2-2). The emission of light or photons due to the radiative recombination of these free electron and hole pairs is called photoluminescence (PL). Steady-state and time-resolved photoluminescence are two well-known PL spectroscopy techniques that are used to determine the optical and electronic properties of the thin film. In case of steady-state PL, the average emission on the scale of microseconds to milliseconds is measured through the samples upon excitation. Contrary to steady-state PL spectroscopy, in TPRL measurement, a short light pulse in a scale of picosecond or femtosecond is used to generate free charge carriers. This allows us to investigate the dynamic process occurring in the sample after excitation such as temporal decay in PL spectra, thus providing useful information on the charge carrier recombination dynamics. As discussed in Chapter 2, not all excited electrons can be radiatively recombined, as the presence of the defects enhances the possibility of non-radiative recombination (such as trap-assisted non-radiative recombination). As a result, a shorter lifetime of charge carriers reflects the low quality of the absorber layer due to the enhanced non-radiative recombination losses.

In this thesis, TPRL measurements were performed in the air for the perovskite absorber layer in gated mode with a pulsed laser of 532 nm. For the excitation of the sample, a repetition rate of 1 kHz and a pulse width of 0.8 ns was employed. All measurements were carried out with a pump fluence of ~20-30 nJ/cm^2. The PL emission was detected using an ACTON spectrometer and a CCD camera PIMAX512 at room temperature.

3.2.5. X-ray diffraction

X-ray diffraction (XRD) is a prevalent technique to determine the crystallographic properties (crystallite grain size and preferred orientation, lattice parameters) of the material based on interaction of X-ray waves in a crystalline substance. Figure 3.6 demonstrates a schematic representation of the working principle of XRD. When the X-rays with the wavelengths in the same order as the spacing atoms hits the periodically arranged atoms, it is scattered from the crystal plane, resulting in constructive and destructive interference according to Bragg's law of diffraction:

$$2d\sin\theta = n\lambda;\ n = 1, 2, 3.... \quad 3.4$$

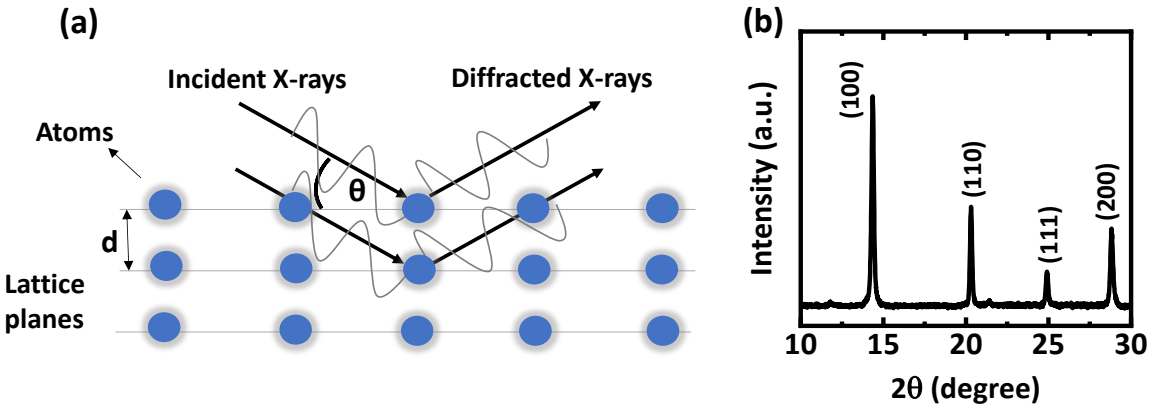

Figure 3-6: (a) X-ray diffraction (XRD) in accordance with Bragg's law. (b) A typical XRD diffraction pattern of a double-cation perovskite layer used in Chapter 4.

where d is the distance between the crystal lattice planes of atoms, λ is the wavelengths of X-rays, θ is the incident angle of the X-rays and n is a constant. Subsequently, detecting the intensity of the diffracted X-rays as a function of scattering angle provides information on the density of the electrons that can determine the mean position of the atoms within the crystal. Therefore, the XRD pattern exhibits the position and intensity of the resulting diffraction peaks which is as unique as a fingerprint and can be used to identify the unknown material and its phase. In this thesis, XRD measurements were conducted to determine the crystal plane diffraction from 2D-RP perovskite and 3D perovskite absorbers. The crystal structure of the perovskite layers was carried out utilizing XRD (Bruker D2Phaser system) with Cu-Kα radiation (λ = 1.5405 Å) in Bragg–Brentano configuration using a LynxEye detector. High-resolution XRD was performed by a Bruker D8 DISCOVER system with Cu-Kα radiation in Bragg–Brentano configuration.

3.2.6. X-ray photoelectron spectroscopy

To analyze the chemical composition and the chemical environment of the material on the surface of the thin film (probing depth of a few nanometers), X-ray photoelectron spectroscopy (XPS) as a surface-sensitive technique is used. This is based on the photoelectric effect by utilizing X-ray illumination to ionize the atoms (exciting electrons from a core level into the vacuum) and probing the kinetic energies (E_k) of the ejected photoelectrons (Figure 3-7 a). As the E_k of emitted electrons is detected, the binding energy (E_b) of the excited electron is calculated by the following equation:

$$E_b = h\nu - (E_K + \phi) \qquad 3.5$$

where $h\nu$ is the energy of the X-ray photons and ϕ is the work function (energy difference between the vacuum level and the Fermi level) of the sample. As the binding energy of the core level electrons for each element is specific and depends on the chemical environment, therefore, it provides information about the elemental composition and the bonds at the surface. The sensitivity toward surface chemistry arises from a relatively short depth that

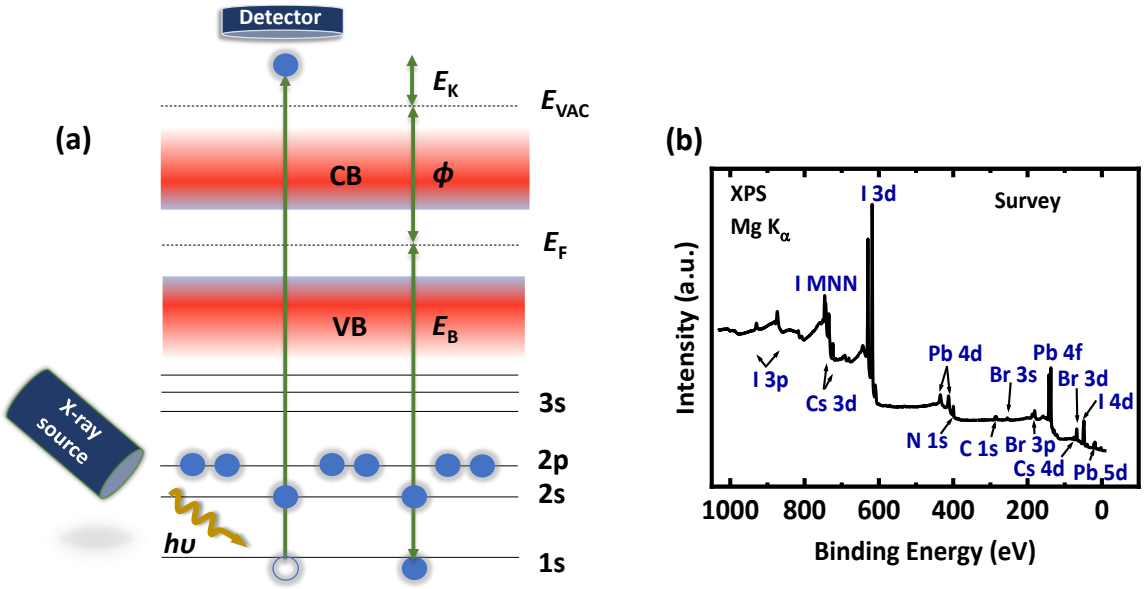

Figure 3-7: Schematic illustration of the X-ray photoelectron spectroscopy (XPS) principle. (b) A typical XPS survey pattern of double-cation perovskite thin film used in Chapter 4.

a photoelectron can travel before it losses its energy due to an inelastic scattering process with another electron, a photon, and/or composition impurity.

In this thesis, we used the XPS technique to determine the chemical compositional changes at the surface of the perovskite absorber layer upon deposition of the ultrathin 2D RP perovskite layer. Figure 3-7b demonstrates an XPS spectrum of the perovskite absorber layer used in Chapter 4, in which the intensity of the detected photoelectrons is plotted as a function of binding energy (in eV). Each element exhibits a distinct set of XPS peaks correlated to the electron's configuration, e.g., 1s, 2s, 2p, etc. The XPS measurement in Chapter 4 was carried out by UHV experimental system in the Materials for Energy (MFE) Lab at KIT by Dr. Dirk Hauschild. The samples were sealed under Argon gas and introduced into the ultra-high vacuum (UHV) system via an Argon-filled glovebox without air exposure. The UHV experimental system was equipped with an Omicron Argus CU electron analyzer, a DAR 450 twin anode (Mg Kα and Al Kα) X-ray source, and a He gas discharge lamp. In order to avoid beam-induced changes due to X-rays prior to the reported measurements, extensive time-resolved measurements were performed to characterize beam damage. Based on this study, measurement times of 10 min (or less) for XPS were determined suitable to avoid the influence of beam-induced changes on the spectra. The XPS measurement in Chapter 6 was performed by Dr. Fredricks at Innovation Lab GmbH in Heidelberg using photoelectron spectroscopy with a PHI 5000 Versa Probe at the Cluster tool.

3.2.7. Scanning electron microscopy and cathodoluminescence

Scanning electron microscopy (SEM) is one of the main techniques for imaging thin films (surface, cross-section) with resolutions less than 1 nm which can provide useful

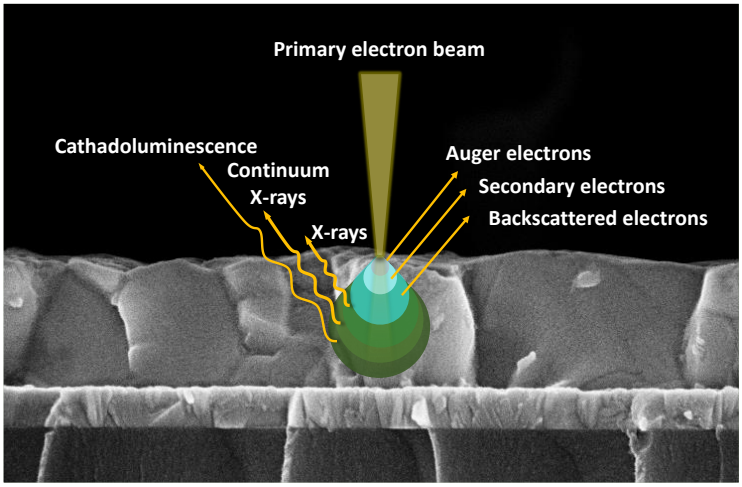

Figure 3-8: Illustration of the incident electron beam interaction with the sample, generating variety effects at different depth of thin fil. For scanning electron microscopy, the secondary electrons are collected and detected for surface imaging.

information about the microstructure and composition of the layer. In principle, in an SEM setup, a thermionic electron gun produces electron beams that are accelerated and then concentrated and focused by a series of electromagnetic lenses before being directed towards the sample. The focused beams (with kinetic energies in the keV range) moved across the sample surface via scanning coils. Upon impinging of these electron beams at various depths of the surface, multiple processes occur including reflection of high-energy backscattered electrons (BSE), emission of low-energy secondary electrons (SEs) by inelastic scattering and Auger electrons which are detected by specified detectors (Figure 3-8). Apart from electron signals, a broad spectrum of electromagnetic radiation (emission of X-rays) and cathodoluminescence (CL) are also detected (Figure 3-8).[179] The SEM images are captured based on using SEs and BSEs. Owing to low kinetic energy, the SEs are emitted only from the top few nanometers of the samples and can be detected either at a low-angle cone to provide information on material contrast, or at high angles to image the surface topography of the sample. Furthermore, high-energy BSEs are emitted from the deeper regions of the samples, yielding information on compositional and elemental distribution.

In this thesis, cross-sectional and top-view SEM images of all perovskite thin films were performed by high-resolution field emission SEM using a Zeiss LEO1530 VP SEM with an in-lens and secondary detector and an aperture size of 20 µm. The SEM images were captured using a 3-kV acceleration voltage. As we mentioned above, electron beam interaction with the sample can also excite an electron from the valence band to the conduction band. However, due to the high energy of primary electrons, inelastic scattering of these electrons generates secondary electrons, Auger electrons and X-rays. Subsequently, these are the secondary electrons with energy three times higher than the bandgap of the sample that can promote the valence electrons into the conduction band. Upon thermalization, the electrons and holes combine radiatively, resulting in the emission of photons with an

energy range between 0.5 to 6 eV (known as CL). This technique can be used for controlling the quality of the samples and detecting the structural composition, electrical conductivity/insulating feature and defect distribution. The CL measurement was conducted at the Australian National University by Dr T. Duong using an FEI Verios SEM equipped with a GatanMonoCL4 Elite at 3 kV accelerating voltage / 25 pA beam current. The CL images were captured in panchromatic mode with appropriate dichroic filters (bandpass filter with 500 ± 40 nm)

3.2.8. Atomic force microscopy

To determine the surface roughness and topography of the perovskite films on a few nanometers scale, atomic force microscopy (AFM) technique is used. This technique comprises a cantilever with a small radius tip for probing the surface, a four-quadrant photodiode, a scanner unit and a laser. In principle, there are two different modes of measurement: static contact and dynamic noncontact or dynamic contact. In a contact mode, once the tip is in contact with the surface, the static deflection of the cantilever due to the forces between tip and sample such as mechanical contact forces, van der Waals forces, or electrostatic forces is detected by the four-quadrant photodiode. In contrast to contact mode which can damage the surface of the samples, in a dynamic or noncontact mode, the tip scans the surface of the sample at a minimal distance and the force interaction varies the resonance frequency of the cantilever oscillation (due to material changes or height differences. This modulation can be measured optically via the reflection of a laser beam pointed onto the cantilever head. Assuming a constant chemical composition of the surface, variations can be primarily traced back to differences in the distance between the sample and the measuring tip. The spatially resolved measurement over a surface thus allows the determination of the roughness of the sample surface. In this work, all the AFM figures were measured on a Bruker Dimension Icon AFM.

3.2.9. Determining of ideality factor by intensity-dependent measurement of the quasi-Fermi level splitting

The ideality factor (n_{id}) of solar cells provides information on the dominant recombination mechanism in the solar cell as we discussed earlier in Chapter 2. A common way to identify the n_{id} of the PSCs is based on the slope of a logarithmic fit of a V_{OC} or internal quasi-Fermi level splitting *vs*. light intensity plot, using the following equation derived from Equation 2-4:

$$n_{\mathrm{id}}(I) = \frac{q}{k_{\mathrm{B}}\,T}\,\frac{\mathrm{d}V_{\mathrm{OC}}}{\mathrm{d}ln\,\frac{I}{1\ \mathrm{mW/cm^2}}} \qquad 3.6$$

Where q is the electron charge, k_B is the Boltzmann constant, I is the irradiation intensity and T is the temperature.[180] This equation indicates that V_{OC} is completely independent of

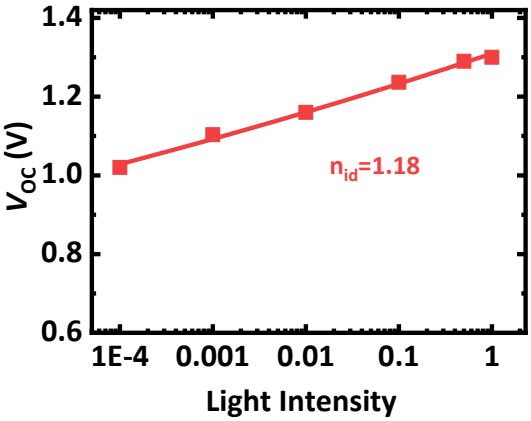

Figure 3-9: Ideality factor (n_{id}) of the perovskite solar cell derived from light-intensity dependent open-circuit voltage (V_{OC}).

series resistance because no current flows at open-circuit conditions. According to the literature, n_{id} has been proven to be governed by bulk as well as interfacial recombination properties.[153,180,181] For high-performing PSCs that are not limited by failures at either of the perovskite/CTL interfaces, a reduction of n_{id} towards a value of 1 is typically associated with a predominant bimolecular radiative and reduced trap-assisted Shockley–Read Hall recombination.[153,159] In this thesis, n_{id} of PSCs in Chapter 4 was conducted by plotting V_{OC} as a function of the light intensity using an all-in-one measurement system Paios (Fluxim AG). A white LED (Cree XP-G) was used for the illumination in all experiments. An exemplary measurement of n_{id} for PSC used in Chapter 4 is shown in Figure 3-9.

3.2.10. Space-charge-limited current

Space-charge-limited current (SCLC) measurement is a well-known technique for estimating charge carrier mobility and trap density in semiconductors and has been widely used in metal halide perovskites as well. To estimate the charge carrier mobility in the perovskite layer, the electron-only or hole-only devices are fabricated, meaning that the perovskite layer is sandwiched between the two ETL with a device configuration of ITO/SnO_2/Perovskite/C_{60}/BCP/Ag for electron only or two HTL with a structure of ITO/2PACz/Perovskite/Spiro-MeOTAD/Ag for the hole-only device. The dark *J-V* measurements of the devices plotted on a log-log scale show three distinct regions: (1) Ohmic region with a slope of ~1, (2) trap filling region with a slope larger than 2 and (3) trap-free SCLC region with a slope of ~2. The mobility value is extracted from the quadratic region of the dark *J-V* curve that is governed by the Mott-Gurney equation:

$$J = \frac{9}{8}\mu\varepsilon\varepsilon_0\frac{V^2}{d^3} \qquad 3.7$$

where J is the current density, V is the applied voltage, ε_0 is the permittivity of the vacuum, ε is the dielectric constant of the material, μ is the mobility of the charge carrier (electron or hole) and d is the thickness of the active layer. This equation is also referred to as the

square law for trap-free SCLC. In SCLC measurement, *J* is dominated by charge carriers injected from the contacts, thus it is only dependent on the mobility and no more on the charge carrier density.

The trap densities are also calculated from the trap-filled-limit voltage (V_{TFL}):

$$V_{\mathrm{TFL}} = \frac{qn_t d^2}{2\varepsilon\varepsilon_0} \qquad 3.8$$

Where n_t is the trap density of the perovskite absorber layer, V_{TFL} is the voltage at the intersection point of the tangent with slope 1 and tangent with a slope higher than 2 in the dark *J*-*V* curve. In our experiment, SCLC measurements were conducted on Paios (Fluxim AG)-platform for all cells and OLEDs.

4. Wide-Bandgap n-i-p Perovskite Solar Cells with 2D/3D Heterostructure

This chapter deals with open-circuit voltage (V_{OC}) losses in wide-bandgap (1.72 eV) perovskite solar cells (PSCs) based on the standard n-i-p device architecture. It introduces an effective approach to reducing these losses by employing a large alkylammonium interlayer at the interface between the perovskite and hole extracting layer. We demonstrate that this strategy strongly surpasses non-radiative and interfacial recombination that typically occurs between the charge transport layer (CTL) and perovskite, enabling one of the highest V_{OC} and power conversion efficiency (PCE) reported for wide-bandgap PSCs so far.

This chapter is based on our publication in *Advanced Energy Materials* with the title "Record Open-Circuit Voltage Wide-Bandgap Perovskite Solar Cells Utilizing 2D/3D Perovskite Heterostructure". Most of the figures in this chapter are adapted or reproduced with the permission of *Advanced Energy Materials*.[182]

Acknowledgments and contributions

Saba Gharibzadeh as the first author of this study conceived the initial idea, designed the experiments, fabricated the perovskite films, and performed the current density–voltage (J–V), external quantum efficiency (EQE), X-ray diffraction (XRD) and ultraviolet-visible spectroscopy (UV-Vis) of the devices. Dr. Dirk Hauschild performed and analyzed the X-ray and Ultraviolet photoelectron spectroscopy (XPS/UPS) of the perovskite thin films. Dr. Tobias Abzieher carried out additional high-resolution XRD measurements. The calculation of the intermediate phase of the 2D Ruddlesden Popper was proceeded by Dr. Amir Abbas Haghighirad. The transient photoluminescence photoluminesce spectroscopy (TPRL) of the sample was provided by Dr. Marious Jakoby, and further analyzed by Dr. Ian A. Howard. Dr. Ulrich Paetzold supervised the entire project. Saba Gharibzadeh acknowledges the fruitful discussion with Dr. Bahram Abdollahi for the data analysis and also the support of Dr. Somaye Moghadamzadeh, Dr. Jonas Schwenzer, and Dr. Philipp Brenner, who helped with the initial development of perovskite solar cells with the n-i-p architecture.

4.1. Introduction

High-efficiency mixed-halide wide-bandgap PSCs (1.65–1.80 eV) in combination with well-established photovoltaic (PV) technologies as a tandem configuration bear an excellent potential to achieve the PCE beyond the Shockley-Queisser (S-Q) limit of single-junction solar cells (~33 %).[143,183,184] Nevertheless, the issue of a large V_{OC} loss in such wide-bandgap PSCs hinders further enhancement of PCE, as the V_{OC} deficit increases when the bandgap widens.[97,185,186] This large V_{OC} deficit is partly attributed to the segregation of halides under illumination. In fact, to widen the bandgap of the mixed-halides perovskite, the partial replacement of iodide (I^-) with bromide (Br^-) anions in the X site of the crystal lattice is needed (see discussion in Chapter 2).[56] However, once illuminated, the mixed-halides perovskite phase is prone to separate into low-bandgap I-rich and wide-bandgap Br-rich domains. Consequently, the formation of I-rich domains with a lower bandgap during photo-induced phase segregation can generate more charge carrier traps that increase the recombination rate, thus deteriorating the device performance.[187–189]

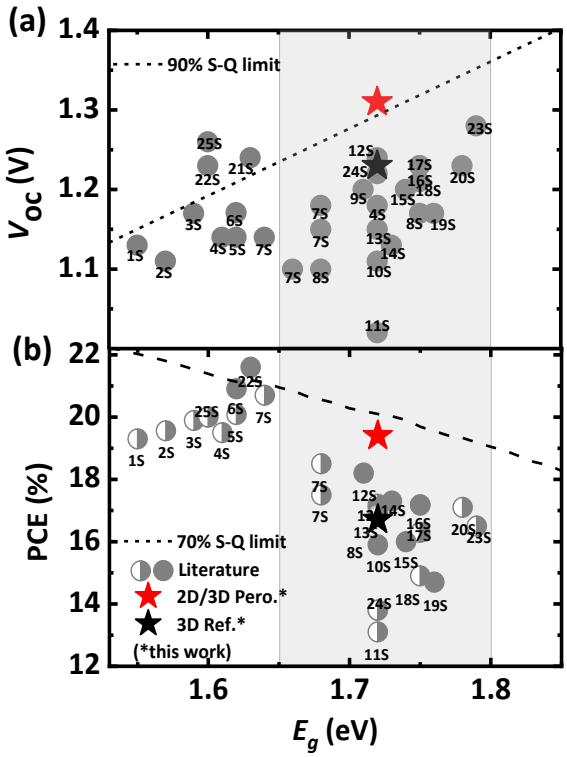

Figure 4-1: Champion (a) open-circuit voltage (V_{OC}) and (b) power conversion efficiency (PCE) of perovskite solar cell (PSC) without (3D Ref.) and with 2D/3D perovskite heterostructure (2D/3D Pero.) as a function of bandgap (E_g) (marked with black and red star). For comparison, the data of the best-performing mixed-halide PSCs with high V_{OC} (marked with gray circles) and decent PCE (>13%) (marked with full-colored and half-colored circles corresponding to the PCEs determined by maximum power point tracking and current-voltage measurements, respectively) reported in the literature as of **2019**. The updated data can be found in Chapter 1. The dashed line represents 90% of Shockley-Queisser (S-Q) limit values for V_{OC} and 70% for maximum attainable PCE with respect to a certain E_g. The gray region displays the ideal bandgap range (1.65–1.8 eV) for the top perovskite cell in tandem configuration. All references are provided in Appendix A, Table A1. Adapted with permission from reference [182]. Copyright 2019, Wiley.

In addition to the photo-induced phase segregation, the non-radiative recombination process, which is responsible for four to five times the V_{OC} loss compared to the loss from phase segregation, is identified as a dominant recombination loss in mixed-halide PSC.[43,49] Defects are one of the predominant non-radiative recombination pathways arising from both potentially poor quality of the perovskite absorber and perovskite/CTL interfaces.[109] For this reason, intensive studies have been undertaken to minimize the phase segregation and detrimental defects in PSCs with emphasis on controlling the crystallization of the perovskite film, incorporating additives into the perovskite bulk, engineering the interface and passivating the surface of the perovskite layer.[44,45,122,190,191] Recently, a post-treatment of perovskite films by employing a wider bandgap layered, namely 2D Ruddlesden-Popper (2D-RP) perovskite, has emerged as among the most effective strategy to reduce non-radiative recombination and consequently enhance V_{OC} of PSCs by the formation of 2D/3D perovskite heterostructure.[96,97,99,191–193] Nevertheless, despite all the great developments so far, the V_{OC} of all reported wide-bandgap PSCs with respect to the given bandgap is still less than the record value achieved using a low-bandgap of ~1.6 eV perovskite as shown in Figure 4-1 and Appendix, Table A1. This clearly demonstrates that V_{OC} does not proportionally increase with the bandgap. Thereby, further effort remains vital in order to reduce the V_{OC} loss for wide-bandgap PSCs to achieve a value close to their maximum theoretical limit predicted by the S-Q limit.

To address this challenge, in this chapter, we demonstrate a post-treatment strategy by introducing a novel ultrathin 2D/3D heterostructure interlayer at perovskite/hole transporting layer interface for wide-bandgap PSCs (E_g ~1.72 eV) via spin coating n-butylammonium bromide (n-BABr) on top of the 3D perovskite layer. Through effective interface passivation, 2D/3D heterostructure PSC delivers a V_{OC} 80 mV higher than the reference devices with an enhanced stabilized PCE of up to 19.4%. As shown in Figure 4-1 this achievement exhibits one of the highest V_{OC} reported so far in the literature for such bandgap in PSCs with n-i-p architecture, which also corresponds to 90% of the S-Q limit for the given bandgap. The results show that the formation of the 2D/3D heterostructure interlayer not only acts as an efficient strategy to passivate the surface of the perovskite layer but also as an electron blocking layer due to its wider bandgap. As a result, the interfacial non-radiative recombination decreases, leading to a remarkable reduction in the photovoltage loss of the devices. In the follow-up sections, a detailed investigation of the material properties, as well as the photovoltage characterization of the samples treated with an optimized concentration of n-BABr is performed.

4.2. Performance of solar cells with n-BABr surface treatment

In this section, we investigate the photovoltaic characteristics of PSCs without and with n-BABr surface treatment. Using a double-cation (FA and Cs) perovskite absorber layer in the composition $Cs_{0.17}FA_{0.83}Pb(I_{0.6}Br_{0.4})_3$, we fabricated wide-bandgap PSCs (E_g ~1.72 eV) in

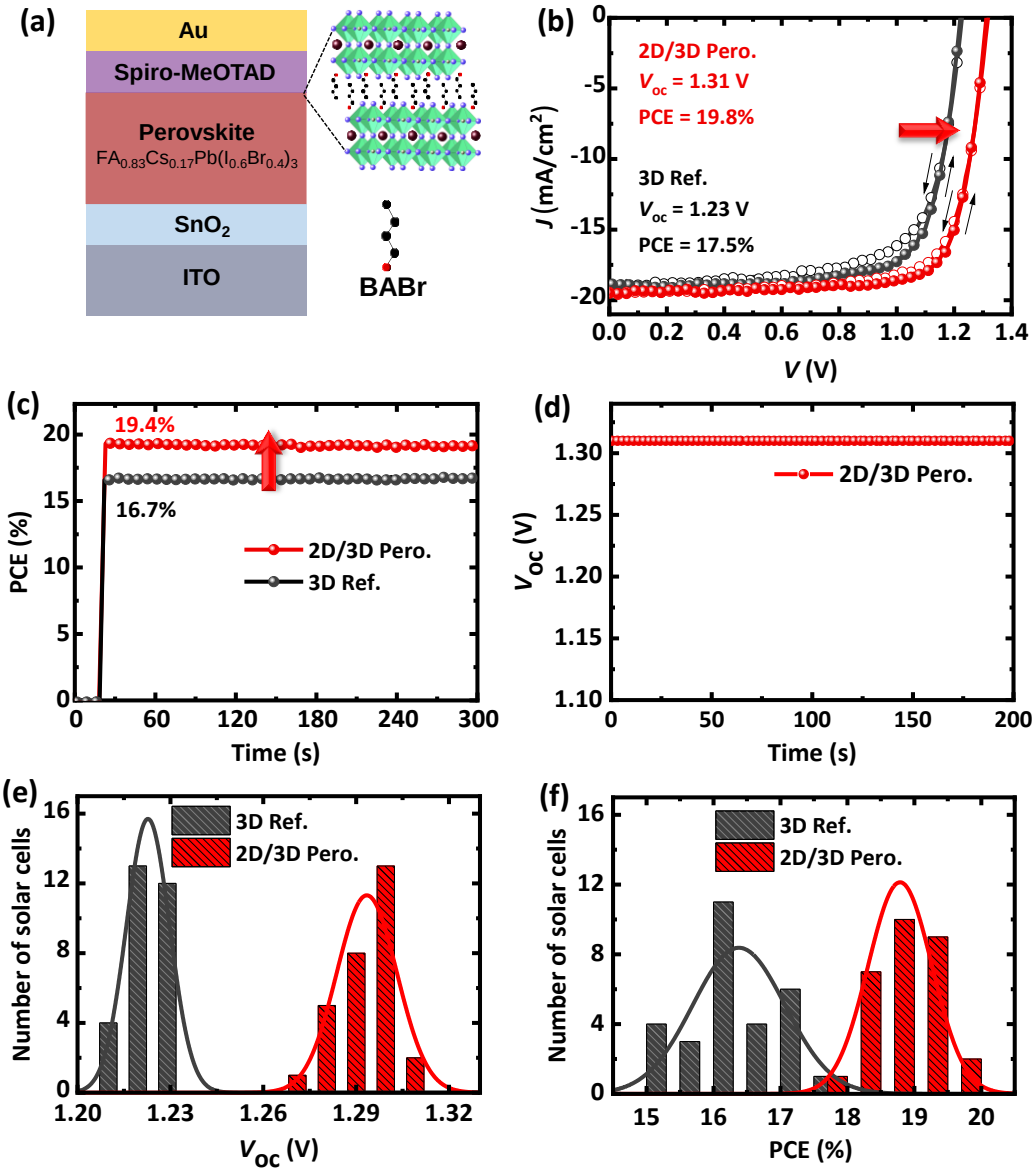

Figure 4-2: (a) Schematic of device architecture based on n-i-p wide-bandgap perovskite solar cells (PSCs) $Cs_{0.17}FA_{0.83}Pb(I_{0.6}Br_{0.4})_3$ treated with n-BABr solution on top of the perovskite absorber layer. (b) Forward (closed symbols) and reverse (opened symbols) current-voltage (*J*–*V*) characteristics of champion 3D reference (3D Ref.) and 2D/3D perovskite heterostructure (2D/3D Pero.) devices measured under solar illumination condition (AM 1.5G, 1000 W m^{-2}. (c) Stabilized PCE of the corresponding devices measured at a constant voltage close to the maximum power point (MPP) under 5 min continuous illumination. (d) Steady-state open-circuit voltage (V_{OC}) of the champion 2D/3D Pero. device measured at continuous illumination (AM 1.5G). (e) The statistic of V_{OC} and (f) PCE distribution for 3D Ref. and 2D/3D Pero. PSCs (from a total of 48 devices), respectively. Adapted with permission from reference [182]. Copyright 2019, Wiley.

a n-i-p layer stack of glass substrate/indium tin oxide (ITO)/nanoparticle-based SnO_2 /perovskite ($Cs_{0.17}FA_{0.83}Pb(I_{0.6}Br_{0.4})_3$)/2,2′,7,7′-tetrakis (N, N′-di-p-methoxy phenylamine)-9,9′-spirobifluorene (spiro-MeOTAD)/Au back electrode (Figure 4-2a). The current-density–voltage (*J*–*V*) measurement of the best-performing reference 3D perovskite solar cell exhibits a V_{OC} of 1.23 V, a fill factor (FF) of 0.74 and a short-circuit current density (J_{SC}) of 19.2 mA/cm^2, yielding a PCE of 17.5% (Figure 4-2b). After n-BABr surface treatment with a

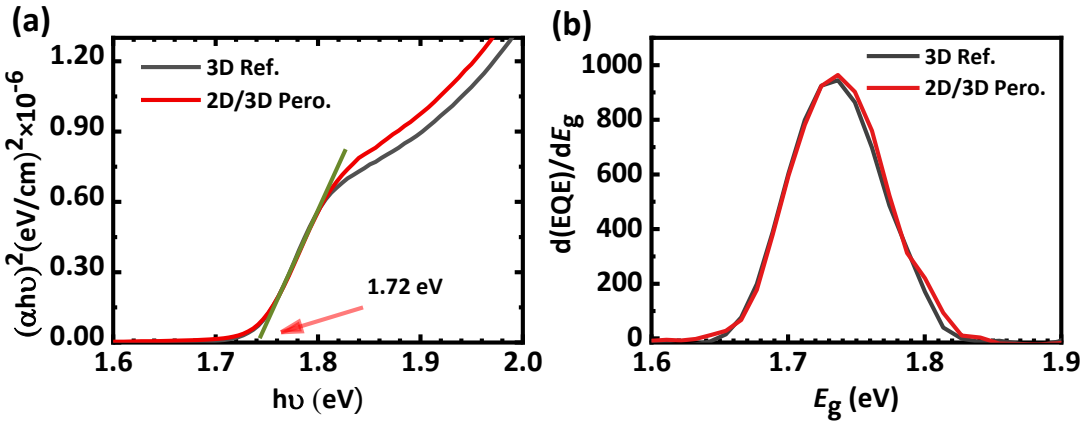

Figure 4-3: Optical bandgap extracted from (a) Tauc plot and (b) inflection point of the external quantum efficiency (EQE) spectra for wide-bandgap double-cation perovskite layers ($FA_{0.83}Cs_{0.17}Pb(I_{0.6}Br_{0.4})_3$) with and without a 2D/3D perovskite heterostructure. Adapted with permission from reference [182]. Copyright 2019, Wiley.

concentration of 2 mg/ml on top of the perovskite absorber layer, an ultrathin 2D/3D interlayer is formed between the 3D perovskite layer and the hole transport layer (HTL) (as we will show later in Section 4-3). The formation of this interlayer results in a substantial increase in device PCE to 19.8% (Figure 4-2b) with negligible hysteresis compared to the reference device. A rapid rise in stabilized PCE of the device incorporating 2D/3D heterostructure is also observed from 16.7% to 19.4% compared to reference PSC measured under 5 min constant illumination at AM 1.5G with 1000 Wm^{-2} (Figure 4-2c). This enhancement primarily arises from a remarkable increase in V_{OC} of up to 1.31 eV, leading to a constant stabilized V_{OC} measured under 5 min constant illumination (Figure 4.2d). This V_{OC} value corresponds to 90% of the maximum theoretical limit V_{OC} achievable for the given bandgap as illustrated in Figure 4.1a. Moreover, the calculated qV_{OC}/E_g ratio for the 2D/3D perovskite heterostructure devices represents one of the highest values of 0.76 achieved so far for wide-bandgap PSCs in the range of 1.65-1.8 eV with PCEs above 13% (Appendix A, Table A1). This is indicative of the high-quality PV material (2D/3D perovskite heterostructure in our case) which demonstrates a high fraction of radiative recombination relative to non-recombination pathways.[151,194,195] It is worth noting that no shift in the bandgap of the 3D perovskite layer after n-BABr treatment is observed, indicating that a widening of the perovskite bandgap, which could be one of the causes for enhanced V_{OC}, does not play any role in V_{OC} enhancement. This observation is supported by comparing the optical bandgap of the perovskite films without and with n-BABr treatment measured by the Tauc plot method as well as the inflection point of the external quantum efficiency (EQE) spectra (Figure 4-3). The statistical distribution of V_{OC} and PCE from 71 devices for both 3D and 2D/3D heterostructure devices verifies the high reproducibility of the surface-treated process with n-BABr solution (Figures 4-1e and f). Along with the improved V_{OC}, we also observe an increase in FF up to 0.78 upon n-BABr treatment, while the J_{SC} remains almost unchanged, indicating that the extraction of charge carriers in 2D/3D heterostructure PSCs occurs effectively as the reference devices. The photovoltaic parameters of the best-performing PSCs are summarized in Table 4-1.

Table 4-1: Current-density–voltage (*J–V*) characteristics of best-performing devices for reference and 2D/3D heterostructure PSCSs treated the various concentrations of n-BABr solution (2, 5 and 7.5 mg/ml) on top of the perovskite absorber layer measured under both reverse- and forward scan direction. Reproduced with permission from reference [182]. Copyright 2019, Wiley.

PSCs	Scan direction	V_{OC} (V)	J_{SC} (mA/cm^2)	FF	PCE (%)
Reference	BW	1.23	19.2	0.74	17.5
	FW	1.22	18.9	0.69	16.2
Treated w. n-BABr (2 mg/ml)	BW	1.31	19.2	0.78	19.8
	FW	1.31	19.2	0.75	19.2
Treated w. n-BABr (5 mg/ml)	BW	1.32	18.2	0.60	14.7
	FW	1.28	18.3	0.58	13.54
Treated w. n-BABr (7.5 mg/ml)	BW	1.18	12.4	0.49	7.1
	FW	1.15	11.9	0.47	6.4

In order to optimize the thickness of the n-BABr interlayer on the performance of the PSCs, we fabricated 2D/3D heterostructure PSCs by varying the concentration of the n-BABr solution dissolved in IPA (2, 5, and 7.5 mg/ml). As depicted from the statistics of the PV

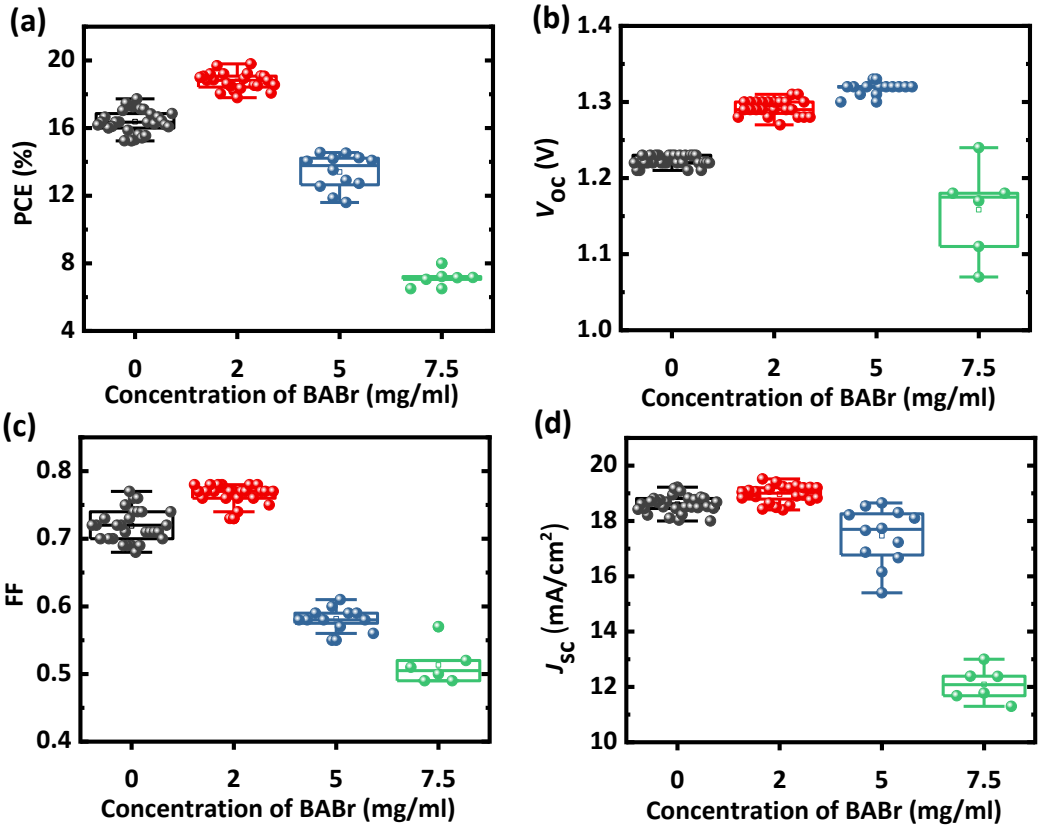

Figure 4-4: Statistical distribution of (a) power conversion efficiency (PCE), (b) open-circuit voltage (V_{OC}), (c) fill factor (FF), and (d) short-circuit current (J_{SC}) determined form the *J–V* characteristic for 70 devices (in total) prepared without (reference) and with 2D/3D perovskite heterostructure interlayer processed by n-BABr treatment with various concentrations of 0, 2, 5, and 7.5 mg/ml. Adapted with permission from reference [182]. Copyright 2019, Wiley.

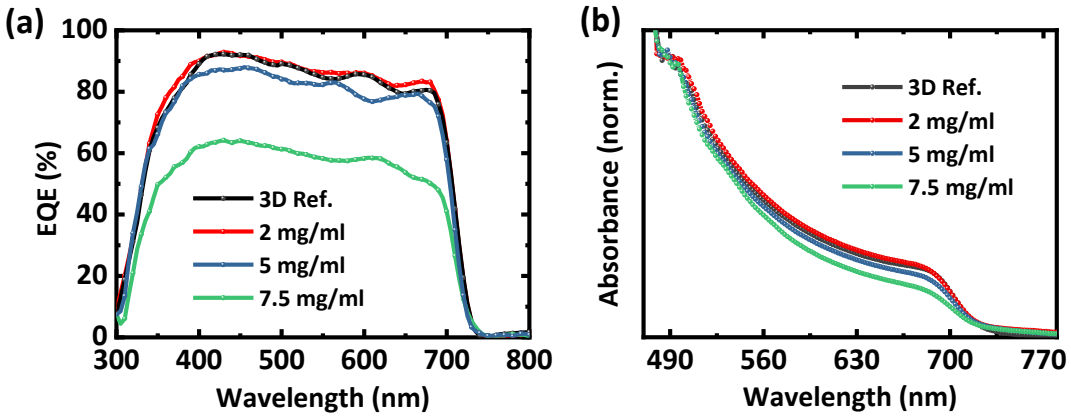

Figure 4-5: (a) External quantum efficiency (EQE) and (b) absorbance of wide-bandgap perovskite solar cells treated without (3D Ref.) and with various concentrations of n-BABr solution (2, 5, 7.5 mg/ml). Adapted with permission from reference [182]. Copyright 2019, Wiley.

parameters in Figure 4-4, we find the concentration of 2 mg/ml as the optimum concentration to achieve the highest performance of the 2D/3D heterostructure PSCs. Although a further enhancement in V_{OC} up to 1.32 V is observed for a concentration of 5 mg/ml, this enhancement is compensated by a decrease in the FF and J_{SC}. For a higher concentration (up to 7.5 mg/ml) the reduction in both FF and J_{SC} becomes more substantial. As we discussed earlier in Chapter 2, this is because of the insulating nature of the 2D layer which hinders the transport of the charge carriers when the thickness of the 2D layer increases, thereby inducing severe charge accumulation and recombination loss.[196,197] The integrated photocurrent obtained from the external EQE spectra is consistent with the trend of J_{SC} derived from the *J*–*V* characteristics for the corresponding devices prepared without and with various concentrations of 2, 5 and 7.5 mg/ml (18.4, 18.6, 17.4 and 11.8 mA/cm^2, respectively). As shown in Figure 4-5a, for 2D/3D PSCs treated with a 2 mg/ml concentration solution, the EQE spectrum demonstrates a similar excellent charge-carrier extraction as the reference PSC, whereas a notable drop in the overall EQE spectrum is observed when the concentration increases to 5 mg/ml. This reduction becomes even more severe for the higher concentration of 7.5 mg/ml, confirming the low resultant J_{SC} for these devices (5 and 7.5 mg/ml). Moreover, the optimum concentration of 2 mg/ml exhibits a similar absorbance spectrum to the reference film, indicating that a thin layer of the 2D perovskite on the surface of the 3D perovskite does not affect the absorption of the underlying 3D perovskite film. In contrast, the expected increase in thickness of the 2D interlayers (volume ratio of 2D to 3D) with increasing n-BABr concentration decreases the absorbance of the 3D perovskite thin film, which is in turn responsible for a reduction in J_{SC}.[198,199]

In the next section, we investigate the material and photophysical characterizations of PSCs based on the optimum concentration of n-BABr (2 mg/ml) to understand how the formation of such an ultrathin 2D perovskite interlayer can induce the significant enhancement in PCE of the devices, in particular an increase in V_{OC}.

4.3. Material characterization of 2D/3D heterostructure

4.3.1. Structural properties

As we discussed in Chapter 2, considering that n-BABr is a large aliphatic alkylammonium spacer cation, which is commonly known to form layered 2D-RP perovskite phase, [76,185] we expect the formation of the 2D layer when n-BABr is coated on top of the 3D double-cation perovskite film. In this context, to obtain information regarding the crystal structure of the perovskite layer and assess whether the interlayer formed upon deposition of n-BABr solution on top of the 3D perovskite is indeed a 2D-RP perovskite, X-ray diffraction (XRD) measurements were performed. As depicted in Figure 4-6a, the characteristic peaks at 2θ ~14.8°, 21.1°, 24.8°, 28.6° are indexed to typical (100), (110), (111) and (200) lattice plane diffraction of double-cation perovskite ($Cs_{0.17}FA_{0.83}Pb(I_{0.6}Br_{0.4})_3$, respectively.[185]

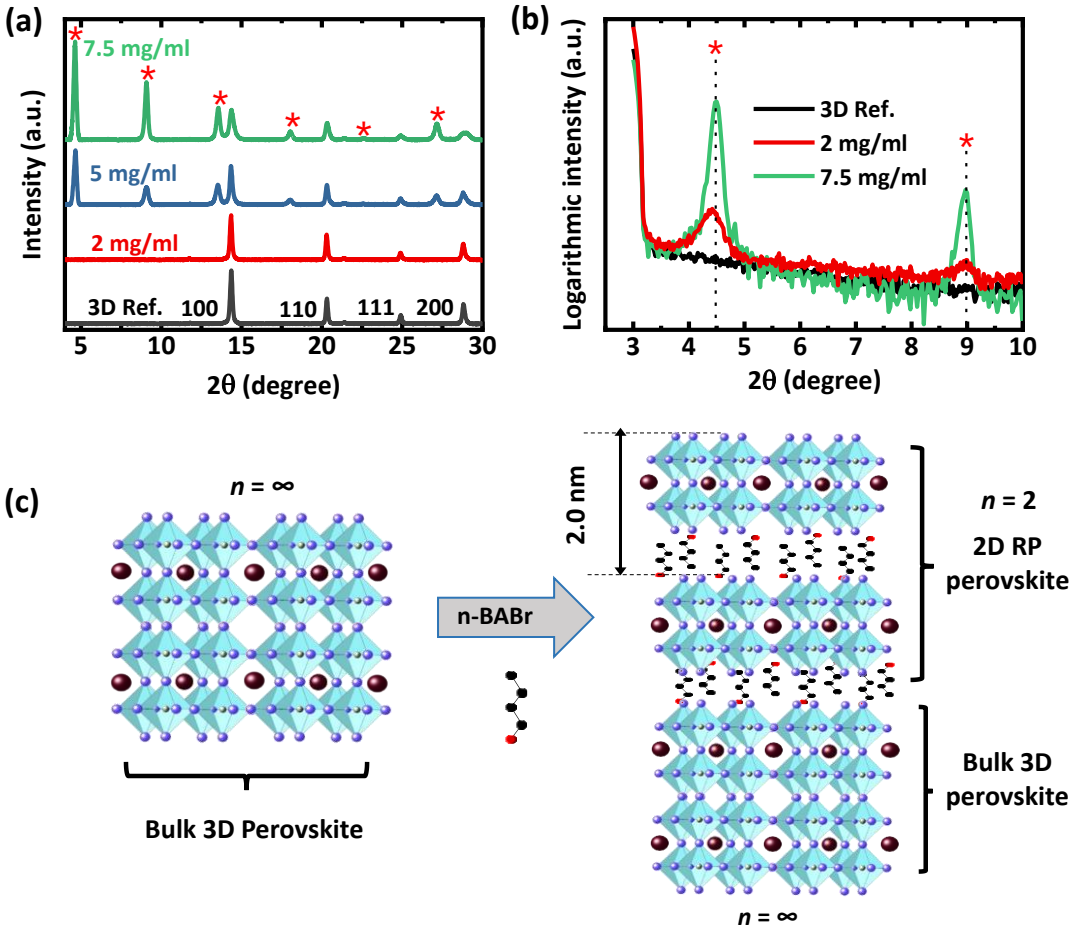

Figure 4-6: (a) X-ray diffraction pattern of wide-bandgap $FA_{0.83}Cs_{0.17}Pb(I_{0.6}Br_{0.4})_3$ perovskite thin-films treated without (3D Ref.) and with various concentrations (2, 5 and 7.5 mg/ml) of n-BABr on top of the 3D perovskite absorber layer. New peaks (denoted by star) indicate periodic reflections and the resulting interference from the 2D perovskite interlayer. (b) Logarithmic intensities of the low angle peaks from 3D Ref., ultra-thin and thick 2D/3D heterostructure layers were performed with higher X-ray intensities and longer integration times. (c) Schematic representation of 2D/3D perovskite heterostructure with a stacking distance of ~2 nm and an intermediate phase n=2.

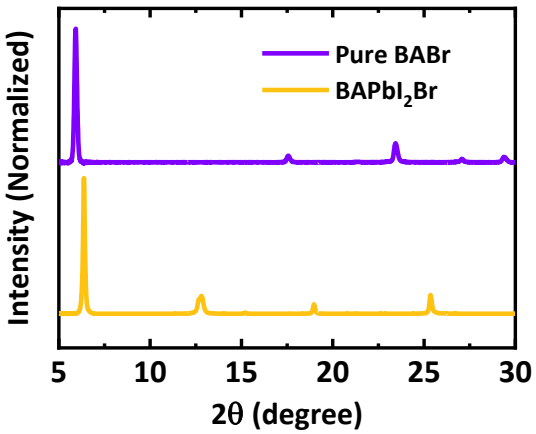

Figure 4-7: X-ray diffraction (XRD) patterns of pure n-BABr and pure 2D Ruddlesden-Popper perovskite ($BAPbI_2Br$) prepared on the glass substrate. Adapted with permission from reference [182]. Copyright 2019, Wiley.

Interestingly, compared to XRD peaks of the 3D reference perovskite film, perovskite samples treated with n-BABr exhibit additional periodic peaks (marked with stars in Figure 4-6a) starting from a very low-angle at 2θ ~4.5°, 9.0°, 13.5°, 18.0°, 22.6°, and 27.2°. These periodic peaks do not correspond to the characteristic peaks of pure n-BABr and pure 2D-RP ($BAPbI_2Br$) perovskite phase (Figure 4-7).[93,200,201] Instead, consistent with the literature, these peaks with a periodic interval of Δ2θ ~4.5°are associated with planes of RP-2D perovskite phase with a composition of $(BA)_2A_{n-1}Pb_n(I_xBr_{1-x})_{3n+1}$ (n=2), where n=2 is the thickness or the number of the inorganic layers and A could be the mixture of FA and Cs in our cases (the exact composition is still unknown).[93,202–205] It is noteworthy that the intensity of the distinct XRD pattern of the 2D-RP is noticeably stronger for the samples treated with higher concentration n-BABr (5 and 7.5 mg/ml), while they are not visually detectable for the optimal low concentration of 2 mg/ml. This could be due to the ultrathin thickness of the 2D layer on top of bulk 3D perovskite which is not sufficient to be determined by the limited sensitivity of the XRD measurement setup to a very thin layer. Therefore, we repeated the measurement with higher X-ray intensities along with long integration times for the perovskite sample treated with low concentration n-BABr. The log-scale plot of the diffraction intensity of the low-angle XRD peaks (below 2θ ~10°) reveals similar peaks located at 2θ ~4.5° and 9° for the low-concentration of 2 mg/ml as the thicker 2D-RP perovskite interlayers, confirming the formation of a 2D perovskite phase even for this optimum concentration (Figure 4-6b). However, the intensity of these peaks is weak and broad, which is due to the low thickness of the stacked 2D perovskite layer formed on top of the bulk 3D perovskite, which results in a low scattering volume reflected from the lattice plane of ultra-thin 2D perovskites.[185] J. Yoo, *et al.* has been reported a similar observation by grazing incident X-ray diffraction (GIXRD) setup after deposition of n-BABr on the perovskite surface. According to this measurement, when the incident angle decreases from ω = 1Θ to ω = 0.2Θ, the intensity of the 2D layer peak reduces, indicating that the 2D layer formation is only limited to the surface of the 3D bulk perovskite film.[93]

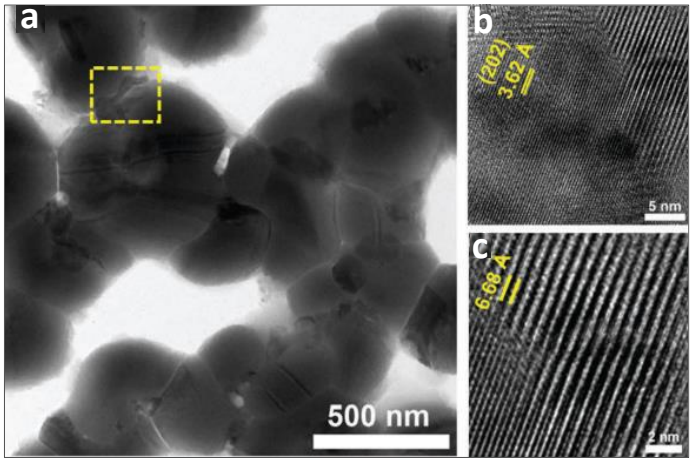

Figure 4-8: (a) Bright-field transmission electron microscopy (TEM) image of the perovskite layer based on n-BABr surface treatment for demonstrating the presence of the 2D-RP perovskite. (b) High-resolution TEM (HRTEM) image of the highlighted region displayed in panel (a). (c) Zoom-in view of the image in panel (b). The figure is adapted with permission from reference [202].

In a separate international collaboration with the Australian National University, a follow-up study based on the surface-coating strategy with n-BABr cation conducted by T. Duong, *et al.* verified the presence of 2D perovskite phases in the perovskite films upon n-BABr surface treatment using transmission electron microscopy (TEM) measurement.[202] Figure 4-8 demonstrates the bright-field TEM image of a perovskite film treated with high concentration n-BABr. The region with 2D perovskite on the surface is highlighted in yellow. From the high-resolution TEM (HRTEM) image of this region (Figure 4-7c and d), two different interplanar lattice spacings of around 6.68 Å and 3.62 Å are observed which can be assigned to the crystal plane of the 2D perovskite at peak 2θ ~13.5° and 3D perovskite at 2θ ~24.8°, respectively.[202,206] Therefore, both XRD and TEM measurements greatly confirm the formation of 2D/3D perovskite heterostructure when n-BABr is coated on the surface of the 3D perovskite layer.

4.3.1. Surface elemental composition and electronic structure

To further identify the chemical composition, distribution and electronic structure of 2D/3D perovskite heterostructure after low concentration n-BABr surface treatment, X-ray and ultraviolet photoelectron spectroscopy (XPS and UPS) were carried out in collaboration with Materials for Energy (MFE) lab at Karlsruhe Institute of Technology by Dr. Dirk Hauschild. As both measurements are surface-sensitive characterization techniques, the following discussion focuses on the surface properties of perovskite layers. Figure 4-9a depicts the XPS overview spectrum of the characteristic emission lines associated with elements of double-cation perovskite including cesium (Cs), nitrogen (N), carbon (C), lead (Pb), iodine (I), and bromine (Br) for both 3D reference and 2D/3D perovskite heterostructure layer. We observe a slight intensity decrease of I, Pb and Cs signals as well as an intensity increase of Br signals for the 2D/3D perovskite heterostructure compared

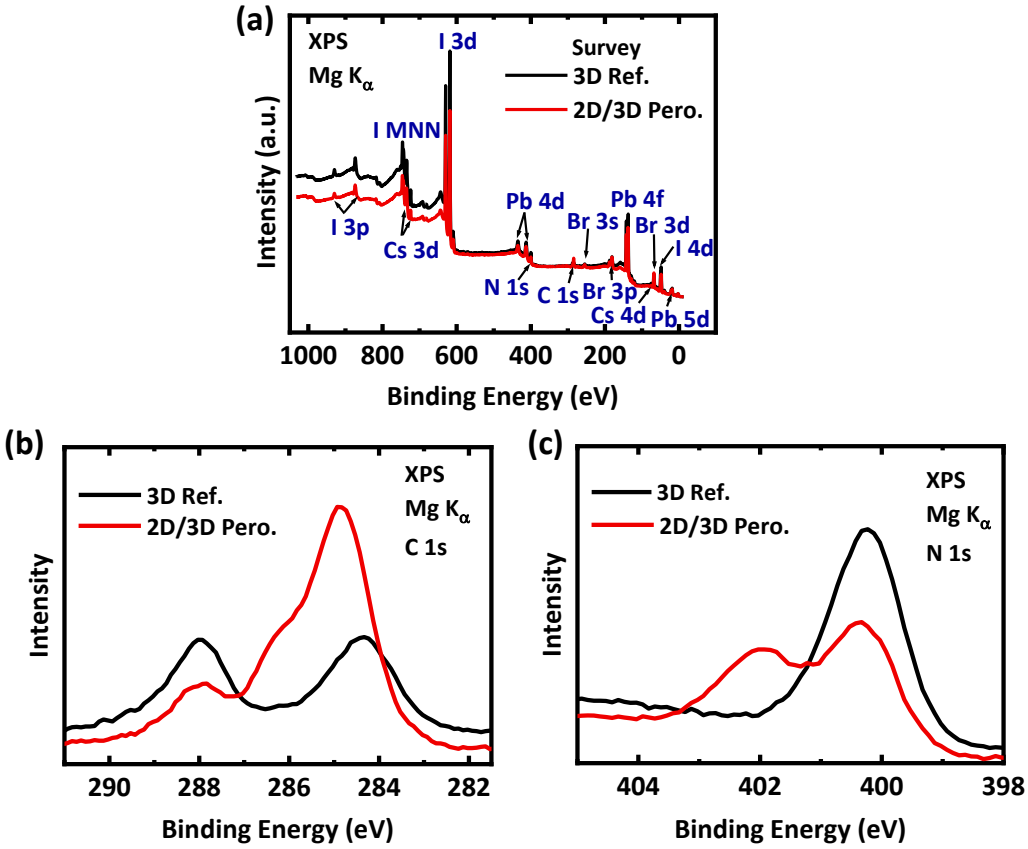

Figure 4-9: (a) Comparison of X-ray photoelectron spectroscopy (XPS) overview spectrum of the double-cation perovskite film prepared without (3D Ref.) and with 2D/3D perovskite heterostructure (2D/3D Pero.) treated with 2 mg/ml n-BABr. XPS spectra of (a) the C 1s and (b) the N 1s peaks. Adapted with permission from reference [182]. Copyright 2019, Wiley.

to the 3D perovskite film. Furthermore, a considerable change in the spectral shapes of the C 1s and N 1s lines is observed (Figures 4-9b and c). To get a better insight into this modification, the detailed core-level energy spectra of the corresponding elements are presented in Figure 4-10. As shown in the C 1s spectrum of the 3D perovskite film (Figure 4-9b), two types of carbon-based chemical bonds are detected at 284.3 and 288.0 eV, which correspond to C-C (or C-H at similar binding energy) and C=N bonding, respectively.[207] Upon n-BABr treatment, the intensity of the C=N signal decreases slightly, while the signal of the C-C bond becomes more intensive and shifts to 285.0 eV. This enhancement is correlated to the presence of the long butylammonium (BA) cation on the surface of the perovskite layer, as the hydrocarbon (-CH_2) in the BA cations has similar binding energy at 285.2 eV.[208,209] Moreover, an additional peak at around 286.2 eV appears which is assigned to a bond between a C and N atom in the organic amide or amine group (C-N).[207] A similar behavior is observed for the N 1s signal (Figure 4-9c), in which two individual peaks located at ~400.2 and 402 eV are detected for the 2D/3D perovskite heterostructure, originating from FA and BA cations respectively, whereas the peak related to BA component is notably absent for the 3D reference film.[210] This result provides strong evidence for the presence of BA^+ cation on the surface of the 2D/3D heterostructure

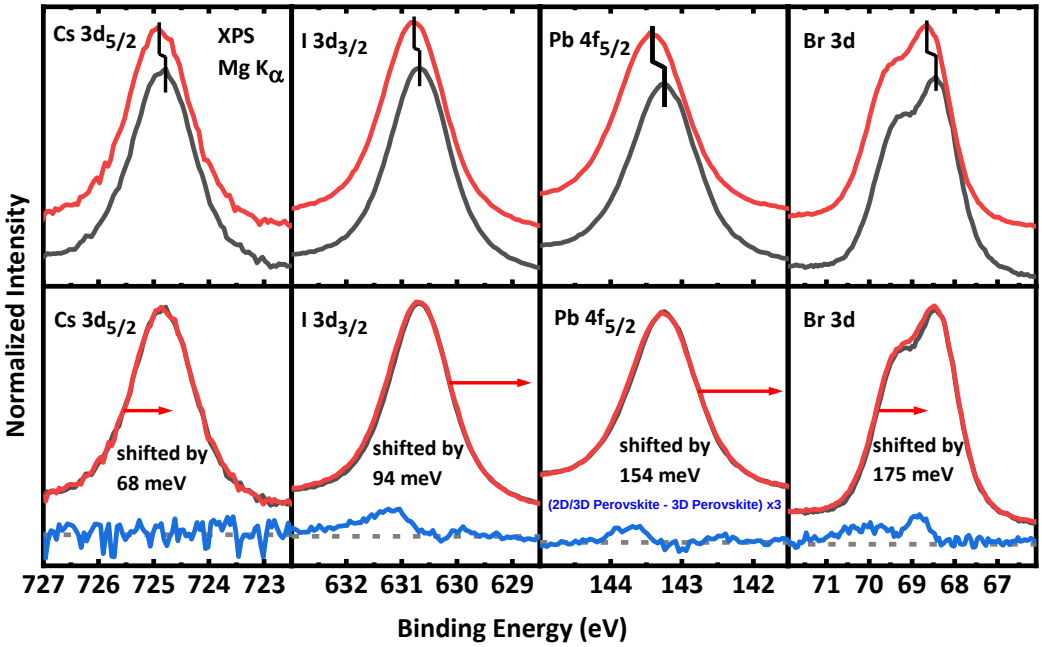

Figure 4-10: X-ray photoelectron spectroscopy (XPS) spectra of the normalized Cs $3d_{5/2}$, I $3d_{3/2}$, Pb $4f_{5/2}$, and Br $3d_{5/2}$ of double-cation perovskite film prepared without (3D perovskite: black) and with 2D/3D perovskite heterostructure (red). The lower and upper panels demonstrate the spectral changes and the peak shits of the corresponding elements by the addition of n-BABr on the surface of the perovskite layer, respectively. The difference "(2D/3D Perovskite – 3D perovskite) x3" is indicated by the blue colour below each spectrum in low panels computes after implementing a shift to each 2D/3D perovskite spectrum. Reproduced with permission from reference [182]. Copyright 2019, Wiley.

perovskite film. Looking at the spectral changes of the Cs $3d_{5/2}$, I $3d_{3/2}$, Pb $4f_{5/2}$ and Br $3d_{5/2}$ emission lines (Figure 4-10), we do not observe any prominent change after the addition of n-BABr. This is particularly evident for the Cs $3d_{5/2}$ peak, where plotting the difference between reference and surface treated sample for this peak only shows noise, suggesting that the chemical environment of Cs is not varied by the addition of n-BABr. However, a small peak shift for Cs $3d_{5/2}$ and I $3d_{3/2}$ (less than 100 meV) and a slightly larger peak shift (between 100 meV to 200 meV) for Pb $4f_{5/2}$ and Br $3d_{5/2}$ is revealed for n-BABr treated perovskite as compared to reference film. This indicates that upon n-BABr surface treatment, even with a low concentration, the chemical environment of these elements at the surface of the perovskite is notably varied and results in a modified composition and bonding structure through the formation of a 2D surface layer.[211] This result strongly supports the finding of the XRD measurement that a thin 2D RP perovskite film is formed on the surface of the 3D perovskite film by the addition of n-BABr.

To assess whether the electronic properties at the surface of the 2D/3D perovskite heterostructure also change upon low concentration n-BABr treatment, UPS measurement was performed. Figure 4-11 presents the secondary electron cut-off region, UPS spectra in the valence band (VB) region and enlarged corresponding UPS spectra of the perovskite layer without and with n-BABr treatment. Compared to the 3D perovskite, the 2D/3D

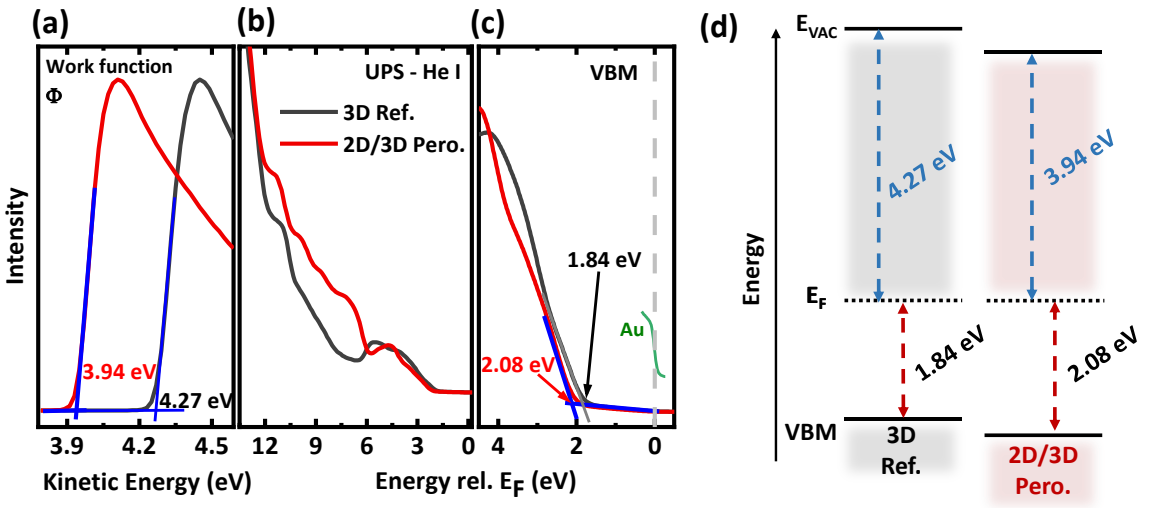

Figure 4-11: Ultraviolet photoelectron spectroscopy (UPS) measurements of (a) Helium Iα ($h\nu$ = 21.22 eV) spectra of secondary electron cut-off, (b) UPS spectra in the valence band and (c) the valence band maximum (VBM) region of the 3D perovskite and the 2D/3D perovskite heterostructure thin films. For energy calibration, a sputter-cleaned Au foil and its Fermi edge (green) are used. A linear extrapolation of the secondary electron cut-off (±0.05 eV) and the leading edge of the valence band (±0.10 eV) indicates the work function and the distance of the VBM with respect to the Fermi level (E_F), respectively. (d) Schematic of the energy band diagram. Adapted with permission from reference [182]. Copyright 2019, Wiley.

perovskite heterostructure exhibits a considerable reduction in work function from 4.27 ± 0.05 to 3.94 ± 0.05 eV (a reduction of 0.33 ± 0.07 eV), as extracted from the intercept in the secondary electron cut-off (Figure 4-11a). Furthermore, the UPS spectral shape of the 2D/3D perovskite heterostructure, which is indicative of valence band/orbital structure, differs considerably from the 3D perovskite film across the entire energy range (Figure 4-11b). Accordingly, a noticeable enhancement in the distance of the valence band maximum (VBM) with respect to the Fermi level (E_F) is determined from linear extrapolation of the leading edge in the magnified UPS spectra (Figure 4-11c) from 1.84 ± 0.10 eV to 2.08 ± 0.10 eV for the 2D/3D perovskite heterostructure compared to the 3D perovskite film. This represents a downward shift of around 0.24 eV for the VBM, as shown in the schematic of the energy level diagram for the corresponding films (Figure 4-11d). This VBM downward shift, along with the decrease of the work function and shifts of XPS signals for the 2D/3D perovskite heterostructure indicates a downward band bending. Besides, a possible bandgap widening may occur at the surface of the perovskite layer after n-BABr treatment due to the formation of the wide-bandgap 2D layer.[92,203,212,213] Such a bandgap widening in conjunction with the downward band bending at the surface of the 2D/3D perovskite heterostructure acts as an efficient electron blocking layer, thereby reducing the charge carrier recombination at the perovskite/HTL interface and in turn results in an enhanced V_{OC}.[93,212,214] It should be noted that this band bending can still facilitate efficient hole transport from perovskite to the HTL, as we will observe from transient photoluminescence (PL) measurement in the next section.

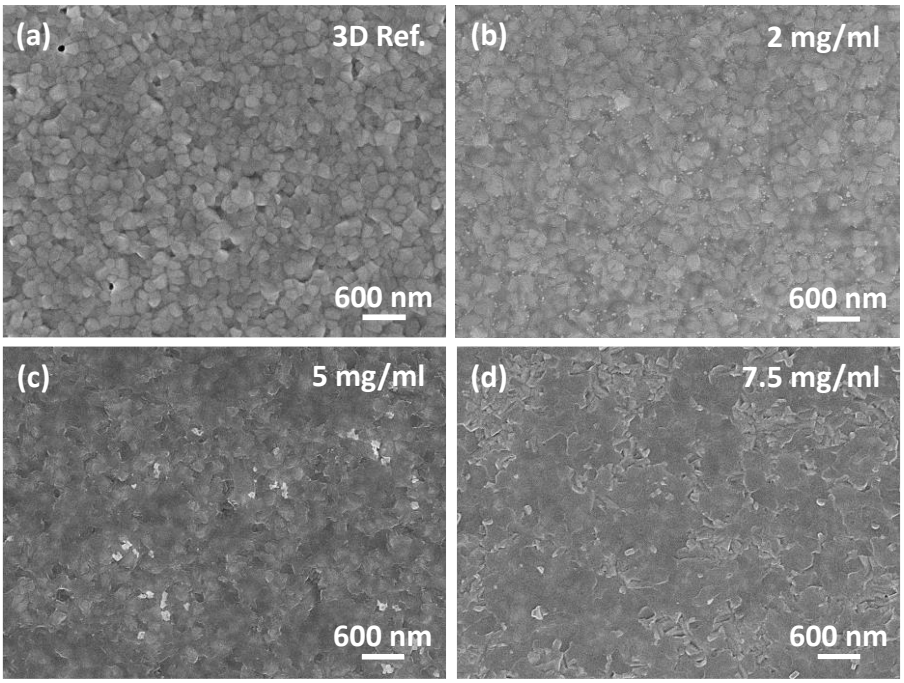

Figure 4-12: Top-view scanning electron microscopy images of the double-cation perovskite ($FA_{0.83}Cs_{0.17}Pb(I_{0.6}Br_{0.4})_3$) layers (a) without (3D Ref.) and with 2D/3D perovskite heterostructure processed by n-BABr treatment with different concentration (b) 2 mg/ml and (c) 5 mg/ml, and (d) 7.5 mg/ml. Reproduced with permission from reference [182]. Copyright 2019, Wiley.

4.3.2. Thin-film morphology

To further investigate the morphological modification of the perovskite surface upon n-BABr treatment, top view scanning electron microscope (SEM) and atomic force microscopy (AFM) were performed. The 3D reference perovskite film exhibits distinct well-crystallized perovskite grains ranging from 300 to 400 nm (Figure 4-12a). Although the size of crystal grains does not change in case of low concentration, they noticeably exhibit less visible valleys on the perovskite surface, which could indicate a smoothing of the perovskite layer surface (Figure 4-12b). A reduced surface roughness is confirmed using atomic force microscopy (AFM) from the root mean square (RMS) roughness of 13.8 nm to 11.4 nm (Figures 4-13a and b).[93] However, no additional layer is observed on the surface of the 3D perovskite layer for the sample treated with 2 mg/ml n-BABr solution, as shown in the top-view SEM as well as cross-section SEM images (Figure 4-12b and Figures 4-14a and b). This is in line with the low XRD intensity detected for such a low concentration due to the ultrathin thickness of the 2D layer. Accordingly, when the concentration of n-BABr increases (> 2 mg/ml), a thin disordered layer with flaky-like features appears on the surface of the 3D perovskite layer, which is determined to be a 2D layered perovskite (Figure 4-12c). This flaky-like layer becomes more distinguishable and inhomogeneous for the case of 7.5 mg/ml (see Figure 4-12d), resulting in high surface roughness with RMS of 17.3 and 21.9 nm for the samples treated with 5 and 7.5 mg/ml, respectively (Figure 4-13 c and d). As a result, this can be in turn responsible for the low FF obtained for devices

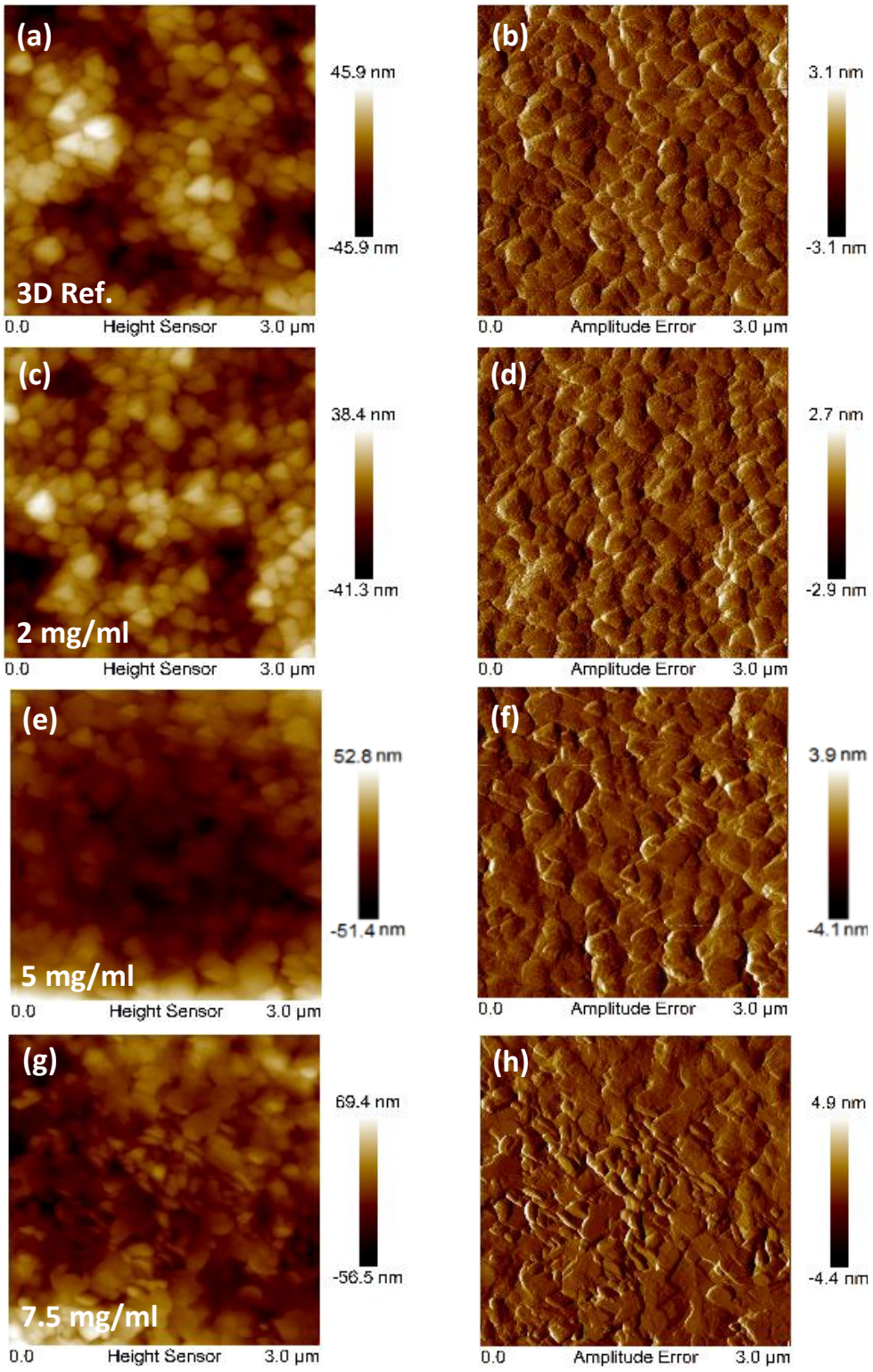

Figure 4-13: Atomic force microscopy (AFM) scans of double-cation perovskite surface prepared without (3D Ref.) and with 2D/3D perovskite heterostructure prepared by spin coating of n-BABr solution with various concentrations (2, 5 and 7.5 mg/ml): (a-d) The height sensor images display the information regarding the surface topography of the samples. (e-h) The amplitude error images demonstrate a better illustration of the contrast. Adapted with permission from reference [182]. Copyright 2019, Wiley.

based on high concentration n-BABr.[215] The formation of the thin 2D interlayer is also

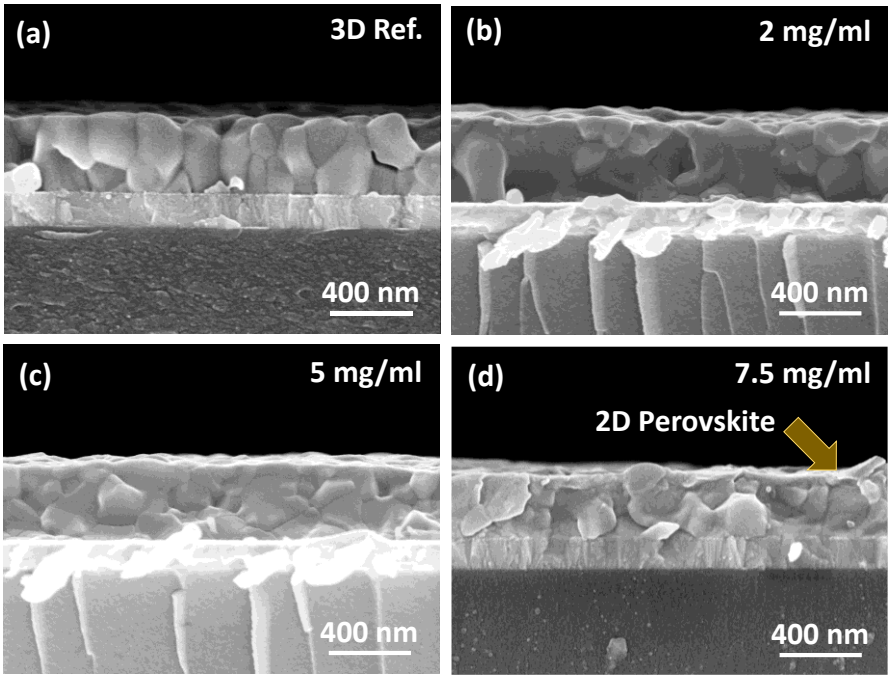

Figure 4-14: Cross-section scanning electron microscopy image of the double-cation perovskite with a layer stack of ITO/SnO_2/ Perovskite prepared (a) without (3D Ref.) and with 2D/3D perovskite heterostructure processed by n-BABr treatment with different concentration (b) 2 mg/ml and (c) 5 mg/ml, and (d) 7.5 mg/ml. The images show that an additional interlayer (2D layer) only appears on the 3D perovskite surface upon n-BABr treatment with a higher concentration (7.5 mg/ml). Reproduced with permission from reference [182]. Copyright 2019, Wiley.

visualized in the cross-sectional SEM images of the corresponding samples (Figures 4-14c and d).

4.4. Photophysical properties of the 2D/3D heterostructure

Having established that the formation of the ultrathin 2D interlayer on the surface of the double-cation perovskite is the origin of enhanced V_{OC}, we next perform photophysical characterizations, such as ideality factor (n_{id}) and time-resolved photoluminescence (TPRL) measurements, to determine the recombination mechanism after this surface treatment. In this regard, as a first step, the ideality factor of the complete devices without and with 2D/3D perovskite heterostructure was examined by measuring the illumination intensity-dependence of the V_{OC}, as we explained previously in Chapter 2.[180] The n_{id} of reference PSCs is estimated to be around 1.35±0.04, while this value considerably reduces to 1.18±0.06 for devices based on 2D/3D perovskite heterostructures (Figure 4-15). It is known that a n_{id} of 2 is typically indicative of trap-assisted Shockley-Read-Hall (SRH) recombination being a dominant recombination mechanism in the bulk of the perovskite thin films. [181] Therefore, the decreased n_{id} value of 2D/3D perovskite heterostructure devices to 1.18 demonstrates that non-radiative SRH recombination is significantly

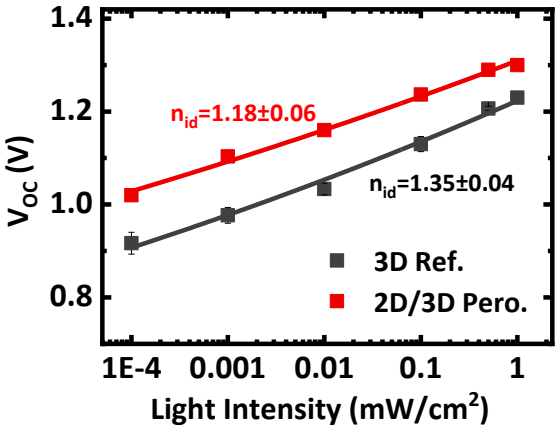

Figure 4-15: Diode ideality factor (n_{id}) of double cation perovskite solar cells prepared without (3D. Ref.) and with 2D/3D perovskite (2D/3D Pero.) heterostructure with the optimum concentration (2 mg/ml). The value of n_{id} is determined from light-intensity-dependent open-circuit voltage (V_{OC}) measurements of the corresponding devices at 25 °C. Adapted with permission from [182]. Copyright 2019, Wiley.

mitigated for these devices, which is in a good agreement with the enhanced V_{OC} (Figure 4-2) and the TRPL results which we will discuss in the following.

Next, a TRPL experiment was performed, where we measure the lifetimes of a charge carrier for the 2D/3D perovskite heterostructure compared to the reference sample. To avoid the lifetime quenching owing to electron extraction, samples were prepared on glass substrates for this measurement. Figure 4-16a shows a strong enhancement in carrier lifetime from τ_2 = 158 to τ_2 = 230 ns for samples with a 2D perovskite interlayer (optimum concentration of 2 mg/ml) compared to the reference 3D perovskite. This indicated that the surface treatment with n-BABr is accompanied by a significant reduction in charge carrier non-radiative recombination pathways by passivating the surface of the 3D perovskite layer, thereby accounting for higher V_{OC} and improved PCE of corresponding

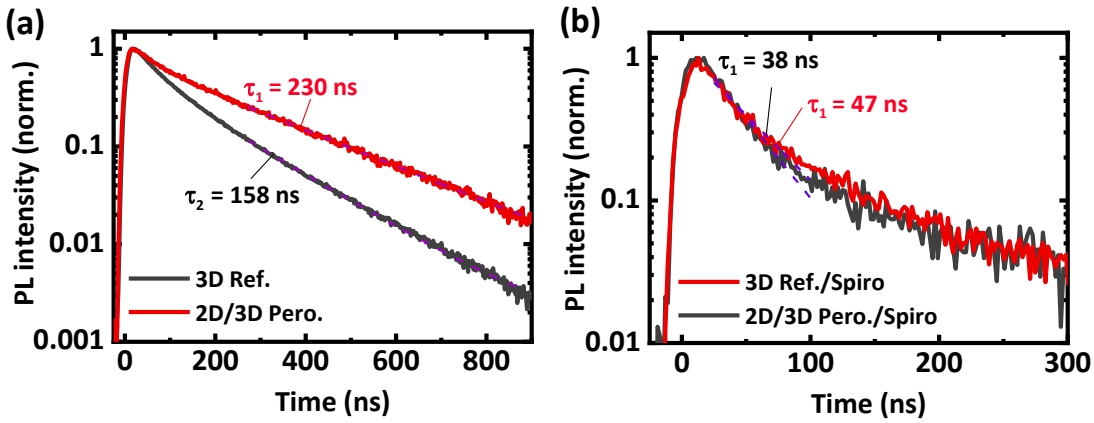

Figure 4-16: Time-resolved photoluminescence (TRPL) measurements of (a) double-cation perovskite film without (3D Ref) and with 2D/3D perovskite heterostructures (2D/3D Pero.) processed by spin coating of n-BABr (2 mg/ml) on top of the 3D perovskite layer. The perovskite layer is deposited on the glass substrate. (b) TRPL measurements of the perovskite/spiro-MeOTAD (Spiro) as a hole transport layer to examine hole extraction through the 2D-RP perovskite interlayers. Adapted with permission from reference [182]. Copyright 2019, Wiley.

devices. Furthermore, to examine the extraction of holes from the surface passivated perovskite layer to the HTL, TPRL measurement was carried out for samples containing the perovskite absorber with a top layer of Spiro-MeOTAD. Interestingly, both 3D and 2D/3D perovskite films exhibit similar TPRL decays (Figure 4-16b), in which the lifetime is considerably decreased upon the addition of the HTL. This implies that the ultrathin 2D interlayer can not only effectively passivate the surface of the perovskite layer but also maintain fast hole extraction at the perovskite/HTL interface. In the next chapter, we will show that employing this 2D/3D perovskite heterostructure strategy is universally applicable to PSCs of different bandgaps.

4.5. Summary

In this chapter, we investigated the effect of the n-BABr surface treatment as a long-chain alkylammonium material on top of the double-cation $FA_{0.83}Cs_{0.17}Pb(I_{0.6}Br_{0.4})_3$ wide-bandgap perovskite thin films and its role in improving the photovoltaic performance of the devices with a layer stack of glass/ITO/SnO_2/$Cs_{0.17}FA_{0.83}Pb(I_{0.6}Br_{0.4})_3$/Spiro-MeOTAD/Au. By determining the optimum concentration of the BABr solution (2 mg/ml), we could significantly improve the PCE of the PSCs to 19.4% from 16.7%, along with a remarkable enhancement in V_{OC} up to 1.31 V from 1.23V compared to the reference 3D PSCs. The reported voltage corresponds to one of the highest observed ratio of V_{OC} over the maximum possible V_{OC} based on the S-Q limit for WBP organic−inorganic mixed-halide perovskite solar cell so far.

Next, we investigated the material and photophysical properties of double-cation perovskite layers treated with the optimum concentration of BABr solution in order to understand the underlying mechanism resulting in such a high performance. Referring to XRD, XPS and SEM results, we identified that this achievement is based on the formation of 2D-RP perovskites, resulting in an ultrathin 2D/3D perovskite heterostructure at the hole extracting side of the device upon deposition of n-BABr. Our results along with the following studies in the literature based on TEM and GIXRD measurements confirmed that the formation of 2D is limited to the surface of the film. Furthermore, results obtained from UPS measurements demonstrated that the formation of such a 2D/3D perovskite heterostructure with a wider bandgap leads to a modification of the electronic structure at the top surface of the perovskite layer, which induced an energy band offset. As a result, this interlayer could block the transfer of excited electrons to the HTM layer, resulting in a reduced charge recombination at the interface of the perovskite/HTL. Besides, TPRL measurements revealed a longer carrier lifetime for the 2D/3D based perovskite films as compared to the 3D reference perovskite film, thereby, leading to reduced non-radiative recombination. Hence, introducing a 2D/3D interlayer could provide excellent surface passivation of our wide-bandgap perovskite absorber layer along with reducing interfacial charge recombination, resulting in an overall V_{OC} enhancement of 80 mV compared to the

reference devices without the 2D-RP surface treatment. These results are particularly important for a step forward in achieving high-efficiency perovskite-based multi-junction photovoltaics (PV) as we will discuss in the following chapter.

5. 2D/3D Semi-transparent Perovskite Solar Cells with Engineered Bandgaps for Tandem Photovoltaics

In this chapter, we investigate the performance of four-terminal (4T) perovskite-based tandem solar cells by stacking top semi-transparent perovskite solar cells (PSCs), based on a 2D/3D perovskite heterostructure, on top of bottom silicon (c-Si) and copper indium gallium selenide (CIGS) solar cells. In this regard, we initially investigate the influence of the 2D/3D perovskite heterostructure on power conversion efficiency (PCE) of double-cation ($FA_{0.83}Cs_{0.17}Pb(I_{1-y}Br_y)_3$ n-i-p opaque PSCs with a bandgap engineered via iodine variation ($0.24 \leq y \leq 0.56$). In the following, we fabricate a series of 2D/3D semi-transparent PSCs with engineered bandgaps in order to determine the optimum bandgap for maximizing the performance of 4T configurations.

This chapter is based on our publication in *Advanced Functional Materials* with the title "2D/3D Heterostructure for Semitransparent Perovskite Solar Cells with Engineered Bandgap Enables Efficiencies Exceeding 25% in Four-Terminal Tandems with Silicon and CIGS".[216] Most of the graphs in this chapter are adapted or reproduced with the permission of *Advanced Functional Materials*.

Acknowledgments and contributions

This work is the result of collaborative research between Karlsruhe Institute of Technology (KIT), Institute for Solar Energy Research GmbH (ISFH) and Zentrum für Sonnenenergie- und Wasserstoff-Forschung Baden-Württemberg (ZSW). Saba Gharibzadeh and Dr. Ihteaz M. Hossein contributed equally to the first authorship of this study. The original ideas and research plan are developed by Saba Gharibzadeh. Saba Gharibzadeh designed the experiments, fabricated opaque perovskite solar cells (PSCs), and performed current density-voltage (J–V), external quantum efficiency (EQE), X-ray diffraction (XRD) and ultraviolet-visible spectroscopy (UV-Vis) of the corresponding opaque devices. Dr. Ihteaz M. Hossein designed the experiments and fabricated semi-transparent PSCs by developing in-house indium tin oxide (ITO) and MgF_2 layers and performed the J–V, EQE and UV-Vis of the corresponding semi-transparent PSCs. 4T c-Si/perovskite and CIGS/perovskite are fabricated and characterized by Saba Gharibzadeh and Dr. Ihteaz M. Hossein. Data analysis

was further developed with the support of Dr. Paul Fassl. Mortiz Schultes and Dr. Erik Ahlswede from Zentrum für Sonnenenergie und Wasserstoff-Forschung Baden-Württemberg (ZSW) provided CIGS samples and helped for measuring J-V of the 4T CIGS/perovskite solar cell. Philip Jackson, Dr. Michael Powalla, Dr. Sören Schäfer, Michael Rienäcker, Dr. Tobias Wietler and Dr. Robby Peibst provide the silicon samples for fabricating 4T c-Si/perovskite solar cell. Dr. Tobias Abzieher carried out the Scanning Electron Microscopy (SEM) measurement. The whole project was supervised by Dr. Ulrich Paetzold.

5.1. Introduction

A pivotal requirement to achieve a high PCE in 4T perovskite/c-Si or perovskite/CIGS tandem solar cell is to combine a highly efficient top semi-transparent perovskite solar cell (PSC) with prominent transparency in order to deliver a high number of long-wavelength photons to the bottom cell. In this context, according to the detailed-balance calculations under standard test conditions (AM1.5G, 1 kW/m^2), developing PSCs with a wide range of bandgaps (E_g) from 1.65 to 1.85 eV (ideally at 1.75 eV) can meet this requirement for the top cell in tandem configurations.[24,33,38] Although, increasing Br content to widen the bandgap of top PSCs results in higher transmission for the long-wavelength photons, it is accompanied by a large open-circuit voltage (V_{OC}) deficit, stemming from increased defect density, severe interfacial recombination as well as photo-induced phase segregation, as previously discussed in Chapter 4.[42,56,217,218] These losses are neglected in detailed-balance calculations such that the optimum bandgap predicted by simulation is different in experimental studies. For example, the current record efficiency for a 4T perovskite/c-Si tandem device is 28.2% which is based on stacking a top semi-transparent PSC with an E_g of 1.63 eV.[219] In addition, a record 4T perovskite/CIGS tandem solar cell with a PCE of 25.9% has been obtained for an optimum E_g of 1.68 eV.[220] Therefore, a more detailed experimental investigation is needed to find the optimum bandgap of the perovskite absorber for developing real prototype tandem devices in order to achieve simultaneously high transmission and maximum V_{OC}.

In Chapter 4, we demonstrated that utilizing the surface passivation strategy by developing a 2D/3D perovskite heterostructure enhanced dramatically the V_{OC} of our wide-bandgap PSC (1.72 eV). Motivated by this successful development, in this chapter, we further extend this strategy to investigate the effect of n-BABr on the performance of PSCs with various bandgaps in order to optimize such devices for incorporation into 4T tandem solar cells. In this regard, we initially (Section 5-2) fabricate PSCs with a wide range of bandgaps (1.65, 1.69, 1.74, 1.78, 1.85 eV) by varying the halide ratio in the perovskite precursor solution ($FA_{0.83}Cs_{0.17}Pb(I_yBr_{1-y})_3$; $(0.24 \leq y \leq 0.56)$. In the next step, the surface of these five mentioned bandgaps is treated with n-BABr, resulting in a strong enhancement in V_{OC} of around 45 mV for all devices compared to the reference PSC, regardless of perovskite

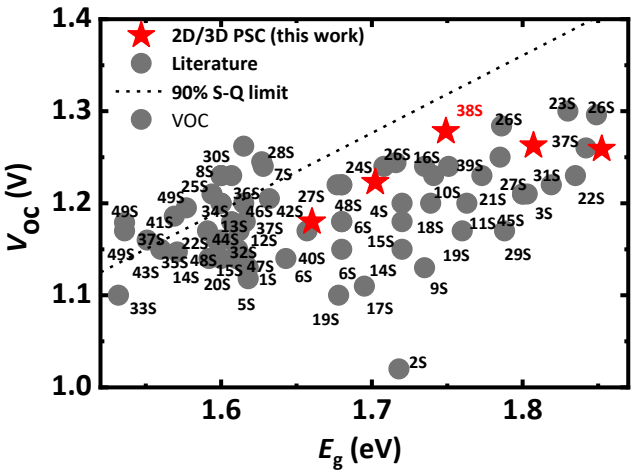

Figure 5-1: Comparison of the best open-circuit voltage (V_{OC}) as a function of perovskite bandgap (E_g) obtained in this chapter (marked by red stars) with the best-performing mixed-halide perovskite solar cells with decent power conversion efficiency (>12%) reported in the literature (dark grey circles). The dashed line represents 90% of the maximum theoretical V_{OC} calculated by the Shockley-Queisser (S-Q) limit. More details are provided in Appendix B, Table B1. Adapted with permission from reference [216]. © John Wiley & Sons.

absorber bandgap. It should be mentioned that obtained V_{OC}s were among the highest values reported in the literature in 2020 for this bandgap region as depicted in Figure 5-1. This result demonstrates that our 2D passivation strategy reduces non-radiative recombination losses not only for devices with E_g of 1.73 eV (discussed in Chapter 4), but also is impressively effective over a broad range of bandgaps. Utilizing this strategy, we further develop a series of semi-transparent PSCs with engineered bandgaps (Section 5-3), followed by integrating them with high-efficiency c-Si and CIGS bottom solar cells in a 4T configuration. Finally, in Section 5-4 we demonstrate comparable tandem PCEs for a broad range of perovskite bandgaps, achieving stabilized PCEs as high as 25.7% and 25% for mechanically stacked 4T perovskite/c-Si and perovskite/CIGS tandem solar cells, respectively, with an optimum bandgap of 1.65 eV for both cases. These results are equivalent to 2.5% and 3.8% absolute enhancement in PCE over the single-junction solar cell, highlighting the importance of high-efficiency top PSCs, enabled via the discussed strategies, as well as the optimization of perovskite bandgap in order to obtain the best configuration for prototype 4T devices.

5.2. 2D/3D heterostructure solar cells with engineered bandgap

In this section, we investigate the effect of n-BABr surface treatment (2 mg/ml) on structural, morphological and optical properties of a series of double-cation perovskite absorber layers with five different bandgaps.

5.2.1. Material properties

We control the bandgap of our perovskites by varying the amount of Br ($0.24 \leq y \leq 0.56$) in the perovskite precursor solution ($FA_{0.83}Cs_{0.17}Pb(I_{1-y}Br_y)_3$). This results in a shift in

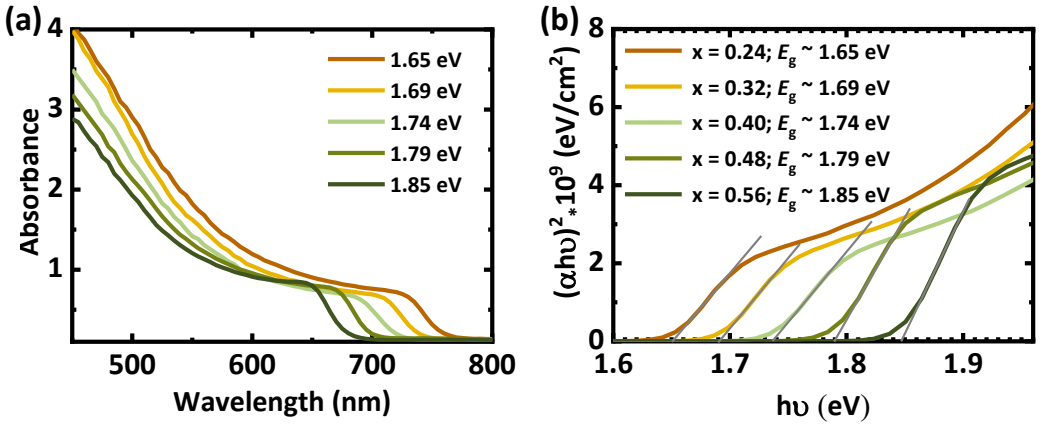

Figure 5-2: (a) Ultraviolet-visible absorbance spectra and (b) Tauc plots of double-cation perovskite layers with 5 different bandgaps as shown in the inset ($FA_{0.83}Cs_{0.17}Pb(I_{1-y}Br_y)_3$); ($0.24 \leq y \leq 0.56$), proceed with spin coating of n-BABr on top of the 3D perovskite. The perovskite layer is deposited on the glass substrate. Adapted with permission from reference [216]. © John Wiley & Sons.

absorption edge towards lower wavelengths, as shown in UV-vis absorbance spectra (Figure 5-2a). Therefore, a broad range of E_g from 1.65 eV (y = 0.24) to 1.85 eV (y = 0.56), determined via Tauc plot, is obtained (Figure 5-2b). To ascertain whether a 2D/3D perovskite heterostructure is formed on top of the 3D perovskite for all five mentioned bandgaps, X-ray diffraction (XRD) was performed. Interestingly, consistent with the XRD result observed for the 2D/3D perovskite layer with the E_g = 1.72 eV in Chapter 4, we observe similar low-intensity diffraction peaks at low angles of 2θ ~4.5° and ~9°, which clearly corresponds to the presence of an ultrathin 2D Ruddlesden-Popper (2D-RP) on top of the perovskite films for all investigated bandgaps (Figure 5-3). It is worth mentioning that when the bandgap of the double-cation perovskite increases, the typical XRD pattern of 3D bulk perovskites reflections from the planes (100), (110), (111) and (200) exhibits a

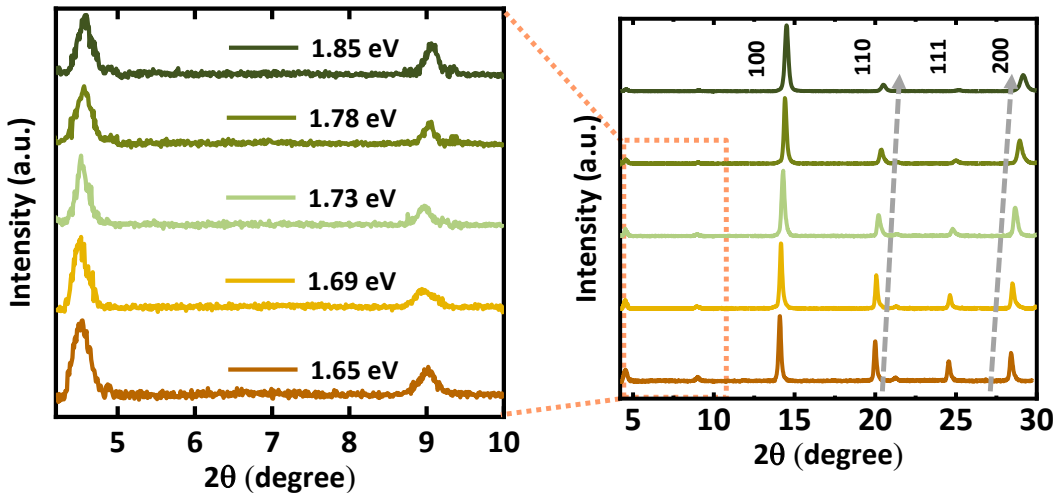

Figure 5-3: X-ray diffraction (XRD) pattern of the double-cation cation perovskite layers with 5 different bandgaps 1.65, 1.69, 1.74, 1.79 and 1.85 eV proceed with spin coating of n-BABr solution on top pf the bulk 3D perovskite layers (right panel). Zoomed region in the left panel shows the diffractions corresponding to crystal planes of two-dimensional Ruddlesden–Popper on the perovskite surface. Adapted with permission from reference [216]. © John Wiley & Sons.

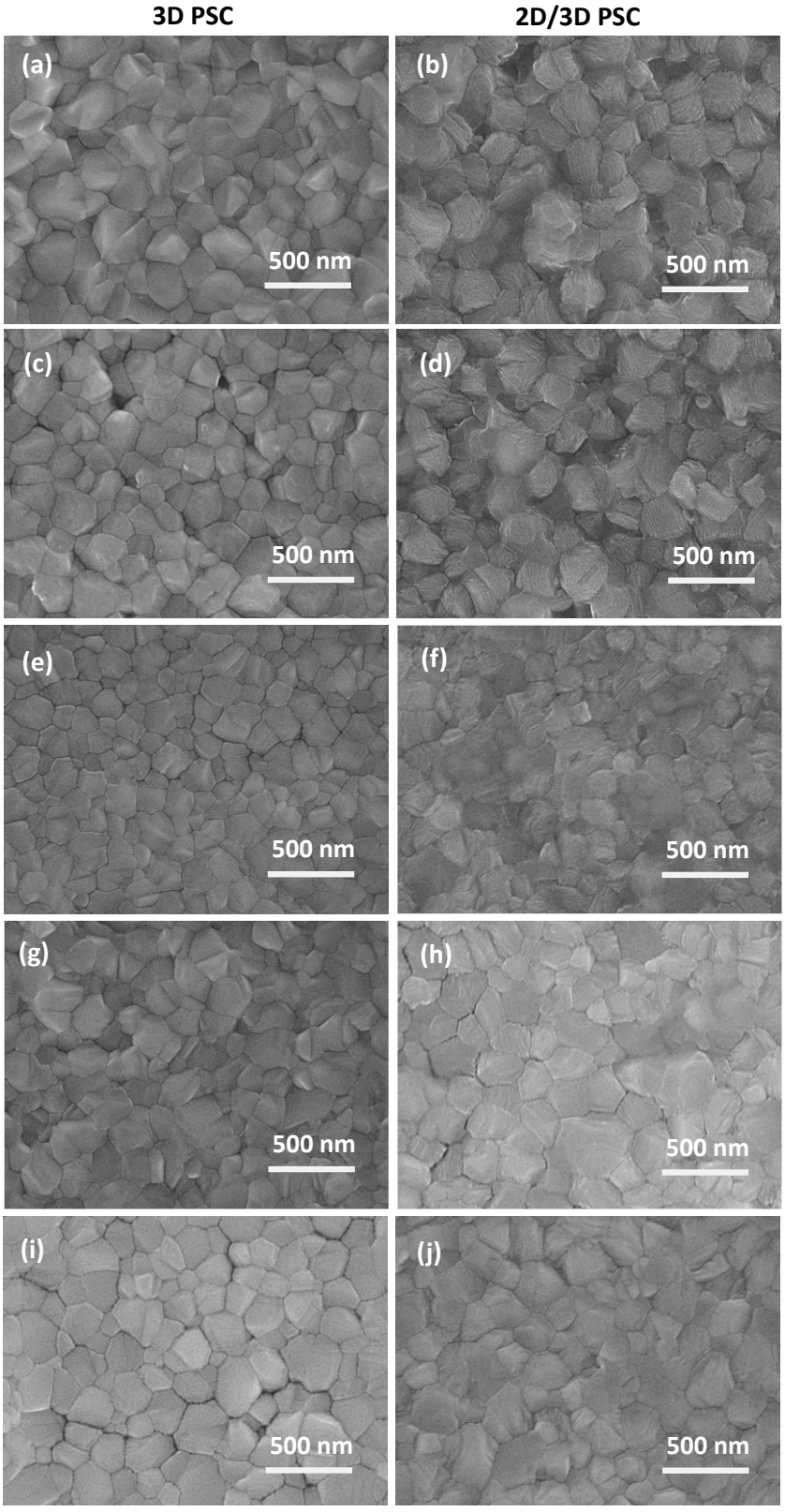

Figure 5-4: Top view scanning electron microscopy images of double-cation perovskite (a, c, e, g, j) without (3D PSC) and (b, d, f, h, j) with 2D/3D perovskite (2D/3D PSC) heterostructure with 5 different bandgaps: 1.65, 1.68, 1.73, 1.78 and 1.85 eV, respectively. Adapted with permission from reference [216]. © John Wiley & Sons.

shift into higher diffraction angles. This is indicative of a lattice contraction arising from the

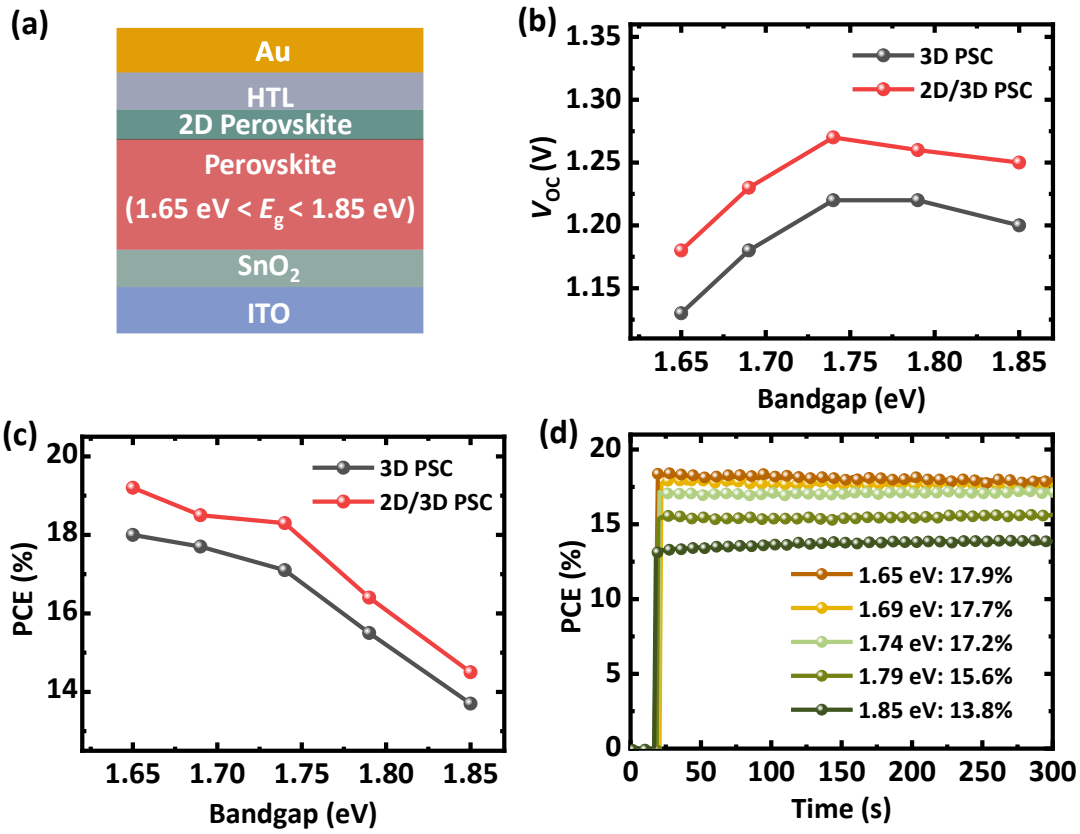

Figure 5-5: (a) Schematic of the perovskite solar cell (PSC) layer stack used in this study. Comparison of (b) open-circuit voltage (V_{OC}) and (c) power conversion efficiency (PCE) (in the reverse scan) as a function of the perovskite absorbers bandgap for opaque PSCs without (3D PSC) and with 2D/3D perovskite (2D/3D PSC) heterostructure derived from current-voltage measurement under the illumination of 100 mW/cm^2. (d) Stabilized PCE of PSCs of the corresponding devices using 2D/3D heterostructure with engineered bandgap after 5 min constant illumination and at constant voltage close to the maximum power point (MPP). Adapted with permission from reference [216]. © John Wiley & Sons.

reduction in the perovskite crystal structure, as upon widening the bandgap of the perovskite absorber iodine ions with a larger ionic radius (2.2 Å) are replaced in the lattice structure by smaller Br ions (1.9 Å).[39] Meanwhile, top-view scanning electron microscopy (SEM) images in Figure 5-4 demonstrate a slight morphological change at the surface texture of the perovskite layer treated with n-BABr compared to the bulk 3D reference for all investigated bandgaps. Although we do not observe any change in the perovskite grain size, such a modification on the surface texture is contributed to the formation of the 2D perovskite layer for all 5 mentioned bandgaps, as verified by our XRD measurement as well as previous studies in the literature.[221,222] In the next section, the photovoltaic parameters of the 2D/3D PSCs with all 5 mentioned bandgaps are investigated.

5.2.2. Photovoltaic characteristics

In order to find out the effect of our 2D/3D perovskite heterostructure on the photovoltaic parameters of PSCs with engineered bandgaps, the *J*–*V* characteristics of opaque PSCs are measured under simulated air mass 1.5 global (AM1.5G) solar irradiation. Devices are

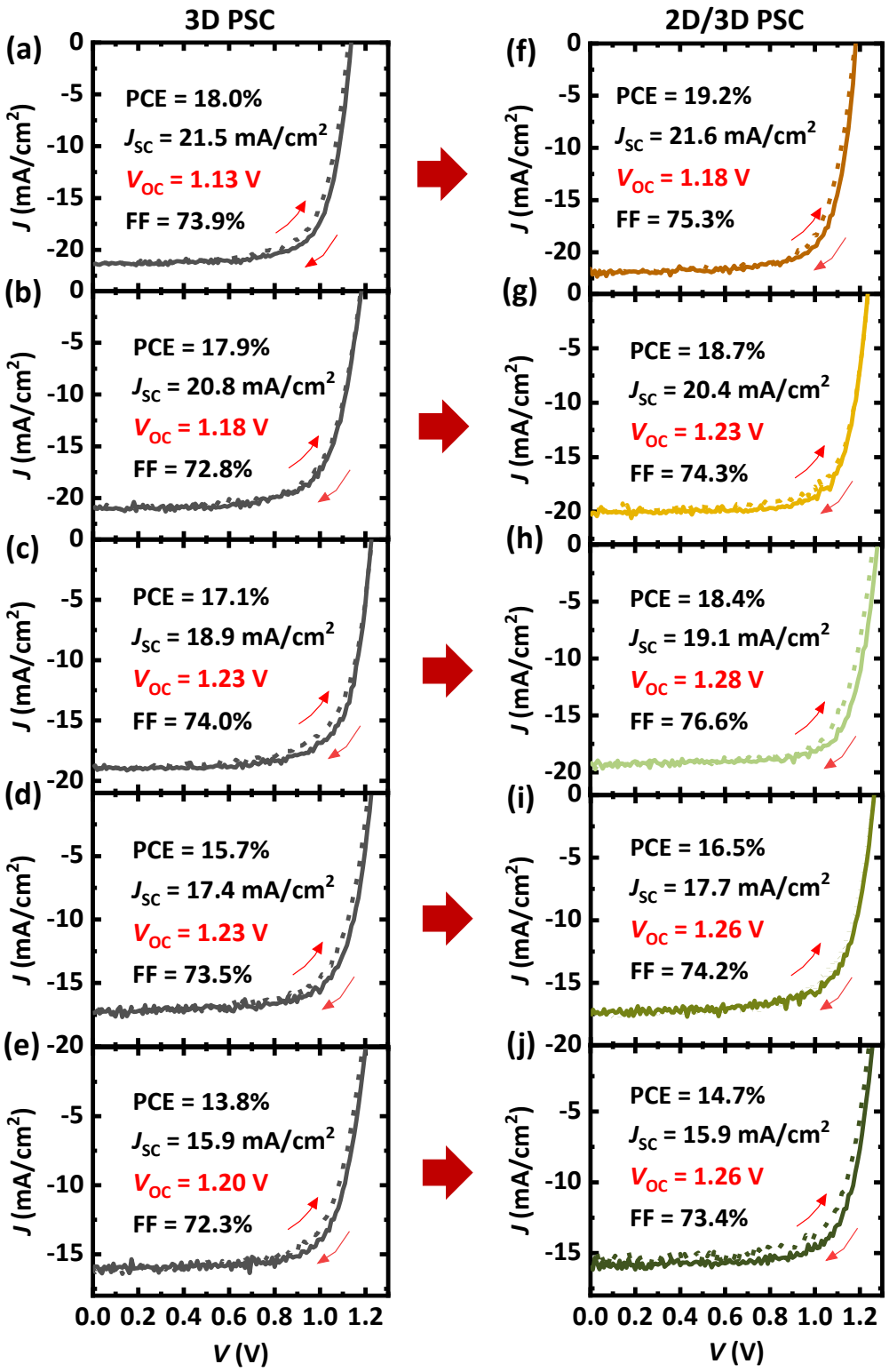

Figure 5-6: Current density-voltage (*J–V*) characteristics of best-performing opaque perovskite solar cells (left panel) without (3D PSC) and (right panel) with 2D/3D perovskite (2D/3D PSC) heterostructure with engineered bandgaps: (a, b) 1.65 eV, (c, d) 1.69 eV, (e, f) 1.74 eV, (g, h) 1.79 eV and (i, j) 1.85 eV measured under full simulated solar illumination conditions (AM1.5, 100 mW/cm^2) in a reverse (solid line) and forward (dashed line) scans. The photovoltaic parameters of each PSC derived from reverse scan measurement are presented in the inset. Adapted with permission from reference [216]. © John Wiley & Sons.

fabricated in a similar planar n-i-p architecture presented in Chapter 4 with a layer stack

glass/ITO/nanoparticle-based SnO_2 (np-SnO_2)/$FA_{0.83}Cs_{0.17}Pb(I_{1-y}Br_y)_3$/2,2',7,7'-tetrakis (N, N'-di-p-methoxy phenylamine)-9,9'-spirobifluorene (spiro-MeOTAD)/Au (Figure 5-5a). Interestingly, all investigated bandgaps using a 2D/3D perovskite heterostructure demonstrate an enhancement in V_{OC} of around 45 mV compared to 3D reference devices (Figure 5-5b). This indicates that employing a 2D-RP perovskite interlayer results in enhanced V_{OC} over a broad range of bandgaps. As previously discussed in Chapter 4, this notable improvement is induced by the effective surface passivation and better energetic alignment at the perovskite/hole transport material (HTL) interface due to the formation of a wider-bandgap 2D-RP interlayer, which leads to a significant reduction in non-radiative recombination.

Apart from the V_{OC} enhancement, we observe that when the bandgap of the perovskite absorber increases from 1.65 to 1.74 eV, the V_{OC} in both 3D and 2D/3D PSCs increases linearly (from 1.13 to 1.23 V and from 1.18 to 1.28 V, respectively) and reaches their maximum value. However, further widening the bandgap to 1.85 eV, results in saturation and subsequent reduction in V_{OC} to 1.20 and 1.26 V, respectively. This large V_{OC} deficit due to bandgap widening is a very common observation that prevails in mixed-halide PSCs with higher Br content, arising from increased recombination losses due to phase segregation and higher defect density, as discussed in detail in Chapter 4.[42,189,223] To better compare V_{OC} values obtained for all 5 mentioned bandgaps in our study with the other studies, a literature survey of reported champion V_{OC} extracted from the best mixed-halide perovskite solar cells along with the corresponding V_{OC} deficits is provided in Table B1 in Appendix B and Figure 5-1. It is worth mentioning that the V_{OC} of the double-cation PSC with an E_g of 1.74 eV reported in this chapter is 30 mV lower than achieved with the same device layer stack in Chapter 4. One main cause is that the PbI_2 material is of inferior quality due to using a different supplier during the course of this study, which is the key component in fabricating highly efficient PSCs.

Consequently, opaque PSCs using 2D/3D perovskite heterostructure yield a remarkable improvement in PCE (0.8-1.3% absolute) compared to the 3D reference PSCs (Figure 5-4c), exhibiting a maximum PCE of 19.2% for 2D/3D PSC with the bandgap of E_g = 1.65 eV. This enhancement is driven not only by the significant boost in V_{OC} but also by a slight increase in fill factor (FF) (≈1.5-2% absolute) derived from the *J-V* measurement of corresponding devices measured in the reverse direction (Figure 5-6). However, by widening the absorber bandgap from 1.65 to 1.85 eV, PCE continuously decreases from 19.2% to 18.7%, 18.4%, 16.5% and 14.7% respectively. This mainly originates not only from the large V_{OC} deficit for wider bandgap perovskites as mentioned previously but also from the decrease in short-circuit current density (J_{SC}) as a result of spectrum onset shift to the shorter wavelengths (Figure 5-3). These reductions cause a strong drop in PCE for both 3D and 2D/3D PSCs, in particular for E_g > 1.74 eV. The *J-V* characteristics and photovoltaic parameters of the best-performing devices measured under AM 1.5G solar illumination are displayed in Figure 5-6

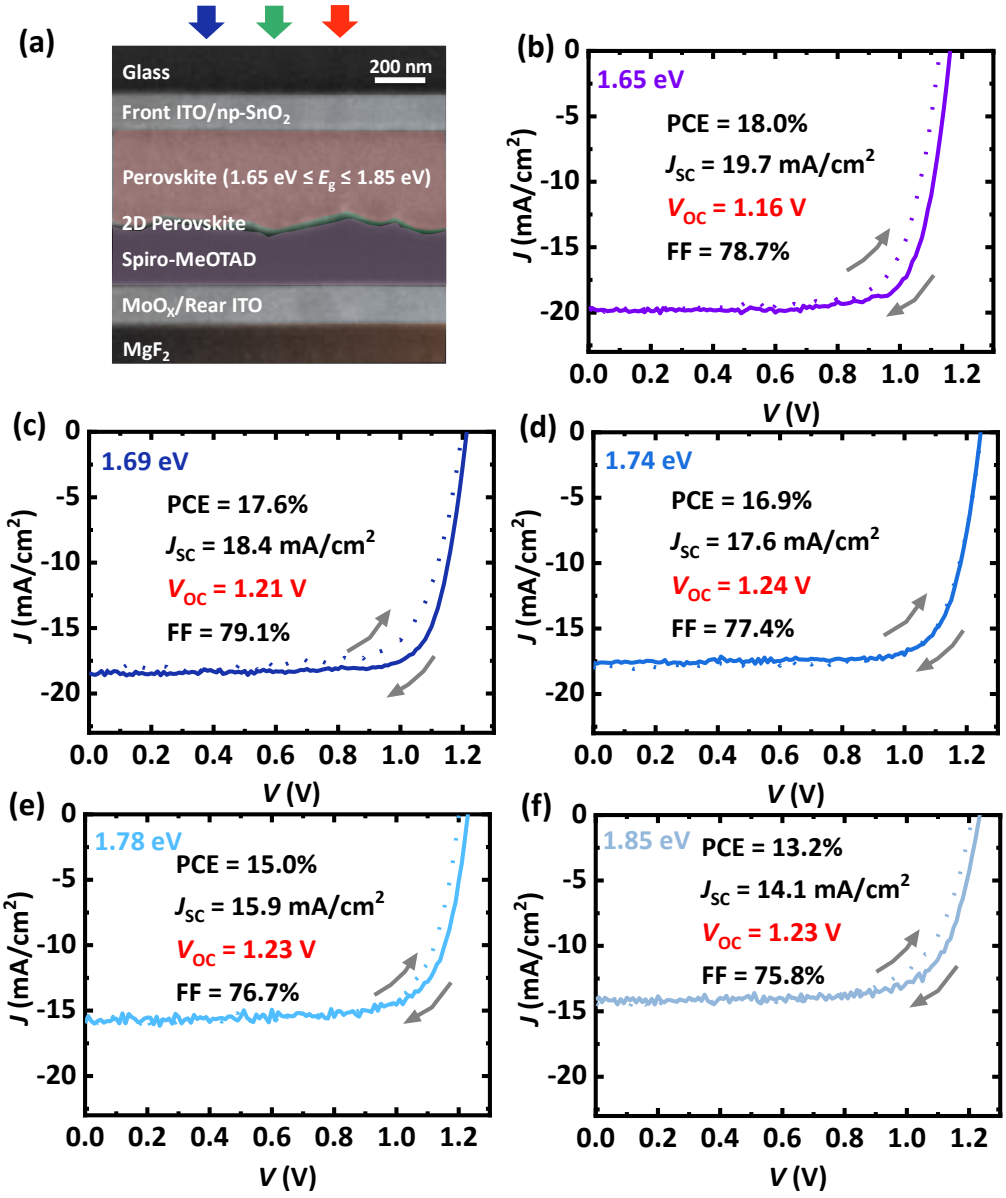

Figure 5-7: (a) Cross-sectional scanning electron microscopy (SEM) image of the semi-transparent perovskite solar cells (PSCs) using 2D/3D heterostructure. Current density-voltage (*J*–*V*) characteristics of best-performing semi-transparent PSCs using 2D/3D heterostructure with engineered bandgap of (b) 1.65 eV, (c) 1.69 eV, (d) 1.74 eV, (e) 1.79 eV and (f) 1.85 eV measured under full solar illumination conditions (AM1.5, 100 mW/cm^2) in a reverse (solid line) and forward (dashed line) scans.

In addition to the improved PCE, opaque PSCs using 2D/3D perovskite heterostructure exhibit stabilized PCEs of up to 17.9%, 17.6%, 17.2%, 15.6%, and 13.8% with increasing bandgap measured for 5 min of constant illumination at a constant voltage near to the maximum power point (MPP) (Figure 5-5d).

5.3. 2D/3D heterostructure for semi-transparent perovskite solar cells

Having verified that employing a 2D/3D perovskite heterostructure results in a remarkable

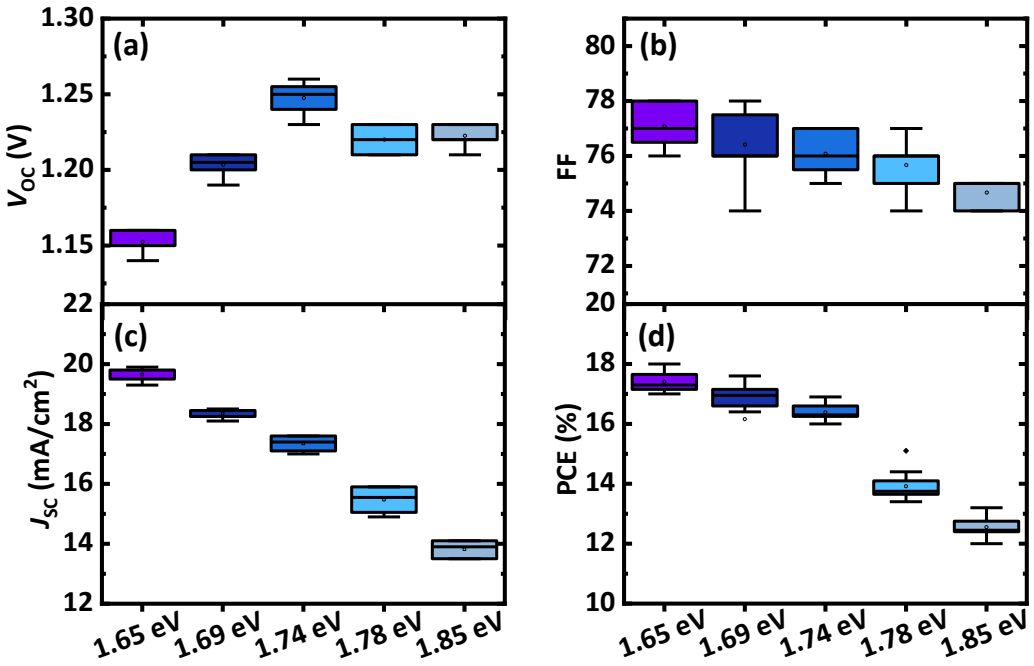

Figure 5-8: (a) Open-circuit voltage V_{OC}, (b) fill factor (FF), (c) short-circuit current density (J_{SC}), and (d) power conversion efficiency (PCE) statistics of semi-transparent perovskite solar cells using 2D/3D perovskite heterostructure with engineered bandgaps measured under 1 sun AM1.5G illumination. Photovoltaic parameters determined form the *J–V* characteristic of a statistically relevant number (> 60 in total). Adapted with permission from reference [216]. © John Wiley & Sons.

enhancement in PCE for opaque PSCs over a wide range of the bandgaps, for the next step we transferred all fabrication processes developed for opaque PSCs directly into semi-transparent devices in order to construct 4T perovskite-based tandem solar cells. For this reason, we replaced the Au electrode with a MoO_x buffer layer and transparent in-house sputtered ITO rear electrode, as illustrated in the cross-sectional SEM in Figure 5-7a. Meanwhile, 125 nm of MgF_2 as an anti-reflection layer was deposited on top of the rear ITO to increase the optical transmission of the semi-transparent device, as we will discuss later.

Similar to the opaque PSC, the best device performance for semi-transparent PSCs using 2D/3D heterostructure is obtained for an E_g of 1.65 eV, exhibiting a PCE of 18%, V_{OC} of 1.16V, FF of 78.7% and J_{SC} of 19.7 mA/cm^2 (Figure 5-7). The *J-V* characteristics, with detailed photovoltaic parameters of the best-performing semi-transparent devices and statistical analysis of all investigated bandgaps can be found in Figures 5-7 and 5-8. For better comparison of opaque and semi-transparent PSC performance over a range of bandgaps, the PCE and V_{OC} values derived from the *J-V* characteristics are normalized to the Shockley–Queisser (S-Q) limit at the relevant bandgaps (Figure 5-9). Although both devices exhibit a similar trend for relative V_{OC}, a slight drop by about 20-30 mV is observed in the V_{OC} of semi-transparent PSCs for all investigated bandgaps (Figure 5-9a). This reduction is primarily correlated to using a shadow mask to measure a reliable J_{SC} by specifying a reduced, but accurate active area of the cell. This is necessary as the area of the semi-transparent PSCs

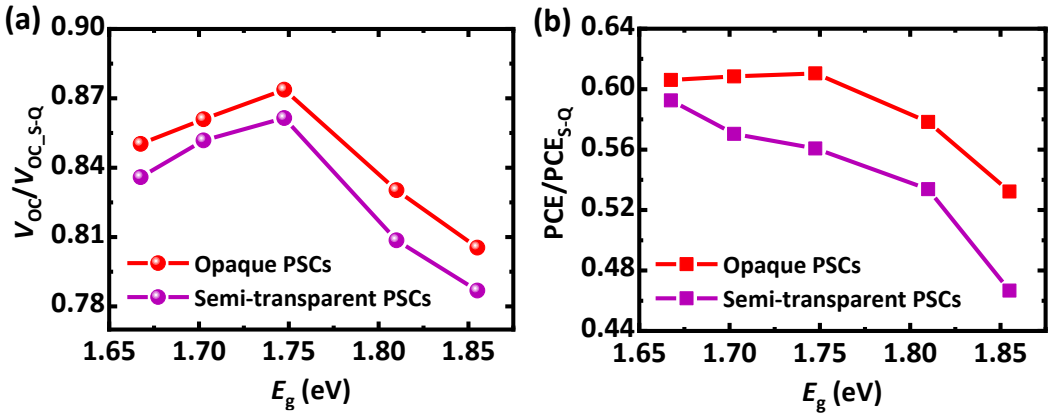

Figure 5-9: Best-performing (a) open-circuit voltage (V_{OC}) and (b) stabilized power conversion efficiency (PCE) of opaque and semi-transparent perovskite solar cells (PSCs) with engineered bandgap normalized to the Shockley-Queisser (S-Q) limit at the respective bandgap. Adapted with permission from reference [216]. © John Wiley & Sons.

is not precisely defined after the ITO rear electrode sputtering. However, we found that, due to the edge effect of the mask, shading the active area induces a dark solar cell parallel with the cell under light illumination which can result in a reduction in V_{OC}.[224] Alternatively, the lower V_{OC} of the semi-transparent devices might be correlated to the change in interface from HTL/Au to HTL/MoOx/ITO.[225] It is worth considering that while the PCE trend of opaque PSCs remains relatively stable up to E_g = 1.74 eV and only reduces for wider bandgaps (E_g > 1.74 eV) (due to an enhanced V_{OC} deficit), semi-transparent PSCs show a significant and continual reduction in relative PCE for E_g > 1.65 eV (Figure 5-9b). This could be explained by an additional reduction in J_{SC} (by about 1-1.5 mA/cm^2) of semi-transparent PSCs compared to opaque PSCs, as indicated from the EQE spectrum (Figure 5-10) in the wavelength range between 550 to 800 nm. The primary cause of this reduction is the reduced optical path length in incident photons due to significantly reduced internal reflection when replacing the rear opaque Au with a rear transparent conductive oxide (TCO) electrode or spiro-MeOTAD. (see Figure B1 in Appendix B).[202,220,225,226]

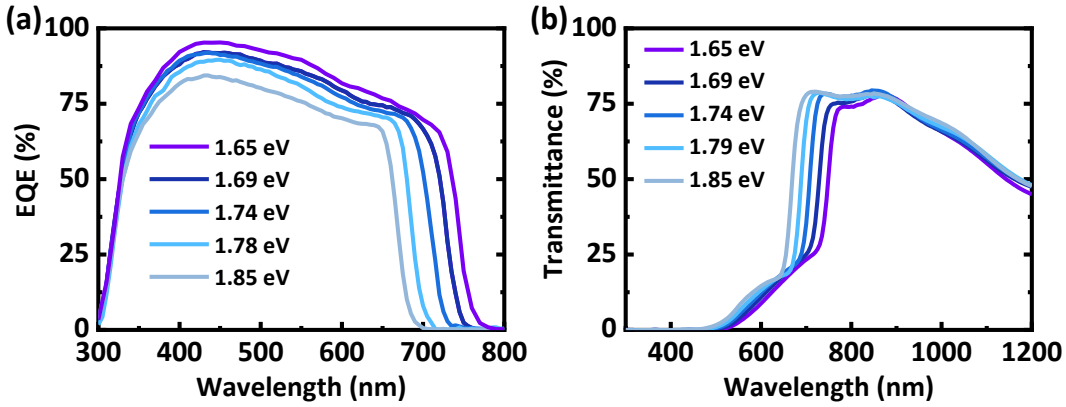

Figure 5-10: (a) External quantum efficiency (EQE) and (b) transmittance of semi-transparent perovskite solar cells using 2D/3D heterostructure with engineered bandgaps. Adapted with permission from reference [216]. © John Wiley & Sons.

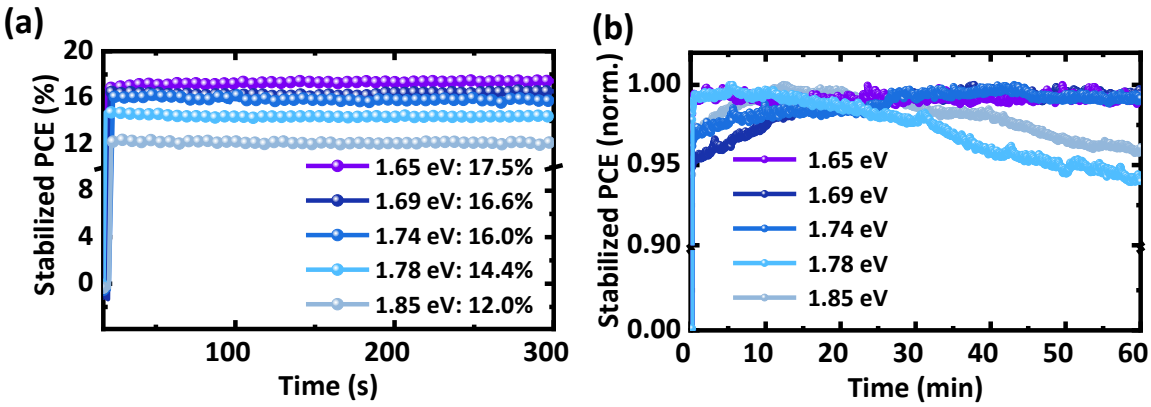

Figure 5-11: Stabilized power conversion efficiency (PCE) of semi-transparent perovskite solar cells (PSCs) using 2D/3D heterostructure with engineered bandgaps measured at a constant voltage near the maximum power point under continuous 1 sun illumination for 5 min. (b) Normalized stabilized PCE of the corresponding devices measured under continuous illumination for 1 hour.

Consistent with the absorbance spectrum (Figure 5-2), the EQE spectrum for semi-transparent PSCs shows a continuous shift towards shorter wavelengths with increasing bandgap of the perovskite absorber (Figure 5-10a). This means more light in the long-wavelength region transmits through the top semitransparent PSCs to reach the bottom solar cell (Figure 5-10b). Moreover, a trend of reduced signal over the sub-bandgap region is observed with increasing bandgap. This trend may be correlated to reduced charge carrier extraction or enhanced carrier trapping in bromine-rich absorber layers, but the exact cause is beyond the scope of this study. Nevertheless, the FF of semi-transparent devices is comparable with opaque PSCs, indicating a high conductivity of our in-house sputtered rear ITO electrode.

To better quantify the PCE of corresponding devices, we performed initial stability measurements by exposing the devices to continuous AM 1.5G illumination for 5 minutes at a constant voltage near MPP tracking. A stabilized PCE of 17.5%, 16.6%, 16.0%, 14.4% and 12.0% is achieved for the best-performing semi-transparent PSCs with a bandgap of 1.65, 1.69, 1.74, 1.78 and 1.85 eV, respectively (Figure 5-11a). As expected, this value is lower than the stabilized PCE of opaque devices (Figure 5-4d). By measuring the long-term normalized stabilized PCE for 60 min continuous irradiation, we do not observe any drop in PCE for $E_g \leq 1.74$ eV, revealing that the PSCs with these bandgaps are not significantly affected by phase segregation or other degradation mechanisms during 60 min. In contrast, when widening the bandgap of the perovskite absorber to 1.79 eV and 1.85 eV, the stabilized PCE of these semi-transparent devices gradually begins to decrease to 96% and 94% of its initial value after 1 hour, respectively (Figure 5-11b). This is expected to arise from the enhancement in photoinduced phase segregation with increasing Br content, thereby affecting the long-term efficiency of wider-bandgap PSCs.[42,56,189]

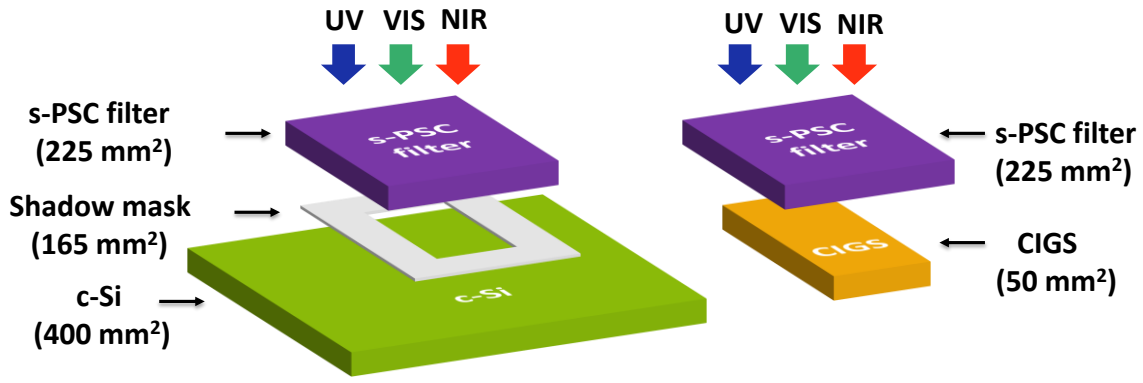

Figure 5-12: (a) Schematic illustration of top semi-transparent perovskite solar cell (s-PSC) and bottom c-Si and CIGS solar cell to measure the performance of 4-terminal tandem configurations. A filter s-PSC is the same layer stack and optical properties as the s-PSC but with a larger area cells. Adapted with permission from reference [216]. © John Wiley & Sons.

5.4. High-efficiency 4-terminal perovskite-based tandem solar cells

In order to fabricate 4T perovskite-based tandem solar cells, as discussed in Chapter 2, each subcells is independently fabricated before mechanical stacking to form a single device (Figure 5-12a). As the size of our semi-transparent PSC active area is smaller than bottom c-Si (aperture area 165 mm^2) or CIGS (designated area 50 mm^2), we fabricated a perovskite optical filter with a substrate area of 225mm^2 under the same processing conditions and device stack as the semi-transparent PSC to directly measure the bottom cell performance (Figure 12b). These semi-transparent filters demonstrate a high transmittance of more than 70% (with a peak at ≈850 nm) at energies below perovskite absorber bandgaps (Figure 5-10b) due to the deposition of MgF_2 on the rear ITO side. The addition of MgF_2 on the semi-transparent devices stack as an anti-reflection coating layer dramatically reduces optical losses in the long-wavelength range,[132,227] which is a critical requirement in a tandem solar cell configuration. The transmittance and reflectance of the semi-transparent perovskite filter with and without MgF_2 are depicted in Appendix B; Figure B2 for better comparison.

To determine the best obtainable PCE of our 4T perovskite/c-Si and perovskite/CIGS tandem solar cell, fabricated semi-transparent PSC filters using 2D/3D perovskite heterostructure with various bandgaps are coupled with an efficient interdigitated back contact (IBC) c-Si (E_g = 1.1 eV, PCE = 23.2%) or CIGS (E_g = 1.13 eV, PCE = 21.2%) solar cells as illustrated in Figure 5-13a and b. The stabilized PCE of both c-Si and CIGS bottom solar cells when operating underneath the semi-transparent PSC filter (termed as filtered c-Si and filtered CIGS) demonstrate a quasi-linear enhancement with the widening bandgap of the top semi-transparent PSC filter (Figure 5-13c). As expected, this is a result of enhanced photo-generated current in the bottom cell. In general, a wider bandgap increases transmitted photon intensity reaching the bottom cell, which is consistent with their transmission spectra (Figure 5-10b). Thereby, we observe a similar quasi-linear increase in

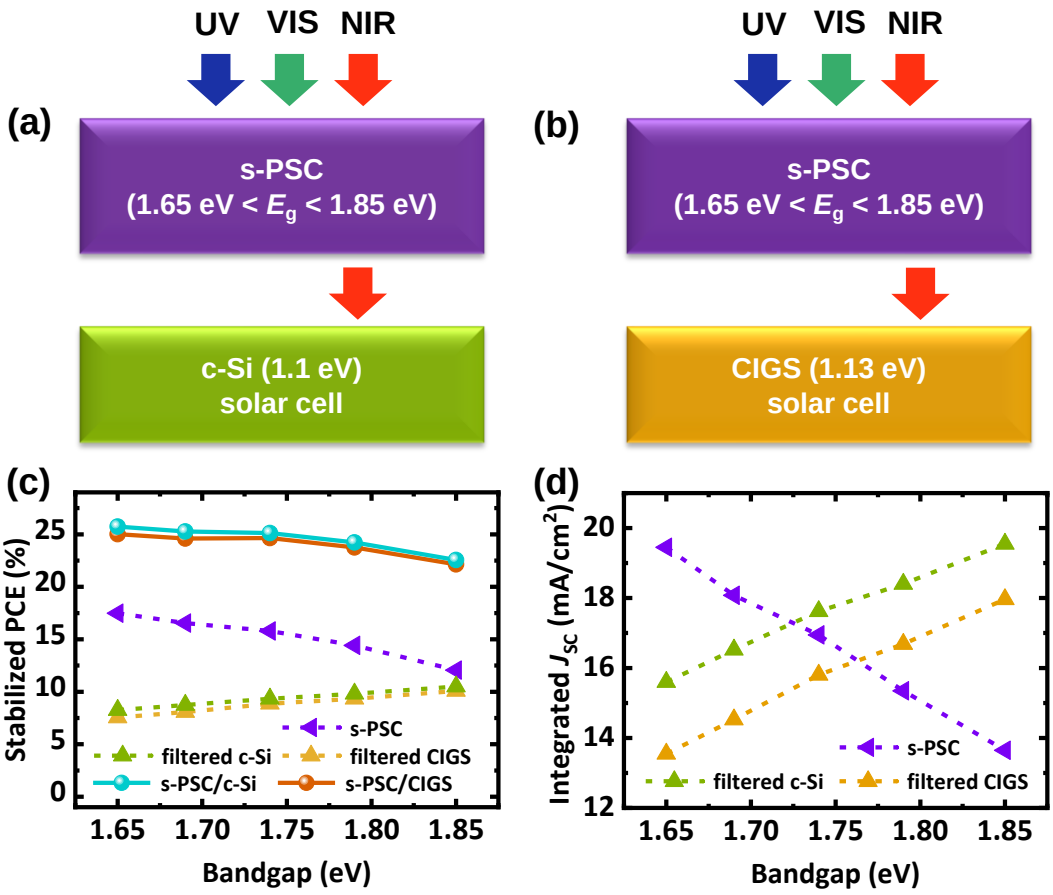

Figure 5-13: Schematic of a 4-terminal (4T) tandem configuration fabricated with a semi-transparent perovskite (s-PSC) filter integrated on top of (a) c-Si (b) CIGS solar cells. (c) Stabilized power conversion efficiency (PCE) of s-PSCs using 2D/3D heterostructure, filtered c-Si solar cell, filtered CIGS solar cells and corresponding tandem solar cells (calculated). (d) Integrated short-circuit current density (J_{SC}) of semi-transparent PSCs, filtered c-Si and filtered CIGS solar cells, extracted from external quantum efficiency. Adapted with permission from reference [216]. © John Wiley & Sons.

the J_{SC} of both bottom solar cells with a widening bandgap (Figure 5-13d), in which an increase in J_{SC} of 2 mA/cm^2 per 0.1 eV is obtained by a linear fitting curve for both c-Si and CIGS bottom cells. However, this enhancement does not entirely compensate for the larger decrease in J_{SC} of top semi-transparent PSCs, with a loss of −2.86 mA/cm^2 per 0.1 eV (Figure 5-13d) for an increasing bandgap, as evidenced by the EQE spectra of corresponding devices in Figure 5-10a. On the other hand, obtained V_{OC} for filtered bottom cells exhibits a slight increase of ≈3-4 mV per 0.1 eV with widening the bandgap, which is a consequence of the increased number of photons and the logarithmic dependency of V_{OC} on light intensity. This enhancement is also not comparable to the large V_{OC} deficit at wider bandgaps of top semi-transparent PSCs due to an increased Br content, as discussed in Section 5-2. As a result, despite the enhanced photogenerated J_{SC} in the bottom cell, the overall PCE of 4T tandem solar cells decreases for wider bandgaps (E_g > 1.74 eV) due to the strong reduction in J_{SC} of top semi-transparent PSC along with the large V_{OC} deficit, which is contrary to the simulations.[33] Therefore, these results underline the importance of

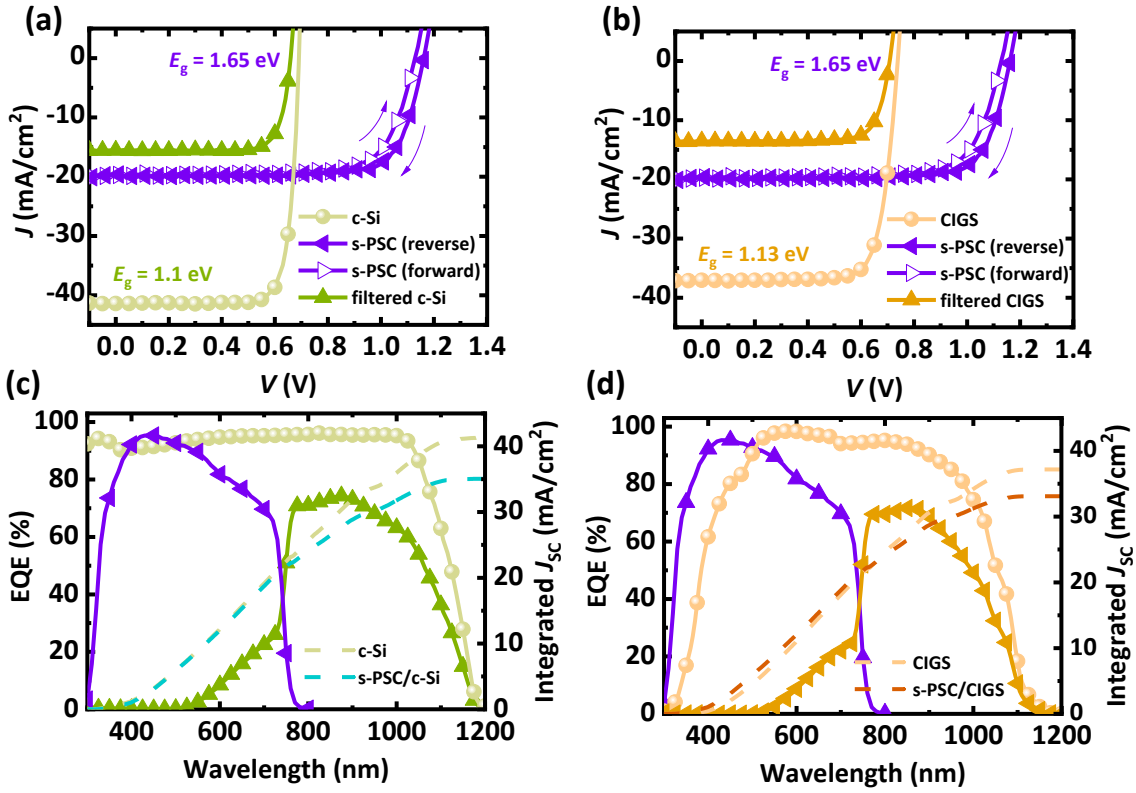

Figure 5-14: (a, b) Current density–voltage (*J–V*) characteristics and (c, d) external quantum efficiency (EQE) of semi-transparent perovskite solar cells (s-PSCs) with an optimum bandgap of 1.65 eV, standalone c-Si, filtered c-Si, standalone CIGS and filtered CIGS solar cells. The corresponding integrated short-circuit current density (J_{SC}) of the standalone and the 4-terminal tandem solar cells are also presented. Adapted with permission from reference [216]. © John Wiley & Sons.

finding the optimum bandgap, as well as reducing the photovoltage loss in top semi-semitransparent PSC to improve the overall performance of 4T tandem solar cells.

Figure 5-14 displays *J-V* characteristics and EQE responses of the best-performing perovskite/c-Si and perovskite/CIGS 4T tandem architectures with E_g of 1.65 eV. Accordingly, by placing high-efficiency c-Si or CIGS solar cells under the semi-transparent filter with an optimum bandgap, PCEs of 8.2% and 7.5% are obtained for filtered c-Si and filtered CIGS, respectively. A lower rise in the PCE of CIGS compared to c-Si solar cells is due to its wider bandgap, which generates 2 mA/cm^2 less J_{SC} (13.6 mA/cm^2) compared to a c-Si solar cell (15.6 mA/cm^2), as observed by a reduction in EQE response of standalone CIGS solar cell at a longer wavelength (Figures 5-14c and d). Thereby, the tandem efficiency reaches a stabilized PCE of 25.7% and 25.0% for 4T perovskite/c-Si and perovskite/CIGS configurations, exhibiting an absolute gain of 2.5% and 3.9% compared to standalone c-Si or CIGS solar cells, respectively. These results clearly emphasize the benefits of tandem configurations. Detailed photovoltaic parameters of corresponding top and bottom solar cells, as well as calculated PCE for 4T tandem devices are summarized in Table 5-1. Yet, the obtained PCE of 4T perovskite-based tandem solar cells in this chapter is still far below the

Table 5-1: Photovoltaic parameters of best-performing device configuration.

Solar cell architecture	Measurement protocol	V_{OC} (V)	J_{SC} (mA/cm^2)	FF (%)	PCE (%)	Stabilized PCE (%)
s-PSC (E_g = 1.65 eV)	BW	1.16	19.7	78.7	18.0	17.5
	FW	1.13	20	74.8	16.9	
c-Si solar cell	Stand-alone	0.69	41.4	81.2	23.2	23.2
	Filtered	0.66	15.6	80.2	8.2	**8.2**
4T perovskite/c-Si	BW	-	-	-	26.2	**25.7**
	FW	-	-	-	25.1	
CIGS solar cell	Stand-alone	0.74	37.2	77.0	21.2	21.2
	Filtered	0.71	13.6	78.1	7.5	**7.5**
4T perovskite/CIGS	BW	-	-	-	25.5	**25.0**
	FW	-	-	-	24.4	

theoretical limit. Therefore, further improvement in both transmission and performance of the top semi-transparent PSC seems to be an imperative requirement in order to increase the overall PCE of 4T perovskite-based tandem solar cells toward 30%in the near future. In this context, in the next chapter, we will discuss a strategy to further reduce non-radiative recombination in the top PSC to enhance performance.

5.5. Summary

In this chapter, we explored the effect of a 2D/3D perovskite heterostructure on the performance of a series of semi-transparent PSCs with engineered bandgaps (1.65, 1.74, 1.69, 1.78 and 1.85 eV) in order to maximize the PCE of a 4T perovskite-based tandem solar cell. For this, we first demonstrated that, regardless of the perovskite absorber bandgap, opaque PSCs exhibit a reduced non-radiative recombination loss, resulting in a significant enhancement in V_{OC} and stabilized PCE compared to reference devices. To the best of our knowledge, it was the first time an effective 2D passivation strategy is reported over such a broad range of bandgaps. By using this strategy to combine a series of semi-transparent PSCs with engineered bandgaps with high-efficiency c-Si and CIGS bottom solar cells, we found out that an E_g of 1.65 eV exhibits an optimum bandgap for the top-semitransparent PSC in real prototype 4T devices. This is contrary to simulations, in which a wide bandgap of 1.75 eV is considered as the ideal bandgap of the top-semitransparent PSC. The disparity between simulations and experimental results primarily originates from the decrease in PCE of the top subcell due to reduced J_{SC} from photon absorption and an enhanced V_{OC} deficit as a result of increased non-radiative recombination losses. However, such losses are not considered in the simulation (detailed balance calculation) and, thereby, the optimum bandgap in our experimental study shifts to a smaller bandgap until these losses can be resolved. As a result, by applying the best-performing semi-transparent PSC with a PCE of 17% and bandgap of 1.65 eV, we achieved a champion stabilized PCE of 25.7% and

25.0% for 4T perovskite/c-Si and perovskite/CIGS tandem solar cells. This exceeds the highest PCE obtained for a single-junction c-Si (23.2%) or CIGS solar cell (21.2%) in this study. Our results highlight the importance of a detailed experimental investigation for finding the optimum bandgap, as well as the need to develop a strategy for suppressing non-radiative recombination in the top semi-transparent perovskite absorber to improve the photovoltaic performance of 4T perovskite-based tandem solar cells.

6. Simultaneous Interfacial and Grain-boundary Passivation for Highly Efficient p-i-n Perovskite Solar Cells for Tandem Photovoltaics

The focus of this chapter is on reducing non-radiative recombination in double-cation perovskite solar cells (PSCs) with a bandgap of 1.57 eV based on the inverted p-i-n architecture. Here, we introduce a dual-functional passivation strategy based on the incorporation of long-chain alkylammonium salt phenethylammonium chloride (PEACl) at both bulk and interface of perovskite/electron transport material (ETL). Therefore, a simultaneous enhancement in both the open-circuit voltage (V_{OC}) and fill factor (FF) of the devices is observed, leading to not only high efficiency but also high stability for p-i-n PSCs.

This chapter is based on our publication in *Energy & Environmental Science* with the title "Two birds with one stone: dual grain-boundary and interface passivation enable > 22% efficient inverted methylammonium-free perovskite solar cells".[228] Most of the graphs in this chapter are adapted or reproduced with the permission of *Energy & Environmental Science*.

Acknowledgments and contributions

The initial idea of this study was conceived by Saba Gharibzadeh. Further development was carried out with the support of Dr. Paul Fassl, Dr. Ihteaz Hossein. and Dr. Ulrich Paetzold Moreover, Saba Gharibzadeh contributed to the design of the experiments, fabrication of the perovskite films and characterization including the current density–voltage (J–V), external quantum efficiency (EQE), X-ray diffraction (XRD), ultraviolet-visible spectroscopy (UV-Vis) and long-term stability measurements. Dr. Paul Fassl carried out the absolute and intensity-dependent photoluminescence quantum yield (PLQY) measurements and data analysis. Dr. Ihteaz Hossein performed the transient photoluminescence (TPRL) measurements and data analysis. Dr. Markus Frericks performed the X-ray photoelectron spectroscopy (XPS) and ultraviolet photoelectron spectroscopy (UPS) measurements and data analysis and Dr. Paul Fassl and Dr. Jan Hofmann supported in data interpretation. Pascal Rohrbeck conducted the Kelvin probe force microscope (KPFM) measurements,

supervised by Dr. Stefan Weber. Saba Gharibzadeh, Pascal Rohrbeck, Dr. Paul Fassl and Dr. Stefan Weber helped for the data analysis. Dr. The Duong performed the cathodoluminescence (CL) measurements. Dr. Motiur Rahman Khan performed the thermal admittance spectroscopy (TAS) and space-charge-limited electron (SCLC) measurements and further analyzed the data. The scanning electron microscope (SEM) measurements were performed by Dr. Tobias Abzieher and Dr. Bahram Abdollahi. Fabian Scackmar conducted the contact angle measurement. Dr. Ulrich Paetzold supervised the entire project.

6.1. Introduction

Although the highest power conversion efficiency (PCE) for single-junction PSC has been achieved based on the standard n-i-p architecture (up to 25.8% certified),[27] applying them into monolithic n-i-p tandem solar cells is limited due to (i) a high-temperature annealing process required for the formation of ETL such as mesoporous or compact TiO_2 and SnO_2, (ii) high parasitic absorption and stability issues arising from ionically doped spiro-MeOTAD as a common hole transport layer (HTL) in n-i-p architecture, and (iii) the complexity of the conformal coverage of the perovskite top subcell on pyramidal textured silicon solar cells.[27,125,202,229,230] In contrast, recently PSCs with inverted planar p-i-n architecture have been intensively developed and employed for monolithic perovskite/c-Si tandem photovoltaics because of their (i) low-processing temperature required for deposition of the charge transport layers (CTL) (≤ 100 ^{o}C), (ii) low parasitic absorption thanks to the newly developed hole transport layer (HTL) as named 2PACz, (iii) impressive operational stability (due to the dopant-free CTL) (iv) along with negligible *J*–*V* hysteresis.[36,37,125,159,231] However, the maximum PCE (not-certified) that has been reported so far for p-i-n PSC is 24.3% (stabilized at 24%)[52] which is still lower than the certified record for standard n-i-p architecture (25.7%).

The most predominant factor causing inferior PCE for p-i-n PSCs is associated with non-radiative recombination at the interface of the perovskite with CTLs,[50,232,233] leading to a relatively large V_{OC} loss for a given bandgap compare to n-i-p PSCs as shown in Figure 6-1a. In particular, a comparison of the V_{OC} × FF product relative to the Shockley-Queisser (S-Q) limit demonstrates severe losses for p-i-n PSCs than n-i-p architecture (Figure 6-1b). Recently, introducing 2PACs as the HTL in p-i-n PSC could significantly minimize the non-radiative recombination losses at the HTL/perovskite interface. However, the perovskite/C_{60} (as the most common ETL used in p-i-n architecture) interface still suffers from severe interfacial recombination.[50,125,232,233] Moreover, the high defect densities within the bulk/grain boundaries of the perovskite absorber are also the sources of non-radiative recombination.[119,120] The presence of these defects facilitates ion migration in perovskite film which is known to accelerate the degradation of the PSC under light and thermal stress.[122,234,235] Therefore, reducing interfacial and bulk recombination by

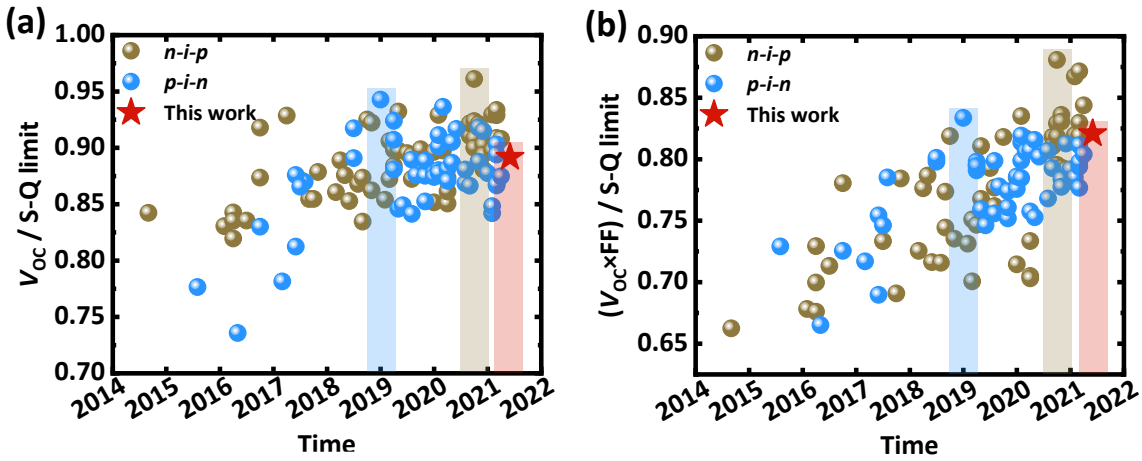

Figure 6-1: Open-circuit voltage (V_{OC}) and (b) V_{OC} x fill factor (FF) product of best-performing PSCs relative to the Shockley-Queisser (S-Q) limit for the given bandgap with n-i-p and p-i-n architecture reported in the literature. Adapted with permission from reference [228]. Copyright 2021, The Royal Society of Chemistry.

passivating the defects at the surface/interface as well as at bulk/grain boundaries of the PSC is an essential requirement to not only reduce the photovoltage loss but also improve the long-term stability issue of the devices which is one of the key bottlenecks for future commercialization of perovskite photovoltaics. . In terms of bulk/grain boundary defects, the incorporation of different additives into the perovskite precursor solutions or antisolvents has been intensively reported as an effective strategy to reduce the density of the defects. This strategy either improves the crystal quality of the perovskite film during the perovskite film formation or passivates detrimental defects within the perovskite layer.[44,45,118,236] In terms of interfacial recombination, post-treatment of the perovskite films by using long (alkyl)ammonium salts and other organic compounds has been effectively employed to reduce interfacial non-radiative recombination.[47,52,53,237,238] This strategy leads to the formation of 2D/3D perovskite heterostructures or wide-bandgap interlayers, resulting in passivation of the dangling bonds (chemical passivation) that exit at the surface of the perovskite layer or better energy level alignment of the perovskite with CTLs.[47,52,53,237,238] Although all these strategies surpass effectively non-radiative recombination losses in PSCs, only two works have been reported to passivate the defects both at bulk/grain boundaries and surface of the perovskite absorber by employing the same passivation material.[239,240]

Having demonstrated the successful surface passivation strategy in reducing non-radiative recombination presented in Chapter 4, in this chapter we aim to develop a dual passivation strategy in order to passivate simultaneously the grain boundaries and the perovskite/C_{60} interface in p-i-n PSC. For this, we use long-chain alkylammonium salt named phenethylammonium chloride (PEACl). Devices developed by this method demonstrate one of the highest PCE (22.7%, stabilized at 22.3%) reported so far for p–i–n PSCs, which is mainly due to the enhancement in the V_{OC} × FF product (Figure 6-1b). In Sections 6-2 and

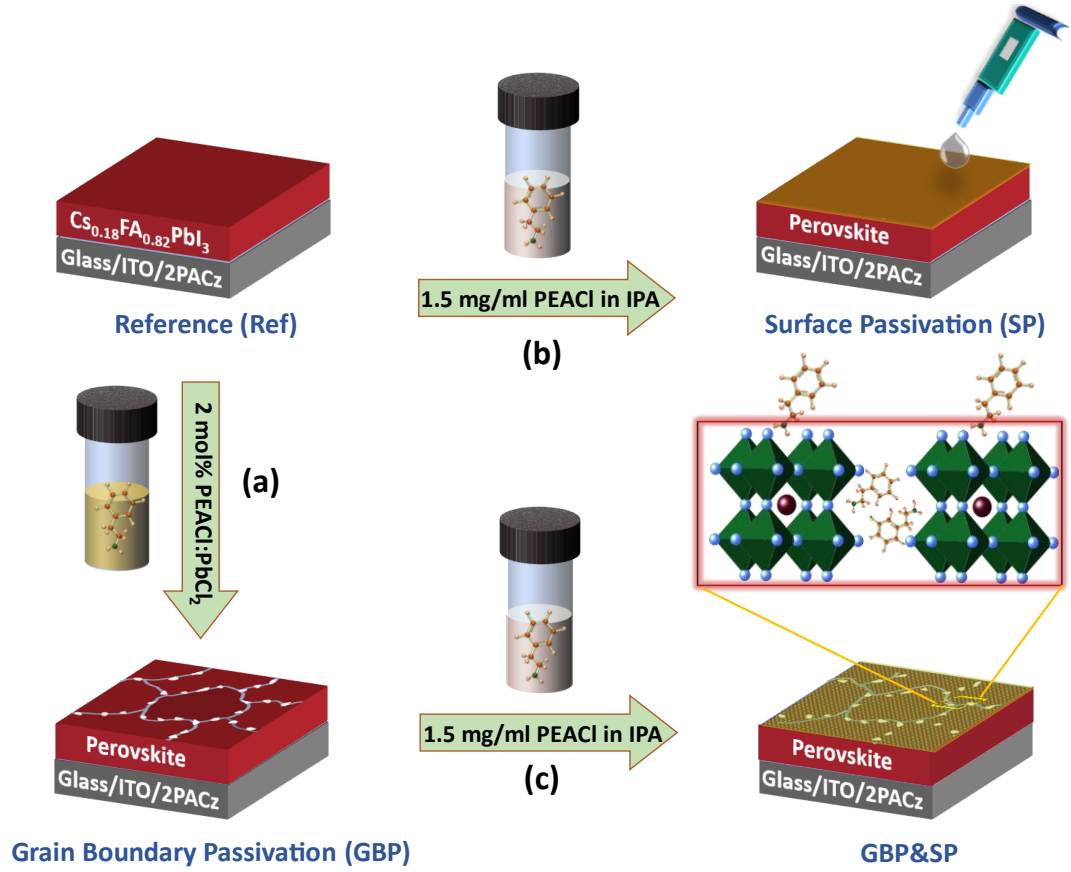

Figure 6-2: Schematic of the dual passivation strategy used for the deposition of the perovskite absorber layer: The process of (a) grain boundary passivation (GBP) by incorporation of PEACl:$PbCl_2$ into the perovskite precursor solution, (b) surface passivation (SP) by treatment of PEACl (1 mg/ml dissolved in IPA) on top of the perovskite absorber layer and (c) combination of grain boundary and surface passivation (GBP&SP).

and 6-3, we first describe the fabrication process of dual passivated PSC and compare the photovoltaic parameters of the devices proceeding either with individual or dual passivation strategies. In the following section, using a wide range of experimental techniques including photophysical and material characterization, we show that this enhancement in both V_{OC} and FF for dual passivated devices is correlated to the formation of a 2D Ruddlesden–Popper (2D-RP) phase at the grain boundaries as well as on the surface of the perovskite films, leading to a substantial reduction in non-radiative recombination. Finally, in the last section, we apply the dual passivated PSC into two-terminal (2T) and four-terminal (4T) perovskite-based tandem solar cells.

6.2. Dual passivation strategy

This approach relies on using long-chain alkylammonium salts (PEACl) incorporated as an additive (PEACl: $PbCl_2$) into the perovskite precursor solution to passivate the perovskite grain boundary (termed as grain-boundary passivation: GBP) (Figure 6-2a) and employed as a post-treatment solution (PEACl in IPA) on the perovskite surface to passivate the

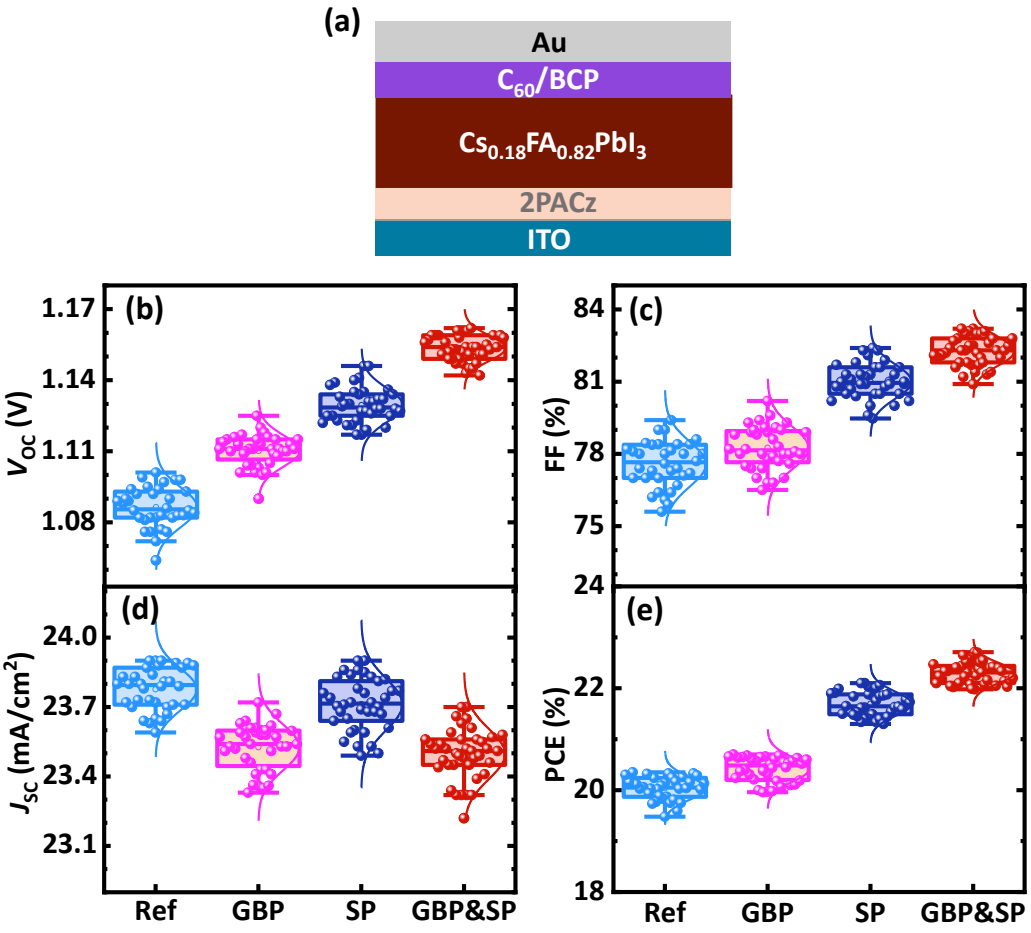

Figure 6-3: (a) Schematic of the device architecture used in this chapter. (b) Statistical photovoltaic parameters of (b) open-circuit voltage (V_{OC}), (c) fill factor (FF), (d) short-circuit current density (J_{SC}), and (e) power conversion efficiency (PCE) of perovskite solar cells without any modification (Ref), with surface passivation (SP), grain boundary passivation (GBP) and combination of grain boundary and surface passivation (GBP&SP). Photovoltaic parameters determined form the *J–V* characteristic of a statistically relevant number of 150 in total. Adapted with permission from reference [228]. Copyright 2021, The Royal Society of Chemistry.

surface of the perovskite layer (termed as surface passivation: SP) (Figure 6-2b). It is worth noting that we refer to the additive incorporation strategy as the "grain boundary passivation" strategy, as we will show later that this process particularly targets the defects at the grain boundary of the perovskite layer. With the combination of both strategies on the reference perovskite film (termed as Ref), we achieve simultaneous grain-boundary and surface passivated perovskite film (termed as GBP&SP) (Figure 6-2c). A detailed description of the experimental method can be found in Chapter 3.

6.3. Photovoltaic performance

To examine the effect of each passivation strategy on the performance of the PSC compared to the reference devices, we fabricated planar p-i-n PSCs with a bandgap (E_g) of

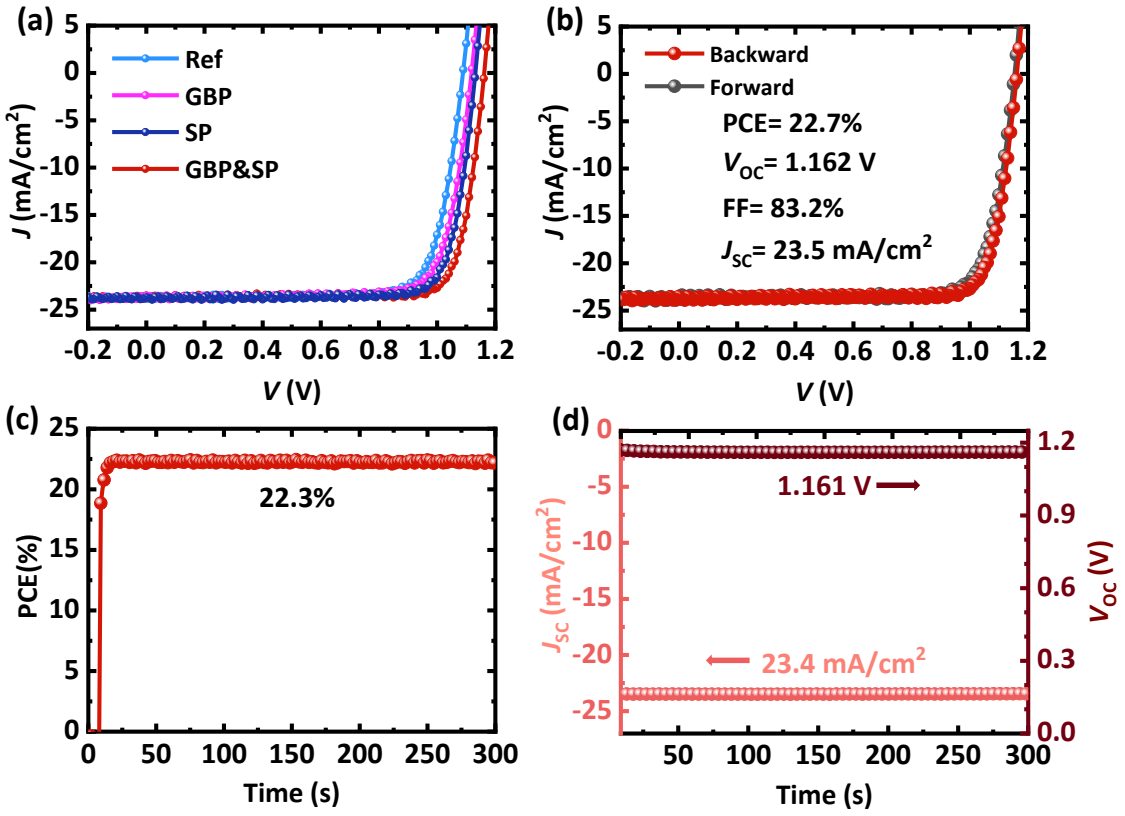

Figure 6-4: (a) Comparison of Current density–voltage (*J–V*) characteristics of the best performing devices without any modification (Ref) and with individual surface or grain boundary passivation (SP or GBP) as well as a combination of grain boundary and surface passivation (GBP&SP). (b) *J–V* characteristics of best performing GBP&SP perovskite solar cell along with stabilized (c) power conversion efficiency (PCE), (e) short-circuit current (J_{SC}) and open-circuit voltage (V_{OC}) at maximum power point (MPP) tracking under continuous 1-sun illumination for 300 s. Adapted with permission from reference [228]. Copyright 2021, The Royal Society of Chemistry.

1.57 eV using the individual as well as dual passivation strategies with a layer stack ITO/2PACz/perovskite/C_{60}/BCP/Ag (Figure 6-3a). As shown in Figure 6-3, a comparison of

Table 6-1: Photovoltaic parameters in reverse (BW) and forward (FW) bias of perovskite solar cells based on the reference (Ref), grain boundary passivation (GBP), surface passivation (SP), and combination of grain boundary & surface passivation (GBP&SP) processes.

PSCs	Scan direction	V_{OC} (V)	J_{SC} (mA/cm²)	FF (%)	PCE (%)
Ref	BW	1.086	23.9	78.6	20.4
	FW	1.080	23.6	75.6	19.3
GBP	BW	1.114	23.5	79.3	20.8
	FW	1.11	23.6	77.9	20.4
SP	BW	1.131	23.7	82.3	22.1
	FW	1.131	23.6	79.9	21.3
GBP&SP	BW	1.162	23.5	83.2	22.7
	FW	1.153	23.6	80.6	22.0

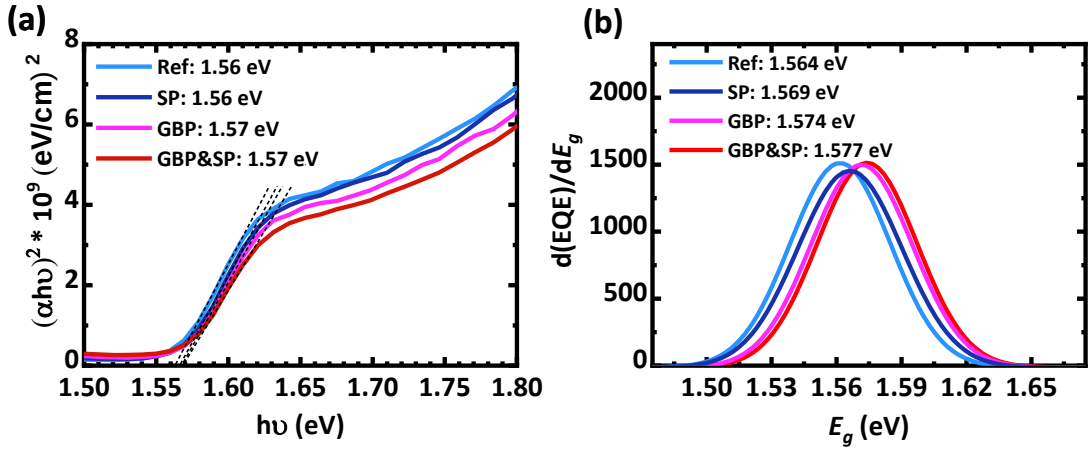

Figure 6-5: Optical bandgap derived from (a) Tauc plot measurement and (b) the inflection point of the external quantum efficiency (EQE) spectra of perovskite films prepared without any modification (Ref) and with surface passivation (SP), grain boundary passivation (GBP) and grain boundary & surface passivation (GBP&SP). Reproduced with permission from reference [228]. Copyright 2021, The Royal Society of Chemistry.

the average photovoltaic parameters obtained from current density–voltage (*J–V*) characteristics of 147 devices (in total) reveal an obvious continuous enhancement in V_{OC} and FF values of the devices based on the passivation strategy. For GBP devices, we observe a 26 mV increase in V_{OC} from 1.086 to 1.114 V and a slight improvement in FF from 78.6% to 79.3% compared to Ref devices obtained from backward scan direction, demonstrating a rise in PCE from 19.7% to 20.4% Figure 6-4a. The SP PSCs exhibit even a very higher V_{OC} of 1.13 V and FF of 82% with a significant improvement in PCE to 22.3% as compared to Ref and GBP PSCs. Impressively, upon dual passivation strategy, these values are further increased to 1.162 V and 83.2% respectively, reaching a maximum PCE of 22.7% with an outstanding stabilized PCE, V_{OC} and J_{SC} of 22.3%, 1.161 V and 23.4 mA/cm^2, respectively, measured under continuous AM1.5G illumination over 300 s at maximum power point tracking (Figures 6-4b,c and d). Figure 6-4a and Table 6-1 summarize the *J–V* characteristics and photovoltaic parameters of the best-performing devices. It is important to mention that the J_{SC} reported in this study is corrected to the integrated J_{SC} derived from the external quantum efficiency (EQE) spectrum to obtain a further accurate determination of the PCE for the fabricated devices, although this leads to a rather conservative PCE. Compared to published high-efficiency p-i-n PSCs with PCEs > 21% in the literature (as displayed in Figure 6-1), this is one of the highest reported V_{OC} × FF achieved for p-i-n PSCs so far. Therefore, our work highlights the necessity of the passivation of both grain boundaries of the perovskite thin film and the perovskite/C_{60} interface. Consistent with our observation for enhanced V_{OC} of n-i-p PSC in Chapter 4, the considerable rise of V_{OC} in this study also does not steam from an increase in the perovskite absorber bandgap as verified by the Tauc plot method and the inflection point of the EQE spectra (Figure 6-5). This enhancement mainly results from reduced non-radiative recombination as we will show later in the following sections. Furthermore, as shown in Figure 6-3c we observe a negligible change in the J_{SC} of SP PSCs compared to Ref devices. This is in line with our observation in Chapter 4, in which

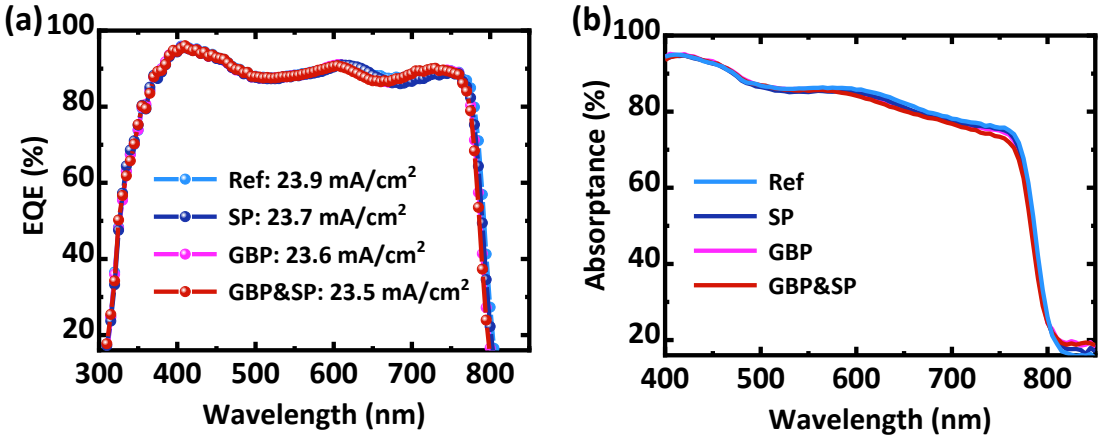

Figure 6-6: External quantum efficiency (EQE) and absorptance spectra of the best-performing perovskite solar cells fabricated without any modification (Ref) and with surface passivation (SP), grain boundary passivation (GBP), and grain boundary & surface passivation (GBP&SP). Adapted with permission from reference [228]. Copyright 2021, The Royal Society of Chemistry.

the thickness of the 3D perovskite absorber is not significantly modified by the low-concentration of n-butylammonium bromide surface treatment. However, GBP PSCs demonstrate a slight drop in J_{SC} from 23.9 to 23.5 mA/cm^2 compared to Ref devices. This reduction is attributed to the insulating nature of long-chain PEACl incorporated into perovskite film which inhibits the charge carrier extraction, thus resulting in a slight decrease in the EQE spectrum (Figure 6-6a).[98,202] For this reason, the reduction in the J_{SC} value becomes even stronger when we increase the concentration of the PEACl additive in the perovskite solution from 10 to 25 and 40 µL named as GBP(25) and GBP(40) (Figure 6-7c). The ultraviolet-visible (UV-vis) measurement also confirms a minor decline in absorptance spectra of the perovskite layer incorporated with PEACl additive compared to Ref or surface passivated films (Figure 6-6b). Therefore, finding the optimum concentration for both GBP and SP devices is essentially required in order to achieve the maximum photocurrent and PCE. In this regard, we varied the concentration of both PEACl:$PBCl_2$ additive (10, 25 and 40 µL) and PEACl solution dissolved in IPA (1.5 and 3 mg/ml). It can be seen that the optimum concentration of 25 µL for GBP and 1.5 mg/ml for SP PSCs are found to deliver the highest photovoltaic parameters for dual-passivated PSCs (Figure 6-7). Here, it should be noted that although the higher concentration of PEACl (3mg) treated on the surface of GBP PSCs (termed as GBP&SP(3)) results in a further enhancement in V_{OC} to 1.18 V, the J_{SC} and FF of the resultant devices concurrently decline which is due to the mentioned insulating nature of a thicker 2D-RP passivation layer at the surface,[98,202] leading to a low PCE of 21.8%.

To figure out that employing other chloride-based long-chain organic ammonium can also be used as dual passivation in the bulk and at the surface of the perovskite layer, we exploded using n-Butylammonium chloride (BACl) and n-Octylammonium Chloride (OACl), as n-Butylammonium iodide (BAI), n-Butylammonium bromide (BABr), Octylammonium

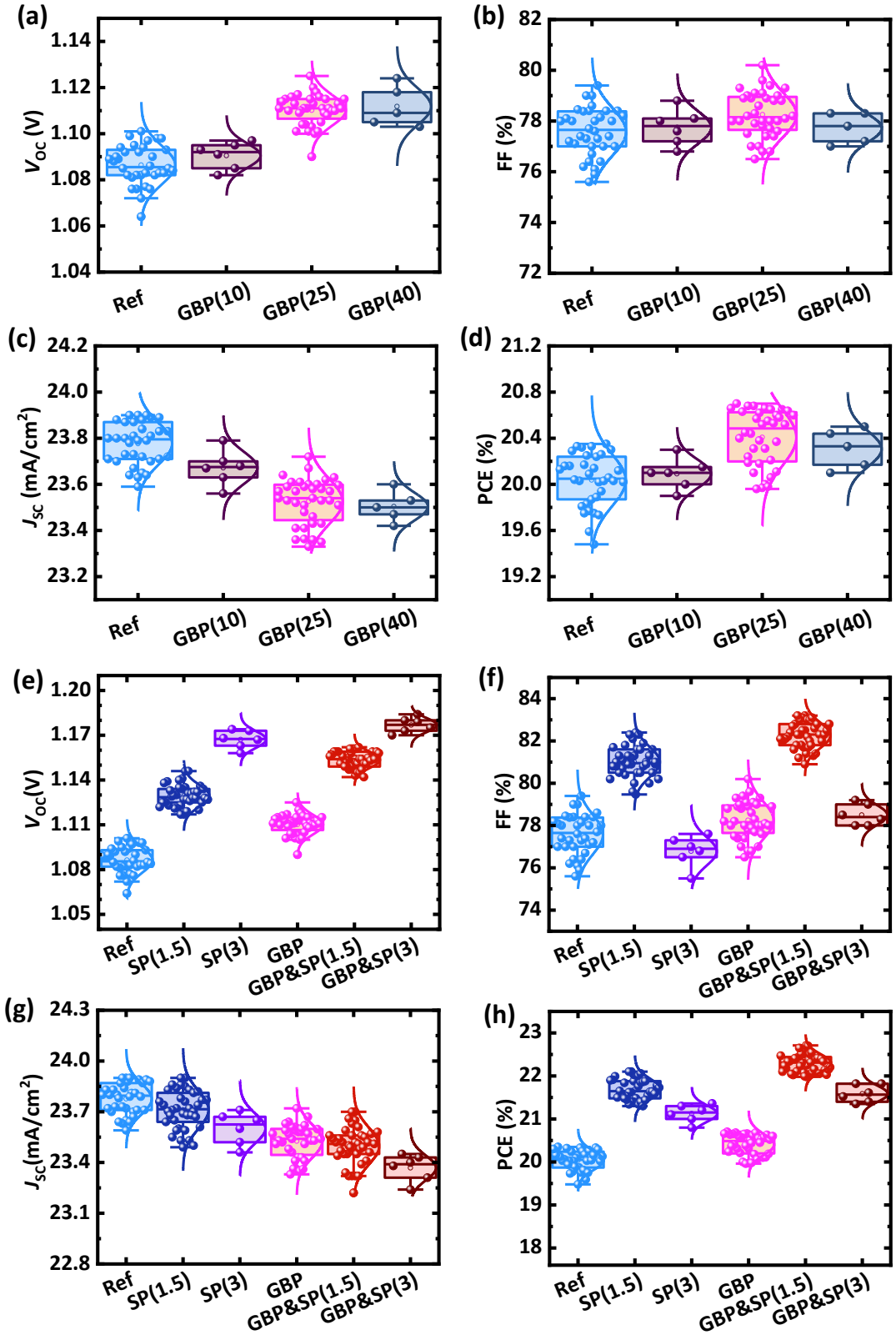

Figure 6-7: (a-d) Statistical photovoltaic parameters of perovskite solar cells (PSCs) (relevant number of 80) without any modification (Ref) and with various concentrations of PEACl:$PbCl_2$ (10, 25 and 40 µL, referred to as GBP(10), GBP(25) and GBP(40), respectively) as an additive solution. (e-h) The effect of the PEACl concentration (1.5 mg/ml and 3 mg/ml) as a surface passivation interlayer on the performance of the Ref and GBP PSCs with optimum concentration of 40 µL referred to as: SP(1.5), SP(3), GBP&SP(1.5) and GBP&SP(3), respectively, obtained from relevant number of 160 devices. (a, e) Open-circuit voltage (V_{OC}), (b, f) fill factor (FF), (c, g) short-circuit current density (J_{SC}), and (d, h) power conversion efficiency (PCE).

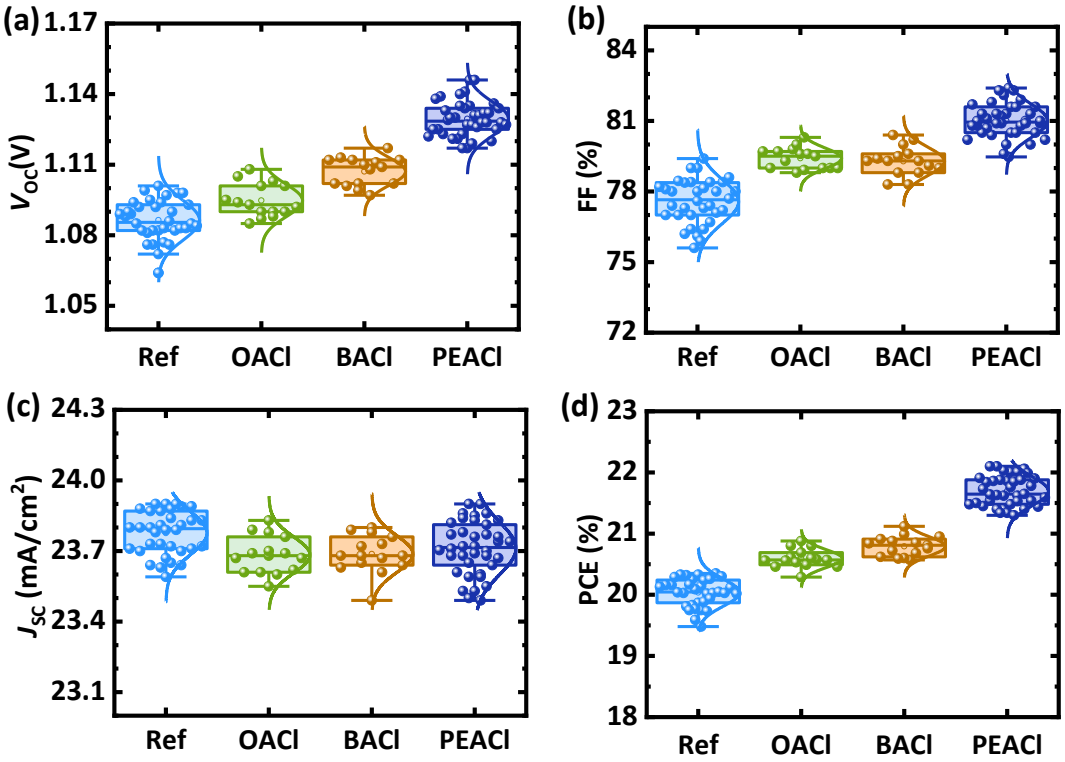

Figure 6-8: Comparison of the Photovoltaic parameters of the reference (Ref) perovskite solar cells and surface passivated devices treated with OACl, BACl and PEACl solution respectively. (a) Power conversion efficiency (PCE), (b) open-circuit voltage (V_{OC}), (c) fill factor (FF), (d) short- circuit current density (J_{SC}). Photovoltaic parameters determined form the *J–V* characteristic of a statistically relevant number of 100 in total Reproduced with permission from reference [228]. Copyright 2021, The Royal Society of Chemistry.

iodide (OAI) and Octylammonium bromide (OABr) have been previously reported for passivating of the perovskite films in numerous works.[241–244] Under a similar preparation method, first we fabricated the surface passivated devices based on these materials (OACl and BACl solution dissolved in IPA). Interestingly, both devices demonstrate a slight increase in PCE compared to the Ref PSCs, which is mainly associated with an enhancement in V_{OC} and FF (Figure 6-8). Nevertheless, the enhancements are most substantial in the case of PEACl-based devices. In the second step, we employed the dual passivation strategy by incorporating OACl:$PbCl_2$ or BACl:$PbCl_2$ (termed as Oc-Cl or Bu-Cl) into the bulk, as well as treating the surface of the perovskite layer with OACl or BACl solution (termed: Oc-Cl/OACl and Bu-Cl/BACl, respectively). As displayed in Figure 6-9, GBP&SP devices based on Oc-Cl/OACl and Bu-Cl/BACl demonstrate a V_{OC} enhancement by about 30 mV compared to Ref PSCs, whereas this value is much higher (70 mV) in case of GBP&SP devices based on the PEACl. Besides, contrary to Bu-Cl/BACl PSCs with a small drop in J_{SC} and no noticeable change in FF compared to Ref PSCs, these parameters decrease even strongly for Oc-Cl/OACl PSC. This reduction is in agreement with previous observation based on utilizing too large amounts of alkylammonium salts as an additive.[47,98,185,202] As a result, this reduction in charge carrier transport hinders the effect of reduced interfacial

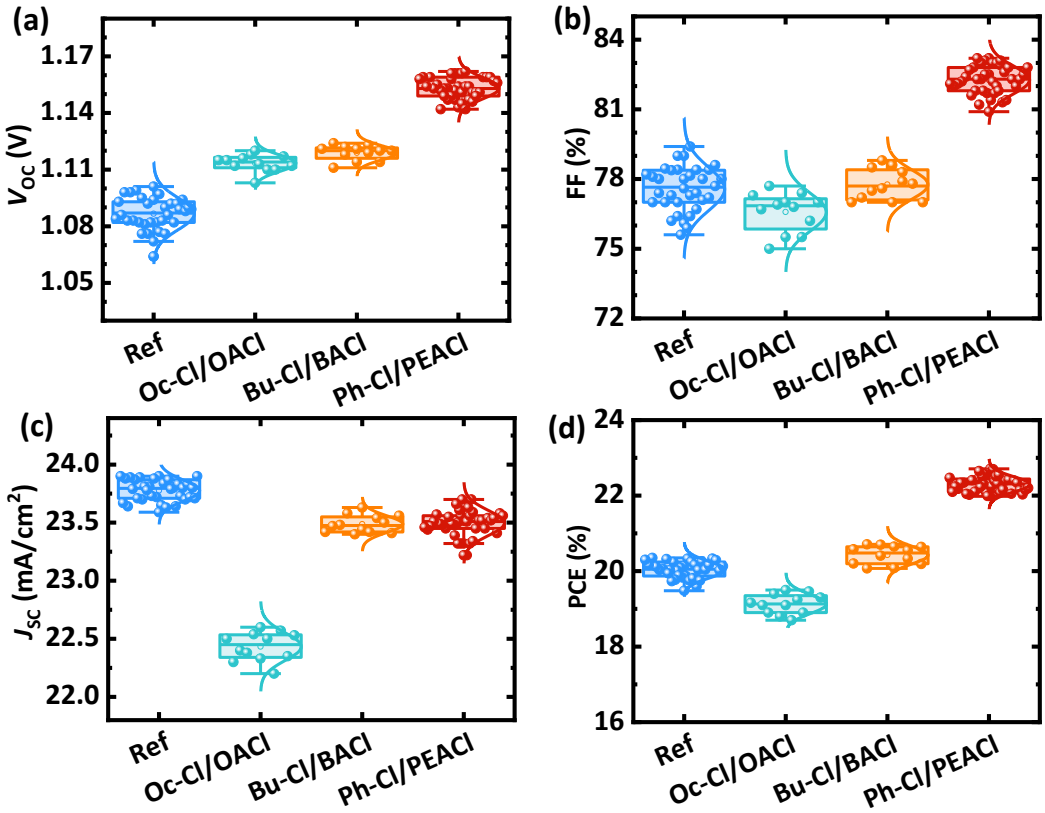

Figure 6-9: Comparison of historical photovoltaic parameters of the perovskite solar cells without any modification (Ref) and with combined grain boundary & surface passivation processes based on the incorporation of OACl:$PbCl_2$ (Oc-Cl), BACl:$PbCl_2$ (Bu-Cl) and PEACl:$PbCl_2$ (Ph-Cl) in the precursor solution, as well as surface treatment with OACl, BACl and PEACl solution, respectively (referred to as: Oc-Cl/OACl, Bu-Cl/BACl and Ph-Cl/PEACl). (a) Open-circuit voltage (V_{OC}), (b) fill factor (FF), (c) short-circuit current density (J_{SC}) and (d) power conversion efficiency (PCE). Photovoltaic parameters determined form the *J*–*V* characteristic of a statistically relevant number of 95 in total. Reproduced with permission from reference [228]. Copyright 2021, The Royal Society of Chemistry.

recombination (i.e., higher V_{OC}), leading to the average PCE of 20.6% and 20.9% for the Oc-Cl/OACl and Bu-Cl/BACl based devices, respectively. Given that the dual passivated PSC based on PEACl demonstrated the highest performance in comparison with other Cl-based long-chain alkylammonium salts, our focus in the following section will be the investigation of the photophysical and material characterization of the PEACl-based GBP&SP film in order to understand the mechanism behind the enhancement in the V_{OC} × FF product.

6.4. Photophysical characteristics

To identify the impact of GBP, SP and GBP&SP on the charge carrier recombination dynamics of the perovskite film, we first investigate transient photoluminescence (TRPL) of ITO/2PACz/perovskite/C_{60} layer stacks (Figure 6-10a). A clear trend toward increasing the carrier lifetime (by more than one order of magnitude) is observed for Ref (19 ns) → GBP (48 ns) → SP (113 ns) → GBP&SP (256 ns) samples. This carrier lifetime

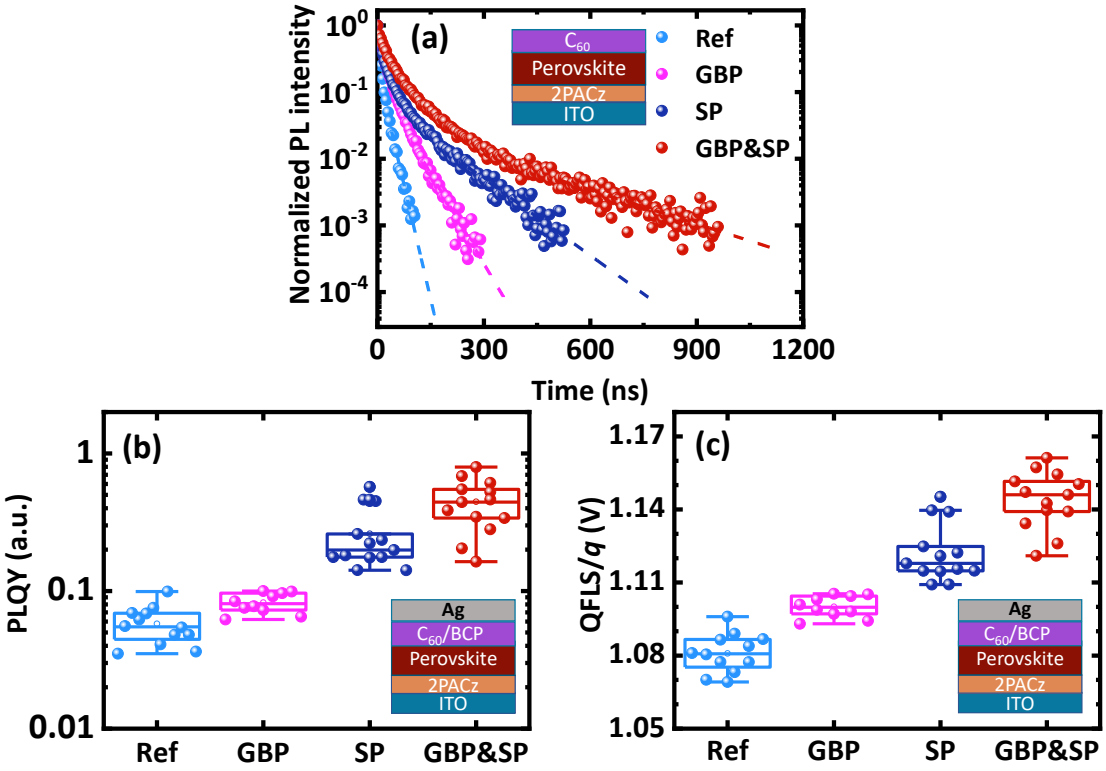

Figure 6-10: (a) Time-resolved photoluminescence (TRPL) of ITO/2PACz/Perovskite/C_{60} layer stack. (b) Photoluminescence quantum yield (PLQY) and (c) the quasi-Fermi level splitting/elementary charge (QFLS/q) of the perovskite solar cell without any modification (Ref), and with surface passivation (SP), grain boundary passivation (GBP) and grain boundary & surface passivation (GBP&SP) strategy. Adapted with permission from reference [228]. Copyright 2021, The Royal Society of Chemistry.

enhancement follows the same trend as V_{OC} (Figure 6-3b), indicating the effective suppression of non-radiative recombination. It should be noted that although it is a challenge to interpret such transients,[245] a longer monomolecular charge carrier lifetime (at low-level injection) can be ascribed to the reduction in non-radiative recombination within the bulk (and the grain boundaries) or at the perovskite/CTL interfaces.[233,245] In order to quantify the non-radiative recombination losses, the internal quasi-Fermi level splitting (QFLS) is calculated by measuring photoluminescence quantum yield (PLQY) according to the equation QFLS = $qV_{OC\text{-}rad}$ + k_BT ln(PLQY) as previously explained in Chapter 2. [153,246] In this regard, first, PLQY measurement is carried out for the half layer stack ITO/2PACz/perovskite without C_{60} to determine whether the non-radiative recombination at the HTL/perovskite side restricts the V_{OC} of our PSCs.[50,153,247] The average PLQY (Figure 6-11a) exhibits already a high value of ~7.2% for the Ref perovskite thin film, correlating to internal voltage (QFLS/q) of ~1.20 V. For GBP, SP and GBP&SP films, these values only rise slightly to ~7.9% (1.218 V), 9.8% (1.218 V) and 9.7% (1.225 V) (Figure 6-11b), respectively, which is above the V_{OC} values of full device stack obtained in this study (Figure 6-3a). This is in line with previous reports, where 2PACz/perovskite interface induces minimal non-radiative recombination losses, verifying that the V_{OC} of our PSCs is not limited by the HTL

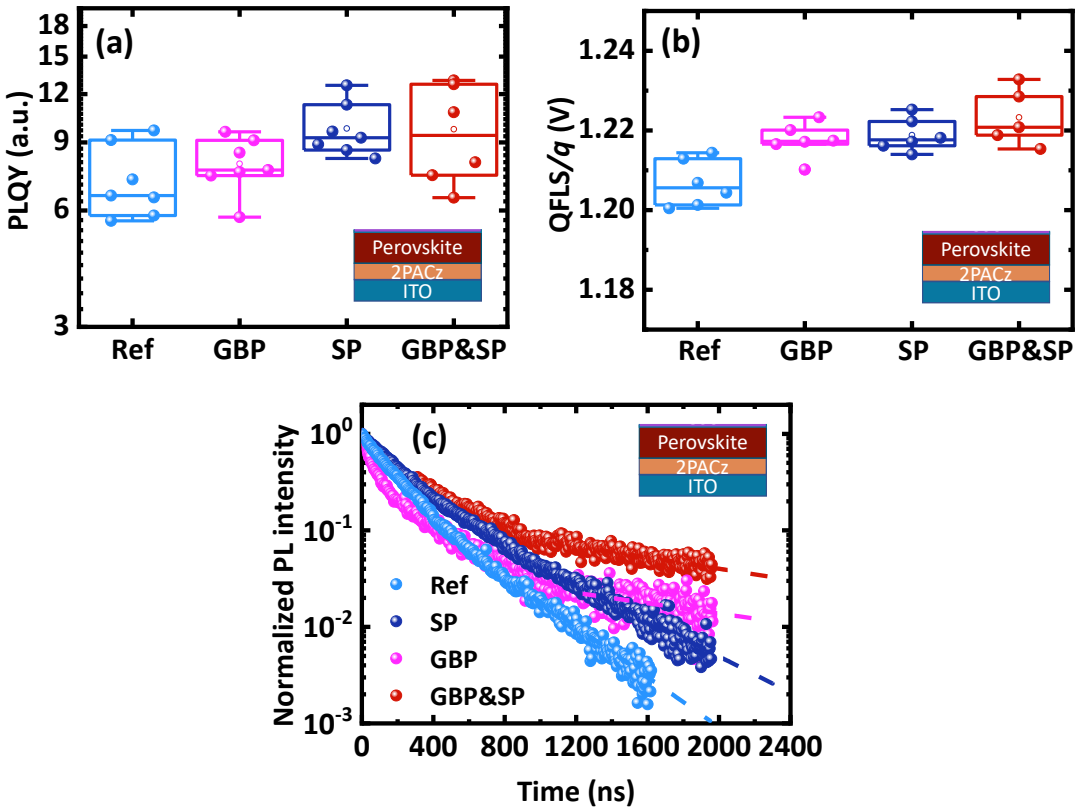

Figure 6-11: (a) Photoluminescence quantum yield (PLQY), (b) the quasi-Fermi level splitting/elementary charge (QFLS/*q*) and (c) time-resolved photoluminescence (TRPL) of the half layer stack ITO/2PACz/perovskite prepared without any modification (Ref), and with surface passivation (SP), grain boundary passivation (GBP) and grain boundary & surface passivation (GBP&SP) strategy. Adapted with permission from reference [228]. Copyright 2021, The Royal Society of Chemistry.

interface.[50,125] Nevertheless, as the obtained QFLS/*q* for the perovskite layer deposited on the half layer stack ITO/2PACz (Figure 6-11b) only slightly rises for all passivation strategies in comparison to the Ref films, the positive effect of each passivation strategy (either PEACl:$PbCl_2$ additive or PEACl post-treatment) on the device performance is not clear. To get a deep-going vision, we measure representative TPRL of the same layer stack (ITO/2PACz/perovskite) prepared for Ref, GBP, SP and GBP&SP films (Figure 6-11c). Interestingly, TPRL measurement reveals a longer monomolecular lifetime at low-level injection for GBP (1624), GBP&SP (1497 ns) and SP films (~464 ns). as compared to Ref perovskite films (335 ns). This longer lifetime of GBP film can be explained by the passivation of shallow grain boundary traps via the self-assembly of PEA^+ molecules and/or the formation of a PEACl-based 2D-RP phase as observed in the literature. [47,109,185,248–252] However, it should be noted that under 1-sun illumination these shallow traps are typically filled which could roughly clarify the reason for similar values obtained for PLQY and QFLS/*q* for all passivation strategies deposited on the ITO/2PACz substrate.[250,251,253]

Notably, for the complete device stack (ITO/2PACz/perovskite/C_{60}/BCP/Ag as shown in Figures 6-10b and c, the average PLQY exhibits a significant reduction to 0.058% for the Ref

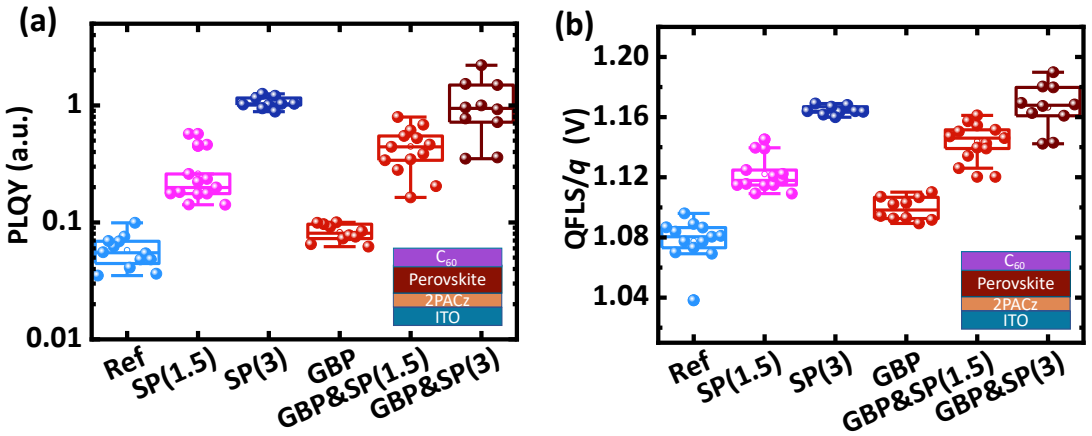

Figure 6-12: (a) Photoluminescence quantum yield (PLQY) and (b) the quasi-Fermi level splitting/elementary charge (QFLS/q) of the reference (Ref) and grain boundary passivated (GBP) perovskite treated with various concentrations of PEACl (1.5 and 3 mg/ml) (termed as: SP (1.5), SP(3), GBP&SP(1.5) and GBP&SP(1.5), respectively. These measurements were performed on half-layer stack ITO/2PACz/perovskite without C_{60}. Reproduced with permission from reference [228]. Copyright 2021, The Royal Society of Chemistry.

perovskite films, leading to a consequence of low QFLS/q ~1.081 V. This low value of QFLS/q upon deposition of C_{60} is clear evidence that imperfect perovskite/C_{60} interface dominates the photovoltage loss in the full device stack, as reported in the previous studies as well.[46,153] Strikingly, upon employing individual and dual passivation strategies, the PLQY increases one order of magnitude to 0.083%, 0.26% and 0.45% for GBP, SP and GBP&SP (Figure 6-10b). Accordingly, these PLQY values correspond to an increased QFLS/q of 1.100 V, 1.122 V and 1.144 V for GBP, SP and GBP&SP respectively (Figure 6-10c), showing a similar trend as the measured V_{OC} of the corresponding devices. This result vigorously indicates that to maximize the PLQY and lifetime in the PSC, the combination of both grain boundary and surface passivation strategy must be considered to minimize the non-radiative recombination losses. In case of PSC passivated by the higher concentration of PEACl (3mg/ml), a further enhancement in PLQY and QFLS/q values up to 2.3% and 1.19 V is observed (Figure 6-12), which is in line with the higher V_{OC} obtained for the respective devices (Figure 6-7e). Nevertheless, as discussed in Section 6-3, this enhancement does not compensate for the severe reduction in FF and J_{SC}.

To better understand the mechanism of the observed reduction in non-radiative recombination via passivation of the defects, the trap-state density (n_t) and charge carrier mobility (μ) of electrons and holes in the perovskite layer were measured. In this context, as previously discussed in Chapter 2, we sandwiched the perovskite layer between two ETL or HTL to fabricate electron-/or hole-only devices with the structure of ITO/SnO_2/Perovskite/C_{60}/BCP/Ag or ITO/2PACz/Perovskite/Spiro-MeOTAD/Ag. By measuring the dark J–V characteristics of devices according to the space charge-limited current (SCLC) method,[254] the electron mobility of 4.9×10^{-3} $cm^2V^{-1}s^{-1}$ is obtained for the Ref device, whereas a comparable enhancement to 6.3×10^{-3} and $7.2 \times 10^{-3}cm^2V^{-1}s^1$ is

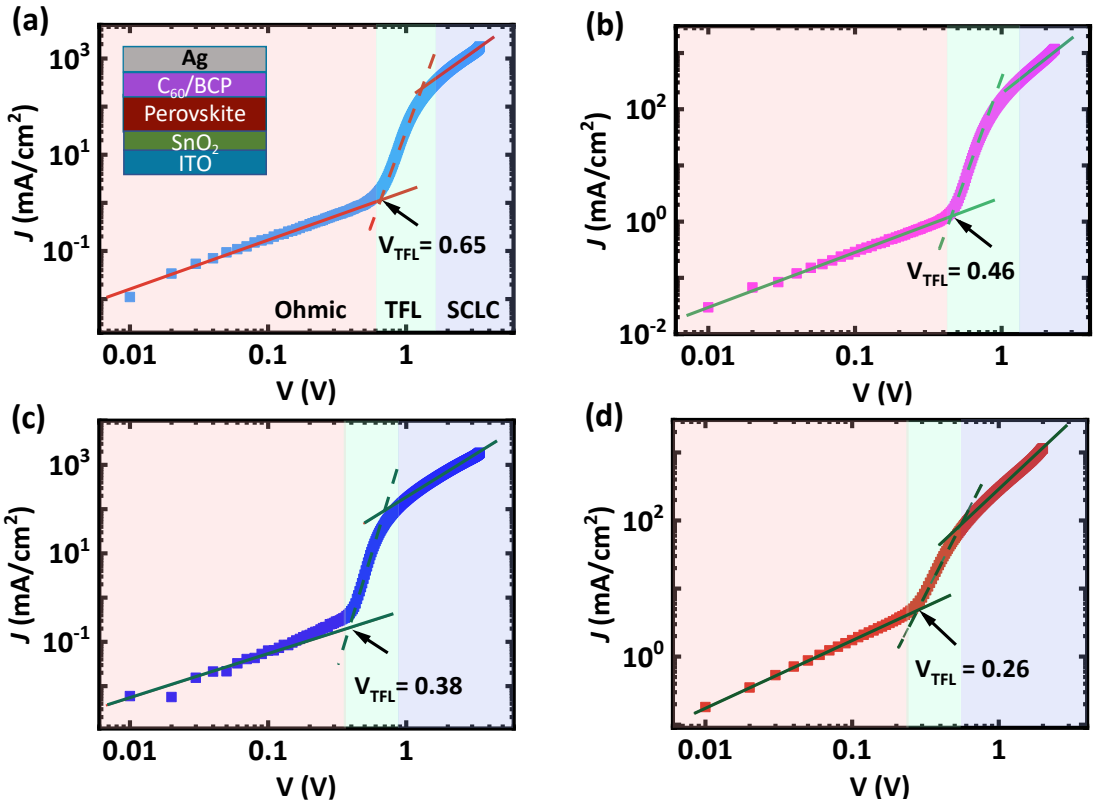

Figure 6-13: The dark *J–V* characteristics (log scale) of hole-only devices with an architecture of ITO/2PACz/Perovskite/Spiro-MeOTAD/Ag based on perovskite (a) without any modification (Ref) and with (b) grain boundary passivation (GBP), (c) surface passivation (SP), and (d) grain boundary & surface passivation (GBP&SP) films. The curve is divided into three distinct regimes: ohmic, trap-filled limit (TFL), and trap-free space charge-limited current (SCLC) regime. Adapted with permission from reference [228]. Copyright 2021, The Royal Society of Chemistry.

observed for both SP and GBP, respectively (Figure 6-13). For the GBP&SP device, this value further enhances to 10.0 × $10^{-3}$$cm^2V^{-1}s^{-1}$. Next to carrier mobility, the value of trap-filled limit voltage (V_{TFL}) exhibits a significant reduction in the order Ref → GBP → SP → GBP&SP

Table 6-2: The calculated electron/hole mobility along with respective electron/hole trap densities obtained from dark *J–V* characteristic of the electron-/hole-only devices based on the perovskite without any modification (Ref), and with grain boundary passivation (GBP), surface passivation (SP) and combination of grain boundary & surface passivation (GBP&SP) strategies.

Device	Electron mobility ($cm^2V^{-1}s^{-1}$)	Electron trap density (cm^{-3})	Hole mobility ($cm^2V^{-1}s^{-1}$)	Hole trap density (cm^{-3})
Ref	4.9×10^{-3}	9.2×10^{15}	4.0×10^{-3}	4.2×10^{15}
GBP	7.2×10^{-3}	6.5×10^{15}	6.2×10^{-3}	3.4×10^{15}
SP	6.3×10^{-3}	5.4×10^{15}	5.3×10^{-3}	3.0×10^{15}
GBP&SP	10.0×10^{-3}	3.7×10^{15}	7.9×10^{-3}	2.9×10^{15}

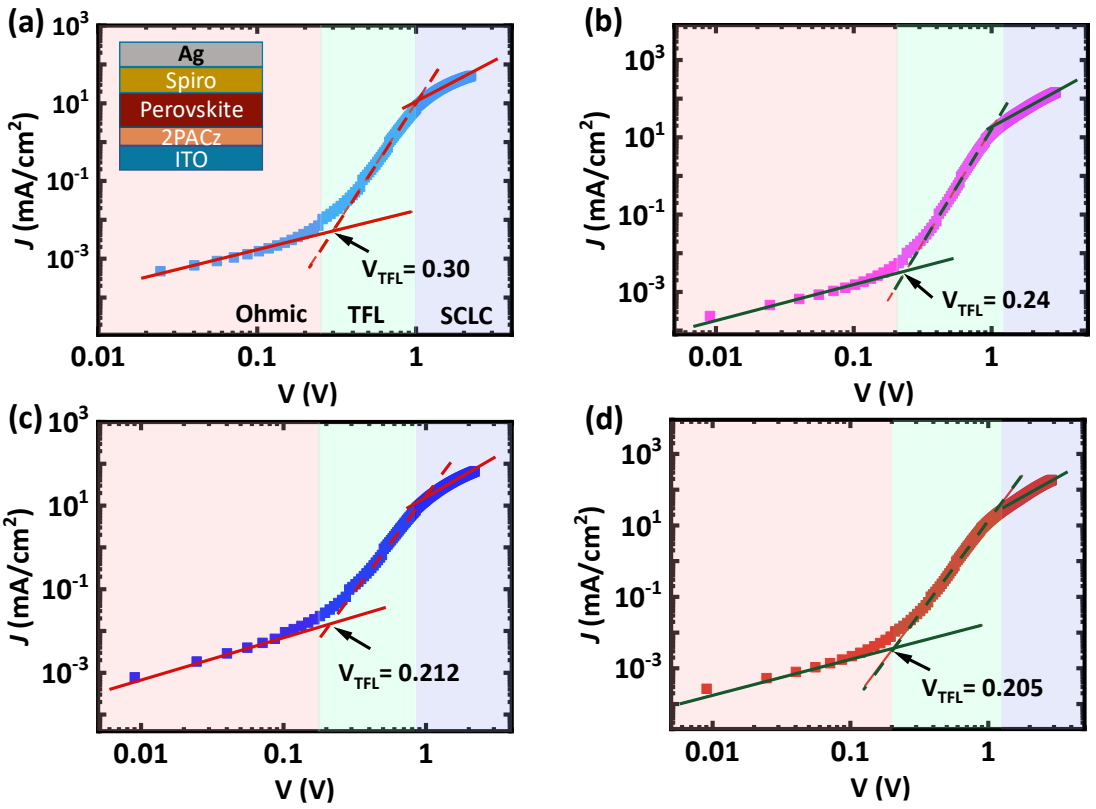

Figure 6-14: The dark *J–V* characteristics (log scale) of hole-only devices with a configuration of ITO/2PACz/Perovskite/Spiro-MeOTAD/Ag based on perovskite (a) without any modification (Ref) and with (b) grain boundary passivation (GBP), (c) surface passivation (SP), and (d) grain boundary & surface passivation (GBP&SP) films. The curve is divided into three distinct regimes: ohmic, trap-filled limit (TFL), and trap-free space charge-limited current (SCLC) regime. Adapted with permission from reference [228]. Copyright 2021, The Royal Society of Chemistry.

which according to equation 3-7 ($V_{TFL}= qn_tL^2/2\varepsilon\varepsilon_0$) discussed in Chapter 3 results in a decreased electron trap density from 9.2×10^{15} cm^{-3} to 6.5×10^{15}, 5.4×10^{15} and 3.7×10^{15} cm^{-3}, respectively (Table 6-2). The calculated hole mobility also follows a very similar trend as the electron mobility (Figure 6-14). Therefore, based on the TPRL and SCLC results together, we conclude that each passivation strategy either at the grain boundaries or surface of the perovskite film individually participates in enhancing the charge carriers lifetime and reducing the charge trap densities. Thereby, the combination of GBP and SP strategy (GBP&SP) leads to substantial enhancement in the photovoltaic performance of the devices.

Having identified that by measuring the ideality factor (n_{id}) we can establish a better understanding of the dominant type of recombination behaviors in our dual passivate devices as previously discussed in Chapter 3, in the next step, we measured intensity-dependent PLQY measurements. The n_{id} is extracted from the slope of calculated QFLS/q versus the logarithm of the illumination intensity data.[153] Figure 6-15a depicts the value of the n_{id} attained for all PSCs with complete layer stacks, exhibiting a significant decrease in

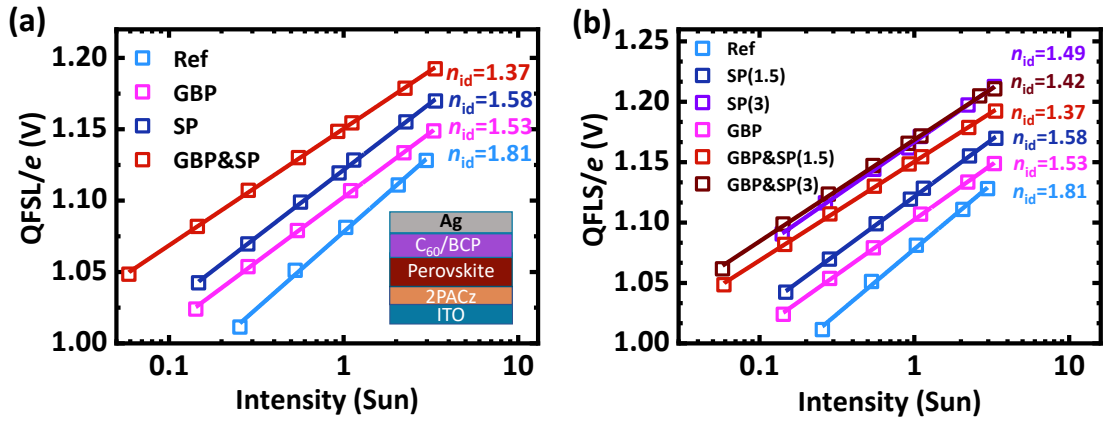

Figure 6-15: Ideality factor (n_{id}) of (a) perovskite solar cell (PSCs) prepared without any modification (Ref) and with surface passivation (SP), grain boundary passivation (GBP) and grain boundary & surface passivation (GBP&SP) strategy determined from the slope of a logarithmic fit to the intensity-dependent QFLS/q. (b) Ref and GBP based PSCs treated with various concentration of PEACl (1.5 and 3 mg/ml) (termed as: SP(1.5) and SP(3)) respectively.

n_{id} of the GBP&SP films to 1.3 compared to GBP (n_{id}~1.48), SP (n_{id}~1.60), and Ref (n_{id}~1.71) perovskite films, respectively. This reduction of n_{id} towards the value of 1 for high-performing GBP&SP PSC demonstrates a predominant radiative bimolecular and decreased trap-assisted Shockley–Read Hall recombination, as evidenced by the reduced trap-state density obtained from SCLC measurement (Figures 6-13 and 6-14) resulting in high V_{OC}. Moreover, there is a direct correlation between the reduced n_{id} and high FF value.[153,159,181,255] Besides, we find that the value of n_{id} for SP and GBP&SP devices treated with higher concentrations of PEACl (3 mg/ml) increases to 1.49 and 1.42 (Figure 6-15b), respectively. This reveals that despite the highest V_{OC} of 1.17 and 1.18 V obtained for the corresponding devices (Figure 6-7), formation of too thick passivation layers increases the possibility of charge carrier recombination, thus leading to low FF.

In brief, our findings based on TPRL and PLQY demonstrate that the V_{OC} of our PSC is mainly limited by the perovskite/C_{60} interface and (ii) that grain boundary passivation becomes specifically crucial in the case where the perovskite/CTL interfaces are already well passivated. Therefore, our results highlight that dual passivation is a critical requirement in order to reach simultaneously high FF and V_{OC} by the reduction in both non-radiative recombination losses and the n_{id}.

6.5. Material characterization

In this section, in order to provide further insights into how both individual and dual passivation strategies modify the morphology, structure and surface composition of the perovskite films, SEM, XRD, CL, XPS, UPS and KPFM measurements were performed.

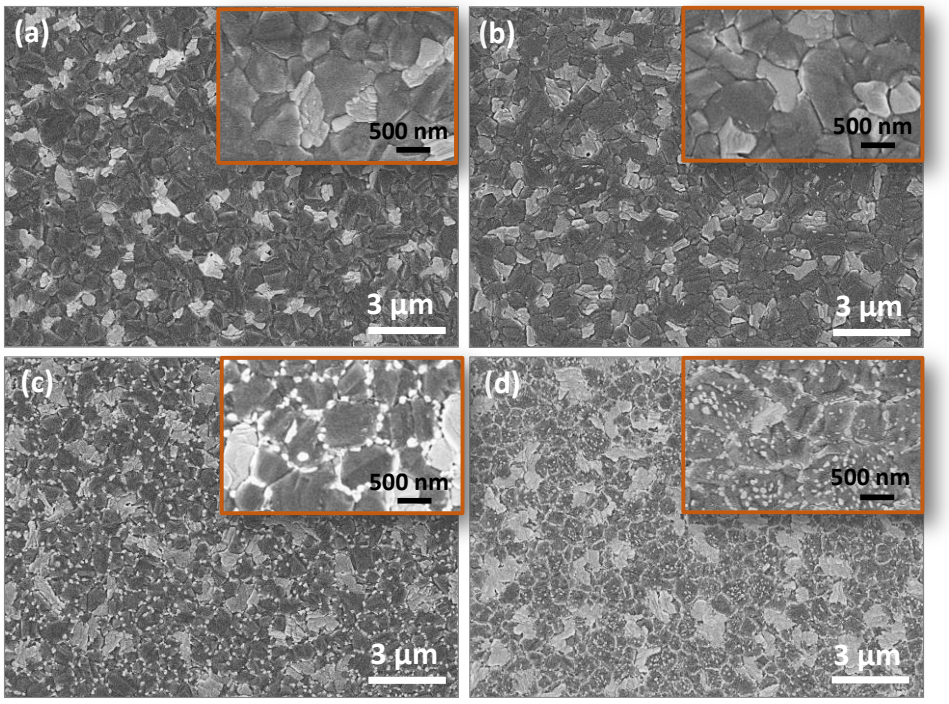

Figure 6-16: Top-view scanning electron microscopy (SEM) images of perovskite films prepare (a) without any modification (Ref) and with (b) surface passivation (SP) (c) grain boundary passivation (GBP), and (d) grain boundary & surface passivation (GBP&SP) strategies. The inset is a high-magnification image of the respective images. Reproduced with permission from reference [228]. Copyright 2021, The Royal Society of Chemistry.

6.5.1. Thin-film morphology

As revealed by top-view SEM images in Figures 6-16a and b, no noticeable change in surface morphology and grain sizes for both Ref and SP perovskite films is observed, which is similar to our previous observation in Chapters 4 and 5 with low-concentration of the 2D-RP layer. In contrast, the surface treatment with higher concentration of PEACl (3 mg/ml) demonstrates multiple grains stacking on each other (Figure 6-17).[256–258] Furthermore, brighter grains are also observed on the surface of both Ref and SP films which later we will

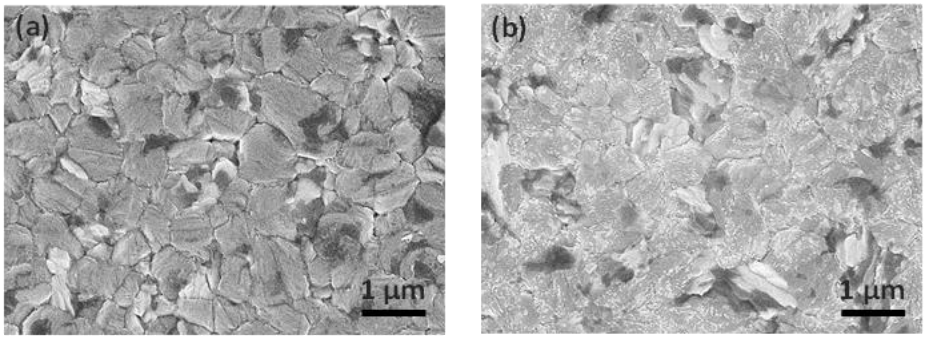

Figure 6-17: Top-view scanning electron microscopy (SEM) images of the perovskite film treated with a high-concentration of PEACl (3 mg/ml) on top of the (a) reference (Ref) and (b) grain boundary passivation (GBP) perovskite layers.

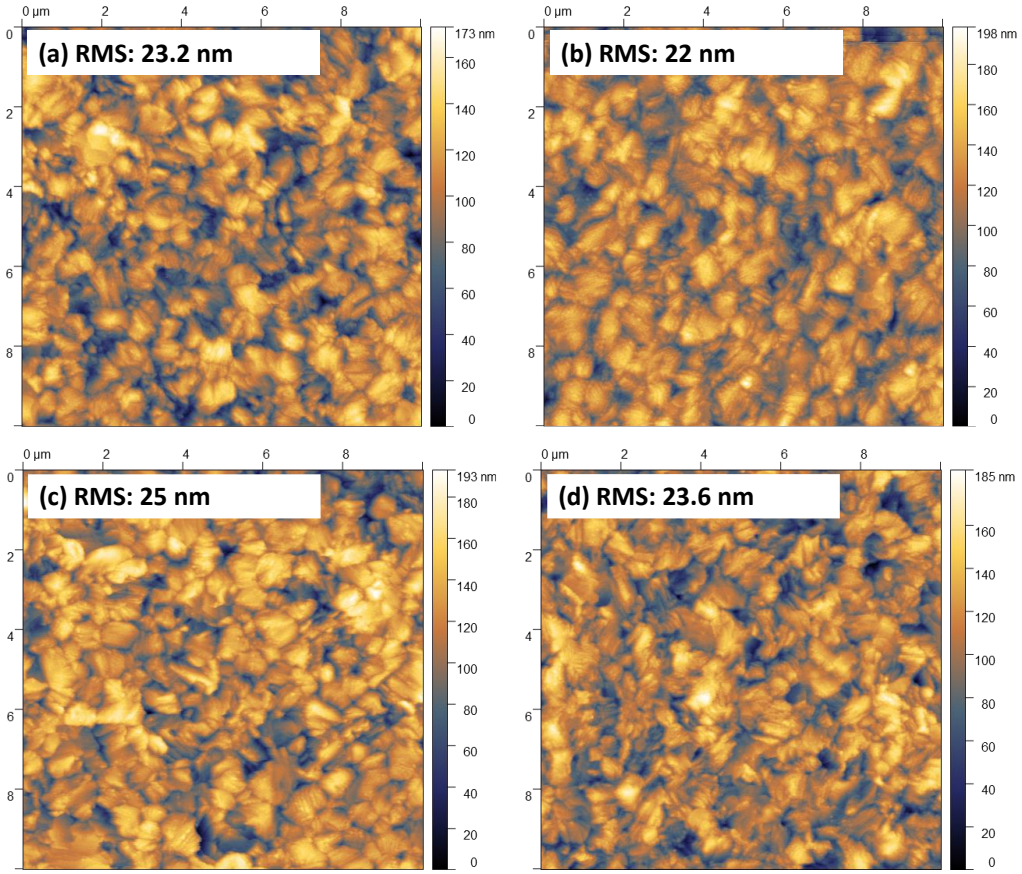

Figure 6-18: Atomic force microscopy (AFM) images of perovskite films prepared (a) without any modification (Ref) and with (b) surface passivation (SP) (c) grain boundary passivation (GBP), and (d) grain boundary & surface passivation (GBP&SP) strategy. The surface roughness of each perovskite film is determined by the root-mean-square (RMS) value.

show that it is related to PbI_2 crystallites. Upon incorporating PEACl:$PbCl_2$ additive into the bulk, similar perovskite grains size as the Ref and SP films are observed (Figure 6-16c). However, the size and amount of the bright grains related to PbI_2-rich grains slightly grow. Intriguingly, for GBB film notable small bright grains (smaller than bright PbI_2-rich grains) also start to appear located close to the grain boundaries, providing us a clue that additive incorporation mainly passivates the regions near the grain boundaries. For the GBP&SP film, these small bright crystallites even become smaller and much more dispersed with a plate-like appearance all over the surface (Figure 6-16d). This intimates that some reaction could happen with these crystallites upon deposition of PEACl on top of GBP films. We further characterized the roughness of the corresponding perovskite films by atomic force microscopy (AFM) measurement (Figure 6-18). The root-mean-squared (RMS) roughness of the Ref, SP, GBP and GBP&SP perovskite films is found to be 23.2, 22, 25 and 23.6 nm, respectively, demonstrating that PEACl preferably fills regions near the grain boundaries.[93,95]

To develop a better understanding of the different phases and chemical composition related to the observed small and large bright grains on the surface of the perovskite layer,

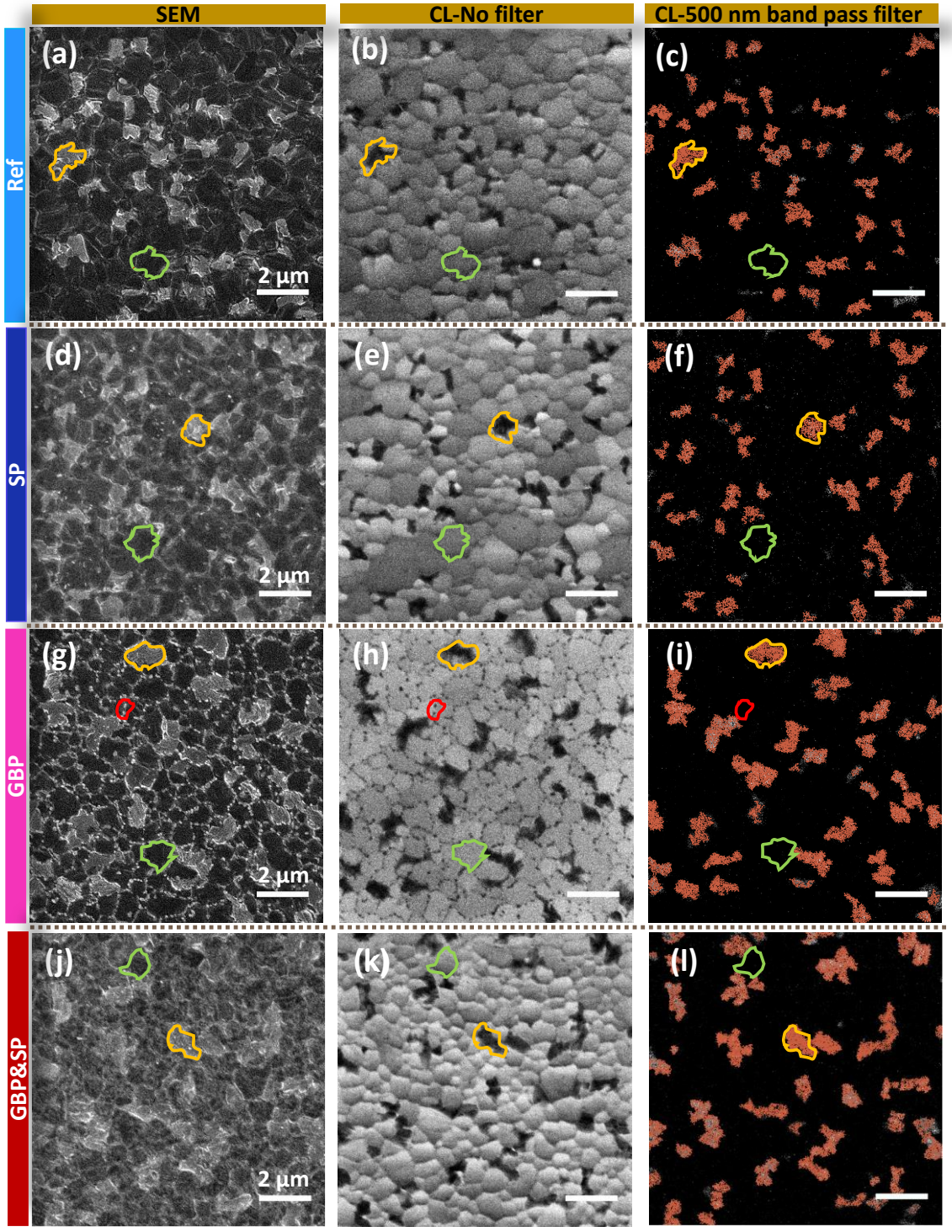

Figure 6-19: Scanning electron microscopy (SEM) and cathodoluminescence (CL) images recorded without and with bandpass filter (500 ± 40 nm) from perovskite film prepared (a–c) without any modification (Ref), (d–f) with surface passivation (SP), (g–i) grain boundary passivation (GBP) and (j–l) grain boundary & surface passivation (GBP&SP), respectively. The green encircled grains represent the expected 3D perovskite phase with a bandgap of 1.57 eV. The yellow encircled grains are attributed to PbI_2-rich crystallites. The small red encircled grains appear close to the grain boundaries for GBP films. Reproduced with permission from reference [228]. Copyright 2021, The Royal Society of Chemistry.

CL measurement was conducted in the following. Figure 6-19 presents the SEM images of

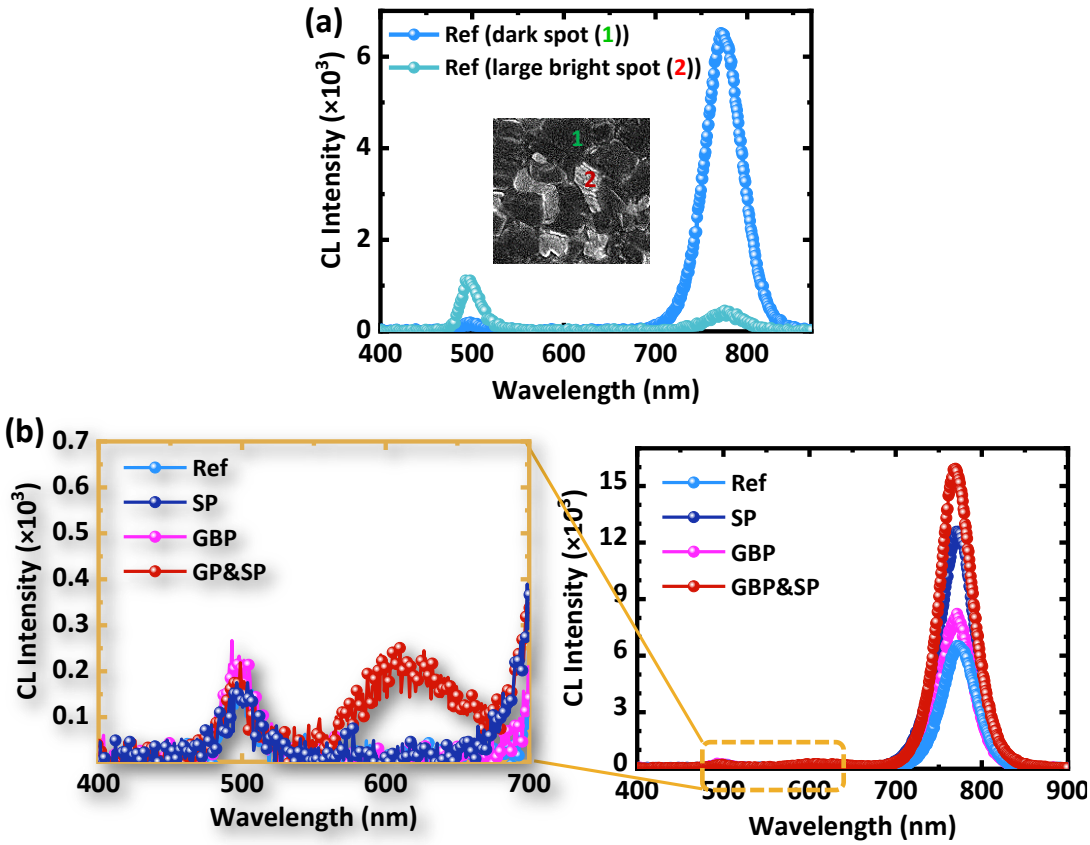

Figure 6-20: Cathodoluminescence (CL) spectra of (a) the reference perovskite film recorded from the dark (1) and bright (2) spots in SEM image (insert). (b) CL spectra of perovskite films prepared without any modification (Ref) and with surface passivation (SP), grain boundary passivation (GBP), and grain boundary & surface passivation (GBP&SP). The left panel is a zoom-in view of the same CL spectra in the wavelength region between 400 to 700 nm. Reproduced with permission from reference [228]. Copyright 2021, The Royal Society of Chemistry.

Ref and all three passivated perovskite films together with the resultant CL images (captured from the same SEM images) without and with a 500 nm long-pass filter. From the CL image in Figure 6-19b, two different CL intensities are observed for the Ref sample. (1) Higher intensity originating from the dark grains in the SEM image (marked by a green circle in Figure 6-19a) and (2) lower intensity originating from the bright grains (marked by a yellow circle in Figure 6-19a). As shown in CL spectra in Figure 6-20a, these dark and bright spots demonstrate CL peaks located at 774 nm and 500 nm that correspond to the optical bandgap of the 3D perovskite phase and PbI_2-crystallites, respectively. Importantly, when we apply 500 nm ± 40 nm bandpass filter, the grains related to 3D perovskite are filtered and only those with low-intensity CL are detectable in Figure 6-19c. This provides us clear evidence that the large bright grain observed in the top-view SEM of all perovskite films (Figure 6-16) is indeed attributed to PbI_2-rich crystallites, as reported in other studies as well.[259,260] For the SP sample, we do not observe any noticeable change in CL images (Figures 6-19d and e) compared to the Ref film. Nevertheless, the SEM image is slightly charging, possibly due to the formation of the 2D-RP phase with insulating nature. Besides,

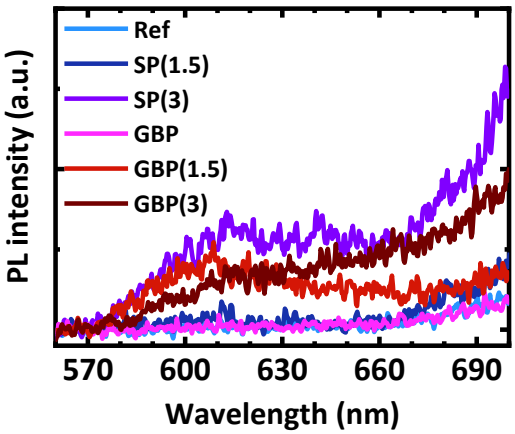

Figure 6-21: Steady-state photoluminescence (PL) of the Reference (Ref) and grain boundary passivation (GBP) perovskite films treated with various PEACl concentrations (termed as: SP(1.5), SP(3), GBP&SP(1.5), GBP&SP(3) in the low-wavelength range (560-700 nm).

the CL emission peak is notably higher compared to the Ref film (Figure 6-20b). Interestingly, for the GBP film, the small bright grains located close to grain boundaries in SEM images (Figures 6-16c and 6-19g) also demonstrate lower CL intensity (similar to PbI_2-rich crystallites), appearing as dark spots around the perovskite grains in CL image in Figure 6-19h (marked by a red circle). However, it is important to note that by applying 500 nm ± 40 nm bandpass filter the signal or features related to these small grains entirely disappear (Figure 6-19i) which is contrary to PbI_2-rich grains. As a result, we conclude that these small grains are not correlated to PbI_2 or $PbCl_2$, but rather to the formation of the 2D close to the grain boundaries. Eventually, for GBP&SP film these small grains become much less visible in the SEM image (Figure 3j) and are no longer trackable in both CL images either without or with the bandpass filter (Figure 6-19k and l). The distinct point of the CL image captured for the GBP&SP compared to Ref, GBP and SP perovskite films is the highest CL signal observed all over the surface, as further confirmed by the CL spectrum (Figure 6-20b). This high CL intensity is a result of combining the passivation effect both in the grain boundary and at the surface of the perovskite layer,[261] which is also in line with a result of combining the passivation effect both in the grain boundary and at the surface of the perovskite layer, [261] which is also in line with the PLQY and TPRL results. Furthermore, an additional CL peak located at a low wavelength of 620 nm is detected for GBP&SP perovskite film, which does not correlate to either the 3D perovskite or the PbI_2-rich phase. A similar peak is also observed in the PL spectrum for both Ref and GBP films treated with higher concertation of PEACl (3 mg/ml) (Figure 6-21). This is attributed to the formation of ultrathin 2D-RP $(PEA)_2(Cs_yFA_{1-y})_{n-1}Pb_n(I_{1-x}Cl_x)_{3n+1}$ phase upon PEACl surface treatment, as will be discussed in the following.[196,262]

We further explored the crystalline properties of the films by performing XRD measurements in order to confirm the presence of the 2D-RP layer by employing our passivation strategies. As revealed in Figure 6-22a, the expected characteristic peaks at 2θ

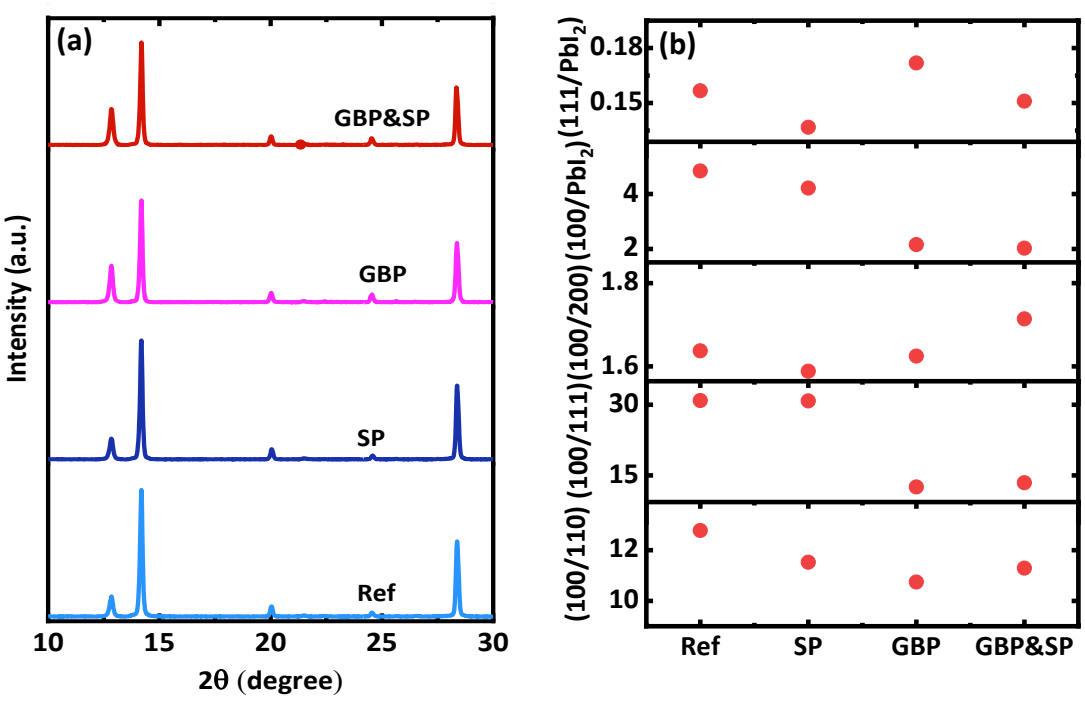

Figure 6-22: (a) X-ray diffraction (XRD) pattern of perovskite films prepared without any modification (Ref) and with surface passivation (SP), grain boundary passivation (GBP), and grain boundary & surface passivation (GBP&SP) strategy. (b) Calculated intensity ratios of the various crystal planes.

~14.21, 20.11, 24.61 and 28.41 corresponding to (100), (110), (111) and (200) diffraction planes of the 3D cubic α-$Cs_{0.18}FA_{0.82}PbI_3$ phase are observed for all perovskite films,[47,165,263] along with a small peak at ~12.9 assigned to PbI_2. Comparing the XRD pattern of the Ref and SP films, no profound change in the position, intensity or full width at half maximum (FWHM) of the peaks is found, which is very similar to our previous observation by using the n-BABr surface treatment discussed in Chapter 4.[182] Besides, a small decrease in the ratio of (100) to (111) peak is seen compared to Ref and SP films, which suggests the less (100) preferential orientation of the perovskite grains (Figure 6-22b).[47,98] The GBP&SP film

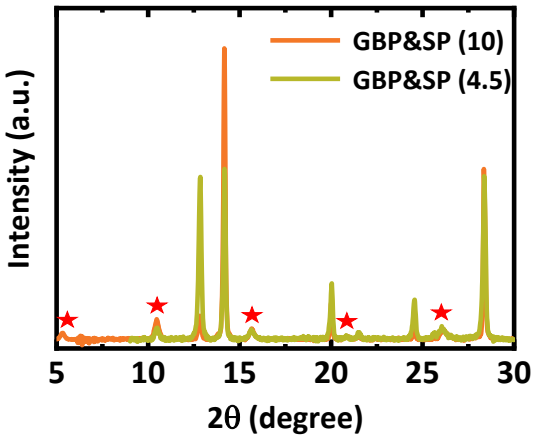

Figure 6-23: XRD patterns of grain boundary & surface passivation (GBP&SP) perovskite film using high concentration PEACl (4.5 and 10 mg/ml) as a surface treatment. The red stars illustrate the diffraction peaks related to pure (n = 1) 2D Ruddlesden-Popper $(PEA)_2Pb(I_{1-y}Cl_y)_4$ phase.

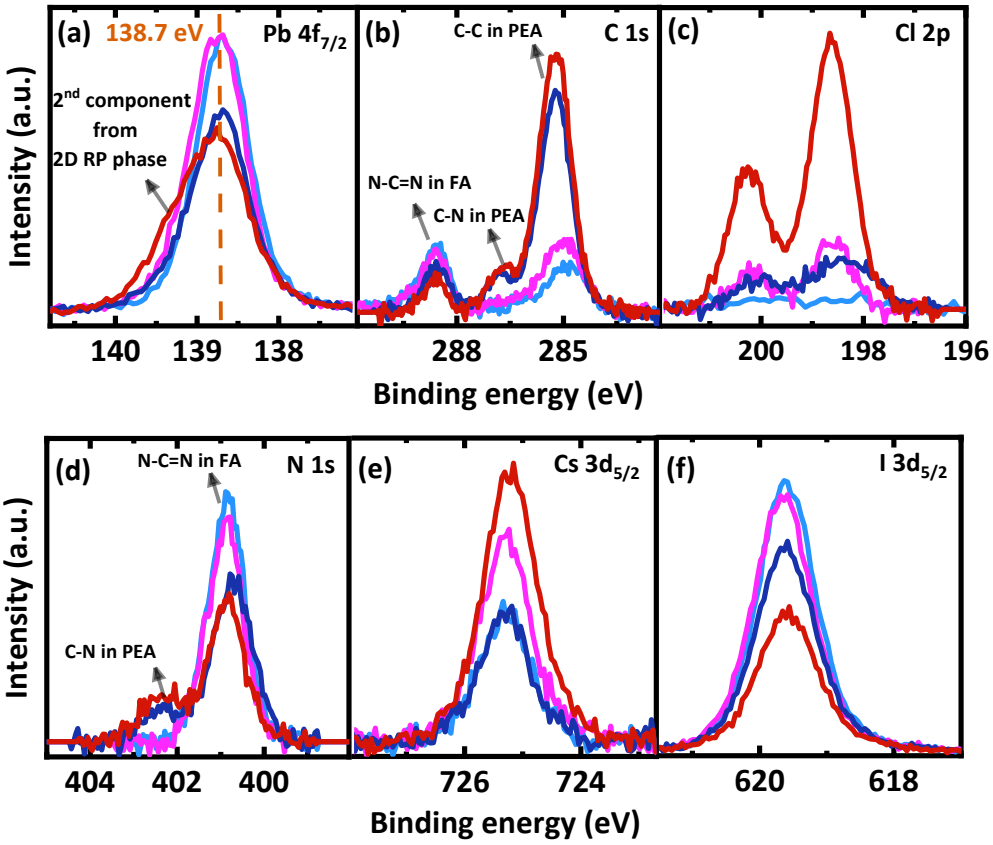

Figure 6-24: X-ray photoelectron spectroscopy (XPS) spectra of (a) Pb $4f_{7/2}$, (b) C 1s, and (c) Cl 2p, (d) N 1s, (e) Cs $3d_{5/2}$ and (f) I $3d_{5/2}$ core levels for perovskite prepared without any modification (Ref), with surface passivation (SP), grain boundary passivation (GBP), and grain boundary & surface passivation (GBP&SP) processes. The perovskite is deposited on the ITO/2PACz substrates. Adapted with permission from reference [228]. Copyright 2021, The Royal Society of Chemistry.

also follows the identical tendency, showing no noticeable change in the XRD pattern as compared to GBP films. It should be noted that for the SP and GBP&SP films the XRD diffraction pattern correlated to the 2D-RP phase is not visible. The possible explanation could be due to the formation of the ultrathin or non-crystalline PEA-based passivation layer which can not be detected by XRD measurement.[182,264–266] Nevertheless, with increasing PEACl concentration to 4.5 or 10 mg/ml, the expected peaks related to 2D-RP appear at ~5.3°, 10.5°, 15.7°, 20.9°, 26.1° and 31.8°. These can be attributed to a formation of pure 2D-RP (n = 1) $(PEA)_2Pb(I_{1-x}Cl_x)_4$ phase at the surface of the perovskite (Figure 6-23).[267–271]

6.5.2. Surface elemental distribution and electronic structure

To gain more detail on the chemical composition at the surface of the perovskite layer upon dual passivation strategy, XPS measurement was analyzed to confirm the presence of the PEACl passivation material. As displayed in XPS core-level spectra in Figure 6-24, the characteristic peaks related to Pb $4f_{7/2}$, C 1s from FA's N–C=N bonding, N 1s, Cs $3d_{5/2}$ and I $3d_{5/2}$ elements with binding energies of ~138.7 eV, 288.6 eV, 400.8 eV, 725.3 eV and 619.6

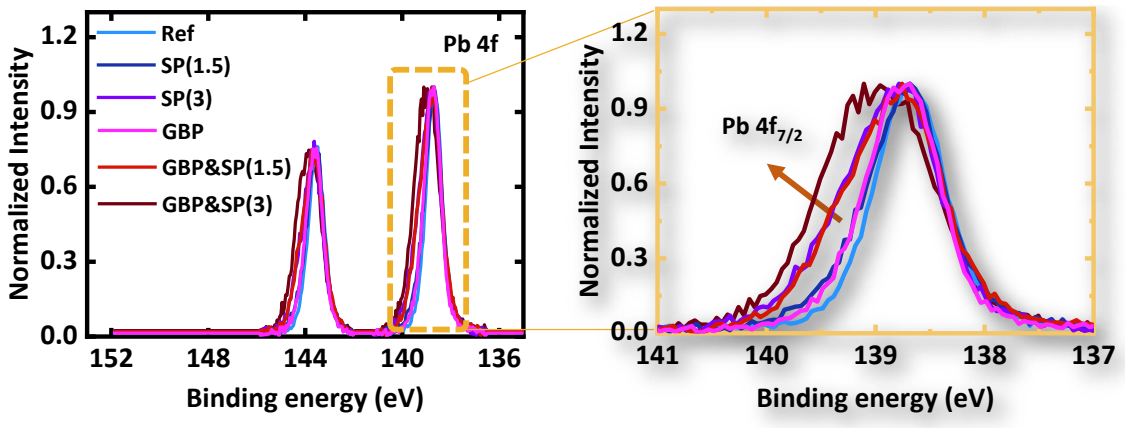

Figure 6-25: Normalized X-ray photoelectron spectroscopy (XPS) spectra related to Pb 4f spectrum (same data as in Figure 6-24a) recorded for reference (Ref) and grain boundary passivation (GBP) perovskite films treated with various concentration (1.5 and 3 mg/ml) of PEACl (termed as: SP (1.5), SP (3) and GBP&SP (1.5), GBP&SP(3)) (left). The right panel shows a zoomed-in view of Pb $4f_{7/2}$ peak. Reproduced with permission from reference [228]. Copyright 2021, The Royal Society of Chemistry.

eV, respectively, is observed from XPS survey of Ref perovskite film with the composition of $Cs_{0.18}FA_{0.82}PbI_3$.[272] Besides, the spectrum shows an additional C 1s peak (~288.8 eV) originating from adventitious carbon (sp3 C–C bonding) at the film surface.[260,273] By comparing the XPS spectra of the Ref perovskite film with either individual (SP and/or GBP) or dual passivated samples (GBP&SP) three major differences can be distinguished. (1) For the GBP film a slight shift to the higher binding energies in the Pb $4f_{7/2}$ spectrum and an increase in FWHM is identified, whereas the intensity of this peak at the binding energy of ~138.7 is considerably reduced for SP and GBP&SP films (Figure 6-24a). Meanwhile, for GBP&SP films, the relevant peaks become even broader and asymmetric shifting to the high-energy side. (2) In the XPS spectra of C 1s signal for SP and GBP&SP films, two new notable peaks at the binding energy of ~285.2 eV and 286.7 eV appear which can be assigned to C 1s emission from PEA (C–C and C–N bonds), respectively (Figure 6-24b). The same peaks but with very low intensity are also detected for GBP film. (3) All three passivated films demonstrate a Cl 2p line at ~198.6 eV (Cl $2p_{3/2}$) and 200.2 eV (Cl $2p_{1/2}$) which is more intensive in case of GBP&SP film (Figure 6-24c). Notably, when the concentration of surface passivation solution (PEACl in IPA) increases to 3 mg/ml, the difference becomes even stronger for the Pb 4f core levels compared to Ref film (Figure 6-25). It should be noted that the peak position or shape of the I $3d_{5/2}$ and Cs $3d_{5/2}$ core levels does not change (Figures 6-24 4 and f), which excludes the probability that the shift arises from the electronic doping of the perovskite bulk.[273–276] Thereby, we correlated all observations of damping signal at the binding energy of ~138.7 eV for SP and GBP&SP films, emerging of a second Pb component (at ~139.1 eV) as well as a Cl 2p (at ~198.2 and 200.2 eV) and PEA signal (at ~285.2 and 286.6) to the formation of an ultrathin PEACl-based passivation layer on the surface of the perovskite films.[95,192,277,278] In brief, our XPS and XRD results together with the observation of a PL signal at 620 nm evidently verify the formation of 2D-RP $(PEA)_2(Cs_yFA_{1-y})_{n-1}Pb_n(I_{1-x}Cl_x)_{3n+1}$ for dual passivated perovskite film.

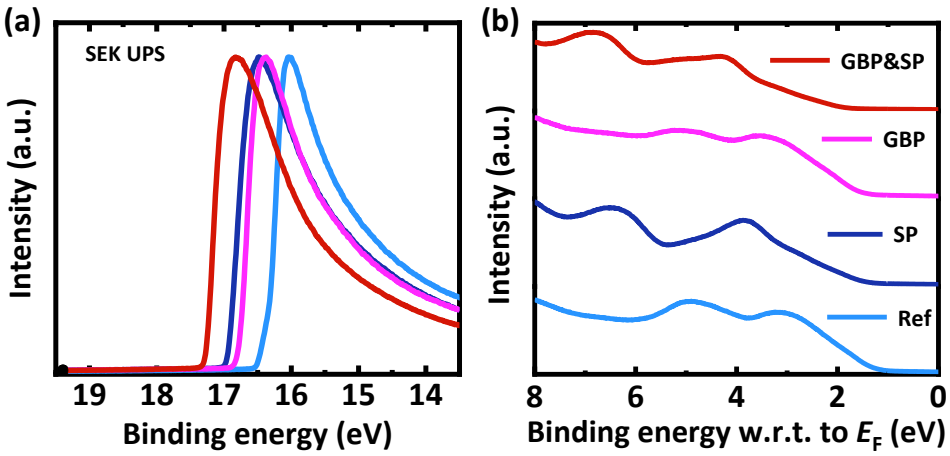

Figure 6-26: (a) Secondary electron cut-off spectra obtained from ultraviolet photoelectron spectroscopy (UPS) for perovskite solar cells without any modification (Ref) and with surface passivation (SP), grain boundary passivation (GBP), and grain boundary & surface passivation (GBP&SP) to determine the work function of the perovskite films. (b) Respective spectra of the region close to the valence band onset.

In the following analysis, UPS measurement was conducted in order to determine the effect of the thin 2D-RP surface layer on the electronic structure of the perovskite films. Derived from the secondary electron cut-off and valence band spectra (Figure 6-26), we plot the energy band diagram for each film as schematically illustrated in Figure 6-27. For the Ref film, a work function (WF) and an ionization potential (IP) of 4.68 eV and 5.1 eV are

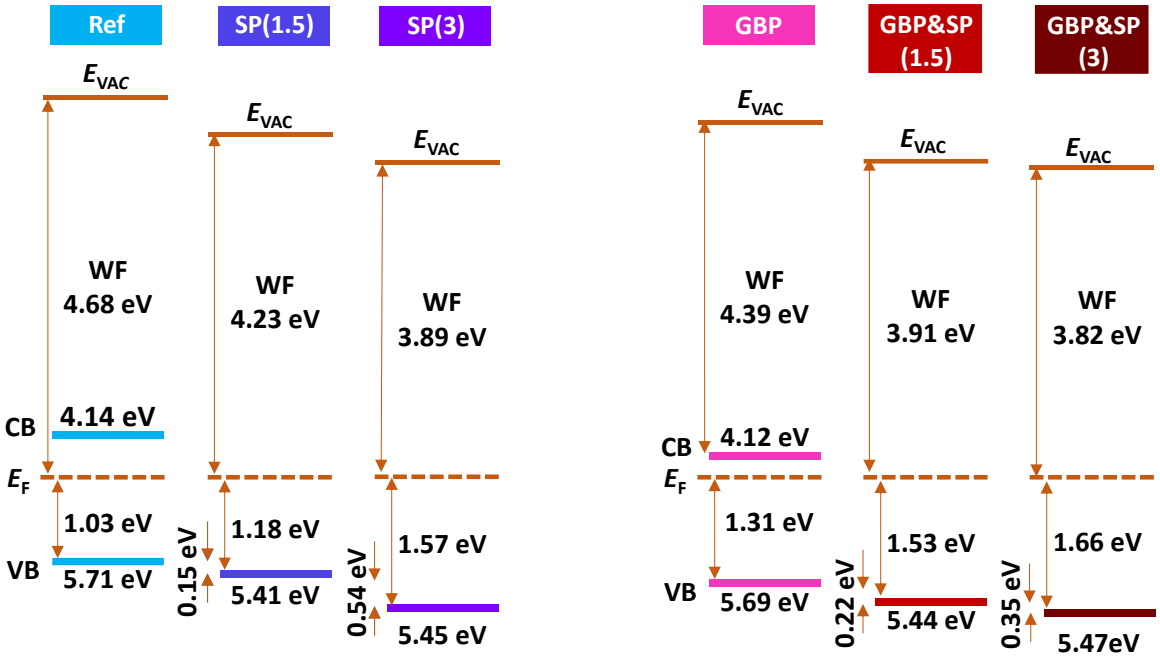

Figure 6-27: Proposed energy band diagrams derived from ultraviolet photoelectron spectroscopy (UPS) measurements for reference (Ref) and grain boundary passivated perovskite films treated with various concentrations of PEACl concentration (1.5 and 3 mg/ml). E_F, E_{vac}, CB and VB demonstrate the Fermi level, vacuum level, conduction band and valence band, respectively. The CB position of the 3D perovskite was determined from the corresponding optical bandgap.

observed, respectively. This represents slightly n-type perovskite film as reported in previous studies.[47,212,237,273,279] With only the GBP strategy, the IP value remains nearly constant at 5.69 eV whereas the WF substantially declines to 4.39 eV. This is an indication of more n-type perovskite which could possibly originate from a reduced electron trap density as observed in our SCLC results or a different surface termination.[47,237,279–281] The WF is further reduced to 4.23 eV and 3.91 eV for SP and GBP&SP films, respectively. A similar reduction in IP to 4.23 eV and 3.91 eV is also observed for both samples. We correlate this reduction to the formation of the wide-bandgap ultrathin 2D-RP phase on the surface of the perovskite with different chemical environments as previously demonstrated by PL, CL and XPS results. This is further verified by measuring the UPS of the SP and GBP&SP films prepared with higher concentration of PEACl (3 mg/ml) (Figure 6-27). For this case, a similar IP value of 5.45 eV and 5.47 eV is observed for SP and GBP&SP films, respectively, while WF further decreases to 3.89 eV and 3.82 eV, which represents a valence band (VB) onset of 1.57 eV and 1.66 eV. Furthermore, the surface passivation also modifies the shape of the VB density states for all passivated perovskite films compared to the Ref sample (Figure 6-26 b), indicating that the electronic properties of the 2D-RP surface layer are different compared to the 3D bulk perovskite.[282] Thus, based on the UPS result we conjecture that in addition to the expected chemical passivation,[121] the increased distance between the VB to the Fermi level leads to the formation of a thin hole blocking layer at the interface between the perovskite and C_{60} layer. This ultrathin hole blocking layer hinders the possible recombination of the holes with electrons at this interface, [47,82,121,283,284] while electrons can still effectively tunnel through the perovskite layer into C_{60}. Thereby, effective charge carrier extraction occurs in the devices that yields a very high FF [47,284–286]. In terms of higher PEACl concentration (3 mg/ml), the formation of the thicker tunneling layer notably reduces the probability of transporting electrons from perovskite to C_{60}, thus, resulting in a lower FF and consequently poor PCE (Figure 6-7).

So far, our results demonstrate that employing the dual passivation strategy results in the reduction of non-radiative recombination particularly at the interface between the perovskite and C_{60} layer as well as at the grain boundaries. To figure out in detail whether the PEACl:$PbCl_2$ additive passivates mainly defects in the grain interior and/or at the grain boundaries and how uniform the surface passivation is formed for each strategy, we used frequency-modulated KPFM (FM-KPFM).[287] This is a technique that provides direct information on the WF of the surface by measuring the local contact potential difference (CPD) between a metallic tip and the sample surface.[288,289] In this regard, we investigate the effect of passivation on the CPD distribution of ITO/2PACz/perovskite/C_{60} layer stacks and establish particularly the main focus on mapping of grain boundaries and PbI_2-rich grains (Figure 6-28). As depicted in Figure 6-28a, a quite uniform CPD of - 430 ± 40 mV is observed for the Ref film which contains darker grains with ∼110–230 mV lower CPD than bright grains. These dark regions correspond to the PbI_2-rich grains as their size and distribution at the surface are in line with SEM and CL observations (Figure 6-19). Note that

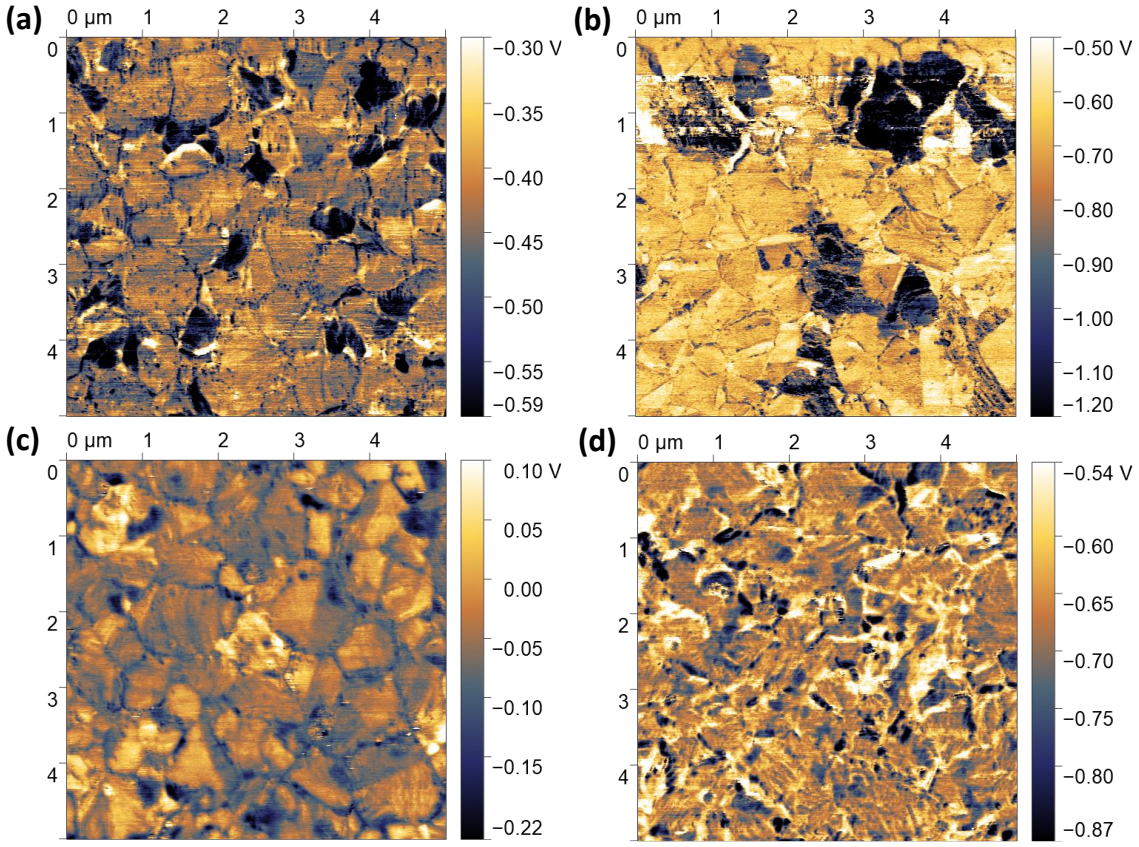

Figure 6-28: Kelvin probe force microscopy (KPFM) images of the ITO/2PACz/perovskite/C_{60} layer stack based on perovskite (a) without any modification (Ref), (b) with grain boundary passivation (GBP), (c) surface passivation (SP), and (d) grain boundary & surface passivation (GBP&SP) strategy. Reproduced with permission from reference [228]. Copyright 2021, The Royal Society of Chemistry.

here the CPD contrast is negative which could be due to the higher WF of PbI_2-rich grains compared to the 3D perovskite which arises from p-type characteristics and wider bandgap of PbI_2,[290–293] as observed in previous reports as well.[294,295] The same trend is observed in CPD contrast for the GBP film, where the uniform perovskite grains and dark regions exhibit a CPD of ∼-700 ± 120 and -1300 ± 120 mV, respectively (Figure 6-28b). It is worthwhile to mention that the value of CPD always relies on tip conditions and the environment that could be potentially affected by contamination during the measurement. Thus, we can not obtain an absolute value but a relative WF. This could explain the overall lower absolute CPD in the GBP films. Thereby, we estimate the relative difference between the CPD value of the bright 3D perovskite and dark PbI_2-rich grains, *i.e.* $\Delta CPD_{3D\text{-}PbI2}$ ($CPD_{3D\text{-}grains}$–$CPD_{PbI2\text{-}grains}$) and achieve a $\Delta CPD_{3D\text{-}PbI2}$ of ∼170 mV and ∼600 mV for Ref and GBP samples, respectively, which can be observed from the scales in Figure 6-30a and b. This 430 mV difference between $\Delta CPD_{3D\text{-}PbI2}$ of both samples is comparable with the reduced WF that was obtained from UPS measurement for GBP film compared to Ref (Figure 6-26). This indicates that additive incorporation mainly decreases the WF of the 3D perovskite grains, whereas the PbI_2-rich grains are not changed by this strategy. Similarly, to figure out the

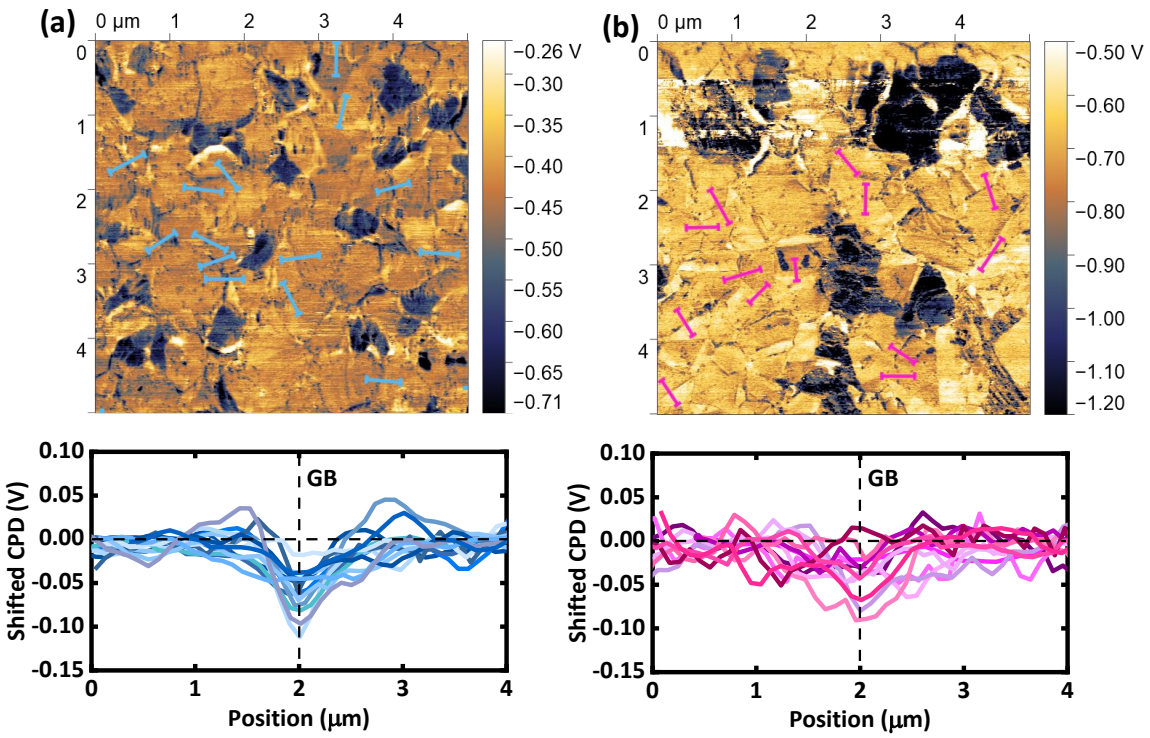

Figure 6-29: Visualization of the relative difference between the contact potential difference (CPD) value of grain boundaries and grain interior for some localized regions between grain boundary and grain interior illustrated in CPD map and CPD profile lines remarked by blue and pink for (a) reference (Ref) and (b) grain boundary passivation (GBP) perovskite films.

difference between CPD at the grain boundaries and grain interior for both Ref and GBP samples, *i.e.*, ΔCPD_{GB} ($CPD_{grain\ boundary}$–CPD_{grain}), line profiles are drawn across some localized grain boundaries areas as displayed in Figure 6-29. For better comparison, the CPD values of the grain interior at different positions are shifted to zero. In the CPD map for the Ref film, the grain boundaries are more distinguishable, showing a ~50–100 mV lower CPD than the grain interiors (Figures 6-29a), as observed in the previous studies as well.[296,297,235,298] This observation has been related to enhanced ionic defects and/or mobile ions at the grain boundaries region, probably arising from the lower energy that is needed for the formation of the defects in these regions.[299,296,300] In contrast, in terms of the GBP sample the contrast between grain boundaries and grain interior can not be clearly identified as compared to Ref film (either in the CPD map or line profiles for some localized regions highlighted by pink arrows in Figure 6-29b). For better statistics, we calculate $CPD_{grain\ boundary} - CPD_{grain}$ for ~60 samples as shown in Figure 6-30. The calculated average CPD shows a difference of ~74 mV for GBP films, which is ~20 mV lower than those estimated for the Ref samples. This reduction implies that the additive incorporation (PEACl: $PbCl_2$) passivates explicitly the grain boundaries, leading to a more notable reduction in WF with respect to the PbI_2-rich grains as compared to the grain interior. In conjunction with CL and XPS results, we correlate this to the formation of a PEACl-based 2D-RP phase particularly close to the grain boundaries. Despite the Ref and GBP samples, the CPD of SP film exhibit

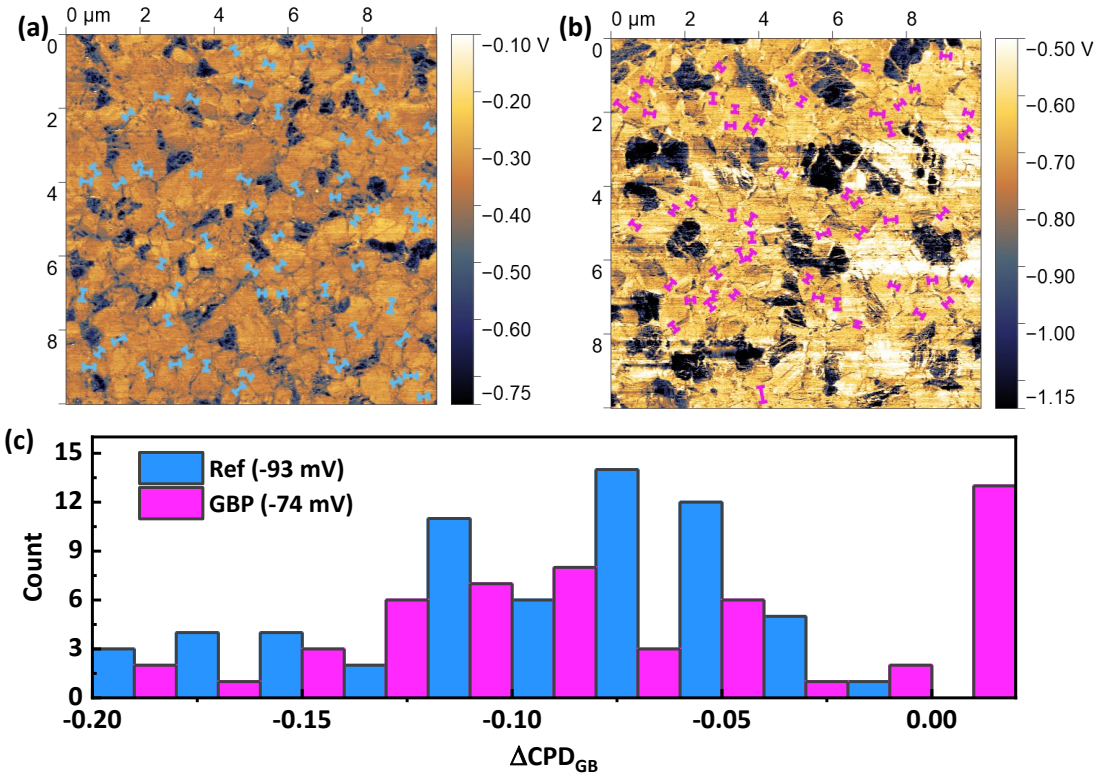

Figure 6-30: Estimation of the average contact potential difference (CPD) offset between grain boundary and grain interior for 60 grain boundaries regions obtained from the sample with the structure of ITO/2PACz/perovskite/C_{60} layer stack based on perovskite (a) without modification (Ref) and (b) grain boundary passivated (GBP) films. (c) Respective histogram of the extracted ΔCPD_{GB} ($CPD_{grain\ boundary} - CPD_{grain}$). Reproduced with permission from reference [228]. Copyright 2021, The Royal Society of Chemistry.

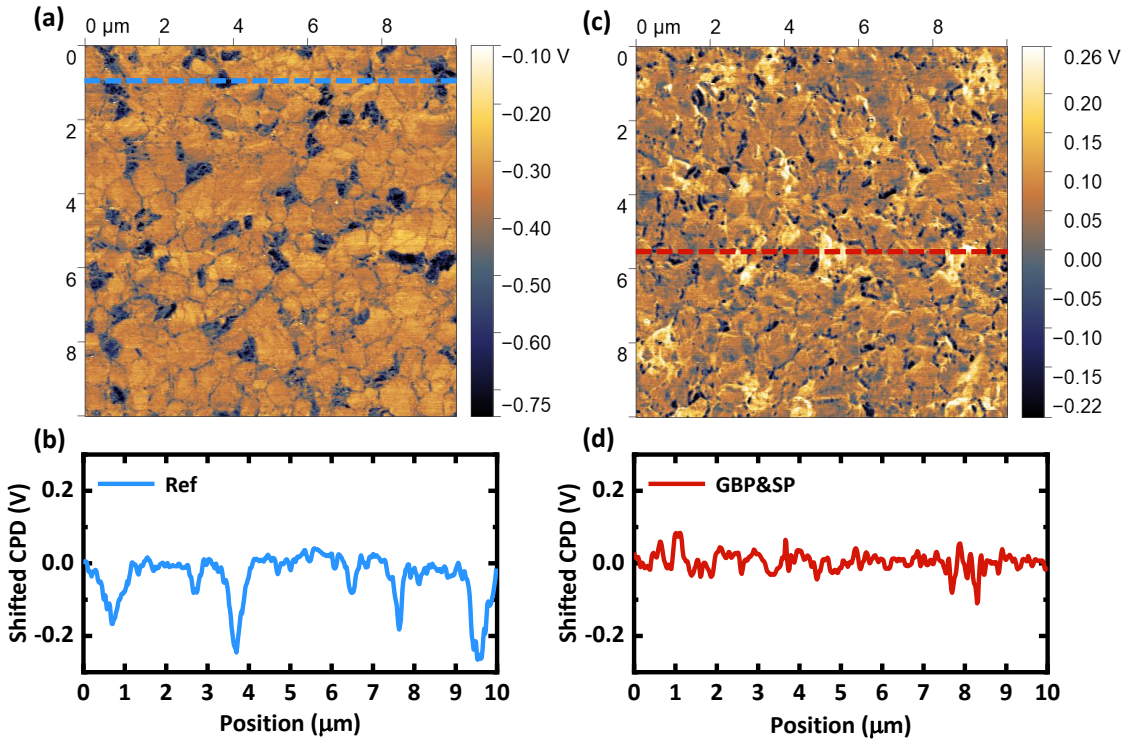

Figure 6-31: Contact potential difference (CPD) images and CPD variation of (a), (b) reference (Ref) and (c), (d) grain boundary & surface passivation (GBP&SP) films measured in dark. The line profiles along the blue line and red lines in the CPD maps correspond to Ref and GBP&SP films, respectively.

no noticeable distinction between high- and low-CPD grains with an enhanced CPD heterogeneity (-52 ± 50 mV) over different grains. We correlate this to formation of ultrathin 2D-RP on top of the perovskite with different electrical properties compared to the Ref sample as verified by XPS and UPS results as well. Yet, a slight grain boundary contrast at the surface is still distinguishable, which could be explained by the interpretation that PEACl cannot completely penetrate and thus passivate the grain boundary regions. More importantly, by looking at the CPD map and the relevant line profile for the GBP&SP sample, no obvious grain boundaries and PbI_2-rich grains can be distinguished, demonstrating even more heterogeneous CPD of -670 ± 70 mV compared to Ref, GBP and SP samples (Figure 6-31). Finally, we note that the CPD value can be affected both by the facet orientation and the existence of 2D-RP phases with various n, which makes it difficult to disentangle these effects in detail.[287,301,302] Briefly, considering the CL, XPS and KPFM results together, we conclude that by using both PEACl:$PbCl_2$ as additive and PEACl as surface treatment a thin heterogeneous 2D-RP phase is formed at the grain boundaries and surface of the perovskite film. This leads to simultaneous passivation at the regions, resulting in considerable enhancement in V_{OC} and PCE.

6.6. Stability of full devices

Defect sites serve as centers that accelerate the degradation of perovskite due to the migration of ionic species or charged defects.[47,303,304] Given that our dual passivation strategy results in simultaneous passivation of the defect at the grain boundaries and the surface of the perovskite film, thereby we expect a considerable enhancement in device stability. To examine whether the stability improvement can be practically observed, we measured the activation energy of ion migration for Ref, SP, GBP and GBP&SP PSCs conducted by thermal admittance spectroscopy (TAS). In this method, the activation energy (E_a) is derived from the derivative of capacitance (C) – frequency (ω) spectra (ωdC/dω) using the equation $\omega_{Peak} = \beta T^2 \exp(E_a/k_B T)$.[89,304] Here, β is a temperature-independent prefactor, T is the absolute temperature between 250–320 K and k_B is the Boltzmann constant, and ω_{Peak} is the angular frequency obtained by the maxima of the capacitance logarithmic derivative as displayed in Figure 6-32. The result presents that the dual passivation strategy remarkably enhances the activation energy of the devices to the highest value of about 696 meV compared to GBP, SP and the Ref PSC with E_a of 580, 551 and 502 meV, respectively (Figure 6-33a). This high activation energy for GBP&SP PSCs indicates that combining grain boundary and surface passivation of the perovskite layer strongly hinders the accumulation of ionic defects in these regions due to building the highest energy barrier for ion migration.[304–306] As a result, the reduced ion migration potentially suggests that the GBP&SP PSC should be more stable than the Ref device.[305,306] To verify this further, we compare the long-term stability of both GBP&SP and Ref devices via measuring their performance under 14 h constant illumination (100 mW/cm^2, AM1.5G) inside the glovebox in a room temperature and MPP tracking conditions. As shown in Figure

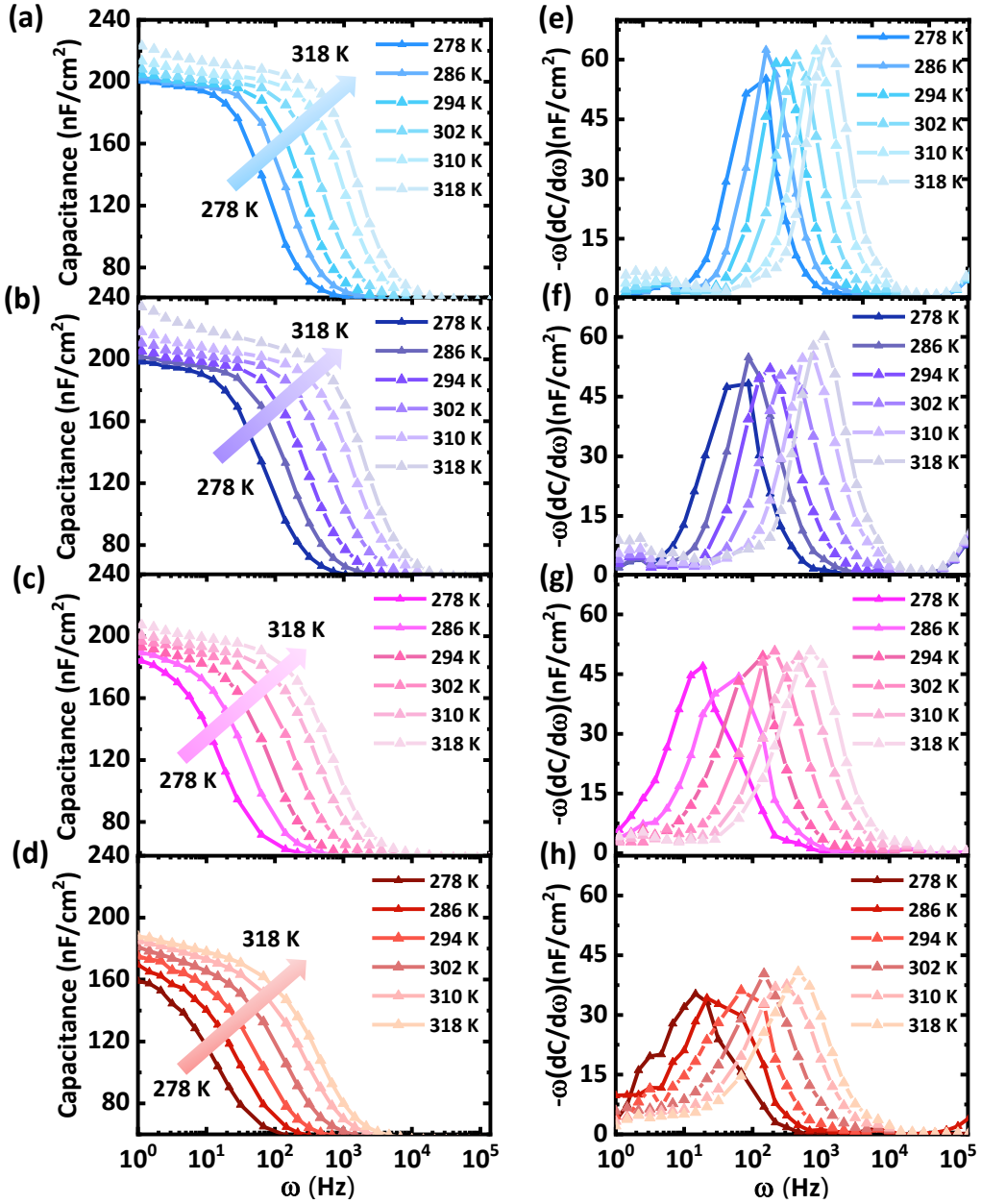

Figure 6-32: (a, b, c, d) Capacitance (C)-frequency (ω) spectra and (e, f, g, h) derivative of admittance spectra of the corresponding perovskite solar cells prepared without modification (Ref) and with surface passivation (SP), grain boundary passivation (GBP), and grain boundary & surface passivation (GBP&SP) strategy. The measurement was performed in a temperature range between 278 to 318 K.

6-33b, GBP&SP PSC demonstrates great photostability compared to Ref device such that its PCE reaches 98% of initial device performance after 14h, while this value drops to 80% for Ref PSC. Apart from the photostability test, we also examined the thermal stability of the devices by tracking their PCE after aging under 85 ^{o}C heating in the dark and inside of an N_2-filled glove box and) for over 1000 h (Figure 6-33c). Consistent with improved photostability under constant AM1.5G illumination, the GBP&SP device also exhibits

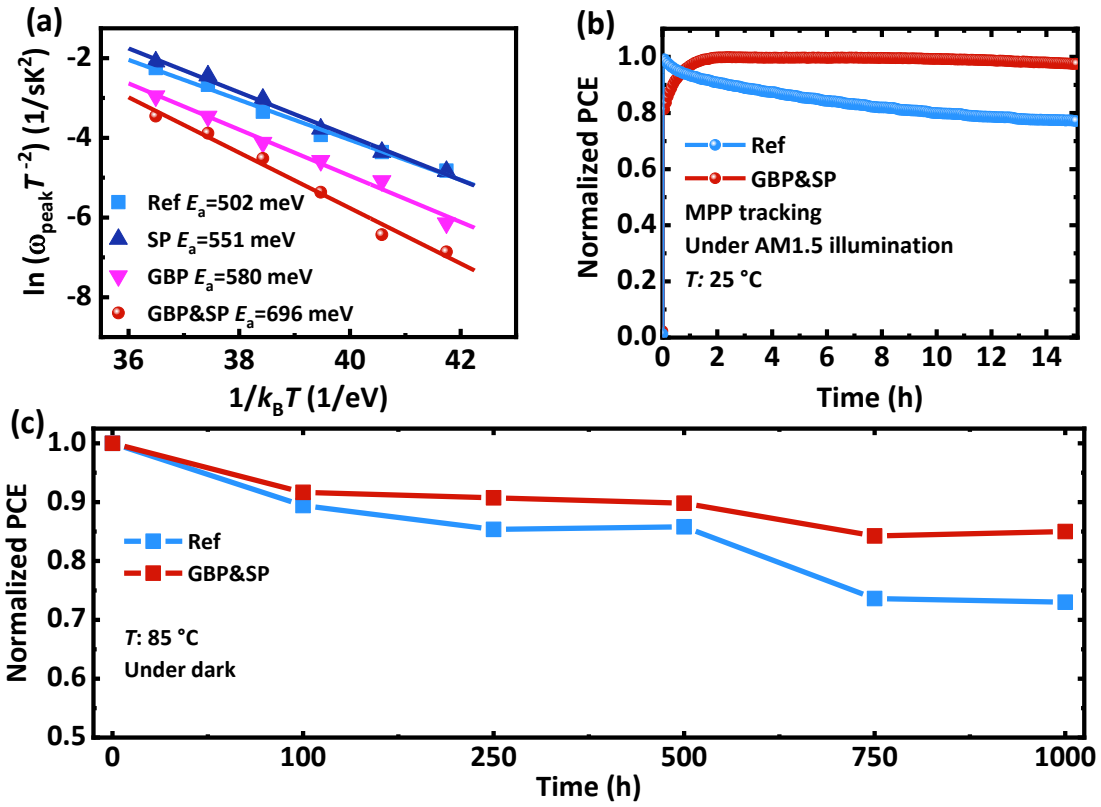

Figure 6-33: (a) Arrhenius plots of ln (ω_{Peak}/T^2) versus $1/k_BT$ obtained from the derivative of admittance spectra to determine the activation energy (E_a) for the perovskite solar cells (PSCs) prepared without any modification (Ref) and with grain boundary & surface passivation (GBP&SP). (b) The stabilized power conversion efficiency of the Ref and GBP&SP PSCs measured under maximum power point (MPP) tracking and continuous solar illumination (100 mW/cm^2) in a nitrogen atmosphere. (c) Normalized PCE of the devices heated at the temperature of 85 °C in dark condition inside of a glovebox extracted from *J–V* curves at various time intervals to determine the thermal stability.

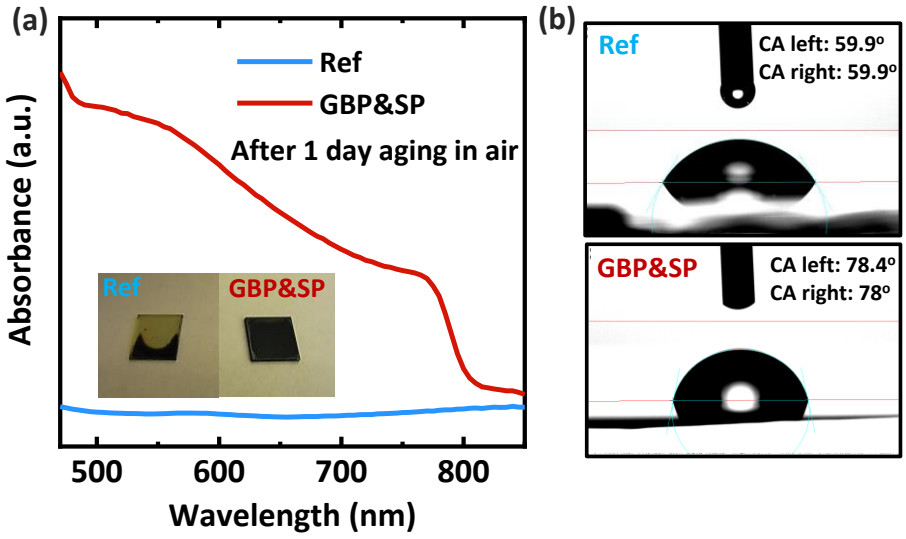

Figure 6-34: (a) The ultraviolet-visible absorption spectra obtained for perovskite without and modification (Ref) and with grain boundary & surface passivation (GBP&SP) measured after 1 day of their exposure to the 50% humidity. Contact angle of the water droplet on top of the (b) Ref (c) GBP&SP perovskite film.

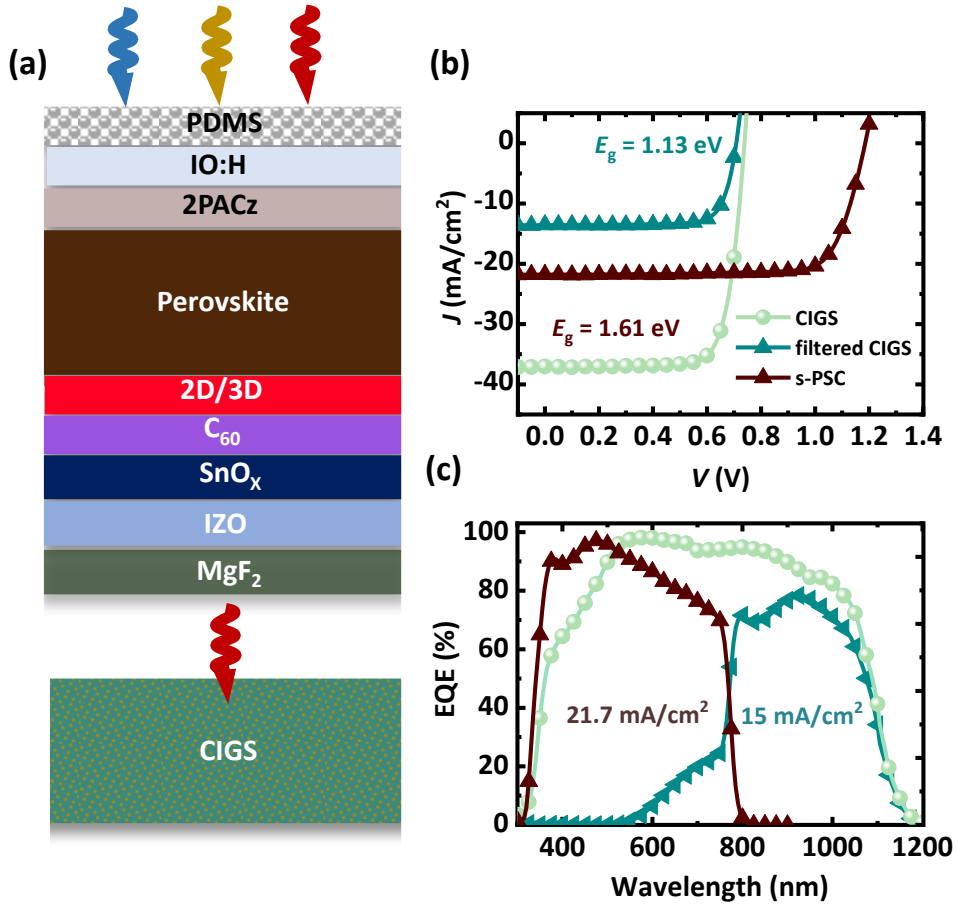

Figure 6-35: (a) Schematic stack of the 4-terminal (4T) perovskite/CIGS tandem solar cell. (b) Current density–voltage (*J*–*V*) characteristics and (c) external quantum efficiency (EQE) of semi-transparent perovskite solar cells (PSCs) with an optimum bandgap of 1.61 eV, standalone and filtered CIGS solar cells.

superior thermal stability, retaining 85% of its initial PCE, while for Ref PSC it declines to 73% after 1000h. Moisture sensitivity of the devices was further investigated by exposing the humidity of 50% and room temperature for 24 h. As illustrated in Figure 6-34a, thanks to the presence of hydrophobic PEA^+ cations at grain boundaries and the surface of the perovskite films that act as a hydrophobic barrier, no obvious change in the photographs and absorption data of GBP&SP film is observed.[47,244,306] In contrast, for Ref film without any modification, the penetration of moisture/water causes an exclusive degradation of the perovskite composition to PbI_2 (Figure 6-34a). The high moisture resistance capability is further confirmed by the increased contact angle of water droplets from 59.9° for the Ref film to 78.4° for the GBP&SP film (Figure 6-34b). In summary, our dual passivation strategy emphasizes the importance of defect passivation at both the surface and the grain boundaries of perovskite films to not improve the PCE but also is beneficial for enhancing the stability of the devices.

6.7. 4-terminal perovskite/CIGS tandem solar cell

Having demonstrated that employing the dual passivation strategy resulted in a significant

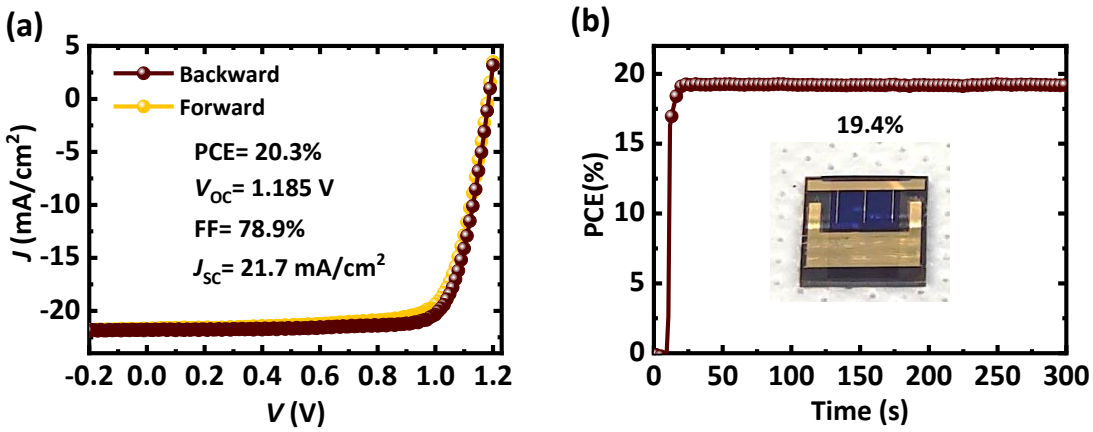

Figure 6-36: (a) Current density–voltage (*J–V*) characteristics of the best performing semi-transparent perovskite solar cell based on dual passivation strategy. (b) stabilized PCE of the corresponding device at maximum power point tracking under continuous 1-sun illumination for 300 s.

enhancement in photovoltaic performance of the p-i-n PSC with a bandgap of E_g ~1.57 eV, we fabricated a wide bandgap p-i-n PSC $Cs_{0.18}FA_{0.83}Pb(I_{0.9}Br_{0.1})_3$; E_g ~1.61 eV with the same strategy in order to combine it as the top cell in a 4T CIGS/perovskite solar cell. Figure 6-37a displays schematic illustration of the 4T perovskite/CIGS solar cell, based on a semi-transparent top solar cell with a layer stack of glass/IO:H (front contact)/2PACz (HTL)/$Cs_{0.18}FA_{0.83}Pb(I_{0.9}Br_{0.1})_3$ (absorber)/C_{60} (ETL)/SnO_2 (buffer layer)/IZO (Back contact)/Au (metal fingers)/MgF_2 (antireflection coating layer)/ polydimethylsiloxane (PDMS) as the top PSC (Figure 6-35a). As mentioned earlier in Chapter 2, SnO_2 deposited with atomic layer deposition systems is used to protect the C_{60} and perovskite layer from ion bombardment during the sputtering of the rear IZO. Besides, to achieve better light trapping and more transmission from the top semi-transparent cell into the CIGS bottom cell, here we attach PDMS anti-reflection foil textured with randomly-inverted pyramids on the front electrode of the top PSC,[170–173] as discussed in Chapter 2. The dual passivation strategy utilized in this semi-transparent PSC is based on employing MACl: $PbCl_2$ as a bulk additive and PEACl dissolved in IPA as a surface passivation layer. The semi-transparent device exhibit a high PCE of 20.3% with a V_{OC} of 1.185 V, J_{SC} of 21.7 mA/cm^2 and FF of 0.79 as well as stabilized PCE of 19.4% (Figure 6-36). It should be mentioned that for this

Table 6-3: Photovoltaic parameters of best-performing device configuration.

Solar cell architecture	Measurement protocol	V_{OC} (V)	J_{SC} (mA/cm^2)	FF (%)	PCE (%)	Stabilized PCE (%)
s-PSC (E_g = 1.65 eV)	BW	1.185	21.7	78.8	20.3	**19.4**
	FW	1.182	21.7	76.2	19.6	
CIGS solar cell	Stand-alone	0.74	37.2	77.0	21.2	21.2
	Filtered	0.71	1	78.1	7.5	**8.3**
4T perovskite/CIGS	BW	-	-	-	28.6	**27.7**

experiment we increase the size of the active area to 0.5 cm^2, which is three times larger than the active area of the semi-transparent devices in Chapter 5 with the size of 0.16 cm^2.

To determine the PCE of the 4T perovskite/CIGS solar cell, we individually calculate the PCE of each top and bottom cell. In this regard, the PCE of the bottom CIGS solar cell (as called filtered CIGS solar cell) is measured while placing a semi-transparent PSC with a matching active area on top, as previously illustrated in Chapter 5, showing a PCE of 8.3%. By combing the PCE of semi-transparent top PSC (19.3%) and filtered CIGS bottom cell (8.3%), we approach a high PCE value of 28.6% (stabilized PCE of 27.7%) for 4T perovskite/CIGS tandem solar cell (Figure 6-35b). This PCE is one of the highest values reported so far for 4T perovskite-CIGS tandem solar cells in the literature.[13] The *J–V* characteristics of the best performing top and bottom solar cell as well as calculated values for the 4T tandem solar cell are summarized in table 6-3. It should be noted that the high PCE achieved in this chapter is not only due to the employing dual passivation strategy, but also using PDMS anti-reflection foil. Thanks to PDMS, J_{SC} of the semi-transparent PSC and filtered CIGS solar cell increase by about 1 and 1.5 mA/cm^2 (Appendix C, Figure C1), respectively, resulting in J_{SC} of 21.7 and 15 mA/cm^2 as shown from EQE measurements (Figure 6-35c).

6.8. 2-terminal perovskite/c-Si tandem solar cell

In this section, we integrate dual passivated semi-transparent PSC with a bandgap of 1.68 eV into a monolithic perovskite-silicon tandem solar cell. As discussed earlier in Chapter 2, due to the series interconnection of the top and bottom cell in the 2T tandem configuration, the photocurrents of both subcells are needed to match. For this reason, PSC with an E_g of 1.68 eV is identified to be a suitable candidate to combine with a c-Si (1.12 eV) in the 2T configuration.[23,33] Figure 6-37 demonstrates the schematic illustration and cross-section SEM image of the 2T devices used in this thesis composed of a p-type c-Si solar cell covered by ITO as a recombination layer and a p-i-n semi-transparent PSC with a layer stack of NiOx (HTL)//2PACz (HTL)/$Cs_{0.05}MA_{0.15}FA_{0.75}Pb(I_{0.77}Br_{0.23})_3$ (absorber)/C_{60} (ETL)/SnO_2 (buffer layer)/ IZO (Back contact)/Ag (metal fingers)/MgF_2 (antireflection coating layer). It should be noted that, here in this experiment, we use PEAI as a bulk additive and lithium fluoride (LiF) as a surface passivation layer. To investigate the effect of the dual passivation strategy on the performance of the 2T devices, we measure the PCE of the devices based on perovskite without and with this strategy as shown in the *J–V* curves (Figure 6-37 d and e). As expected, 2T devices based on the dual passivation strategy exhibit a significant enhancement in V_{OC} from 1.79 V to 1.85 V compared to the reference device. This results in a noticeable improvement in PCE from 23.9% to 24.2%. Accordingly, the EQE measurements reveal a perfect current matching with the photocurrent of both subcells for the reference and dual passivated device, exhibiting integrated J_{SC} of 17.5 and 17.3 mA/cm^2, respectively (Figures 4.37 f and g). Therefore, our result highlight that the combination of passivation strategy both in the bulk/grain boundaries and surface of the

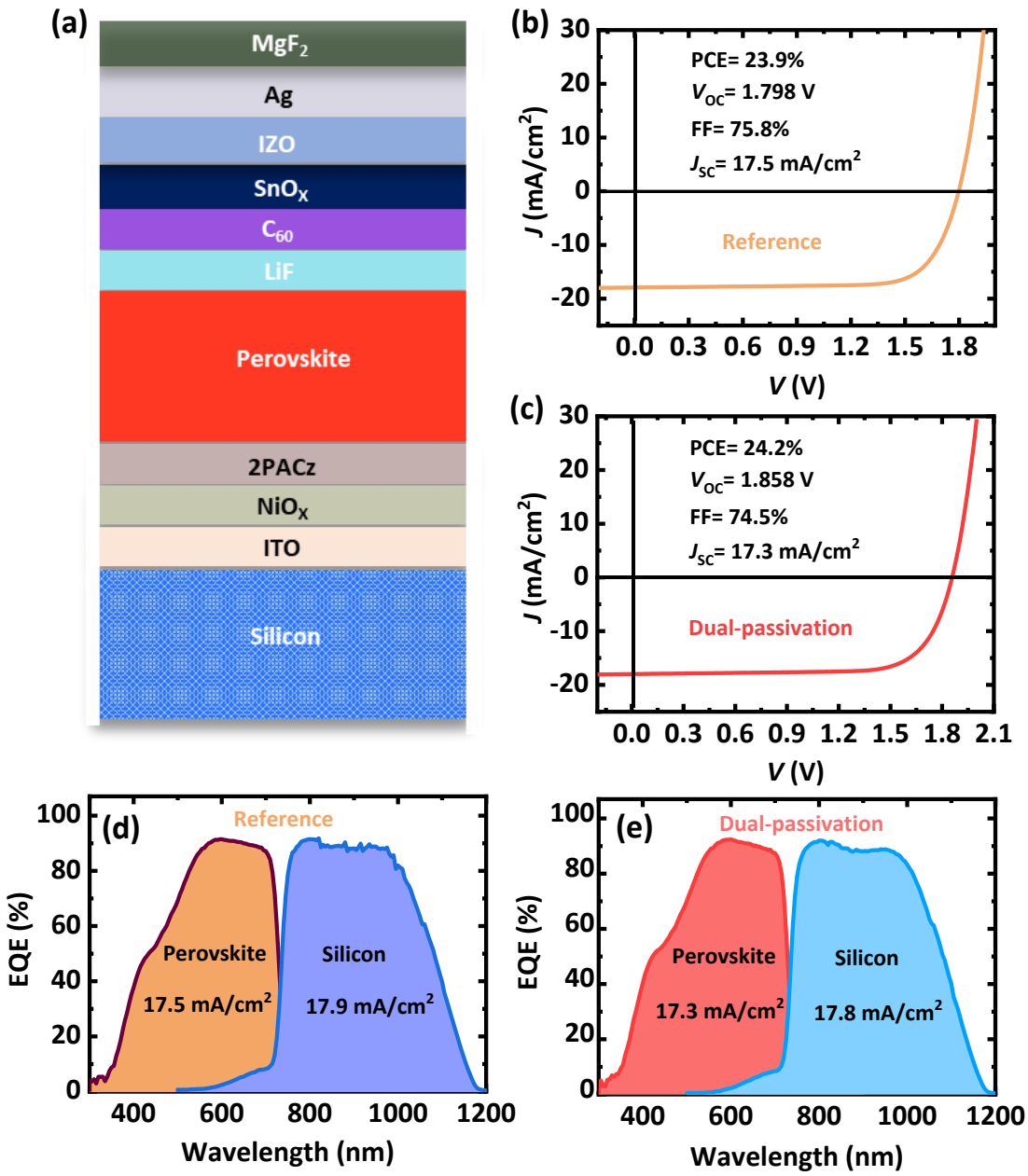

Figure 6-37: (a) Schematic illustration of the 2T perovskite/c-Si tandem layer stack. (b, c) Champion current density–voltage (*J*–*V*) characteristics and (e, g) external quantum efficiency of 2T devices based on perovskite without (Reference) and with dual passivation strategy, respectively.

perovskite layer is an essential requirement in the PSC fabrication process in order to improve the performance of 2T or 4T tandem solar cell.

6.9. Summary

In the first part of this chapter, we demonstrated that using long-chain alkylammonium salt (PEACl) incorporated into the perovskite precursor solution and treated on the surface of the perovskite layer passivate the defects simultaneously in the grain boundaries of the

perovskite as well as at the interface between perovskite and C_{60} layer. The devices based on the dual passivation strategy exhibited a substantial enhancement in performance compared to the reference and each individual passivated PSCs, yielding one of the highest reported PCE for p–i–n PSCs (E_g ~1.57 eV) with stabilized PCE of 22.3%. This enhancement mainly originated from the simultaneous increase in V_{OC} (76 mV) and FF (4.6%), respectively.

Next, we performed a series of photophysical measurements including PLQY and TPRL to determine the causes for the performance increase. These results collectively showed a remarkable enhancement in quasi-Fermi level splitting and charge carrier lifetime for dual passivated films compared to each individual grain boundary or surface passivated films. From SEM, CL, XPS, XRD results we found that this performance improvement is correlated to the formation of the 2D-RP phase at the surface and grain boundaries of the films. Further characterization by SCLC, UPS and KPFM measurements demonstrate that incorporating PEACl into the bulk and surface of the perovskite layer could result in (1) effective chemical passivation of grain boundary and surface defects and also (2) act as an additional hole blocking at the perovskite/C_{60} interface. Finally, TAS measurement revealed an outstanding increase in the activation energy of the ions upon dual passivation strategy which resulted in enhanced operational stability under continuous illumination at MPP tracking as well as the thermal stability of the devices for 1000 h.

Accordingly, by employing the dual passivated PSC as the top subcell in 4T and 2T tandem solar cells, we observed a significant improvement in the performance of the perovskite-based tandem devices. These results emphasize the necessity of reduced defect-assisted non-radiative recombination at the interface and the grain boundaries of the perovskite absorber to not only promote the performance of the PSCs and consequently perovskite-based tandem solar cell but also improve the long-term stability of the devices.

7. Conclusion and Outlook

The combination of a wide-bandgap (1.6 - 1.85 eV) perovskite solar cell (PSC) with a c-silicon or copper indium gallium selenide (CIGS) in a two-terminal (2T) or four-terminal (4T) tandem configuration demonstrates a promising approach to surpass the Shockley-Queisser (S-Q) limit of 33% for single-junction photovoltaic solar cells. To fulfill this objective, one of the critical challenges in wide-bandgap PSCs - the open-circuit voltage deficit (E_g/q - V_{OC}) - that originates from non-radiative recombination losses must be addressed. The presence of defects in the bulk and at the interfaces of the perovskite thin film and charge-transport layers (CTL) is identified as the dominant source of non-radiative recombination in n-i-p and p-i-n architectures of PSCs. This thesis highlights the importance of a passivation strategy either at the grain boundaries or at the surface/interface of the perovskite absorber layer and CTLs to reduce these defects that lead to pronounced voltage losses in wide-bandgap perovskites to boost the PCE of the perovskite-based tandem solar cell.

At the beginning of my Ph.D. study, the record efficiency of the PSC in the literature was based on low-bandgap planar n-i-p architecture (1.56 eV) using ITO/SnO_2/perovskite/p-doped spiro-MeOTAD /Au.[308] Nonetheless, theoretical studies demonstrate that such low bandgap perovskite absorbers are not ideal to maximize the PCE in a tandem application. Therefore, in **Chapter 4**, the focus lies on improving the bandgap to a near-ideal 1.73 eV in the same architecture with a foremost emphasis placed on reducing the voltage deficit as said earlier. In this regard, an emerging 2D perovskite (Ruddlesden–Popper (RP)) is used as surface passivation of the perovskite absorber layer, owing to its potential to enhance the V_{OC} of the devices.[42,92,97,99,192,193] We introduce a novel n-butylammonium bromide (n-BABr) as an interlayer between the perovskite and spiro-MeOTAD (hole transport layer), as non-radiative losses at this interface are more pronounced than to its counterpart interface with SnO_2 (electron transport layer).[50,214,232] The fabricated devices reveal the formation of the ultrathin 2D/3D perovskite heterostructure, exhibiting a significant enhancement in V_{OC} by about 80 mV (close to 90% of the theoretical maximum) compared to reference devices and thereby, resulting in a high PCE of 19% for wide-bandgap n-i-p PSC. We indicate that this enhancement mainly originates from the improved lifetime of the charge carrier due to the passivation of the perovskite surface. Furthermore, we observe that this interlayer also acts as an electron blocking layer at the interface, leading to an overall reduction in non-radiative recombination. Overall, these results demonstrate that employing 2D/3D perovskite heterostructure as surface passivation is an effective approach to successfully reduce the voltage deficit loss in wide-bandgap PSC, which is highly essential for the tandem application.

In **Chapter 5**, we employ this 2D/3D perovskite heterostructure in a series of double-cation PSCs ($FA_{0.83}Cs_{0.17}PbI_{3-y}Br_y$ ($0.24 \leq y \leq 0.56$)) with different bandgaps (E_g) between 1.65 eV

and 1.85 eV to determine the optimum bandgap of the top perovskite absorber and maximize the PCE of 4T perovskite/c-Si and perovskite/CIGS tandem solar cells. Our results demonstrate that irrespective of the bandgap of the perovskite absorber, employing the surface passivation strategy resulted in an overall improvement of ≈ 45 mV for all devices. This implies that n-butylammonium bromide can be used effectively for a wide range of bandgaps to reduce voltage deficit loss. Further, applying 2D/3D based semi-transparent PSC as a top solar cell in a perovskite/c-Si or perovskite/CIGS 4T tandem solar cell reveals that bandgaps ranging from 1.65-1.74 eV exhibit a comparable and yet high PCE, while this is not the case for E_g > 1.74 eV. This experimental finding for the first time indicates that wide-bandgap PSC with E_g > 1.74 eV is not the ideal bandgap to reach the highest PCE for the 4T tandem configuration, which contradicts predictions made by simulations based on the detailed-balance principle.[33,38,183] This is due to the fact that simulations do not account for the extensive non-radiative recombination processes that incur in real wide bandgap (E_g > 1.74) PSCs, even though more light is transmitted to a bottom cell for such bandgaps in the tandem configuration.

In **Chapter 6**, we investigate the effect of the passivation strategy on the performance of the 2T perovskite/silicon solar cell, which is a cost-effective architecture compared to 4T devices. In this regard, PSCs in p-i-n configuration are developed, as implementing n-i-p architecture into a 2T perovskite/silicon tandem solar cell is accompanied by a lack of a low-temperature ETL deposition process and high optical losses associated with the transparent conductive oxide and the HTL.[36,37] The main limitation for the p-i-n PSC though is the significant non-radiative recombination at the perovskite/organic ETL interface (such as C_{60}) compared to a PSC with n-i-p architecture.[50,232,233] In this work, we establish a multi-functional passivation strategy using long-chain alkylammonium salt phenethylammonium chloride (PEACl) as a 2D material to not only passivate the interface between the perovskite/C_{60} layer but also reduce the number of defects that exist in the perovskite grain boundaries. As a result, a dual passivated PSC exhibits a significant enhancement in the V_{OC} along with the FF, leading to a high PCE of 23%, which is one of the highest efficiency for p-i-n PSC reported in the literature to date. Furthermore, we demonstrate that the device stability of the dual passivated PSCs under maximum power point (MPP) tracking and heat treatment is enhanced notably due to the increased activation energy of ion migration. Further, we apply the dual passivated PSC in both 4T and 2T configurations and we could achieve one of the highest PCE (27%) for 4T perovskite/CIGS and 24% for 2T perovskite/silicon tandem solar cells, respectively. To conclude, our work highlights the importance of passivation for both the perovskite/ETL interface as well as grain boundaries inside the bulk of the perovskite thin film to reduce the voltage-deficit losses in perovskite-based solar cells.

7.1 Outlook

This thesis contributes to the applicability of PSCs for tandem solar cells that show the great potential to induce a substantial boost in device performance and thus superior adaptation in the solar cell industry. The study intensively focuses on reducing electrical losses in tandem-relevant wide-bandgap PSCs with both common architectures (regular n-i-p and inverted p-i-n) via the composition and interface engineering using emerging 2D-RP materials. This method proves to reduce successfully non-radiative recombination and therefore, voltage losses in the resultant devices. Despite this significant improvement, there is still large room for improving the V_{OC}, FF as well as optical losses present in wide-bandgap PSCs to reach their full potential in tandem applications. The directions for continuing work on the further developments of the performance are presented in the following:

While in Chapter 4, we demonstrate the formation of 2D/3D perovskite heterostructure at the interface of the perovskite/ spiro-MeOTAD layer by using n-BABr, the specific chemical bonding is unclear. Therefore, a further fundamental investigation using density-functional theory calculations is required for understanding the exact interaction such as the electronic coupling and chemical bonding between the n-BABr and the perovskite. This guides the finding or designing of the new multifunctional passivation molecules (2D-hybrid Dion–Jacobson or Ruddlesden popper perovskite) to fully passivate multiple defects (either positive or negative charged defects), thus can further increase the PCE of wide-bandgap PSCs. Moreover, this can further decrease the ion migration and consequently prolong the stability of PSCs which is still the largest obstacle in the step of entering them into industrial production. In this regard, intensively shifting the focus toward reaching higher stability by tailoring the dimensionality (n) of the 2D-perovskite layer via varying the annealing temperature or developing high-efficiency pure 2D PSC shows an effective strategy to further increase the stability of the PSC compared to the method we present in this thesis.[52,309]

Although the passivation strategy used either at the surface of the perovskite layer (presented in Chapters 4 and 5) or in both bulk (grain-boundaries) & surface of the perovskite (presented in Chapter 6) shows reduced V_{OC} deficit for wide-bandgap mixed-halide PSCs, they still suffer from photo-induced phase segregation under illumination, affecting both V_{OC} and the stability of the devices. It has been reported that the partial substitution of the large cation at the A site such as dimethylammonium or guanidinium can be an alternative approach for increasing the bandgap of the perovskite absorber while maintaining low amounts of bromide (< 20%) in the ABX_3 perovskite structure. Therefore, further studies could explore various large monovalent cations in dual passivated PSC and their impact on the phase segregation effect and stability.

In terms of optical losses, these losses arise from parasitic absorption and reflection losses. Not only do these losses decrease the PCE of the top semi-transparent PSC, but they also limit the sub-bandgap transmission of the photons through the perovskite top cell to the bottom cell in a tandem configuration. Though every active layer contributes in some form to parasitic absorption, the main contributors in a 4T tandem device are the two TCOs at the front and rear side of the top semitransparent perovskite sub-cell. The reflection losses are more complex, stemming from numerous interfaces in the tandem stack, for instance, air/glass, perovskite/CTL, TCO/air, etc. Thus, further studies could focus on reducing these losses, such as using highly transparent conductive oxides, micro- and nano-textures, grids, etc.

Appendix

A. Appendix for Chapter 4

Table A1: Detailed information for the references in Figure 4-1. The bandgap (E_g) is determined from the differential of the EQE (d(EQE)/dE) close to the absorption edge. Open-circuit voltage (V_{OC}) deficit is calculated by subtracting V_{OC} from E_g (from d(EQE)/dE). For the V_{OC} deficit in brackets, as no EQE data was provided, E_g from the literature reference was used. Therefore these values should be considered with care.

Nominal perovskite composition as reported	E_g as reported	E_g (from d(EQE)/dE)	V_{OC} (V)	V_{OC} deficit	Reference
$CH_3NH_3PbI_{3-x}Cl_x$	1.55	1.618	1.13	1.13	1S
$CH_3NH_3PbI_{3-x}Br_x$	1.72	1.718	1.02	0.698	2S
$MAPbBr_xI_{3-x}$	1.75	1.803	1.21	0.593	3S
$FA_{0.83}Cs_{0.17}Pb(I_{0.6}Br_{0.4})_3$	1.74	1.72	1.2	0.52	4S
$(FAPbI_3)_{0.85}(MAPbBr_3)_{0.15}$	1.6	1.618	1.118	0.5	5S
$FA_{0.67}MA_{0.33}Pb(I_{0.83}Br_{0.17})_3$	1.64	1.643	1.14	0.503	6S
$FA_{0.83}MA_{0.17}Pb(I_{0.67}Br_{0.33})_3$	1.68	no EQE	1.18	(0.5)	6S
$FA_{0.67}MA_{0.33}Pb(I_{0.67}Br_{0.33})_3$	1.68	1.684	1.15	0.534	6S
$Rb_{0.05}(Cs_{0.05}(FA_{0.83}MA_{0.17})_{0.95})_{0.95}Pb(I_{0.83}Br_{0.17})_3$	1.63	1.628	1.24	0.388	7S
$Cs_{0.05}(FA_{0.83}MA_{0.17})_{0.95}Pb(I_{0.83}Br_{0.17})_3$	1.6	no EQE	1.23	(0.37)	8S
$Rb_{0.05}(FA_{0.75}MA_{0.15}Cs_{0.1})_{0.95}Pb(I_{0.67}Br_{0.33})_3$	1.73	1.735	1.13	0.605	9S
$FA_{0.8}Cs_{0.2}Pb(I_{0.7}Br_{0.3})_3$ w/ Pb(SCN)	1.75	1.741	1.23	0.511	10S
$Cs_{0.05}(FA_{0.83}MA_{0.17})_{0.95}Pb(I_{0.6}Br_{0.4})_3$	1.71	1.763	1.2	0.563	11S
$MAPbI_3$	1.59	1.612	1.17	0.442	12S
$Cs_{0.07}Rb_{0.03}FA_{0.765}MA_{0.135}Pb(I_{0.85}Br_{0.15})_3$	*non*	1.607	1.18	0.427	13S
$FA_{0.85}MA_{0.15}Pb(I_{0.85}Br_{0.15})_3$	1.592	1.592	1.14	0.452	14S
$FA_{0.83}MA_{0.17}Pb(I_{0.6}Br_{0.4})_3$	1.72	1.72	1.15	0.57	14S
$BA_{0.05}(FA_{0.83}Cs_{0.17})_{0.95}Pb(I_{0.8}Br_{0.2})_3$	1.61	1.61	1.14	0.47	15S
$BA_{0.09}(FA_{0.83}Cs_{0.17})_{0.91}Pb(I_{0.6}Br_{0.4})_3$	1.72	1.72	1.18	0.54	15S
$FA_{0.85}Cs_{0.15}Pb(I_{0.73}Br_{0.27})_3$	1.72	1.735	1.24	0.495	16S
$MAPb(I_{0.8}Br_{0.2})_3$	1.72	1.695	1.11	0.585	17S

$FA_{0.8}Cs_{0.2}Pb(Br_{0.3}I_{0.7})_3$	1.75	1.739	1.2	0.539	18S
$FA_{0.6}Cs_{0.4}Pb(I_{0.7}Br_{0.3})_3$	1.75	1.76	1.17	0.59	19S
$FA_{0.75}Cs_{0.25}Pb(I_{0.8}Br_{0.2})_3$	1.68	1.678	1.1	0.578	19S
$Cs_{0.1}FA_{0.74}MA_{0.13}PbI_{2.48}Br_{0.39}$	1.62	1.6	1.14	0.46	20S
$FA_{0.83}Cs_{0.17}Pb(I_{0.6}Br_{0.4})_3$	1.75	1.773	1.23	0.543	21S
$K_{0.1}(Cs_{0.06}FA0_{0.79}MA_{0.15})_{0.9}Pb(I_{0.85}Br_{0.15})_3$	1.56	1.591	1.17	0.421	22S
$K_{0.1}(Cs_{0.06}FA0_{0.79}MA_{0.15})_{0.9}Pb(I_{0.4}Br_{0.6})_3$	1.78	1.835	1.23	0.605	22S
$MAPb(I_{0.6}Br_{0.4})_3$	1.82	1.83	1.30	0.53	23S
$MAPb(I_{1-x}Br_x)_3$	1.71	1.708	1.24	0.468	24S
$(FA_{0.95}PbI_{2.95})_{0.85}(MAPbBr_3)_{0.15}$	1.62	1.594	1.21	0.384	25S

Additional references for Table A.1

[1S] H. Zhou, Q. Chen, G. Li, S. Luo, T. -b. Song, H.-S. Duan, Z. Hong, J. You, Y. Liu, Y. Yang, Science **2014**, 345, 542.

[2S] C. Bi, Y. Yuan, Y. Fang, J. Huang, Adv. Energy Mater. **2015**, 5, 1401616.

[3S] M. Hu, C. Bi, Y. Yuan, Y. Bai, J. Huang, Adv. Sci. **2016**, 3, 1500301.

[4S] D. P. McMeekin, G. Sadoughi, W. Rehman, G. E. Eperon, M. Saliba, M. T. Horantner, A. Haghighirad, N. Sakai, L. Korte, B. Rech, M. B. Johnston, L. M. Herz, H. J. Snaith, Science **2016**, 351, 151.

[5S] F. Giordano, A. Abate, J. P. Correa Baena, M. Saliba, T. Matsui, S. H. Im, S. M. Zakeeruddin, M. K. Nazeeruddin, A. Hagfeldt, M. Graetzel, Nat. Commun. **2016**, 7, 10379.

[6S] T. Jesper Jacobsson, J.-P. Correa-Baena, M. Pazoki, M. Saliba, K. Schenk, M. Grätzel, A. Hagfeldt, Energy Environ. Sci. **2016**, 9, 1706.

[7S] M. Saliba, T. Matsui, K. Domanski, J.-Y. Seo, A. Ummadisingu, S. M. Zakeeruddin, J.-P. Correa-Baena, W. R. Tress, A. Abate, A. Hagfeldt, M. Gratzel, Science **2016**, 354, 206.

[8S] J. P. Correa-Baena, W. Tress, K. Domanski, E. H. Anaraki, S. H. Turren-Cruz, B. Roose, P. P. Boix, M. Grätzel, M. Saliba, A. Abate, A. Hagfeldt, Energy Environ. Sci. **2017**, 10, 1207.

[9S] T. Duong, Y. Wu, H. Shen, J. Peng, X. Fu, D. Jacobs, E.-C. Wang, T. C. Kho, K. C. Fong, M. Stocks, E. Franklin, A. Blakers, N. Zin, K. McIntosh, W. Li, Y.-B. Cheng, T. P. White, K. Weber, K. Catchpole, Adv. Energy Mater. **2017**, 7, 1700228.

[10S] Y. Yu, C. Wang, C. R. Grice, N. Shrestha, D. Zhao, W. Liao, L. Guan, R. A. Awni, W. Meng, A. J. Cimaroli, K. Zhu, R. J. Ellingson, Y. Yan, ACS Energy Lett. **2017**, 2, 1177.

[11S] Y. Lin, B. Chen, F. Zhao, X. Zheng, Y. Deng, Y. Shao, Y. Fang, Y. Bai, C. Wang, J. Huang, Adv. Mater. **2017**, 29, 1700607.

[12S] Y. Bai, S. Xiao, C. Hu, T. Zhang, X. Meng, H. Lin, Y. Yang, S. Yang, Adv. Energy Mater. 2017, 7, 1701038.

[13S] J. Peng, Y. Wu, W. Ye, D. A. Jacobs, H. Shen, X. Fu, Y. Wan, T. Duong, N. Wu, C. Barugkin, H. T. Nguyen, D. Zhong, J. Li, T. Lu, Y. Liu, M. N. Lockrey, K. J. Weber, K. R. Catchpole, T. P. White, Energy Environ. Sci. **2017**, 10, 1792.

[14S] X. Zheng, B. Chen, J. Dai, Y. Fang, Y. Bai, Y. Lin, H. Wei, X. C. Zeng, J. Huang, Nat. Energy **2017**, 2, 17102.

[15S] Z. Wang, Q. Lin, F. P. Chmiel, N. Sakai, L. M. Herz, H. J. Snaith, Nat. Energy **2017**, 2, 17135.

[16S] Y. Zhou, F. Wang, Y. Cao, J.-P. Wang, H.-H. Fang, M. A. Loi, N. Zhao, C.-P. Wong, Adv. Energy Mater. **2017**, 7, 1701048.

[17S] G. Longo, C. Momblona, M.-G. La-Placa, L. Gil-Escrig, M. Sessolo, H. J. Bolink, ACS Energy Lett. **2018**, 3, 214.
[18S] D. Zhao, C. Wang, Z. Song, Y. Yu, C. Chen, X. Zhao, K. Zhu, Y. Yan, ACS Energy Lett. **2018**, 3, 305.
[19S] K. A. Bush, K. Frohna, R. Prasanna, R. E. Beal, T. Leijtens, S. A. Swifter, M. D. McGehee, ACS Energy Lett. **2018**, 3, 428.
[20S] K. T. Cho, G. Grancini, Y. Lee, E. Oveisi, J. Ryu, O. Almora, M. Tschumi, P. A. Schouwink, G. Seo, S. Heo, J. Park, J. Jang, S. Paek, G. Garcia-Belmonte, M. K. Nazeeruddin, Energy Environ. Sci. **2018**, 11, 952.
[21S] J. Kim, M. I. Saidaminov, H. Tan, Y. Zhao, Y. Kim, J. Choi, J. W. Jo, J. Fan, R. Quintero-Bermudez, Z. Yang, L. N. Quan, M. Wei, O. Voznyy, E. H. Sargent, Adv. Mater. **2018**, 30, 1706275.
[22S] M. Abdi-Jalebi, Z. Andaji-Garmaroudi, S. Cacovich, C. Stavrakas, B. Philippe, J. M. Richter, M. Alsari, E. P. Booker, E. M. Hutter, A. J. Pearson, S. Lilliu, T. J. Savenije, H. Rensmo, G. Divitini, C. Ducati, R. H. Friend, S. D. Stranks, Nature **2018**, 555, 497.
[23S] A. Rajagopal, R. J. Stoddard, S. B. Jo, H. W. Hillhouse, A. K. Y. Jen, Nano Lett. **2018**, 18, 3985.
[24S] D. B. Khadka, Y. Shirai, M. Yanagida, T. Noda, K. Miyano, ACS Appl. Mater. Interfaces **2018**, 10, 22074.
[25S] D. Luo, W. Yang, Z. Wang, A. Sadhanala, Q. Hu, R. Su, R. Shivanna, G. F. Trindade, J. F. Watts, Z. Xu, T. Liu, K. Chen, F. Ye, P. Wu, L. Zhao, J. Wu, Y. Tu, Y. Zhang, X. Yang, W. Zhang, R. H. Friend, Q. Gong, H. J. Snaith, R. Zhu, Science **2018**, 360, 1442.

B. Appendix for Chapter 5

Table B1: Detailed information for the references in Figure 5-1. It should be noted that the references related to 1s to 25s has been already mentioned in Appendix A, Table A1.

Nominal perovskite composition as reported	E_g as reported	E_g (from d(EQE)/dE)	V_{OC} (V)	V_{OC} deficit	Reference
$FA_{0.83}Cs_{0.17}Pb(I_{0.73}Br_{0.27})_3$ w/ Pb(SCN)	1.72	1.716	1.244	0.472	26S
$FA_{0.83}Cs_{0.17}Pb(I_{0.6}Br_{0.4})_3$ w/ Pb(SCN)	1.79	1.786	1.284	0.502	26S
$FA_{0.83}Cs_{0.17}Pb(I_{0.5}Br_{0.5})_3$ w/ Pb(SCN)	1.86	1.849	1.296	0.553	26S
$FA_{0.83}Cs_{0.17}Pb(I_{0.4}Br_{0.6})_3$ w/ Pb(SCN)	1.93	1.91	1.312	0.598	26S
$Cs_{0.12}MA_{0.05}FA_{0.83}Pb(I_{0.6}Br_{0.4})_3$	1.74	1.785	1.25	0.535	27S
$Cs_{0.05}MA_{0.15}FA_{0.8}Pb(I_{0.75}Br_{0.25})_3$	1.65	1.677	1.22	0.457	27S
$Cs_{0.05}((FA_{0.85}MA_{0.15})Pb(I_{0.85}Br_{0.15})_3)_{0.95}$	1.61	1.627	1.245	0.382	28S
$MA_{0.6}FA_{0.4}Pb(I_{0.6}Br_{0.4})_3$	1.76	1.788	1.17	0.618	29S
$MAPbI_3$	1.6	1.615	1.262	0.353	30S
$FA_{0.85}Cs_{0.15}Pb(I_{0.71}Br_{0.29})_3$	1.72	1.819	1.22	0.599	31S
$Cs_{0.05}MA_{0.14}FA_{0.81}Pb(I_{0.85}Br_{0.15})_3$	non	1.611	1.15	0.461	32S
$FA_{0.8}Cs_{0.2}PbI_3$	1.56	1.532	1.1	0.432	33S
$GA_5(Cs_5(MA_{0.17}FA_{0.83})_{0.95})_{0.95}Pb(I_{0.83}Br_{0.17})_3$	1.6	*no EQE*	1.2	(0.4)	34S
$Cs_y(FA_{0.57}MA_{0.43})_{1-y}Pb(I_{1-x}Br_x)_3$	1.56	1.571	1.147	0.413	35S

$Cs_{0.05}MA_{0.14}FA_{0.81}Pb(I_{0.85}Br_{0.15})_3$	1.57	1.607	1.23	0.34	36S
$Cs_{0.05}FA_{0.70}MA_{0.25}PbI_3$	1.51	1.551	1.16	0.391	37S
$MAPbI_3$	1.55	1.616	1.18	0.436	37S
$FA_{0.8}Cs_{0.2}Pb(I_{0.6}Br_{0.4})_3$	1.82	1.842	1.26	0.582	37S
$FA_{0.83}Cs_{0.17}Pb(I_{0.6}Br_{0.4})_3$	1.72	1.747	1.31	0.434	38S
$GA_xFA_{0.8}Cs_{0.2}Pb(I_{0.7}Br_{0.3+x/3})_3$	1.75	1.751	1.24	0.511	39S
$(FA_{0.65}MA_{0.20}Cs_{0.15})Pb(I_{0.8}Br_{0.2})_3$	1.68	1.657	1.17	0.487	40S
$(FAPbI_3)_{0.92}(MAPbBr_3)_{0.08}$	1.53	1.569	1.186	0.383	41S
$(CsPbI_3)_{0.05}[(FAPbI_3)_{0.83}(MAPbBr_3)_{0.17}]_{0.95}$	1.6	1.632	1.205	0.427	42S
$Cs_{0.07}FA_{0.9}MA_{0.03}Pb(I_{0.92}Br_{0.08})_3$	*non*	1.56	1.15	0.41	43S
$Cs_{0.05}FA_{0.81}MA_{0.14}PbI_{2.55}Br_{0.45}$	1.6	1.6	1.16	0.44	44S
$FA_{0.6}Cs_{0.4}Pb(I_{0.65}Br_{0.35})_3$	1.8	no EQE	1.21	(0.59)	45S
$Cs_{0.07}Rb_{0.03}FA_{0.765}MA_{0.135}Pb(I_{0.85}Br_{0.15})_3$	1.6	1.615	1.2	0.415	46S
$Cs_{0.05}FA_{0.81}MA_{0.14}Pb(I_{0.86}Br_{0.14})_3$	1.61	1.615	1.14	0.46	47S
$MAPbI_3$	1.59	1.597	1.16	0.43	48S
$MAPb(I_{0.8}Br_{0.2})_3$	1.68	no EQE	1.22	(0.46)	48S
Not stated	--	1.577	1.195	0.382	49S
Not stated	--	1.536	1.17	0.366	49S
Not stated	--	1.536	1.179	0.357	49S
$FA_{0.83}Cs_{0.17}Pb(I_{0.76}Br_{0.24})_3$	1.65	1.667	1.18	0.487	This work
$FA_{0.83}Cs_{0.17}Pb(I_{0.68}Br_{0.32})_3$	1.69	1.702	1.223	0.479	This work
$FA_{0.83}Cs_{0.17}Pb(I_{0.6}Br_{0.4})_3$	1.74	1.748	1.278	0.47	This work
$FA_{0.83}Cs_{0.17}Pb(I_{0.52}Br_{0.48})_3$	1.79	1.809	1.263	0.546	This work
$FA_{0.83}Cs_{0.17}Pb(I_{0.44}Br_{0.56})_3$	1.85	1.855	1.259	0.596	This work

Additional references for Table B.1

[26S] Y. Zhou, Y.-H. Jia, H.-H. Fang, M. A. Loi, F.-Y. Xie, L. Gong, M.-C. Qin, X.-H. Lu, C.-P. Wong, N. Zhao, Adv. Funct. Mater. **2018**, 28, 1803130.

[27S] H. Tan, F. Che, M. Wei, Y. Zhao, M. I. Saidaminov, P. Todorović, D. Broberg, G. Walters, F. Tan, T. Zhuang, B. Sun, Z. Liang, H. Yuan, E. Fron, J. Kim, Z. Yang, O. Voznyy, M. Asta, E. H. Sargent, Nat. Commun. 2018, 9, 3100.

[28S] M. M. Tavakoli, W. Tress, J. V. Milić, D. Kubicki, L. Emsley, M. Grätzel, Energy Environ. Sci. **2018**, 11, 3310.

[29S] S. Chen, Y. Hou, H. Chen, X. Tang, S. Langner, N. Li, T. Stubhan, I. Levchuk, E. Gu, A. Osvet, C. J. Brabec, Adv. Energy Mater. **2018**, 8, 1701543.

[30S] Z. Liu, L. Krückemeier, B. Krogmeier, B. Klingebiel, J. A. Márquez, S. Levcenko, S. Öz, S. Mathur, U. Rau, T. Unold, T. Kirchartz, ACS Energy Lett. **2019**, 4, 110.

[31S] M. Jaysankar, B. A. L. Raul, J. Bastos, C. Burgess, C. Weijtens, M. Creatore, T. Aernouts, Y. Kuang, R. Gehlhaar, A. Hadipour, J. Poortmans, ACS Energy Lett. **2019**, 4, 259.

[32S] P. Guo, Q. Ye, X. Yang, J. Zhang, F. Xu, D. Shchukin, B. Wei, H. Wang, J. Mater. Chem. A **2019**, 7, 2497.

[33S] D. Prochowicz, R. Runjhun, M. M. Tavakoli, P. Yadav, M. Saski, A. Q. Alanazi, D. J. Kubicki, Z. Kaszkur, S. M. Zakeeruddin, J. Lewiński, M. Grätzel, Chem. Mater. **2019**, 31, 1620.

[34S] D. Prochowicz, M. M. Tavakoli, A. Kalam, R. D. Chavan, S. Trivedi, M. Kumar, P. Yadav, J. Mater. Chem. A **2019**, 7, 8218.

[35S] Y. Chen, N. Li, L. Wang, L. Li, Z. Xu, H. Jiao, P. Liu, C. Zhu, H. Zai, M. Sun, W. Zou, S. Zhang, G. Xing, X. Liu, J. Wang, D. Li, B. Huang, Q. Chen, H. Zhou, Nat. Commun. **2019**, 10, 1112.

[36S] S. Yang, J. Dai, Z. Yu, Y. Shao, Y. Zhou, X. Xiao, X. C. Zeng, J. Huang, J. Am. Chem. Soc. **2019**, 141, 5781.

[37S] W.-Q. Wu, Z. Yang, P. N. Rudd, Y. Shao, X. Dai, H. Wei, J. Zhao, Y. Fang, Q. Wang, Y. Liu, Y. Deng, X. Xiao, Y. Feng, J. Huang, Sci. Adv. **2019**, 5, eaav8925.

[38S] S. Gharibzadeh, B. Abdollahi Nejand, M. Jakoby, T. Abzieher, D. Hauschild, S. Moghadamzadeh, J. A. Schwenzer, P. Brenner, R. Schmager, A. A. Haghighirad, L. Weinhardt, U. Lemmer, B. S. Richards, I. A. Howard, U. W. Paetzold, Adv. Energy Mater. **2019**, 9, 1803699.

[39S] C. Chen, Z. Song, C. Xiao, D. Zhao, N. Shrestha, C. Li, G. Yang, F. Yao, X. Zheng, R. J. Ellingson, C.-S. Jiang, M. Al-Jassim, K. Zhu, G. Fang, Y. Yan, Nano Energy **2019**, 61, 141.

[40S] D. H. Kim, C. P. Muzzillo, J. Tong, A. F. Palmstrom, B. W. Larson, C. Choi, S. P. Harvey, S. Glynn, J. B. Whitaker, F. Zhang, Z. Li, H. Lu, M. F. A. M. van Hest, J. J. Berry, L. M. Mansfield, Y. Huang, Y. Yan, K. Zhu, Joule **2019**, 3, 1734.

[41S] J. J. Yoo, S. Wieghold, M. C. Sponseller, M. R. Chua, S. N. Bertram, N. T. P. Hartono, J. S. Tresback, E. C. Hansen, J.-P. Correa-Baena, V. Bulović, T. Buonassisi, S. S. Shin, M. G. Bawendi, Energy Environ. Sci. **2019**, 12, 2192.

[42S] M. Stolterfoht, P. Caprioglio, C. M. Wolff, J. A. Márquez, J. Nordmann, S. Zhang, D. Rothhardt, U. Hörmann, Y. Amir, A. Redinger, L. Kegelmann, F. Zu, S. Albrecht, N. Koch, T. Kirchartz, M. Saliba, T. Unold, D. Neher, Energy Environ. Sci. **2019**, 12, 2778.

[43S] E. A. Alharbi, A. Y. Alyamani, D. J. Kubicki, A. R. Uhl, B. J. Walder, A. Q. Alanazi, J. Luo, A. Burgos-Caminal, A. Albadri, H. Albrithen, M. H. Alotaibi, J.-E. Moser, S. M. Zakeeruddin, F. Giordano, L. Emsley, M. Grätzel, Nat. Commun. **2019**, 10, 3008.

[44S] S. Yang, S. Chen, E. Mosconi, Y. Fang, X. Xiao, C. Wang, Y. Zhou, Z. Yu, J. Zhao, Y. Gao, F. De Angelis, J. Huang, Science **2019**, 365, 473.

[45S] Z. Yang, Z. Yu, H. Wei, X. Xiao, Z. Ni, B. Chen, Y. Deng, S. N. Habisreutinger, X. Chen, K. Wang, J. Zhao, P. N. Rudd, J. J. Berry, M. C. Beard, J. Huang, *Nat. Commun.* **2019**, *10*, 4498.

[46S] M. A. Mahmud, T. Duong, Y. Yin, H. T. Pham, D. Walter, J. Peng, Y. Wu, L. Li, H. Shen, N. Wu, N. Mozaffari, G. Andersson, K. R. Catchpole, K. J. Weber, T. P. White, Adv. Funct. Mater. **2019**, doi: 10.1002/adfm.201907962.

[47S] Y. Lv, X. Song, Y. Yin, Y. Feng, H. Ma, C. Hao, S. Jin, Y. Shi, ACS Appl. Mater. Interfaces **2020**, 12, 698.

[48S] C.-T. Lin, J. Lee, J. Kim, T. J. Macdonald, J. Ngiam, B. Xu, M. Daboczi, W. Xu, S. Pont, B. Park, H. Kang, J.-S. Kim, D. J. Payne, K. Lee, J. R. Durrant, M. A. McLachlan, Adv. Funct. Mater. 2019, 1906763, 1906763.

[49S] M. A. Green, A. W. Y. Ho-Baillie, ACS Energy Lett. **2019**, 4, 1639.

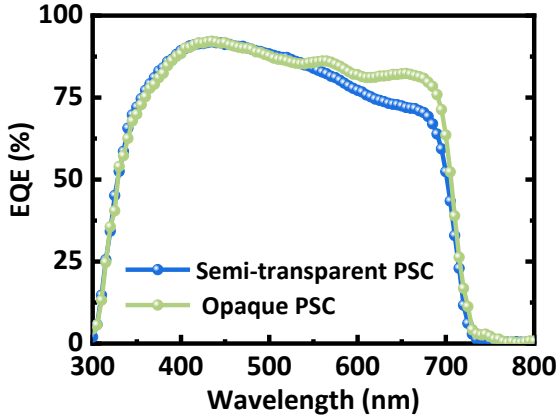

Figure B1: Comparison of external quantum efficiency (EQE) of opaque and semi-transparent perovskite solar cell (PSC).

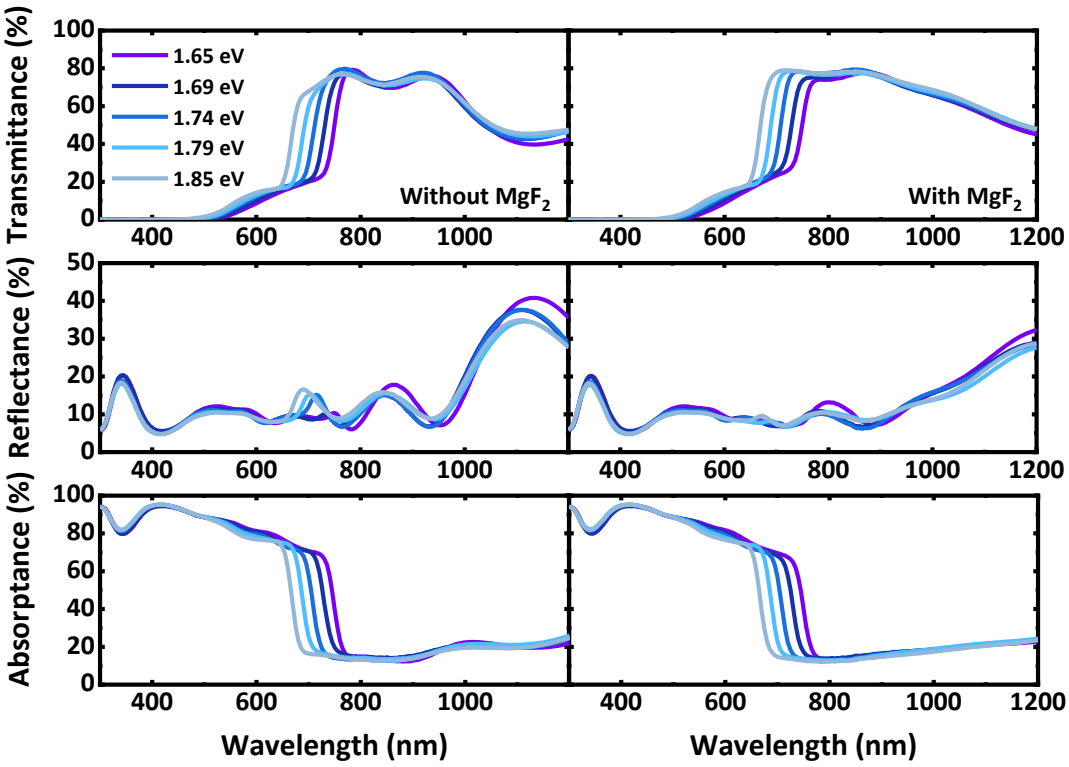

Figure B2: Comparison of transmittance (top), reflectance (middle) and absorptance (bottom) spectra of semi-transparent perovskite solar cells using 2D/3D perovskite heterostructure and engineered bandgap without and with MgF_2 layer deposition on the rear ITO.

C. Appendix for Chapter 6

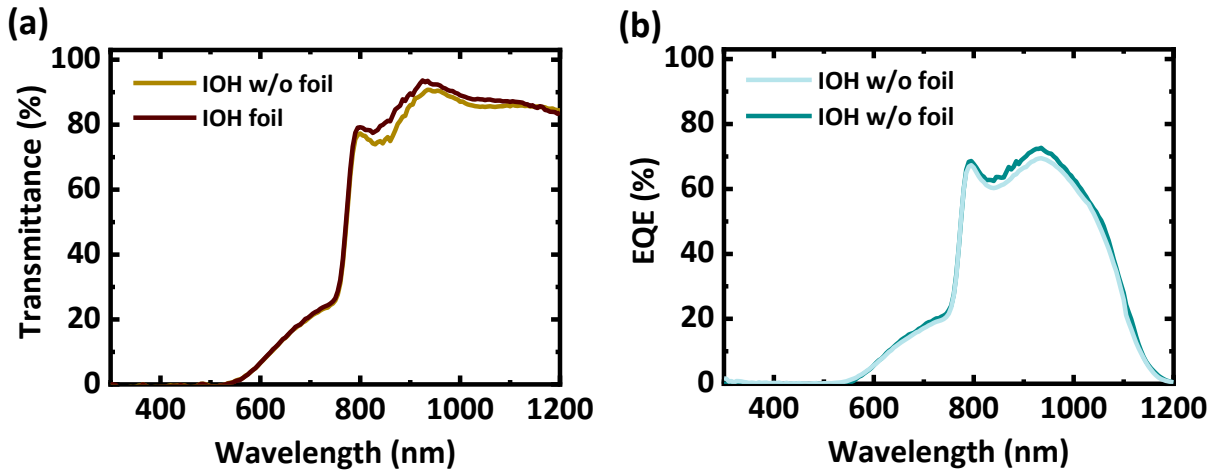

Figure C1: (a) Transmittance and (b) external quantum efficiency of semi-transparent perovskite solar cell without and with using polydimethylsiloxane as an anti-reflection foil textured

References

1. Masson-Delmotte, V. et al. IPCC: Climate Change 2021: The Physical Science Basis. Cambridge Univ. Press. Press. 42 (2021).

2. Friedlingstein, P. *et al.* Global Carbon Budget 2020. *Earth Syst. Sci. Data* **12**, 3269–3340 (2020).

3. Heede, R. & Oreskes, N. Potential emissions of CO2 and methane from proved reserves of fossil fuels: An alternative analysis. *Glob. Environ. Chang* **36**, 12–20 (2016).

4. International Panel on Climate Change (IPCE). CLIMATE CHANGE 2013, https://www.ipcc.ch/site/assets/uploads/2018/03/WG1AR5_SummaryVolume_FINAL.pdf.

5. Wigley, T. M. L., Jones, P. D. & Kelly, P. M. Global warming?. *Nature* **291**, 285 (1981).

6. Suckling, J. H. & Frasier, J. T. Streak interferometric measurements of transient displacements. *Exp. Mech* **8**, 513–519 (1968).

7. International Energy Outlook 2021 with projection to 205, Administration, U. S. E. I. Independent Statistics, (2021).

8. IRENA. Future of solar photovoltaic*:* 2019. https://irena.org/-/media/Files/IRENA/Agency/Publication/2019/Nov/IRENA_Future_of_Solar_PV_2019.pdf.

9. BMWi. Renewable Energy Sources in Figures. 1–88 (2020). https://www.bmwk.de/Redaktion/EN/Publikationen/Energie/renewable-energy-sources-in-figures.pdf.

10. IEA, World Energy Outlook 2019, Paris. https://www.iea.org/reports/world- energy-outlook-2019.

11. Kost, C., *et al.* Levelized cost of electricity renewable energy technologies. *Levelized Cost of Electricity- Renewable Energy Technologies*. Fraunhofer Institute for Solar Energy Systems (ISE) (2021).

12. Schafer, S. & Brendel, R. Accurate calculation of the absorptance enhances efficiency limit of crystalline silicon solar cells with light trapping. *IEEE J. Photovoltaics* **8**, 1156–1158 (2018).

13. National Renewable Energy Laboratory (NREL), Efficiency Chart,https://www.nrel.gov/pv/cell-efficiency.html (2022).

14. Richter, A., Hermle, M. & Glunz, S. W. Reassessment of the limiting efficiency for crystalline silicon solar cells. *IEEE J. Photovoltaics* **3**, 1184–1191 (2013).

15. De Vos, A. Detailed balance limit of the efficiency of tandem solar cells. *J. Phys. D. Appl. Phys* **13**, 839–846 (1980).

16. Essig, S. *et al.* Raising the one-sun conversion efficiency of III-V/Si solar cells to 32.8% for two junctions and 35.9% for three junctions *Nat. Energy* **2**, 1-9 (2017).

17. GREEN, M. *et al.* Solar cell efficiency tables (version 40). *Ieee Trans Fuzzy Syst* **20**, 1114–1129 (2012).

18. Bett, A. W. *et al.* Overview about technology perspectives for high efficiency solar cells for space and terrestrial applications. *28th Eur. Photovolt. Sol. Energy Conf. Exhib9* **0**, 1–6 (2013).

19. Park, N. G., Grätzel, M., Miyasaka, T., Zhu, K. & Emery, K. Towards stable and commercially available perovskite solar cells. *Nat. Energy* **1**, 1-8 (2016).

20. Green, M. A., Ho-Baillie, A. & Snaith, H. J. The emergence of perovskite solar cells. *Nat. Photonics* **8**, 506–514 (2014).

21. Snaith, H. J. Perovskites: The emergence of a new era for low-cost, high-efficiency solar cells. *J. Phys. Chem. Lett* **4**, 3623–3630 (2013).

22. McMeekin, D. P. *et al.* A mixed-cation lead mixed-halide perovskite absorber for tandem solar cells. *Science* **351**, 151–155 (2016).

23. Leijtens, T., Bush, K. A., Prasanna, R. & McGehee, M. D. Opportunities and challenges for tandem solar cells using metal halide perovskite semiconductors. *Nat. Energy* **3**, 828–838 (2018).

24. Werner, J., Niesen, B. & Ballif, C. Perovskite/Silicon Tandem Solar Cells: Marriage of Convenience or True Love Story? – An Overview. *Adv. Mater. Interfaces* **5**, 1–19 (2018).

25. Ho-Baillie, A. W. Y. *et al.* Recent progress and future prospects of perovskite tandem solar cells. *Appl. Phys. Rev* **8**, 041307 (2021).

26. Kojima, A., Teshima, K., Shirai, Y. & Miyasaka, T. Organometal Halide Perovskites as Visible-Light Sensitizers for Photovoltaic Cells. *J. Am. Chem. Soc* **131**, 6050–6051 (2009).

27. Min, H. *et al.* Perovskite solar cells with atomically coherent interlayers on SnO2 electrodes. *Nature* **598**, 444–450 (2021).

28. Kamaraki, C., Klug, M. T., Green, T., Miranda Perez, L. & Case, C. Perovskite/silicon tandem photovoltaics: Technological disruption without business disruption. *Appl. Phys. Lett* **119**, 070501 (2021).

29. Werner, J. *et al.* Efficient Near-Infrared-Transparent Perovskite Solar Cells Enabling Direct Comparison of 4-Terminal and Monolithic Perovskite/Silicon Tandem Cells. *ACS Energy Lett* **1**, 474–480 (2016).

30. Todorov, T., Gunawan, O. & Guha, S. A road towards 25% efficiency and beyond: Perovskite tandem solar cells. *Mol. Syst. Des. Eng* **1**, 370–376 (2016).

31. Jaysankar, M. *et al.* Perovskite-silicon tandem solar modules with optimised light harvesting. *Energy Environ. Sci* **11**, 1489–1498 (2018).

32. International Renewable Energy Agency (IRENA). Renewable power generation costs in 2012: An Overview. *Irena* 1–8 (2013).

33. Eperon, G. E., Hörantner, M. T. & Snaith, H. J. Metal halide perovskite tandem and multiple-junction photovoltaics. *Nat. Rev. Chem* **1**, 1-18 (2017).

34. Battaglia, C., Cuevas, A. & De Wolf, S. High-efficiency crystalline silicon solar cells: Status and perspectives. *Energy Environ. Sci* **9**, 1552–1576 (2016).

35. Sahli, F. *et al.* Improved Optics in Monolithic Perovskite/Silicon Tandem Solar Cells with a Nanocrystalline Silicon Recombination Junction. *Adv. Energy Mater* **8**, 1–8 (2018).

36. Bush, K. A. *et al.* 23.6%-Efficient Monolithic Perovskite/Silicon Tandem Solar Cells With Improved Stability. *Nat. Energy* **2**, 1–7 (2017).

37. Magomedov, A. *et al.* Self-Assembled Hole Transporting Monolayer for Highly Efficient Perovskite Solar Cells. *Adv. Energy Mater* **8**, 1801892 (2018).

38. Futscher, M. H. & Ehrler, B. Efficiency Limit of Perovskite/Si Tandem Solar Cells. *ACS Energy Lett* **1**, 863–868 (2016).

39. Jesper Jacobsson, T. *et al.* Exploration of the compositional space for mixed lead halogen perovskites for high efficiency solar cells. *Energy Environ. Sci* **9**, 1706–1724 (2016).

40. Chen, C. *et al.* Achieving a high open-circuit voltage in inverted wide-bandgap perovskite solar cells with a graded perovskite homojunction. *Nano Energy* **61**, 141–147 (2019).

41. Rajagopal, A., Stoddard, R. J., Jo, S. B., Hillhouse, H. W. & Jen, A. K. Y. Overcoming the Photovoltage Plateau in Large Bandgap Perovskite Photovoltaics. *Nano Lett* **18**, 3985–3993 (2018).

42. Jaysankar, M. *et al.* Minimizing Voltage Loss in Wide-Bandgap Perovskites for Tandem Solar Cells. *ACS Energy Lett* **4**, 259–264 (2019).

43. Mahesh, S. *et al.* Revealing the origin of voltage loss in mixed-halide perovskite solar cells. *Energy Environ. Sci* **13**, 258–267 (2020).

44. Fan, R., Zhou, W., Huang, Z. & Zhou, H. Defect suppression and passivation for perovskite solar cells: from the birth to the lifetime operation. *EnergyChem* **2**, 100032 (2020).

45. Fu, L. *et al.* Defect passivation strategies in perovskites for an enhanced photovoltaic performance. *Energy Environ. Sci* **13**, 4017–4056 (2020).

46. Warby, J. *et al.* Understanding Performance Limiting Interfacial Recombination in

pin Perovskite Solar Cells. *Adv. Energy Mater* **12**, 2103567 (2022).

47. Zheng, X. *et al.* Managing grains and interfaces via ligand anchoring enables 22.3%-efficiency inverted perovskite solar cells. *Nat. Energy* **5**, 131–140 (2020).

48. Chen, B. *et al.* Passivation of the Buried Interface via Preferential Crystallization of 2D Perovskite on Metal Oxide Transport Layers. *Adv. Mater* **2103394**, 1–8 (2021).

49. Penã-Camargo, F. *et al.* Halide Segregation versus Interfacial Recombination in Bromide-Rich Wide-Gap Perovskite Solar Cells. *ACS Energy Lett* **5**, 2728–2736 (2020).

50. Stolterfoht, M. *et al.* The impact of energy alignment and interfacial recombination on the internal and external open-circuit voltage of perovskite solar cells. *Energy Environ. Sci* **12**, 2778–2788 (2019).

51. Yoo, J. J. *et al.* Efficient perovskite solar cells via improved carrier management. *Nature* **590**, 587–593 (2021).

52. Azmi, R. *et al.* Damp heat – stable perovskite solar cells with tailored-dimensionality 2D / 3D heterojunctions - Supplementary Materials. *Science* **376**, 71–73 (2022).

53. Ge, C., Xue, Y. Z. B., Li, L., Tang, B. & Hu, H. Recent Progress in 2D / 3D Multidimensional Metal Halide Perovskites Solar Cells. *Frontiers in Materials* **7**, 380 (2020).

54. Kim, E., Akhtar, M. S., Shin, H., Ameen, S. & Khaja, M. C : Photochemistry Reviews A review on two-dimensional (2D) and 2D-3D multidimensional perovskite solar cells : Perovskites structures, stability, and photovoltaic performances. *J. Photochem. Photobiol. C Photochem. Rev* **48**, 100405 (2021).

55. Whitfield, P. S. *et al.* Structures, Phase Transitions and Tricritical Behavior of the Hybrid Perovskite Methyl Ammonium Lead Iodide. *Sci. Rep* **6**, 1–16 (2016).

56. Bush, K. A. *et al.* Compositional Engineering for Efficient Wide Band Gap Perovskites with Improved Stability to Photoinduced Phase Segregation. *ACS Energy Lett* **3**, 428–435 (2018).

57. Fu, Y. *et al.* Incorporating Large A Cations into Lead Iodide Perovskite Cages: Relaxed Goldschmidt Tolerance Factor and Impact on Exciton-Phonon Interaction. *ACS Cent. Sci* **5**, 1377–1386 (2019).

58. Goldschmidt, V. M. et al. Krystallbau und chemische Zusammensetzun (1927).

59. Correa-Baena, J.-P. *et al.* Promises and challenges of perovskite solar cells. *Science* **358**, 739–744 (2017).

60. Chen, Y. *et al.* 2D Ruddlesden–Popper Perovskites for Optoelectronics. *Adv. Mater* **30**, 1–15 (2018).

61. Gharibzadeh, S. *et al.* Record Open-Circuit Voltage Wide-Bandgap Perovskite Solar Cells Utilizing 2D/3D Perovskite Heterostructure. *Adv. Energy Mater* **9**. 1970079

(2019).

62. Ahmad, S. *et al.* Dion-Jacobson Phase 2D Layered Perovskites for Solar Cells with Ultrahigh Stability. *Joule* **3**, 794–806 (2019).

63. De Wolf, S. *et al.* Organometallic halide perovskites: Sharp optical absorption edge and its relation to photovoltaic performance. *J. Phys. Chem. Lett* **5**, 1035–1039 (2014).

64. Miyata, A. *et al.* Direct measurement of the exciton binding energy and effective masses for charge carriers in organic–inorganic tri-halide perovskites. *Nat. Phys* **11**, 582-587 (2015).

65. Wehrenfennig, C., Eperon, G. E., Johnston, M. B., Snaith, H. J. & Herz, L. M. High charge carrier mobilities and lifetimes in organolead trihalide perovskites. *Adv. Mater* **26**, 1584–1589 (2014).

66. Alcocer, M. J. P., Leijtens, T., Herz, L. M., Petrozza, A. & Snaith, H. J. Electron-Hole Diffusion Lengths Exceeding Trihalide Perovskite Absorber. *Science* **342**, 341–344 (2013).

67. Eperon, G. E. *et al.* Formamidinium lead trihalide: A broadly tunable perovskite for efficient planar heterojunction solar cells. *Energy Environ. Sci* **7**, 982–988 (2014).

68. Correa-Baena, J. P. *et al.* The rapid evolution of highly efficient perovskite solar cells. *Energy Environ. Sci* **10**, 710–727 (2017).

69. Yin, W.-J., Shi, T. & Yan, Y. Unique Properties of Halide Perovskites as Possible Origins of the Superior Solar Cell Performance. *Adv. Mater* **26**, 4653–4658 (2014).

70. Prasanna, R. *et al.* Band Gap Tuning via Lattice Contraction and Octahedral Tilting in Perovskite Materials for Photovoltaics. *J. Am. Chem. Soc* **139**, 11117–11124 (2017).

71. Kumawat, N. K., Liu, X. K., Kabra, D. & Gao, F. Blue perovskite light-emitting diodes: Progress, challenges and future directions. *Nanoscale* **11**, 2109–2120 (2019).

72. Brenner, P. *et al.* Triple cation mixed-halide perovskites for tunable lasers. *Opt. Mater. Express* **7**, 4082 (2017).

73. Hu, J., Yan, L. & You, W. Two-Dimensional Organic – Inorganic Hybrid Perovskites : A New Platform for Optoelectronic Applications. *Adv. Mater* 30, 1802041 (2018).

74. Lan, C., Zhou, Z., Wei, R. & Ho, J. C. Two-dimensional perovskite materials : From synthesis to energy-related applications. *Mater. Today Energy* **11**, 61–82 (2019).

75. Zhang, F. *et al. Advances in two-dimensional organic-inorganic hybrid perovskites*. *Energy Environ.Sci* **13**, 1154-1186 (2020).

76. Stoumpos, C. C. *et al.* Ruddlesden-Popper Hybrid Lead Iodide Perovskite 2D Homologous Semiconductors. *Chem. Mater* **28**, 2852–2867 (2016).

77. Ahmad, S. *et al.* Strong Photocurrent from Two-Dimensional Excitons in Solution-

Processed Stacked Perovskite Semiconductor Sheets. *ACS Appl. Mater. Interfaces* **7**, 25227–25236 (2015).

78. Cao, D. H., Stoumpos, C. C., Farha, O. K., Hupp, J. T. & Kanatzidis, M. G. 2D Homologous Perovskites as Light-Absorbing Materials for Solar Cell Applications. *J. Am. Chem. Soc.* **137**, 7843–7850 (2015).

79. Stoumpos, C. C. *et al.* High Members of the 2D Ruddlesden-Popper Halide Perovskites: Synthesis, Optical Properties, and Solar Cells of (CH3(CH2)3NH3)2(CH3NH3)4Pb5I16. *Chem* **2**, 427–440 (2017).

80. Grancini, G. & Nazeeruddin, M. K. Dimensional tailoring of hybrid perovskites for photovoltaics. *Nat. Rev. Mater* **4**, 4–22 (2019).

81. Mahmud, M. A. *et al.* In Situ Formation of Mixed-Dimensional Surface Passivation Layers in Perovskite Solar Cells with Dual-Isomer Alkylammonium Cations. *Small* **16**, 1–10 (2020).

82. Kim, H. *et al.* Optimal Interfacial Engineering with Different Length of Alkylammonium Halide for Efficient and Stable Perovskite Solar Cells. *Adv. Energy Mater* **9**, 1902740 (2019).

83. Liu, G. *et al.* Introduction of Hydrophobic Ammonium Salts with Halogen Functional Groups for High-Efficiency and Stable 2D/3D Perovskite Solar Cells. *Adv. Funct. Mater* **29**, 1–9 (2019).

84. Smith, I. C., Hoke, E. T., Solis-Ibarra, D., McGehee, M. D. & Karunadasa, H. I. A Layered Hybrid Perovskite Solar-Cell Absorber with Enhanced Moisture Stability. *Angew. Chemie - Int. Ed* **53**, 11232–11235 (2014).

85. Quan, L. N. *et al.* Ligand-Stabilized Reduced-Dimensionality Perovskites. *J. Am. Chem. Soc.* **138**, 2649–2655 (2016).

86. Mahmud, M. A., *et al.* Origin of efficiency and stability enhancement in high‐performing mixed dimensional 2D‐3D perovskite solar cells: a review. Adv. Funct. Mater **32**, 2009164 (2022).

87. Gao, P., Bin Mohd Yusoff, A. R. & Nazeeruddin, M. K. Dimensionality engineering of hybrid halide perovskite light absorbers. *Nat. Commun* **9**, 1–14 (2018).

88. Etgar, L. The merit of perovskite's dimensionality; Can this replace the 3D halide perovskite? *Energy Environ. Sci* **11**, 234–242 (2018).

89. Chen, C. *et al.* Arylammonium-Assisted Reduction of Open Circuit Voltage Deficit in Wide-Bandgap Perovskite Solar Cells : The Role of Suppressed Ion Migration Arylammonium-Assisted Reduction of Open Circuit Voltage Deficit in Wide-Bandgap Perovskite Solar Cells. *ACS Energy Lett* **5**, 2560-2568 (2020).

90. Huang, Z. *et al.* Suppressed Ion Migration in Reduced-Dimensional Perovskites Improves Operating Stability. *ACS Energy Lett* **4**, 1521–1527 (2019).

91. Meggiolaro, D., Mosconi, E. & De Angelis, F. Formation of Surface Defects Dominates Ion Migration in Lead-Halide Perovskites. *ACS Energy Lett* **4**, 779–785 (2019).

92. Cho, K. T. *et al.* Selective growth of layered perovskites for stable and efficient photovoltaics. *Energy Environ. Sci* **11**, 952–959 (2018).

93. Yoo, J. J. *et al.* An interface stabilized perovskite solar cell with high stabilized efficiency and low voltage loss. *Energy Environ. Sci* **12**, 2192–2199 (2019).

94. Jung, E. H. *et al.* Efficient, stable and scalable perovskite solar cells using poly(3-hexylthiophene). *Nature* **567**, 511–515 (2019).

95. Jiang, Q. *et al.* Surface passivation of perovskite film for efficient solar cells. *Nat. Photonics* **13**, 460–466 (2019).

96. Lin, Y. *et al.* Enhanced Thermal Stability in Perovskite Solar Cells by Assembling 2D/3D Stacking Structures. *J. Phys. Chem. Lett* **9**, 654–658 (2018).

97. Zhou, Y. *et al.* Benzylamine-Treated Wide-Bandgap Perovskite with High Thermal-Photostability and Photovoltaic Performance. *Adv. Energy Mater* **7**, 1701048 (2017).

98. Lee, D. S. *et al.* Passivation of Grain Boundaries by Phenethylammonium in Formamidinium-Methylammonium Lead Halide Perovskite Solar Cells. *ACS Energy Lett* **3**, 647–654 (2018).

99. Bai, Y. *et al.* Dimensional Engineering of a Graded 3D–2D Halide Perovskite Interface Enables Ultrahigh Voc Enhanced Stability in the p-i-n Photovoltaics. *Adv. Energy Mater* **7**, 1701038. (2017).

100. Bisquert, J. The physics of solar cells: perovskites, organics, and photovoltaic fundamentals. CRC press (2017).

101. Jacobs, D. A. *et al.* Hysteresis phenomena in perovskite solar cells: The many and varied effects of ionic accumulation. *Phys. Chem. Chem. Phys* **19**, 3094–3103 (2017).

102. Lopez-Varo, P. *et al.* Device Physics of Hybrid Perovskite Solar cells: Theory and Experiment. *Adv. Energy Mater* **8**, 1–36 (2018).

103. Mora-Seró, I. How Do Perovskite Solar Cells Work? *Joule* **2**, 585–587 (2018).

104. Kirchartz, T. *Generalized detailed balance theory of solar cells*. *Vol. 38. Forschungszentrum Jülich* (2009).

105. Rau, U. & Kirchartz, T. Charge Carrier Collection and Contact Selectivity in Solar Cells. *Adv. Mater. Interfaces* **6**, 1900252 (2019).

106. Kirchartz, T., Bisquert, J., Mora-Sero, I. & Garcia-Belmonte, G. Classification of solar cells according to mechanisms of charge separation and charge collection. *Phys. Chem. Chem. Phys* **17**, 4007–4014 (2015).

107. Wurfel, U., Cuevas, A. & Wurfel, P. Charge carrier separation in solar cells. *IEEE J. Photovoltaics* **5**, 461–469 (2015).

108. Bergmann, V. W. *et al.* Local Time-Dependent Charging in a Perovskite Solar Cell. *ACS Appl. Mater. Interfaces* **8**, 19402–19409 (2016).

109. Luo, D. Minimizing non-radiative recombination losses in perovskite solar cells. *Nat. Rev. Mater* **5**, 44-60 (2020).

110. Chen, J. & Park, N. Causes and Solutions of Recombination in Perovskite Solar Cells. *Adv. Mater* **31**, 1803019 (2019).

111. Neukom, M. T. Comprehensive Characterization and Modelling of Operation Mechanisms in Third Generation Solar Cells (2019).

112. Qin, J., Liu, X. K., Yin, C. & Gao, F. Carrier Dynamics and Evaluation of Lasing Actions in Halide Perovskites. *Trends Chem* **3**, 34–46 (2021).

113. Stranks, S. D. Nonradiative Losses in Metal Halide Perovskites. *ACS Energy Lett* **2**, 1515–1525 (2017).

114. Davies, C. L. *et al.* Bimolecular recombination in methylammonium lead triiodide perovskite is an inverse absorption process. *Nat. Commun* **9**, 1–9 (2018).

115. Davis, R. Fundamental constants: Big G revisited. *Nature* **468**, 181–183 (2010).

116. Auger, P. On the compound photoelectric effect. *J. phys. Radium* **6**, 205–208 (1925).

117. Tress, W. Perovskite Solar Cells on the Way to Their Radiative Efficiency Limit – Insights Into a Success Story of High Open-Circuit Voltage and Low Recombination. *Adv. Energy Mater* **7**, 1602358 (2017).

118. Pratheek, M., Abhinav, T., Bhattacharya, S., Chandra, G. K. & Predeep, P. Recent progress on defect passivation in perovskites for solar cell application. *Mater. Sci. Energy Technol* **4**, 282–289 (2021).

119. Ball, J. M. & Petrozza, A. Defects in perovskite-halides and their effects in solar cells. *Nat. Energy* **1**, 1-13 (2016).

120. Singh, S., Laxmi & Kabra, D. Defects in halide perovskite semiconductors: impact on photo-physics and solar cell performance. *J. Phys. D. Appl. Phys* **53**, 503003 (2020).

121. Aydin, E., Bastiani, M. & Wolf, S. Defect and Contact Passivation for Perovskite Solar Cells. *Adv. Mater* **31**, 1900428 (2019).

122. Dunfield, S. P. *et al.* From Defects to Degradation : A Mechanistic Understanding of Degradation in Perovskite Solar Cell Devices and Modules. *Adv. Energy Mater* **2**, 1–35 (2020).

123. Zhang, S. *et al.* Defect/Interface Recombination Limited Quasi-Fermi Level Splitting and Open-Circuit Voltage in Mono-and Triple-Cation Perovskite Solar Cells. *ACS Appl. Mater. Interfaces* **12**, 37647–37656 (2020).

124. Mali, S. S. & Hong, C. K. P-i-n/n-i-p type planar hybrid structure of highly efficient perovskite solar cells towards improved air stability: Synthetic strategies and the role

of p-type hole transport layer (HTL) and n-type electron transport layer (ETL) metal oxides. *Nanoscale* **8**, 10528–10540 (2016).

125. Al-Ashouri, A. *et al.* Conformal monolayer contacts with lossless interfaces for perovskite single junction and monolithic tandem solar cells. *Energy Environ. Sci* **12**, 3356–3369 (2019).

126. Mahmood, K., Sarwar, S. & Mehran, M. T. Current status of electron transport layers in perovskite solar cells: materials and properties. *RSC Adv* **7**, 17044–17062 (2017).

127. Lai, W. C., Lin, K. W., Guo, T. F., Chen, P. & Liao, Y. Y. Perovskite-based solar cells with inorganic inverted hybrid planar heterojunction structure. *AIP Adv* **8**, 015109 (2018).

128. Yang, G., Tao, H., Qin, P., Ke, W. & Fang, G. Recent progress in electron transport layers for efficient perovskite solar cells. *J. Mater. Chem. A* **4**, 3970–3990 (2016).

129. Chueh, C. C., Li, C. Z. & Jen, A. K. Y. Recent progress and perspective in solution-processed Interfacial materials for efficient and stable polymer and organometal perovskite solar cells. *Energy Environ. Sci* **8**, 1160–1189 (2015).

130. Saliba, M. *et al.* How to Make over 20% Efficient Perovskite Solar Cells in Regular (n-i-p) and Inverted (p-i-n) Architectures. *Chem. Mater* **30**, 4193–4201 (2018).

131. Stolterfoht, M. *et al.* Approaching the fill factor Shockley-Queisser limit in stable, dopant-free triple cation perovskite solar cells. *Energy Environ. Sci* **10**, 1530–1539 (2017).

132. Shen, H. *et al.* Mechanically-stacked perovskite/CIGS tandem solar cells with efficiency of 23.9% and reduced oxygen sensitivity. *Energy Environ. Sci* **11**, 394–406 (2018).

133. Paper, C. Determination of the surface recombination velocity of unpassivated silicon from spectral photoconductance measurements. In 3rd World Conference on Photovoltaic Energy Conversion, *IEEE* **1**, 71-74 (2003).

134. Snaith, H. J. *et al.* Anomalous Hysteresis in Perovskite Solar Cells. *J. Phys. Chem. Lett* **5**, 1511–1515 (2014).

135. Practices, B., Cell, P. S., Bad, M. & Look, C. Best Practices in Perovskite Solar Cell Efficiency Measurements. Avoiding the Error of Making Bad Cells Look Good. *J. Phys. Chem* **6**, 852-857 (2015).

136. Tress, W. Metal Halide Perovskites as Mixed Electronic–Ionic Conductors: Challenges and Opportunities—From Hysteresis to Memristivity. *J. Phys. Chem. Lett* **8**, 3106–3114 (2017).

137. Merdasa, A. *et al.* Impact of Excess Lead Iodide on the Recombination Kinetics in Metal Halide Perovskites. *ACS Energy Lett* **4**, 1370–1378 (2019).

138. DeQuilettes, D. W. *et al.* P*hoto-induced halide redistribution in organic-inorganic perovskite films*. *Nat. Commun* **7**, 1-9 (2016).

139. Tress, W. *et al.* Understanding the rate-dependent J-V hysteresis, slow time component, and aging in CH3NH3PbI3 perovskite solar cells: The role of a compensated electric field. *Energy Environ. Sci* **8**, 995–1004 (2015).

140. Ding, C. *et al.* Effect of the conduction band offset on interfacial recombination behavior of the planar perovskite solar cells. *Nano Energy* **53**, 17–26 (2018).

141. Nelson, C. A., Monahan, N. R. & Zhu, X. Exceeding the Shockley–Queisser limit in solar energy conversion. *Energy Environ. Sci* **6**, 3508–3519 (2013).

142. M. Chuang, Calculation and visualization tools for theoretical solar cell efficiencies based on the Shockley Queisser limit, (2019). www.github.com/marcus-cmc/Shockley-Queisser-limit (accessed March 5, 2020).

143. Shockley, W. & Queisser, H. J. Detailed balance limit of efficiency of p-n junction solar cells. *J. Appl. Phys* **32**, 510–519 (1961).

144. Kirchartz, T. & Rau, U. Detailed balance and reciprocity in solar cells. *Phys. Status Solidi Appl. Mater. Sci* **205**, 2737–2751 (2008).

145. Green, M. A. Radiative efficiency of state of the art photovoltaic cells. *Prog. Photovoltaics Res. Appl* **20**, 472-476 (2012).

146. Kirchartz, T., Mattheis, J., & Rau, U. Detailed balance theory of excitonic and bulk heterojunction solar cells. *Phys. Rev. B* **78**, 235320, 2008.

147. Wolff, C. M. *et al.* Reduced Interface-Mediated Recombination for High Open-Circuit Voltages in CH3NH3PbI3 Solar Cells. *Adv. Mater* **29**, 1700159 (2017).

148. Würfel, P. & Ruppel, W. The chemical potential of luminescent radiation. *J. Lumin* **24**–**25**, 925–928 (1981).

149. Rau, U. Reciprocity relation between photovoltaic quantum efficiency and electroluminescent emission of solar cells. *Phys. Rev. B* **76**, 1–8 (2007).

150. Ross, R. T. Some thermodynamics of photochemical systems. *J. Chem. Phys* **46**, 4590–4593 (1967).

151. Kirchartz, T. & Rau, U. What Makes a Good Solar Cell? *Adv. Energy Mater* **8**, 1703385. (2018).

152. Caprioglio, P. *et al.* On the Relation between the Open-Circuit Voltage and Quasi-Fermi Level Splitting in Efficient Perovskite Solar Cells. *Adv. Energy Mater* **9**, 1901631 (2019).

153. Stolterfoht, M. *et al.* How To Quantify the Efficiency Potential of Neat Perovskite Films: Perovskite Semiconductors with an Implied Efficiency Exceeding 28%. *Adv. Mater* **32**, 2000080 (2020).

154. Barkhouse, D. A. R., Gunawan, O., Gokmen, T., Todorov, T. K. & Mitzi, D. B. Yield predictions for photovoltaic power plants:empirical validation, recent advances and

remaining uncertainties. *Prog. Photovoltaics Res. Appl* **20**, 6–11 (2015).

155. Jošt, M., Kegelmann, L., Korte, L. & Albrecht, S. Monolithic Perovskite Tandem Solar Cells: A Review of the Present Status and Advanced Characterization Methods Toward 30% Efficiency. *Adv. Energy Mater* **10**, 1904102 (2020).

156. Lal, N. N. *et al.* Perovskite Tandem Solar Cells. *Adv. Energy Mater* **7**. 1602761 (2017).

157. Bailie, C. D., Mailoa, J. P., America, N. & Unger, E. L. Semi-transparent Perovskite Solar Cells for Tandems with Silicon and CIGS. *Energy Environ. Sci* **8**, 956-963 (2015).

158. Bush, K. A. *et al.* Minimizing Current and Voltage Losses to Reach 25 % -Efficient Monolithic Two- Terminal Perovskite-Silicon Tandem Solar Cells. *ACS Energy Lett* **3**, 2173-2180 (2018).

159. Al-Ashouri, A. *et al.* Monolithic perovskite/silicon tandem solar cell with >29% efficiency by enhanced hole extraction. *Science* **370**, 1300–1309 (2020).

160. Gota, F., Langenhorst, M., Schmager, R., Lehr, J. & Paetzold, U. W. Energy Yield Advantages of Three-Terminal Perovskite-Silicon Tandem Photovoltaics. *Joule* **4**, 2387–2403 (2020).

161. Tockhorn, P. *et al.* Three-Terminal Perovskite/Silicon Tandem Solar Cells with Top and Interdigitated Rear Contacts. *ACS Appl. Energy Mater* **3**, 1381–1392 (2020).

162. Warren, E. L. *et al.* Maximizing tandem solar cell power extraction using a three-terminal design. *Sustain. Energy Fuels* **2**, 1141–1147 (2018).

163. Bett, A. J. *et al.* Semi-Transparent Perovskite Solar Cells with ITO Directly Sputtered on Spiro-OMeTAD for Tandem Applications. *ACS Appl. Mater. Interfaces* **11**, 45796–45804 (2019).

164. Santbergen, R. *et al.* Minimizing optical losses in monolithic perovskite/c-Si tandem solar cells with a flat top cell. *Opt. Express* **24**, A1288 (2016).

165. Prochowicz, D. *et al.* Engineering of Perovskite Materials Based on Formamidinium and Cesium Hybridization for High-Efficiency Solar Cells. *Chem. Mater* **31**, 1620-1627 (2019).

166. Caprioglio, P. *et al.* perovskitMonolithice/silicon tandem solar cell with >29% efficiency by enhanced hole extraction. *Science* **370**, 1300–1309 (2020).

167. Schultes, M. *et al.* Sputtered Transparent Electrodes (IO:H and IZO) with Low Parasitic Near-Infrared Absorption for Perovskite–Cu(In,Ga)Se2 Tandem Solar Cells. *ACS Appl. Energy Mater* **2**, 7823–7831 (2019).

168. Palmstrom. A. S. *et al.* Interfacial Effects of Tin Oxide Atomic Layer Deposition in Metal Halide Perovskite Photovoltaics. *Adv. Energy Mater* **8**, 1800591 (2018).

169. Hossain, I. M. Semitransparent perovskite solar cells for perovskite-based tandem photovoltaics. Doctoral dissertation, Karlsruher Institut für Technologie (KIT) (2021).

170. Manzoor, S. *et al.* Improved light management in planar silicon and perovskite solar cells using PDMS scattering layer. *Sol. Energy Mater. Sol. Cells* **173**, 59–65 (2017).

171. Langenhorst, M. *et al.* Liquid Glass for Photovoltaics: Multifunctional Front Cover Glass for Solar Modules. *ACS Appl. Mater. Interfaces* **11**, 35015–35022 (2019).

172. Schmager, R. *et al.* Texture of the Viola Flower for Light Harvesting in Photovoltaics. *ACS Photonics* **4**, 2687–2692 (2017).

173. Dottermusch, S. *et al.* Micro-cone textures for improved light in-coupling and retroreflection-inspired light trapping at the front surface of solar modules. *Prog. Photovoltaics Res. Appl* **27**, 3133 (2019).

174. Haase, F. *et al.* Laser contact openings for local poly-Si-metal contacts enabling 26.1%-efficient POLO-IBC solar cells. *Sol. Energy Mater. Sol. Cells* **186**, 184–193 (2018).

175. Jackson, P. *et al.* Properties of Cu(In,Ga)Se2 solar cells with new record efficiencies up to 21.7%. *Phys. Status Solidi - Rapid Res. Lett* **9**, 28–31 (2015).

176. Phung, N. *et al.* Enhanced Self-Assembled Monolayer Surface Coverage by ALD NiO in p-i-n Perovskite Solar Cells. *ACS Appl. Mater. Interfaces* **14**, 2166–2176 (2022).

177. J. Tauc: Optical Properties and Electronic Structure of Amorphous Ge and Si. *Materials Research Bulletin*, 3:37 (1968).

178. Makuła, P., Pacia, M. & Macyk, W. How To Correctly Determine the Band Gap Energy of Modified Semiconductor Photocatalysts Based on UV-Vis Spectra. *J. Phys. Chem. Lett* **9**, 6814–6817 (2018).

179. Abou-Ras, D., Kirchartz, T. & Rau, U. *Advanced Characterization Techniques for Thin Film Solar Cells*. *John Wiley & Sons* (2016).

180. Tress, W. *et al.* Interpretation and evolution of open-circuit voltage, recombination, ideality factor and subgap defect states during reversible light-soaking and irreversible degradation of perovskite solar cells. *Energy Environ. Sci* **11**, 151–165 (2018).

181. Caprioglio, P. *et al.* On the Origin of the Ideality Factor in Perovskite Solar Cells. *Adv. Energy Mater* **10**, 2000502 (2020).

182. Gharibzadeh, S. *et al.* Record Open-Circuit Voltage Wide-Bandgap Perovskite Solar Cells Utilizing 2D/3D Perovskite Heterostructure. *Adv. Energy Mater* **9**, 1803699 (2019).

183. Rühle, S. The detailed balance limit of perovskite/silicon and perovskite/CdTe tandem solar cells. *Phys. Status Solidi Appl. Mater. Sci* **214**, 1600955 (2017).

184. Hörantner, M. T. *et al.* The Potential of Multijunction Perovskite Solar Cells. *ACS Energy Lett* **2**, 2506–2513 (2017).

185. Wang, Z. *et al.* Efficient ambient-air-stable solar cells with 2D-3D heterostructured butylammonium-caesium-formamidinium lead halide perovskites. *Nat. Energy* **2**, 1–10 (2017).

186. Yu, Y. *et al.* Synergistic Effects of Lead Thiocyanate Additive and Solvent Annealing on the Performance of Wide-Bandgap Perovskite Solar Cells. *ACS Energy Lett* **2**, 1177–1182 (2017).

187. Wang, L. *et al.* Potassium-Induced Phase Stability Enables Stable and Efficient Wide-Bandgap Perovskite Solar Cells. *Sol. RRL* **4**, 1–10 (2020).

188. Brennan, M. C., Draguta, S., Kamat, P. V. & Kuno, M. Light-Induced Anion Phase Segregation in Mixed Halide Perovskites. *ACS Energy Lett* **3**, 204–213 (2018).

189. Hoke, E. T. *et al.* Reversible photo-induced trap formation in mixed-halide hybrid perovskites for photovoltaics. *Chem. Sci* **6**, 613–617 (2015).

190. Wang, N. *et al.* Defect passivation of grain surface toward perovskite solar cells with a high open-circuit voltage exceeding 1.16 V. *J. Appl. Phys* **128**, 044504, (2020).

191. Knight, A. J. *et al.* Preventing phase segregation in mixed-halide perovskites: a perspective. *Energy Environ. Sci* **13**, 2024-2046 (2020).

192. Chen, P. *et al.* In Situ Growth of 2D Perovskite Capping Layer for Stable and Efficient Perovskite Solar Cells. *Adv. Funct. Mater* **28**, 1706923 (2018).

193. Koh, T. M. *et al.* Enhancing moisture tolerance in efficient hybrid 3D/2D perovskite photovoltaics. *J. Mater. Chem. A* **6**, 2122–2128 (2018).

194. Nayak, P. K., Bisquert, J. & Cahen, D. Assessing possibilities and limits for solar cells. *Adv. Mater* **23**, 2870–2876 (2011).

195. Braly, I. L. *et al.* Hybrid perovskite films approaching the radiative limit with over 90% photoluminescence quantum efficiency. *Nat. Photonics* **12**, 355–361 (2018).

196. Hu, J. *et al.* Synthetic control over orientational degeneracy of spacer cations enhances solar cell efficiency in two-dimensional perovskites. *Nat. Commun* **10**, 1–11 (2019).

197. Tsai, H. *et al.* High-efficiency two-dimensional ruddlesden-popper perovskite solar cells. *Nature* **536**, 312–317 (2016).

198. Abbas, M. S. *et al.* Orientationally engineered 2D/3D perovskite for high efficiency solar cells. *Sustain. Energy Fuels* **4**, 324–330 (2019).

199. Li, M. H. *et al.* Highly Efficient 2D/3D Hybrid Perovskite Solar Cells via Low-Pressure Vapor-Assisted Solution Process. *Adv. Mater* **30**, 1–13 (2018).

200. Nie, L., Ke, X. & Sui, M. Microstructural study of two-dimensional organic-inorganic hybrid perovskite nanosheet degradation under illumination. *Nanomaterials* **9**, 15–21 (2019).

201. Cohen, B. El, Wierzbowska, M. & Etgar, L. High efficiency quasi 2D lead bromide perovskite solar cells using various barrier molecules. *Sustain. Energy Fuels* **1**, 1935–1943 (2017).

202. Duong, T. *et al.* High Efficiency Perovskite-Silicon Tandem Solar Cells : Effect of Surface Coating versus Bulk Incorporation of 2D Perovskite. Adv. Energy Mater **10**,1903553 (2020).

203. Yang, G. *et al.* Stable and low-photovoltage-loss perovskite solar cells by multifunctional passivation. *Nat. Photonics* **15**, 681–689 (2021).

204. Blancon, J. C. *et al.* Extremely efficient internal exciton dissociation through edge states in layered 2D perovskites. *Science* **355**, 1288–1292 (2017).

205. Weidman, M. C., Seitz, M., Stranks, S. D. & Tisdale, W. A. Highly Tunable Colloidal Perovskite Nanoplatelets through Variable Cation, Metal, and Halide Composition. *ACS Nano* **10**, 7830–7839 (2016).

206. Duong, T. *et al.* Efficient and stable wide bandgap perovskite solar cells through surface passivation with long alkyl chain organic cations. *J. Mater. Chem. A* **9**, 18454–18465 (2021).

207. P, L. G., Drozdov, V. A., Sedanova, A. V & Kornienko, N. V. An X-ray Photoelectron Spectroscopic Study of the Poly -N- vinylpyrrolidone Desorption from the Surface of a Granulated Carbon Sorbent. *Russian Journal of Applied Chemistry* **92**, 940–945 (2019).

208. Huang, W. Controllable transformation between 3D and 2D perovskites through cation exchange. *Chem. Comm* **54**, 7944–7947 (2018).

209. Milosavljević, A. R., Huang, W., Sadhu, S. & Ptasinska, S. Low-Energy Electron-Induced Transformations in Organolead Halide Perovskite. *Angew. Chemie - Int. Ed* **55**, 10083–10087 (2016).

210. Zhou, Q. *et al.* High-Performance Perovskite Solar Cells with Enhanced Environmental Stability Based on a (p-FC6H4C2H4NH3)2[PbI4] Capping Layer. *Adv. Energy Mater* **9**, 1802595 (2019).

211. Hauschild, D. *et al.* Impact of n -Butylammonium Bromide on the Chemical and Electronic Structure of Double-Cation Perovskite Thin Films. *ACS Appl. Mater. Interfaces* **13**, 53202-53210 (2021).

212. Sutanto, A. A. *et al.* 2D / 3D Perovskite Engineering Eliminates Interfacial Recombination Losses in Hybrid Perovskite Solar Cells. *Chem* **7**, 903-1916 (2021).

213. Liu, J., Leng, J., Wu, K., Zhang, J. & Jin, S. Observation of internal photoinduced electron and hole separation in hybrid two-dimentional perovskite films. *J. Am. Chem. Soc* **139**, 1432–1435 (2017).

214. Wolff, C. M., Caprioglio, P., Stolterfoht, M. & Neher, D. Nonradiative Recombination in Perovskite Solar Cells: The Role of Interfaces. *Adv. Mater* **31**, 1902762 (2019).

215. Menda, U. D. *et al.* High-performance wide bandgap perovskite solar cells fabricated in ambient high-humidity conditions. *Mater. Adv* **2**, 6344–6355 (2021).

216. Gharibzadeh, S. *et al.* 2D/3D Heterostructure for Semitransparent Perovskite Solar Cells with Engineered Bandgap Enables Efficiencies Exceeding 25% in Four-Terminal Tandems with Silicon and CIGS. *Adv. Funct. Mater* **30**, 1909919 (2020).

217. Levine, I. *et al.* Deep Defect States in Wide-Band-Gap ABX 3 Halide Perovskites. *ACS Energy Lett* **4**, 1150–1157 (2019).

218. Yang, T. C. J., Fiala, P., Jeangros, Q. & Ballif, C. High-Bandgap Perovskite Materials for Multijunction Solar Cells. *Joule* **2**, 1421–1436 (2018).

219. Chen, B. *et al.* Enhanced optical path and electron diffusion length enable high-ef fi ciency perovskite tandems. *Nat. commun* 11, 1-9 (2020).

220. Kim, D. H. *et al.* Bimolecular Additives Improve Wide-Band-Gap Perovskites for Efficient Tandem Solar Cells with CIGS. *Joule* **3**, 1734–1745 (2019).

221. Liu, Y. *et al.* Ultrahydrophobic 3D/2D fluoroarene bilayer-based water-resistant perovskite solar cells with efficiencies exceeding 22%. *Sci. Adv* **5**, 1–9 (2019).

222. Zhu, H. *et al.* Synergistic Effect of Fluorinated Passivator and Hole Transport Dopant Enables Stable Perovskite Solar Cells with an Efficiency near 24%. *J. Am. Chem. Soc* **143**, 3231-3237 (2021) .

223. Unger, E. L. *et al.* Roadmap and roadblocks for the band gap tunability of metal halide perovskites. *J. Mater. Chem. A* **5**, 11401–11409 (2017).

224. Tong, C. *et al.* Modeling the edge effect for measuring the performance of mesoscopic solar cells with shading masks. *J. Mater. Chem. A* **7**, 10942–10948 (2019).

225. Duong, T. *et al.* Semitransparent Perovskite Solar Cell With Sputtered Front and Rear Electrodes for a Four-Terminal Tandem. *IEEE J. Photovoltaics* **6**, 679–687 (2016).

226. Jaysankar, M. *et al.* Perovskite-silicon tandem solar modules with optimised light harvesting. *Energy Environ. Sci* **11**, 1489–1498 (2018).

227. Han, Q. *et al.* High-performance perovskite/Cu(In,Ga)Se 2 monolithic tandem solar cells. *Science* **361**, 904–908 (2018).

228. Gharibzadeh, S. *et al*.Two birds with one stone: dual grain-boundary and interface passivation enable> 22% efficient inverted methylammonium-free perovskite solar cells *Energy Environ. Sci* **14**. 5875-5893 (2021).

229. Drigo, N. *et al.* Doped but Stable: Spirobisacridine Hole Transporting Materials for Hysteresis-Free and Stable Perovskite Solar Cells. *J. Am. Chem. Soc* **142**, 1792–1800 (2020).

230. Seo, J. Y. *et al.* Novel p-dopant toward highly efficient and stable perovskite solar cells. *Energy Environ. Sci* **11**, 2985–2992 (2018).

231. Chen, B., Yang, M., Priya, S. & Zhu, K. Origin of J-V Hysteresis in Perovskite Solar Cells. *JJ. Phys. Chem. Lett* **7**, 905–917 (2016).

232. Sarritzu, V. *et al.* Optical determination of Shockley-Read-Hall and interface recombination currents in hybrid perovskites. *Sci. Rep* **7**, 1–10 (2017).

233. Kirchartz, T., Márquez, J. A., Stolterfoht, M. & Unold, T. Photoluminescence-Based Characterization of Halide Perovskites for Photovoltaics. *Adv. Energy Mater.* **10**, 1904134 (2020).

234. Shao, Y. *et al.* Grain boundary dominated ion migration in polycrystalline organic-inorganic halide perovskite films. *Energy Environ. Sci* **9**, 1752–1759 (2016).

235. Pokharel, J. *et al.* Grain Boundary Defect Passivation of Triple Cation Mixed Halide Perovskite with Hydrazine-Based Aromatic Iodide for Efficiency Improvement. *ACS Appl. Mater. Interfaces* **12**, 41312-41322(2020).

236. Liu, S. *et al.* A Review on Additives for Halide Perovskite Solar Cells. *Adv. Energy Mater* **13***.* 1902492 (2019).

237. Li, F. *et al.* Regulating Surface Termination for Efficient Inverted Perovskite Solar Cells with Greater Than 23% Efficiency. *J. Am. Chem. Soc* **142**, 20134-20142 (2020)

238. Degani, M. *et al.* 23 . 7 % Efficient inverted perovskite solar cells by dual interfacial modification. *Sci. Adv* **7**, 7930 (2021).

239. Liu, X. *et al.* Full Defects Passivation Enables 21% Efficiency Perovskite Solar Cells Operating in Air. *Adv. Energy Mater* **10**, 2001958 (2020).

240. Isikgor, F. H. *et al.* Concurrent cationic and anionic perovskite defect passivation enables 27.4% perovskite/silicon tandems with suppression of halide segregation. *Joule* **5**, 1566–1586 (2021).

241. Yoo, J. J. *et al.* An interface stabilized perovskite solar cell with high stabilized efficiency and low voltage loss. *Energy Environ. Sci* **12**, 2192–2199 (2019).

242. Mahmud, M. A. *et al.* Double-Sided Surface Passivation of 3D Perovskite Film for High-Efficiency Mixed-Dimensional Perovskite Solar Cells. *Adv. Funct. Mater* **30**, 1907962 (2020).

243. Jeong, M. *et al.* Stable perovskite solar cells with efficiency exceeding 24.8% and 0.3-V voltage loss. *Science* **1620**, 1615–1620 (2020).

244. Tan, S. *et al.* Shallow Iodine Defects Accelerate the Degradation of α-Phase Formamidinium Perovskite. *Joule* **4**, 2426–2442 (2020).

245. Krückemeier, L., Krogmeier, B., Liu, Z., Rau, U. & Kirchartz, T. Understanding Transient Photoluminescence in Halide Perovskite Layer Stacks and Solar Cells. *Adv. Energy Mater* **11**, 2003489 (2021).

246. Fassl, P. *et al.* Revealing the internal luminescence quantum efficiency of perovskite

films via accurate quantification of photon recycling. *Matter* **4**, 1391–1412 (2021).

247. Zhang, S. *et al.* Defect/Interface Recombination Limited Quasi-Fermi Level Splitting and Open-Circuit Voltage in Mono- and Triple-Cation Perovskite Solar Cells. *ACS Appl. Mater. Interfaces* **12**, 37647–37656 (2020).

248. Wu, W., Rudd, P. N., Wang, Q., Yang, Z. & Huang, J. Blading Phase-Pure Formamidinium-Alloyed Perovskites for High-Efficiency Solar Cells with Low Photovoltage Deficit and Improved Stability. *Adv. Mater* **32**, 2000995 (2020).

249. Fei, C., Zhou, M., Ogle, J., Smilgies, D. & Whittaker-, L. Self-assembled propylammonium cations at grain boundaries and the film surface to improve the efficiency and stability of perovskite solar cells. *J. Mater. Chem* **7**, 23739–23746 (2019).

250. Castro-Méndez, A., Hidalgo, J. & Correa-Baena, J. The Role of Grain Boundaries in Perovskite Solar Cells. *Adv. Energy Mater* **9**, 1901489 (2019).

251. Jin, H. *et al.* It's a trap! On the nature of localised states and charge trapping in lead halide perovskites. *Mater. Horizons* **7**, 397-410 (2020).

252. Wu, W. *et al.* Reducing Surface Halide Deficiency for Efficient and Stable Iodide-Based Perovskite Solar Cells. *J. Am. Chem. So*c **42**, 3989-3996 (2020)

253. Lee, J.-W. *et al.* The role of grain boundaries in perovskite solar cells. *Mater. Today Energy* **7**, 149–160 (2018).

254. Bube, R. H. Trap Density Determination by Space-Charge-Limited Currents. *J. Appl. Phys* **33**, 1733–1737 (1962).

255. Green, M. A. & Ho-Baillie, A. W. Y. Pushing to the Limit: Radiative Efficiencies of Recent Mainstream and Emerging Solar Cells. *ACS Energy Lett* **4**, 1639–1644 (2019).

256. Duong, T. *et al.* High Efficiency Perovskite-Silicon Tandem Solar Cells: Effect of Surface Coating versus Bulk Incorporation of 2D Perovskite. *Adv. Energy Mater.* **10**, 1903553 (2020).

257. Li, Z. *et al.* Minimized surface deficiency on wide-bandgap perovskite for efficient indoor photovoltaics. *Nano Energy* **78**, 105377 (2020).

258. Zhu. T. *et al.* PEAI-Based Interfacial Layer for High-Efficiency and Stable Solar. *ACS Appl. Mater. Interfaces* **12**,37197-37207 (2020).

259. Moghadamzadeh, S. *et al.* Triple-cation low-bandgap perovskite thin-films for high-efficiency four-terminal all-perovskite tandem solar cells. *J. Mater. Chem* **8**, 24608–24619 (2020).

260. Yang, X. *et al.* Superior Carrier Lifetimes Exceeding 6 µ s in Polycrystalline Halide Perovskites. *Adv. Mater* **32**, 2002585 (2020).

261. Guthrey, H. & Moseley, J. A Review and Perspective on Cathodoluminescence

Analysis of Halide Perovskites. *Adv. Energy Mater* **10**, 1903840 (2020).

262. Wang, H. *et al.* Interfacial Residual Stress Relaxation in Perovskite Solar Cells with Improved Stability. *Adv. Mater* **31**, 1–10 (2019).

263. Groeneveld, B. G. H. M. *et al.* Stable Cesium Formamidinium Lead Halide Perovskites : A Comparison of Photophysics and Phase Purity in Thin Films and Single Crystals. *Energy Technol* **8**, 1901041 (2020).

264. Jiang, Q. *et al.* Surface passivation of perovskite film for efficient solar cells. *Nat. Photonics* **13**, 460–466 (2019).

265. Dong, H. *et al.* A Modulated Double-Passivation Strategy Toward Highly Efficient Perovskite Solar Cells with Efficiency Over 21 %. *Solar RRL* **3**, 1900291 (2019).

266. Zhang, F. *et al.* Growth of Amorphous Passivation Layer Using Phenethylammonium Iodide for High-Performance Inverted Perovskite Solar Cells. *Sol. RRL* **4**, 1900243 (2020).

267. Cho, K. T. *et al.* Selective growth of layered perovskites for stable and efficient photovoltaics. *Energy Environ. Sci* **11**, 952–959 (2018).

268. Du, K. *et al.* Two-Dimensional Lead(II) Halide-Based Hybrid Perovskites Templated by Acene Alkylamines: Crystal Structures, Optical Properties, and Piezoelectricity. *Inorg.chem* **56**, 9291-9302 (2017).

269. Thirumal, K. *et al.* Morphology-Independent Stable White-Light Emission from Self-Assembled Two-Dimensional Perovskites Driven by Strong Exciton − Phonon Coupling to the Organic Framework. *Chem. Mater* **29**, 3947-3953 (2017).

270. Br, C. H. C. H. N. H. P., Phys, A. & Cai, P. Bluish-white-light-emitting diodes based on two-dimensional lead halide perovskite. *Appl. Phys. Lett* **112**, 153901 (2019).

271. Chen, X. *et al.* Impact of Layer Thickness on the Charge Carrier and Spin Coherence Lifetime in Two- Dimensional Layered Perovskite Single Crystals. *ACS Energy Lett* **3**, 2273-2279 (2018).

272. Béchu, S., Ralaiarisoa, M., Etcheberry, A. & Schulz, P. Photoemission Spectroscopy Characterization of Halide Perovskites. *Adv. Ene. Mater* **10**, 1904007 (2020).

273. Fassl, P. *et al.* Fractional deviations in precursor stoichiometry dictate the properties, performance and stability of perovskite photovoltaic devices. *Energy Environ. Sci* **11**, 3380-3391 (2018).

274. Liu, Z., Cao, F., Wang, M., Wang, M. & Li, L. Observing Defect Passivation of the Grain Boundary with 2- Aminoterephthalic Acid for Efficient and Stable Perovskite Solar Cells Research Articles. *Angewandte* **10**, 4161–4167 (2020).

275. Noel, N. K. *et al.* Environmental Science Interfacial charge-transfer doping of metal halide perovskites for high performance photovoltaics†. *Energy Environ. Sci* **12**, 3063-3073 (2019).

276. Hellmann, T. *et al.* The Electronic Structure of MAPI-Based Perovskite Solar Cells : Detailed Band Diagram Determination by Photoemission Spectroscopy Comparing Classical and Inverted Device Stacks. *Adv. Energy Mater* **10**, 2002129 (2020).

277. Zhang, C. *et al.* Fabrication Strategy for Efficient 2D/3D Perovskite Solar Cells Enabled by Diffusion Passivation and Strain Compensation. *Adv. Energy Mater* **10**, 2002004 (2020).

278. Lee, K. *et al.* A highly stable and efficient carbon electrode-based perovskite solar cell achieved via interfacial growth of 2D PEA2PbI4 perovskite. *J. Mater. Chem* **6**, 24560-24568 (2018).

279. Luo, D., Yang, W., Wang, Z., Sadhanala, A. & Hu, Q. Enhanced photovoltage for inverted planar heterojunction perovskite solar cells. *Science* **1446**, 1442–1446 (2018).

280. Draguta, S. . *et al.* A quantitative and spatially resolved analysis of the performance-bottleneck in high efficiency, planar hybrid perovskite solar cells, *Energy Environ. Sci* **11**, 960–969 (2018).

281. Xiong, S. *et al.* Direct observation on p- to n-type transformation of perovskite surface region during defect passivation driving high photovoltaic efficiency. *Joule* **5**, 467–480 (2020).

282. Emara, J. *et al.* Impact of Film Stoichiometry on the Ionization Energy and Electronic Structure of CH3NH3PbI3 Perovskites. *Adv. Mater* **28**, 553-559 (2016).

283. Wol, C. M. *et al.* Perfluorinated Self-Assembled Monolayers Enhance the Stability and Efficiency of Inverted Perovskite Solar Cells. *ACS nano* **14**, 1445-1456 (2020).

284. Wang, Q., Dong, Q., Li, T., Gruverman, A. & Huang, J. Thin Insulating Tunneling Contacts for Efficient and Water-Resistant Perovskite Solar Cells. *Adv. Mater* **28**, 553-559 (2016).

285. Stolterfoht, M. *et al.* Visualization and suppression of interfacial recombination for high-efficiency large-area pin perovskite solar cells. *Nat. Energy* **3**, 847–854 (2018).

286. Zhai, H. *et al.* 2D PEA2PbI4-3D MAPbI3Composite Perovskite Interfacial Layer for Highly Efficient and Stable Mixed-Ion Perovskite Solar Cells. *ACS Appl. Energy Mater* **12**, 13482-13491 (2021).

287. Lanzoni, E. M. *et al.* The impact of Kelvin probe force microscopy operation modes and environment on grain boundary band bending in perovskite and Cu(In,Ga)Se2 solar cells. *Nano Energy* **88**, 10627 (2021).

288. Axt, A., Hermes, I. M., Bergmann, V. W., Tausendpfund, N. & Weber, S. A. L. Know your full potential : Quantitative Kelvin probe force microscopy on nanoscale electrical devices. *Beilstein J. Nanotechnol* **9**, 1809–1819 (2018).

289. Garrett, J. L. & Munday, J. N. Fast, high-resolution surface potential measurements in air with heterodyne Kelvin probe force microscopy. *Nanotechnol* **27**, 245705

(2016).

290. Caputo, M. *et al.* Electronic structure of MAPbI3 and MAPbCl3 : importance of band alignment. *Sci. Rep* **9**, 1–11 (2019).

291. Sun, Y. *et al.* Band Structure Engineering of Interfacial Semiconductors Based on Atomically Thin Lead Iodide Crystals. *Adv.Mater* **31**, 1806562 (2019).

292. You, A., Be, M. A. Y. & In, I. Electronic transport in polycrystalline films. **2660**, (2014).

293. Cao, D. H. *et al.* Remnant PbI2, an unforeseen necessity in high-efficiency hybrid perovskite-based solar. *Apl Materials* **2**, 091101 (2014).

294. Xie, Y. *et al.* Synergistic E ff ect of Pseudo-Halide Thiocyanate Anion and Cesium Cation on Realizing High-Performance Pinhole-Free MA-Based Wide-Band Gap Perovskites, *ACS Appl. Mater. Interfaces* **9**, 6072-6078 (2019).

295. Yang, W. S., Noh, J. H., Seo, J., Seok, S. Il & Ho-baillie, A. Spatial Distribution of Lead Iodide and Local Passivation on Organo- Lead Halide Perovskite. *ACS Appl. Mater. Interfaces* **9**, 6072-6078 (2017).

296. Reza, K. M. *et al.* Grain Boundary Defect Passivation in Quadruple Cation Wide-Bandgap Perovskite Solar Cells. *Sol. RRL* **5**,2000740 (2021).

297. Gallet, T. *et al.* Co-evaporation of CH 3 NH 3 PbI 3 : How Growth Conditions Impact Phase Purity, Photostriction, and Intrinsic Stability, *ACS Appl. Mater. Interfaces* **13**, 2642-2653 (2021).

298. Toth, D. *et al.* Nanoscale Charge Accumulation and Its Effect on Carrier Dynamics in Tri-cation Perovskite Structures. *ACS Appl. Mater. Interfaces* **12**, 48057-48066 (2020).

299. Phung, N. *et al.* The Role of Grain Boundaries on Ionic Defect Migration in Metal Halide Perovskites. *Adv. Energy Mater* **10**, 1903735 (2020).

300. Park, J. & Walsh, A. Modeling Grain Boundaries in Polycrystalline Halide Perovskite Solar Cells. arXiv preprint, 2004.04416 (2021).

301. Kim, D. *et al.* Probing Facet-Dependent Surface Defects in MAPbI3 Perovskite Single Crystals. *J. Phys. Chem. C* **123**, 14144–14151 (2019).

302. Gallet, T., Grabowski, D., Kirchartz, T. & Redinger, A. Fermi-level pinning in methylammonium lead iodide perovskites. *Nanoscale* **11**, 16828–16836 (2019).

303. Zheng, X. *et al.* Defect passivation in hybrid perovskite solar cells using quaternary ammonium halide anions and cations, *Nat. Energy*. **17102**, 1–9 (2017).

304. Tan, S. *et al.* Steric Impediment of Ion Migration Contributes to Improved Operational Stability of Perovskite Solar Cells. *Adv. Mater* **32**, 1–11 (2020).

305. Lee, J. W. *et al.* 2D perovskite stabilized phase-pure formamidinium perovskite solar cells. *Nat. Commun* **9**, 1–10 (2018).

306. Yang, S. *et al.* Stabilizing halide perovskite surfaces for solar cell operation with wide-bandgap lead oxysalts. *Science* **478**, 473–478 (2019).

307. Koh. T. M. *et al.* Enhancing moisture tolerance in efficient hybrid 3D/2D perovskite photovoltaics M. *J. Mat. Chem. A* **5**,2122–2128 (2018).

308. Jiang, Q. *et al.* Planar-Structure Perovskite Solar Cells with Efficiency beyond 21%. *Adv. Mater* **29**, 1–7 (2017).

309. Chen, H. *et al.* Quantum-size-tuned heterostructures enable efficient and stable inverted perovskite solar cells. *Nat. Photonics* **16**, 352-358 (2022).

List of Publications and Conference Contributions

Peer-reviewed publications (first author)

S. Gharibzadeh[*], P. Fassl[*], I. M. Hossain, P. Rohrbeck, M. Frericks, M. Schmidt, T Duong, M. Rahman Khan, T, Abzieher, B. Abdollahi Nejand, F. Schackmar, O. Almora, T. Feeney, R. Singh, U. Lemmer, J. P. Hofmann, S. A.L. Weber, U. W. Paetzold, One Bird with Two Stones: Dual Grain-Boundary and Interface Passivation Enables > 22% Efficient Inverted Methylammonium-Free Perovskite Solar Cells, *Energy & Environmental Science*, 14, 5875-5893, 2021.

S. Gharibzadeh[*], I. M. Hossain[*], P. Fassl, B. Abdollahi Nejand, T. Abzieher, M. Schultes, E. Ahlswede, P. Jackson, M. Powalla, S. Schäfer, M. Rienäcker, T. Wietler, R. Peibst, U. Lemmer, B. S. Richards, U. W. Paetzold, 2D/3D Heterostructure for Semitransparent Perovskite Solar Cells with Engineered Bandgap Enables Efficiencies Exceeding 25% in Four-Terminal Tandems with Silicon and CIGS. *Advanced Functional Material*s, 30, 1909919, 2020.

S. Gharibzadeh, B. Abdollahi Nejand, M. Jakoby, T. Abzieher, D. Hauschild, S. Moghadamzadeh, J. A. Schwenzer, P. Brenner, R. Schmager, A. A. Haghighirad, L. Weinhardt, U. Lemmer, B. S. Richards, I. A. Howard, U. W. Paetzold, Record Open-Circuit Voltage Wide-Bandgap Perovskite Solar Cells Utilizing 2D/3D Perovskite Heterostructure. *Advanced Energy Materials*, 9, 1803699, 2019.

Peer-reviewed publications (co-author)

I. M. Hossain, T. Feeney, S. Gharibzadeh, F. Gota, R. Singh, P. Fassl, A. Mertens, J.P. Becker, S. Paetel, E. Ahlswede, U. W. Paetzold, Mastering perovskite-on-CIGS four-terminal tandem solar cells: unveiling the path to achieve over 27% in power conversion efficiency, Under submission.

B. Abdollahi Nejand, D. B. Ritzer, H. Hu, R. Schmager, S. Moghadamzadeh, T. Feeney, R. Singh, R. Azmi, F. Laufer, F. Schackmar, T. Abzieher, S. Gharibzadeh, E. Ahlswede, U. Lemmer, B. S. Richards, and U. W. Paetzold, High-Efficiency Monolithic All-Perovskite Tandem Solar Mini-Modules, Nature Energy, 2022.

M. A. Ruiz-Preciado, F. Gota, I.M. Hossain, P. Fassl, F. Laufer, T. Feeney, A. Farag, I. Allegro, H. Hu, S. Gharibzadeh, B. Abdollahi, V. S. Gevaerts, M. Simor, P.J. Bolt, U. W. Paetzold. Acs Energy Letter, 2022.

M. Kaiser, Y. Li, S. Gharibzadeh, B.S. Richards, U. W. Paetzold, I.A. Howard. Charge Carrier and Exciton Dynamics in Perovskites Revealed by Time-integrated Photoluminescence after Double-Pulse Excitation, Advanced Materials Technologies, 2022.

H. Eggers, S. Gharibzadeh. S. Koch, F. Schackmar, D. Ritzer, T. Abzieher, B. S. Richards, C. Erban, U. W. Paetzold, Perovskite Solar Cells with Vivid, Angle-Invariant and Customizable Inkjet-Printed Colorization for Building-Integrated Photovoltaics, Sol. RRL, 6, 2100897, 2022.

D. Hauschild, L. Seitz, S. Gharibzadeh, R. Steininger, N. Jiang, W. Yang, U. Wilhelm Paetzold, C. Heske, and L. Weinhardt, Impact of n-Butylammonium Bromide on the Chemical and Electronic Structure of Double-Cation Perovskite Thin Films, ACS Applied Materials & Interfaces, 1344, 53202, 2021.

R. Singh, E. Madirov, D. Busko, I.M Hossain, V.A. Konyushkin, A.N. Nakladov, S. V. Kuznetsov, A. Farooq, S. Gharibzadeh, U.W Paetzold, B.S Richards, A.Turshatov, Harvesting sub-bandgap photons by up-conversion for perovskite solar cells, ACS Applied Materials & Interfaces, 13, 54874-54883, 2021.

T. Duong, H. Pham, T. C. Kho, P. Phang, K. C. Fong, D. Yan, Y. Yin, J. Peng, M. Arafat Mahmud, S. Gharibzadeh, B. Abdollahi Nejand, I. M. Hossain, M. Rahman Khan, N. Mozaffari, Y. Wu, H. Shen, J. Zheng, H. Mai, W. Liang, C. Samundsett, M. Stocks, K. McIntosh, G. G. Andersson, U. Lemmer, B. S. Richards, U. W. Paetzold, A. Ho‐Ballie, Y. Liu, D. Macdonald, A. Blakers, J. Wong‐Leung, T. White, K.Weber, K. Catchpole, Effect of Surface Coating versus Bulk Incorporation of 2D Perovskite. Advanced Energy Materials, 10, 1903553, 2020.

J. A. Schwenzer, L. Rakocevic, T. Abzieher, D. Rueda-Delgado, S. Moghadamzadeh, S. Gharibzadeh, I. M. Hossain, R. Gehlhaar, B. S Richards, U. Lemmer, U. W. Paetzold, Toward Stable Perovskite Solar Cell Architectures: Robustness Against Temperature Variations of Real-World Conditions. IEEE Journal of Photovoltaics, 10, 777-784 (2020).

B. Abdollahi Nejand, I. M. Hossain, M. Jakoby, S. Moghadamzadeh, T. Abzieher, S. Gharibzadeh, J. A. Schwenzer, P. Nazari, F. Schackmar, D. Hauschild, L. Weinhardt, U. Lemmer, B. S. Richards, I. A. Howard, U. W. Paetzold, Vacuum‐Assisted Growth of Low‐Bandgap Thin Films (FA0.8MA0.2Sn0.5Pb0.5I3) for All‐Perovskite Tandem Solar Cells. Advanced Energy Materials .10, 1902583, 2020.

S. Moghadamzadeh, I. M. Hossain, T. Duong, S. Gharibzadeh, T. Abzieher, Huyen Pham, H. Hung, P. Fassl, U. Lemmer, B. Abdollahi Nejand and U. W. Paetzold, Triple-cation low-bandgap perovskite thin-films for high-efficiency four-terminal all-perovskite tandem solar cells. J. Mater. Chem. A , 8, 24608–24619, 2020.

S. Moghadamzadeh, I. M. Hossain, M. Jakoby, B. Abdollahi Nejand, D. Rueda-Delgado, J. A. Schwenzer, S. Gharibzadeh, T. Abzieher, M. R. Khan, A. A. Haghighirad, I. A. Howard, B. S. Richards, U. Lemmer and U. W. Paetzold, Spontaneous enhancement of the stable power conversion efficiency in perovskite solar cells. J. Mater. Chem. A, 8, 670–682, 2019.

J. A. Schwenzer, L. Rakocevic, R. Gehlhaar, T. Abzieher, S. Gharibzadeh, S. Moghadamzadeh, A. Quintilla, B. S. Richards, U. Lemmer, U. W. Paetzold, Temperature variation-induced performance decline of perovskite solar cells. ACS applied materials & interfaces, 10 , 16390-16399, 2018.

Conference contributions

S. Gharibzadeh, P. Fassl, I. M. Hossain, P. Rohrbeck, M. Frericks, M. Schmidt, T Duong, M. Rahman Khan, T, Abzieher, B. Abdollahi Nejand, F. Schackmar, O. Almora, T. Feeney, R. Singh, U. Lemmer, J. P. Hofmann, S. A.L. Weber, U. W. Paetzold, Simultaneous Interfacial and Grain-Boundary Passivation for Highly Efficient Inverted Methylammonium-Free Perovskite Solar Cells, Oral talk, 31st International Photovoltaic Science and Engineering Conference online (PVSEC-31), Sydney, Australia (2021).

S. Gharibzadeh, Paul Fassl, Ihteaz M. Hossain, Pascal Rohrbeck, Markus Frericks, Moritz Schmidt, The Duong, Motiur Rahman Khan, Tobias Abzieher, Bahram Abdollahi Nejand, Fabian Schackmar, Osbel Almora, Thomas Feeney, Roja Singh, Uli Lemmer, Jan P. Hofmann, Stefan A.L. Weber, and Ulrich W. Paetzolda, Simultaneous Interfacial and Grain-Boundary Passivation for Highly Efficient Inverted Methylammonium-Free Perovskite Solar Cells, Oral talk, 2D Halide Perovskites International online Conference (2D-HAPES2021).

S. Gharibzadeh, I. M. Hossain, P. Fassl, A. Mertens, S. Schäfer, M. Rienäcker, T.Wietler, R. Peibst, B. S. Richards, U. W. Paetzold, 2D Surface Passivation in Semi-transparent Perovskite Top Solar Cells with Engineered Bandgap for Tandem Photovoltaics, Oral talk, 47th IEEE Photovoltaic Specialists online Conference (PVSC), (2020).

S. Gharibzadeh, B. Abdollahi Nejand, M. Jakoby, T. Abzieher, D. Hauschild, S. Moghadamzadehe, J. A. Schwenzer, P. Brenner, R. Schmager, A. A. Haghighirad, U. Lemmer, B. S. Richards, I. A. Howard, U. W. Paetzold, Ultra-high open circuit voltage beyond the 90% Shockley-Queisser limit in high efficiency wide bandgap perovskite solar cells, Oral talk, Spring Meeting of the European Materials Research Society (EMRS), Nice, France (2019).

S. Gharibzadeh (presented by U. W. Paetzold), B. Abdollahi Nejand, M. Jakoby, T. Abzieher, D. Hauschild, S. Moghadamzadehe, J. A. Schwenzer, P. Brenner, R. Schmager, A. A. Haghighirad, U. Lemmer, B. S. Richards, I. A. Howard, U. W. Paetzold, Ultra-high open circuit voltage beyond the 90% Shockley-Queisser limit in high efficiency wide bandgap perovskite solar cells. Oral talk, 46th IEEE Photovoltaic Specialists Conference online (PVSC), Chicago, U.S (2019)

S. Gharibzadeh, B. Abdollahi Nejand, M. Jakoby, T. Abzieher, D. Hauschild3, S. Moghadamzadeh, J. A. Schwenzer, P. Brenner, R. Schmager, A. A. Haghighirad, L.Weinhardt, U. Lemmer, B. S. Richards, I. A. Howard, U. W. Paetzold, 2D/3D Perovskite Heterostructures for High Performance and High Open Circuit Voltage in Wide-Bandgap Perovskite Photovoltaics, 5th international conference on perovskite solar cells and optoelectronics (PSCO), Lausanne, Switzerland (2019).

S. Gharibzadeh, I. M. Hossain, P. Fassl, B. Abdollahi Nejand, T. Abzieher, J. A Schwenzer1, U. Lemmer, B. S. Richards, U. W. Paetzold, Engineering the Bandgap of Semitransparent Perovskite Solar Cells with 2D/3D Heterostructure for Perovskite-Based Tandem

Photovoltaics, 12th International Summit on Organic and Hybrid Photovoltaics Stability (ISOS-12), Karlsruhe, Germany (2019).

S. Gharibzadeh, B. Abdollahi Nejand, U. W. Paetzold, B. S. Richards, C. Roldán-Carmona, M. Khaja Nazeeruddin, Dual Function of Fullerene Derivative in Lead Bromide Perovskite Solar Cell Demonstrating High Voltage and Fill Factor, 4th international conference on perovskite solar cells and optoelectronics (PSCO), Lausanne, Switzerland (2018).

Acknowledgements

I would like to take the opportunity to thank everyone who supported me on my journey during my Ph.D. My great and deep gratitude goes to my supervisor Tenure-Track-Prof. Dr. Ulrich W. Paetzold who gave me the chance to pursue my Ph.D. in his research group. Thank you for the continuous discussions, guidance, motivation, and enthusiasm in supervising me and also for giving me a lot of freedom in planning and performing my experiments.

Moreover, I would like to offer my special thanks to Prof. Dr. Bryce S. Richards and Prof. Dr. Uli Lemmer for their continuous support during my time at the Institute of Microstructure Technology and the Light Technology Institute at KIT. Furthermore, I would like to thank Prof. Dr. Michael Saliba for taking his time and agreeing to be my second reviewer.

I am grateful for the stunning working atmosphere and the numerous fruitful discussions and support in our group with Ihteaz, Bahram, Paul, Fabian, Roja, Thomas, Marco, Sara and other colleagues in taskforce meeting. A special thanks go to my close friends at the institute, Ihteaz Hossain, Fabian Schackmar, Roja Singh, Thomas Feeney who were always there to provide me with intellectual and emotional support whenever it was needed. They made every day at work fun even if experiments did not work out and without them, the time during my Ph.D. would not have been exciting as it has been. It will always delight me to look back at the countless fun moments we shared. Also, the leisure activities beyond the scope of work with Ihteaz, Roja, Thomas, Bahram, Pariya, Fabian, Isabel, and Leo made the past 4 years very special to me. I would also like to take the opportunity to thank my Iranian friends: Bahram, Sara, Pariya and Ali who have been there always like my family.

Additionally, I am immensely grateful to all my colleagues during my thesis. I want to thank Tobias, Jonas, Alex, Felix, Ahmed, Simon, Helge, Marco, Hang, David, Adrian, Philip, Leo, Jan, Robert, Julie, Diana, Raphael, Benni, Donie and indeed, all other former and current group members as well. It was truly an enjoyable time with many scientific discussions and lots of fun activities.

I also wish to thank Karlsruhe School of Optics and Photonics (KSOP) for providing a graduate program and for the great organization of many scientific and social events. I am particularly grateful to all the external collaboration partners, namely Dr. The Duong (ANU), Dr. Erik Ahlswede (ZSW), Michael Rienaecker (ISFH), Dr. Robby Peibst (ISFH), and Dr. Tobias Wietler (ISFH).

I sincerely acknowledge the scientific collaboration and effort that I received from Dr. Amir. A. Haghighirad, Dr. Ian Howard, Marius Jakoby, Dr. Motiur Rahman Khan, Dr. Dirk Hauschild, Dr. Lothar Weinhardt.

Finally, I want to express my sincere gratitude to my beloved parents, especially my mother. A single word of gratitude is not enough to acknowledge the support she has given me all

throughout my life. My special thanks go to my lovely boyfriend for his love, affection, support, and understanding that help to keep my enthusiasm alive and push me forward.